Constraining star formation rates and AGN feedback in high-z radio galaxies

Theresa Maria Falkendal

École Doctorale d'Astronomie et Astrophysique d'Île-de-France

SORBONNE UNIVERSITÉ

DOCTORATE THESIS

to obtain the title of Doctor of the
Sorbonne Université in Astrophysics

Presented by
Theresa Maria FALKENDAL

Constraining star formation rates and AGN feedback in high-z radio galaxies

Thesis Advisors: Matt LEHNERT, Carlos DE BREUCK, Joël VERNET

prepared at Institut d'Astrophysique de Paris, CNRS (UMR 7095),
Sorbonne Université

Composition of the jury

Reviewers:	Susanne AALTO	-	Chalmers University of Technology , Gothenburg, Sweden
	Mark ALLEN	-	Strasbourg Astronomical Data Centre, Strasbourg, France
Advisor:	Matt LEHNERT	-	IAP, Paris, France
Co-advisor:	Carlos DE BREUCK	-	European Southern Observatory, Garching, Germany
	Joël VERNET	-	European Southern Observatory, Garching, Germany
President:	Frédéric DAIGNE	-	IAP, Paris, France
Examinators:	David ELBAZ	-	CEA, Saclay, France
	Guillaume DROUART	-	Curtin University, Perth, Australia

Abstract

The evolution of galaxies is something that is still not well understood. Events such as, galaxy mergers, gas accretion from the cosmic web, metal enrichment and galactic nuclear activity affects further galaxy growth and shapes the evolution of galaxies. The cosmic star formation rate density peaks between $1 < z < 3$. It is therefore important to investigate the high-z Universe and the mechanisms which triggers or quenches star-formation. The impact of active galactic nuclei (AGN) have been hypothesized through cosmological simulations to be crucial in quenching the star-formation rate, but the mechanism behind this is not understood in detail. This is where high-z observations of AGN feedback in galaxies are important, to put tight constants on the Physics at play. In this thesis I investigate the effects of in-situ AGN feedback by studying high-z radio galaxies (HzRGs). These objects provide unique laboratories to study the interplay between AGN, gas, stars and feedback processes.

Millimeter Astronomy has recently seen major advances due to the development of the ALMA telescope, which opens up the possibility to probe the cold Universe at resolutions and depths never seen before. During my thesis I utilize the capabilities of ALMA by probing dust emission in a sample of 25 HzRGs at $1 < z < 5.2$. I combine these new observations with previous data to constrain the star formation rates by multi-wavelength spectral energy distribution (SED) fitting. The ALMA data reveal that the morphology of the $\sim$1 mm continuum emission can be complicated, with contributions from several thermal dust emission components and/or synchrotron emission. The sensitivity and spatial resolution of the ALMA data required me to develop a SED fitting routine that can combine multi-resolution photometric observations and simultaneously fit the SED of galaxies detected in multiple components. We disentangle the far-infrared continuum emission of these 25 galaxies into dust heated by star-formation and AGN, as well as from contributions from synchrotron emission. This leads to new much more constraining estimates of the star formation rates of HzRGs, on average 7 times lower compared to estimates based only on *Herschel*. The low star-formation rates in these objects compared to the main-sequence of star forming galaxies show that HzRGs seem to be on their way of being quenched. We might therefore be observing the effect of the AGN suppressing the growth of the host galaxy.

In the second part of the thesis, I explore the possibilities of constraining the gas Physics of the host galaxy and the halo gas by combining MUSE and ALMA data cubes. MUSE is also a relatively new instrument with impressive capabilities to probe ionized gas at rest-frame ultraviolet wavelengths in the high-z Universe. I show extended ionized gas around the HzRG 4C 19.71, where the most remarkable feature is the most distant extension of the C IV gas beyond the radio lobes. This gas is quiescent and coincide with a molecular gas reservoir detected with ALMA in [C I]. These observations show the power of multi-wavelength observations, but also the limitations of putting constraints when only a few emission lines are available.

These studies show how new more detailed observations help constrain important properties of HzRGs. These objects are being revealed to be more complicated than previously thought, showing large differences one source to another and new data sometimes raise more questions than they answer. But these type of studies have the potential of increasing our understanding of the physically mechanisms for AGN feedback and the interplay between the AGN, host galaxy and the halo gas.

Résumé

L'évolution des galaxies n'est toujours pas bien compris. Des évènements tel que des fusions de galaxies, l'accrétion à partir de la toile cosmique, l'enrichissement des métaux et l'activité des noyaux affecte la croissance supplémentaire et façonne l'évolution des galaxies. Le taux de formation d'étoiles culmine entre $1 < z < 3$. Il est donc important d'étudier l'Univers à grand z et les méchanismes qui déclenchent ou étouffent la formation d'étoiles. Les simulations cosmologiques prévoient que l'influence des noyaux actifs de galaxies est primordial dans l'étouffement du taux de formation d'étoiles, mais les détails de ce méchanisme restent à élucider. C'est ici que les observations de la rétroaction à grand z sont primordiaux pour contraindre la Physique. Dans cette thèse, j'étudie les effets de la rétroaction in-situ en utilisant les radiogalaxies distantes. Ces objets fournissent des laboratoires uniques pour étudier l'interaction des noyaux actifs des galaxies, le gaz, les étoiles et les processsus de rétroaction.

L'astronomie (sub)millimétrique a fortement progressé grâce à l'arrivée du télescope ALMA, qui permet les études de l'Univers froid à des résolutions et profondeurs jamais atteints auparavant. Dans cette thèse, j'utilise les capacités d'ALMA en sondant l'émission des poussières dans un échantillon de 25 radiogalaxies à $1 < z < 5.2$. Je combine ces nouvelles observations avec des données précédentes afin de contraindre les taux de formation d'étoiles en utilisant l'ajustement des distributions d'énergie spectrales (SED) multi-longeur d'ondes. Les données ALMA montrent que la morphologie de l'émission continu à $\sim$1 mm peut être compliquée, avec des contributions de plusieurs componsantes d'émission thermique de poussières et/ou du synchrotron. La sensibilité et la résolution spatiale d'ALMA nécessitaient que je développe une routine d'ajustement du SED pouvant combiner des observations photométriques multi-résolutions et ajuster simultanément les SED des galaxies détectés dans multiples composantes. Nous démèlons l'émission du continu infrarouge lointain de ces 25 galaxies en poussières chauffées par formation d'étoiles et noyau actif de galaxie, ainsi que des contributions de l'émission synchrotron. Ceci mène à des nouvaux taux de formation d'étoiles beaucoup plus contraignantes dans ces radiogalaxies, en moyenne 7 fois plus faibles comparés aux estimations basées seulement sur les données *Herschel* sondant le pic de l'émission thermique. Les faibles taux de formation d'étoiles comparés à la séquence principale des galaxies formant des étoiles montrent que les radiogalaxies sont en route d'être étouffées. On pourrait donc observer l'effet du noyau actif supprimant la croissance de la galaxie hôte.

Dans la deuxième partie de la thèse, j'explore les possibilités de contraindre la Physique des gaz de la galaxie hôte en combinant les cubes de données MUSE et ALMA. MUSE est aussi un nouvel instrument avec des capacités impressionnantes pour sonder le gaz ionisé aux longeurs d'onde ultra-violets au repos dans l'Univers lointain. J'étudie le gaz ionisé dans la radiogalaxie 4C 19.71, où la caractéristique la plus remarquable est l'extension la plus éloignée du gaz C IV au delà des lobes radio. Ces observations montrent la puissance des observations multi-longeur d'onde, mais aussi les limitations à mettre des contraintes quand seulement quelques raies d'émission sont disponibles.

Ces études montrent comment des observations plus détaillées peuvent contraindre les propriétés des radiogalaxies. Ces objets deviennent de plus en plus complexes à mesure que de nouvelles données deviennent disponibles. Les galaxies montrent égallement de grandes différences en les regardant source par source, et les nouvelles données soulèvent parfois plus de questions qu'elles ne répondent. Mais ce genre d'études ont le potentiel d'améliorer notre compréhension

des méchanismes physiques de la rétroaction et l'interaction entre la galaxie hôte et le milieu circumgalactique.

Contents

List of Figures

List of Tables

List of Abbreviations

AGN	**A**ctive **G**alactic **N**uclei
BH	**B**lack **H**ole
BLR	**B**road **L**ine **R**egion
BCG	**B**rightest **C**luster **G**alaxies
CGM	**C**ircum**g**alactic **M**edium
CMB	**C**osmic **M**icrowave **B**ackground
CSP	**C**omposite **S**tellar **P**opulation
DSFG	**D**usty **S**tar-**F**orming **G**alaxy
FIR	**F**ar-**I**nfra**r**ed
FR-I	**F**anaroff-**R**iley class **I**
FR-II	**F**anaroff-**R**iley class **II**
FSRQ	**F**lat-**S**pectrum **R**adio **Q**uasars
FWHM	**F**ull **W**idth at **H**alf **M**aximum
HzRG	**H**igh-redshift **R**adio **G**alaxy
IGM	**I**nter**g**alactic **M**edium
IMF	**I**nitial **M**ass **F**unction
ISM	**I**nter**s**tellar **M**edium
IR	**I**nfra**r**ed
ISRF	**I**nter **S**tellar **R**adiation **F**ield
MCMC	**M**arkov **C**hain **M**onte **C**arlo
MS	**M**ain **S**equence (of star-forming galaxies)
NIR	**N**ear-**I**nfra**r**ed
NLR	**N**arrow **L**ine **R**egion
PAHs	**P**olycyclic **A**romatic **H**yrdocarbons
PDR	**P**hoton-**D**ominated **R**egion
SED	**S**pectral **E**nergy **D**istribution
SF	**S**tar-**F**ormation
SFR	**S**tar-**F**ormation **R**ate
SFRD	**S**tar-**F**ormation **R**ate **D**ensity
SMBH	**S**uper **M**assive **B**lack **H**ole
sSFR	**s**pecific **S**tar-**F**ormation **R**ate
SN	**S**uper**n**ova
SSP	**S**imple **S**tella **P**opulation
UV	**U**ltra**v**iolet

List of Symbols

A_λ	Extinction	mag
AU	Astronomical Unit	$1.49597871 \times 10^{13}$ cm
c	Speed of light	299792.458 km s^{-1}
eV	Electronvolt	$1.6021766208 \times 10^{-19}$ J
F_ν	Flux density per unit frequency	erg s^{-1} cm^{-2} Hz^{-1}
F_λ	Flux density per unit wavelength	erg s^{-1} cm^{-2} Å^{-1}
h	Plank's constant	6.626×10^{-34} m^2 kg s-1
I_ν	Specific intensity per unit frequency	erg s^{-1} cm^{-2} Hz^{-1} sr^{-1}
I_λ	Specific intensity per unit wavelength	erg s^{-1} cm^{-2} Å^{-1} sr^{-1}
j_ν	Emission coefficient	erg s^{-1} cm^{-3} Hz^{-1} sr^{-1}
Jy	Jansky	10^{-23} erg s^{-1} cm^{-2} Hz^{-1}
$L_\odot$	Solar luminosity	3.826×10^{33} erg s^{-1}
L_{bulge}	Luminosity of galaxy bulge	$L_\odot$
L^{IR}_{AGN}	Infrared luminosity of AGN component	$L_\odot$
L^{IR}_{SF}	Infrared luminosity of star formation component	$L_\odot$
$M_\odot$	Solar mass	1.989×10^{33} g
$M_\bullet$	Mass of black hole	$M_\odot$
M_{bulge}	Mass of the galaxy bulge	$M_\odot$
$\dot{M}^{acc}_{BH}$	Black hole mass accretion rate	$M_\odot$ yr^{-1}
pc	Parsec	$3.08567758 \times 10^{18}$ cm
S_ν	Source function	erg s^{-1} cm^{-2} Hz^{-1} sr^{-1}
sr	Steradian, unit of solid angle	
n	Particle density	cm^{-3}
T	Temperature	K
Å	Ångström	10^{-8} cm
z	Redshift	
X_{CO}	Co-to-H_2 mass conversion factor	K km s^{-1}
α	Spectral index of synchrotron slope	
α_{CO}	Co-to-H_2 mass conversion factor	$M_\odot$ pc^{-2}(K km s^{-1})$^{-1}$
α_ν	Absorption coefficient	cm^{-1}
β	Dust emissivity	
γ	Slope of AGN power law	
ϵ	Efficiency factor of black hole	~ 0.1
θ	Angular resolution	arcsec
κ_ν	Mass absorption coefficient	cm^2 g^{-1}
κ^{Bol}_{AGN}	Bolometric correction factor	
λ	Wavelength	Å
ν	Frequency	Hz
σ	Velocity dispersion	km s^{-1}
σ_ν	Effective cross section	cm^2
τ_ν	Optical depth	

Chapter 1

Introduction

1.1 Galaxy evolution

Galaxies are some of the most fascinating objects in the Universe. It is not difficult to understand why many people find galaxies so enchanting, since they host the conditions where stars can be born and which in turn make planet formation possible. The human curiosity of understanding our surroundings is the probably the origin of our strive to understand galaxy evolution, which is a complex and difficult task. Nevertheless, today galaxy evolution is one of the most active areas in astrophysics research. Progress is made by combining observational results with theoretical models and cosmological simulations. All of these parts are needed to understand how the first galaxies formed in the early Universe and then evolved into the vast zoo of galaxies we observe in the local Universe.

Ever since the discovery of fast-moving ($v > 1000\,\mathrm{km\,s^{-1}}$) stars (Eckart & Genzel 1997; Ghez et al. 1998) around the compact radio source observed in the center of our own galaxy, the Milky Way, it is believed that this compact object is a supermassive black hole (SMBH). It was named Sagittarius A* (Sgr A*) and has a mass of $M_\bullet = 4.31 \pm 0.38 \times 10^6\,M_\odot$ (Gillessen et al. 2009). It is also now commonly believed that all galaxies host SMBHs in their centers and that the black holes are part of the lifecycle and evolution of galaxies. Supermassive means more massive than ordinary-mass black holes ($\sim$10 $M_\bullet$) which are a possible end product of stellar evolution.

In the local Universe, the most common types of galaxies are "normal" star-forming galaxies, such as the Milky Way, where the SMBH that resides inside in the galaxy is quiescent, meaning it is not accreting substantial amounts of matter. Other, more extreme types of galaxies, contain active galactic nuclei (AGNs) and are much rarer. In the high-redshift Universe on the other hand, the SMBHs seem to be much more active and galaxies with AGNs and dusty star-forming galaxies (DSFGs) are much more common. Understanding the connection between the SMBHs and their host galaxies is one of the most important aspects of modern research in galaxy evolution and is the main topic of this thesis.

1.1.1 Coevolution of supermassive black holes and galaxies

The growths of galaxies are traced via star formation and the build up of galaxies has changed over cosmic time. A common way of quantifying this is by studying the star-formation rate density (SFRD), which represents the total star-formation rate (SFR) occurring per unit time and volume at a given epoch. Lilly et al. (1996) and Madau et al. (1996) were the first to find that there is a steep rise in the SFRD by a factor of 10 between redshifts 0 and 1 and that the SFRD peaks between $z = 2$ and $z = 3$. At higher redshifts, there first seemed to be a clear decline of the SFRD. For some newer samples, the SFRD rather seems to have a shallow slope (e.g., Hopkins & Beacom 2006; Fardal et al. 2007; Barger et al. 2014; López Fernández et al. 2018). The change in SFR history is by now a well established observational result. Similar changes in growth rate over cosmic time have also been observed for SMBHs, traced by AGNs. From X-ray and optical observations of AGNs, Shankar et al. (2009) estimated the growth of the black hole mass function and found that

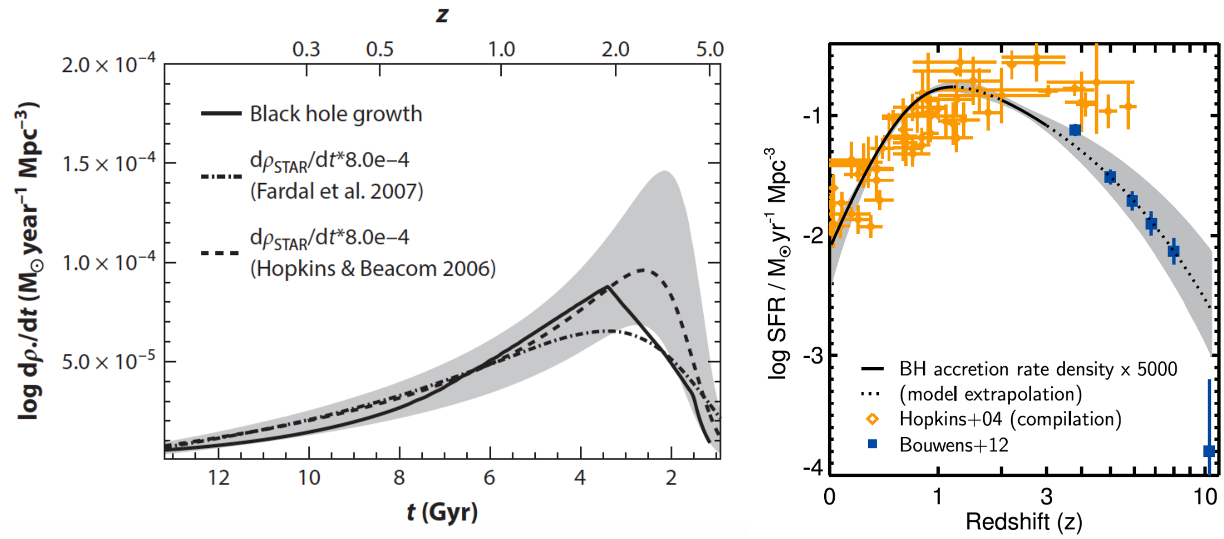

FIGURE 1.1: Black hole accretion rate compared to star-formation rate history. *Left:* average BH accretion rate compared to the SFRD by Hopkins & Beacom (2006) and Fardal et al. (2007) scaled by the factor $M_\bullet/M_{\rm star} = 8 \times 10^{-4}$. Figure reprint from review by Heckman & Best (2014) (originally published by Shankar et al. 2009). *Right:* Black hole accretion rate scaled by a factor of 5000 and compared to the cosmic SFR reported by Hopkins (2004) and Bouwens et al. (2012). Reprinted from Kormendy & Ho (2013) (updated from Aird et al. 2010).

the integrated AGN emissivity closely tracks the cosmic star formation history. In Fig. 1.1, the average black hole accretion rate is compared to the SFR given by Hopkins & Beacom (2006) and Fardal et al. (2007), and they remain roughly proportional. Similar agreement of the black hole accretion rate determined from X-rays and star-formation rates were also reported by Aird et al. (2010). The close agreement between the inferred star formation histories and black hole growth for at least the last $\sim$11 Gyrs seems to suggest that the processes are linked, or at the very least, that we are observing a remarkable coincidence.

Another empirically driven connection between the BH and host galaxy is the famous $M_\bullet$–σ and $M_\bullet - L_{\rm bulge}$ relationship. Magorrian et al. (1998) were the first to show on a larger sample (32 galaxies), that there was a linear relationship between the mass of the black hole and the luminosity of the bulge. This provided a confirmation of previous studies of small samples. The $M_\bullet - L_{\rm bulge}$ relationship was extended to also be expressed in terms of $M_{\rm bulge}$. By deriving bulge masses via the virial theorem, dynamical modeling, or from mass-to-light ratios, it was shown that most results were consistent with $M_\bullet \propto M_{\rm bulge}$. About 10 years later, another observational realization was made, when Ferrarese & Merritt (2000) and Gebhardt et al. (2000) showed that there also was a correlation between the mass of the BH and the velocity dispersion of the bulge. The $M_\bullet$–σ relationship is also linear and has a smaller scatter of only 0.3 dex. Fig 1.2, reprinted from the excellent review by Kormendy & Ho (2013), shows a more up to date version of the $M_\bullet - L_{\rm bulge}$ and $M_\bullet$–σ relations, which includes elliptical galaxies and classical bulges (which are indistinguishable from elliptical galaxies, except that they are embedded in disks). It is important to distinguish classical bulges from pseudobulges (which are disk-grown), since BHs do not correlate with galaxy disks, only the bulges (Kormendy & Ho 2013). The relationship has been now been tested for a range of galaxies with and without AGNs. Galaxies with AGN show a larger scatter in the $M_\bullet$–σ relation than inactive galaxies. These observations imply, that the BHs correlate tightly with elliptical galaxies and classical bulges, but not with disk properties. Because of the tight $M_\bullet$–σ relationship that we see in the local Universe, BH growth and bulge formation seems to be closely linked.

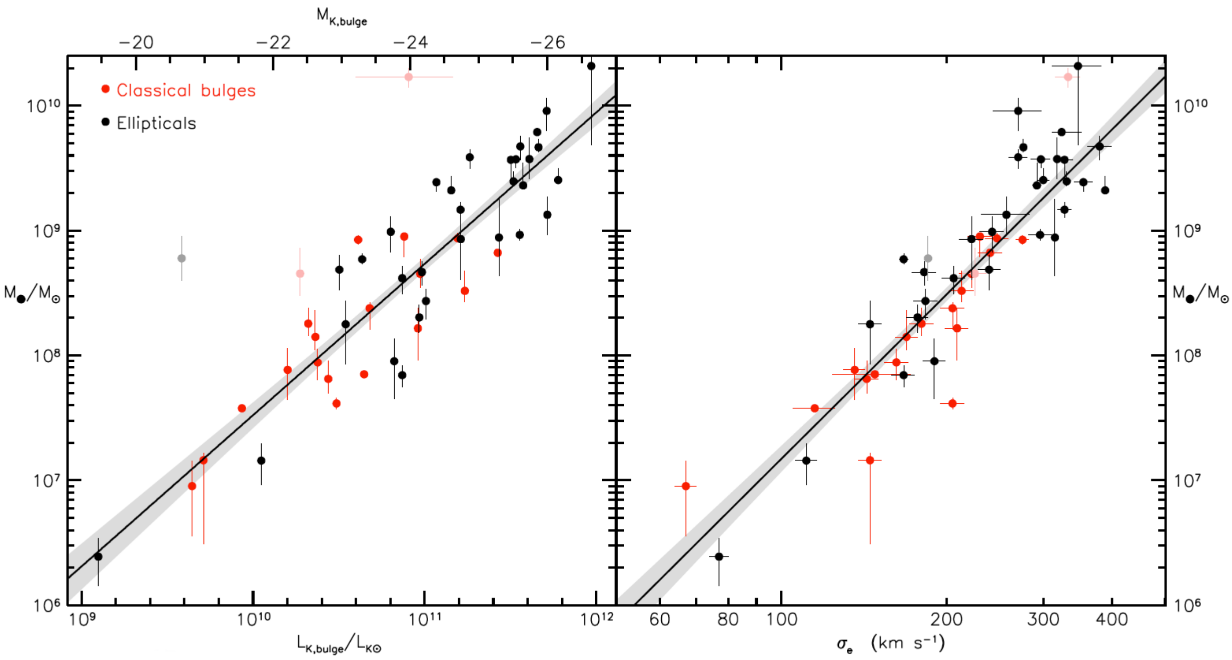

FIGURE 1.2: The $M_\bullet$–$M_{\mathrm{K,bulge}}$ and $M_\bullet$– σ_{e} correlation for ellipitcal galaxies and classical bulges (classified as being indistinguishable from elliptical galaxies, except that they are embedded in disks), with fitted slopes and gray shaded region showing the 1σ of the fits. Figure reprinted from review by (Kormendy & Ho 2013)

However, a tight correlation does not necessarily mean that the relation arises due to AGN feedback. But galaxy evolution models still need to capture this relationship and explain how it arises.

1.1.2 AGN Feedback

Indirect observations strongly suggest that the growth of the SMBH and its host galaxy are connected. The hypothesized process that would regulate the growth of the black hole and stellar components of the galaxy is called AGN feedback. It is thought that energy and/or momentum of the accreting SMBH gets transfered to the galaxy. By coupling with the gas, it influences the conditions for further growth of stars and even the growth of the black hole itself, as both these processes are fueled by gas. One very simple argument for the possibility of the active SMBH affecting its host galaxy is the binding energy of the galactic bulge in comparison to the energy output of the SMBH. The binding energy of the galactic bulge can be approximated as

$$E_{\mathrm{bulge}} \approx M_{\mathrm{bulge}}\,\sigma^2,$$

where σ is the velocity dispersion of the bugle. This equation is derived from the gravitational binding energy $E_{\mathrm{grav}} = GMm/r$ and Kepler's third law, where the centripetal force ($F_{\mathrm{cent}} = mv^2/r$) equals the gravitational force ($F_{\mathrm{grav}} = GMm/r^2$) as $GMm/r = mv^2$. This gives $E_{\mathrm{grav}} = mv^2$ and the binding energy of the galaxy bulge can be approximated as $M_{\mathrm{bulge}}\,\sigma^2$, if $m \approx M_{\mathrm{bulge}}$ and $v^2 \approx \sigma^2$.

The energy that the SMBH releases can be estimated from its accretion energy. If a radiative efficiency of 10% is assumed, then the total energy released by the growth of the black hole can be approximated by,

$$E_{\mathrm{BH}} \approx 0.1\,M_\bullet\,c^2.$$

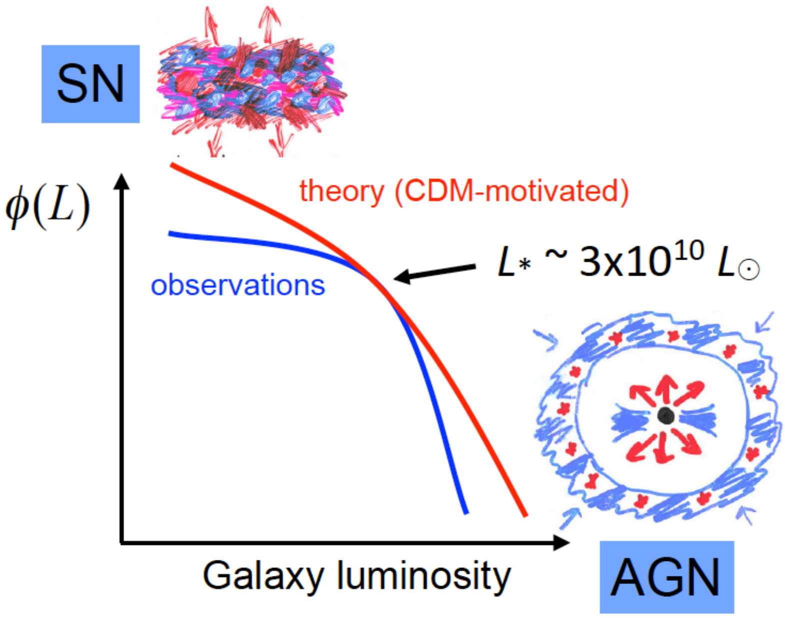

FIGURE 1.3: Schematic representation of the difference between the observed galaxy luminosity function (blue line) and the theoretically predicted one (red line). By invoking supernova and AGN feedback in semi-analytic models, it is possible to closer reproduce observed galaxy properties. Figure reprinted from (Silk & Mamon 2012).

This comes from the energy released by a mass m accreting onto the surface of a central mass M with radius R, $\Delta E_{\mathrm{acc}} = E_{\mathrm{initial}} - E_{\mathrm{final}} = -GmM/r - (-GmM/R) = GmM/R$. For a black hole, the radius R is the Schwarzschild radius $r_{sch} = 2GM/c^2$, which gives $\Delta E_{\mathrm{acc}} = mc^2/2$. Now, not all accreted mass will be radiated away, otherwise the black hole would not grow. This is approximated by a dimensionless quantity ϵ, $\Delta E_{\mathrm{acc}} = \epsilon mc^2$. This means that the total radiation energy of the black hole can be approximated by $E_{\mathrm{rad}} \approx \epsilon M_\bullet c^2$, if the accreted mass is $m \approx M_\bullet$.

From the $\mathrm{M}_\bullet$-σ relationship, the mass of the black hole can be related to the mass of the bulge, $\mathrm{M}_\bullet \approx 1.3 \times 10^{-3}\ \mathrm{M}_{\mathrm{bulge}}$(Kormendy & Gebhardt 2001; Merritt & Ferrarese 2001; Häring & Rix 2004), which gives $E_{\mathrm{BH}}/E_{\mathrm{bulge}} \approx 1.3 \times 10^{-4}(c/\sigma)^2$. For a typical velocity dispersion of $\sigma < 300\,\mathrm{km\,s^{-1}}$, we get $E_{\mathrm{BH}}/E_{\mathrm{bulge}} > 90$. In this simple order of magnitude estimation, the SMBH radiation energy is 90 times the binding energy of the bulge. Even if only a small fraction of the radiation energy from the SMBH gets transfered to the gas of the host galaxy, it is enough to have a substantial impact. While there is enough energy to influence the galaxy, it is important to understanding the mechanisms for transferring the energy from the AGN to the galaxy, in order to quantify the impact of SMBHs on galaxy evolution. A similar energy argument comes from the now 20 year old seminar paper by Silk & Rees (1998). They argue that the energy released from the accretion of matter onto the black holes is sufficient to drive outflows of gas with velocities high enough to become entirely unbound from their host galaxies. Their paper indicates how AGN feedback by means of outflows could potentially have a significant impact on the evolution of the host galaxies, and has since then inspired many follow up publications (Harrison et al. 2018).

Besides simple energy arguments and indirect observations, AGN feedback has also been shown to be an important ingredient in cosmological simulations, and necessary for reproducing realistic galaxy properties. Semi-analytical models have been successful in characterizing the typical galactic halo and stellar mass by requiring that cooling within a dynamical time is a necessary condition for efficient star formation. From the inferred mass-to-light ratio it is possible to compare the halo mass function to the observed quantity, which is the galaxy luminosity function ($\phi(L)$).

The models are able to reproduce the observed values. However, as schematically illustrated in Fig. 1.3, for the low and high mass ends, semi-analytic models predict too many small galaxies and too many big galaxies. The solution to lower the discrepancies between the observed galaxy luminosity function and the one inferred from models, is to invoke feedback mechanisms. The two major ones are supernova (SN) feedback and AGN feedback (Benson et al. 2003). SN feedback has little impact on massive galaxies, but is efficient in regulating the luminosity function of low mass galaxies. In short, more efficient SN feedback leads to fewer low mass galaxies. For the high mass end, the AGN feedback from SMBHs is much more important. The feedback from SMBHs occurs through both the radiative mode (also known as quasar mode, acting via photons) and the kinetic mode (also referred to as radio jet mode, acting via energetic particles). Both modes are important, but act on different time scales and during different epochs. The radiative mode typically operates in the bulge when the SMBH produces winds, which interact with the gas content of the galaxy. This happens when the SMBH is sufficiently massive and the Eddington luminosity is high enough to eject gas. Winds then occur and are thought to terminate star-formation. This is called the early feedback quasar mode. In later epochs, the kinetic feedback becomes more important for SMBHs, which develop powerful jets that propagate outwards. This type of feedback operates on much larger scales. The jets are hypothesized to heat up the halo gas, which prevents cooling and further gas accretion. This stops the supply of fuel to the galaxy and quenching occurs. For a recent review on this topic, see Silk & Mamon (2012).

The scales, on which both SN and AGN feedback act, are unresolved in simulations. Also, the mechanisms of AGN feedback, and how the energy couples to the galaxy, are still not fully understood. The feedback is therefore artificially added to simulations. This is where direct, in situ, observations are needed to constrain the impact of an active SMBH on the host galaxy. This is a huge topic in itself, and possible effects of AGN feedback have been observed through many ways. X-ray observations of hot atmospheres around galaxies and clusters have pointed towards mechanical feedback from the radio jets produced by the AGN as being an important source of heating and driving metals, enhancing the halos gas. The heating slows down the cooling rate of the gas in the galactic atmosphere, and may be enough to suppress star formation (McNamara & Nulsen 2012). Powerful outflows have been observed in optical emission lines. They showed large-scale kinematics consistent with being AGN driven though mechanical energy injection from the radio jets (Nesvadba et al. 2006). Evidence for jet driven outflows have also been seen in absorption (Lehnert et al. 2011; Morganti et al. 2005). This suggests that radio-loud AGNs can have a large impact of the evolution of the host galaxy. Large-scale outflows from galaxies with low radio luminosities, have been observed in optical emission. Here, the outflows were instead radiatively driven by the AGN and/or supernovae winds (e.g., Alexander et al. 2010). Outflows are not only seen in emission from ionized lines, but also from molecular gas tracers. These molecular outflows are massive enough to strip away the cold gas reservoir and shutting down the star formation (e.g., Feruglio et al. 2010; Sturm et al. 2011). Even though there is growing evidence of AGN driven outflows, the direct link to quenching is still not well understood. This is where observations and theoretical modeling are both needed to get a more complete understanding of the interplay between the SMBH, the host galaxy, and the surrounding large-scale structure of gas.

1.2 Interaction of photons and matter

Our main source of information about astrophysical objects comes from photons. Because of the huge distances involved, it is not possible to send probes further out than our own solar system. Besides high energy particles like neutrinos (created by radioactive decay, e.g. in stars, supernova explosions or the spin-down of a neutron star) and the very recent detection of gravitational waves (Abbott et al. 2016) (produced when two massive objects merge), observations of photons remain our only way of gathering information about the Universe. It is thus essential to understand the physics behind the production of photons and how they interact with matter on their way through space, before they are detected by our telescopes. This is an extremely complex task and in many cases some details are impossible to know, for example the exact composition of gas and dust in the Universe is unknown. But even though there are many limitations, studying photons and how they interact with matter can reveal a lot of the physics at play in the Universe. At its most fundamental level, the interaction between photons (or radiation) and matter falls in one of three categories:

- scattering: photon + matter $\rightarrow$ photon + matter
- absorption: photon + matter $\rightarrow$ matter
- emission: matter $\rightarrow$ photon + matter

The probability of absorption or emission of photons by atoms or molecules are quantified by the Einstein coefficients. Einstein A_{ul} coefficients is related to the spontaneous emission from an upper energy level (u) to a lower (l). Einstein B_{ul} and B_{lu} coefficients are related to the rate of absorption and stimulated emission, respectively. Emission (or absorption) from atoms or molecule occur in spectral line at frequency ν, given by the difference in energy $E_u - E_l = h\nu$. The emission and absorption at ν is described by the j_ν emission and α_ν absorption coefficients related to the Einstein coefficients as,

$$j_\nu = \frac{h\nu}{4\pi} n_u A_{ul}, \qquad \alpha_\nu = \frac{h\nu}{4\pi}(n_l B_{lu} - n_u B_{ul}), \tag{1.1}$$

where n_u and n_l are the density of atoms in the upper and lower energy state, respectively. The change in number density of the lower state due to spontaneous emission, stimulated emission and absorption is given by

$$\frac{dn_l}{dt} = A_{ul} n_u, \quad \frac{dn_l}{dt} = B_{ul} n_u \rho(\nu) \quad \text{and} \quad \frac{dn_l}{dt} = -B_{lu} n_l \rho(\nu) \tag{1.2}$$

respectively, where $\rho(\nu)$ is the spectral energy density of the radiation field at ν. In thermal equilibrium the net change in n_l does not change and you have

$$0 = A_{ul} n_u + B_{ul} n_u \rho(\nu) - B_{lu} n_u \rho(\nu), \tag{1.3}$$

where the amount of emission and absorption balance each other.

1.2.1 Scattering

Scattering can be divided into two different types, elastic (photon does not lose energy) and in-elastic (photon changes its energy). The three main elastic scattering processes are Thomson scattering, Rayleigh scattering and resonant scattering. The main in-elastic scattering process is Compton scattering.

Thomson scattering is the elastic scattering of a photon (γ) by a free charged particle (typically an electron)

$$\gamma + \mathrm{e} \rightarrow \gamma + \mathrm{e},$$

where the particle kinetic energy and photon frequency do not change. This is valid as long as the energy of the photon is much lower than the rest-mass energy of the particle. When an electron interacts with a photon, the electric and magnetic component of the wave accelerate the particle. The electron, in turn, radiates away a photon, in effect the original wave/photon is scattered. When a photon is Thomson scattered, the light is polarized to different degrees, depending on the scattering direction. This happens, because the electron moves in the direction of the oscillating electric field of the photon, resulting in electromagnetic dipole radiation. The electron emits radiation preferably perpendicular to its motion. This is because light cannot be polarized along its direction of motion. If the electron emits radiation 90 degrees from its motion, the scattered light is linear polarized. One astrophysical example of Thomson scattering is the cosmic microwave background (CMB) which is observed to be partly polarized (Kovac et al. 2002). The CMB is the electromagnetic radiation we observe from the epoch of recombination, when the Universe became cold enough for electrons and protons to recombine to form neutral hydrogen. The Universe became transparent and photons could "escape", which is what we now see as the CMB radiation, and it is polarized because the photons Thomson scattered off free electrons on the surface of last scattering.

Rayleigh scattering is the elastic scattering of photons by particles much smaller than the wavelength of the photon. Rayleigh scattering is stronger, the smaller the particle. It has a λ^{-4} wavelength dependence. This effect causes the sky to appear blue, because the blue light from the Sun is more efficiently scattered than red light.

Resonant scattering or bound-bound scattering is the scattering of photons by electrons bound to atoms or ions (X),

$$\gamma + X \rightarrow X^{*} \rightarrow \gamma + X,$$

where the atom get excited to a higher energy state (X^{*}) and then emits a photon of the same energy through radiative decay. For resonance scattering to be prominent, the gas has to be diffuse. Then, spontaneous decay can happen before the atom or ion is collisionally excited or de-excited in which case the photon energy is changed or "lost" and the resonance effect stops. An example of resonant scattering is the so called Lyα forest. This is a multiple "absorption line" feature seen in the spectra of some quasars. Along our line-of-sight to the quasar, multiple gas clouds containing neutral hydrogen scatter Lyα photons. If the the clouds are at different redshifts, they appear as absorption lines at different positions of the background quasar's spectrum. The photons are not actually absorbed, but scattered out of the line-of-sight, which is why each individual cloud appears as an "absorption line".

Compton scattering is the in-elastic scattering of a photon by a free electron, where the photon transfers part of its energy to the electron and the scattered photon has an increased wavelength,

$$\gamma + \mathrm{e} \rightarrow \gamma' + \mathrm{e}'.$$

Compton scattering is the high-energy case of Thomson scattering. This way of looking at it, the electron is assumed to be in rest. This is not a very realistic case when it comes to astrophysics, as gas with free electrons is in motion. If the electrons have a high kinetic energy, then it is also possible for them to transfer energy to the photons. This is called **inverse Compton scattering** and is an important process, because it can up scatter photons to very high energies (X-rays). This is thought to happen in accretion disks around AGNs and for synchrotron radiation. Cosmic microwave background (CMB) photons can also be scattered to higher energies while passing though hot gas surrounding galaxies. This is known as the Sunyaev-Zel'dovich effect.

1.2.2 Absorption

Absorption occurs when photons are absorbed by matter. The gain of energy from the photon can have three main effects on the matter.

- Heating the absorbing medium: excitation of gas or heating of dust grains
- Acceleration of the absorbing medium: radiation pressure
- Changing the state of the absorbing medium: ionization (transition from neutral to ionized), sublimation (transition from solid to gas) or dissociation (transition from molecule to atoms)

Absorption is very important in astrophysics and opens up several diagnostics of physical components that would otherwise be hard to observe. One example is the heating of dust by absorption of photons produced by young stars, as discussed in detail in Sect. 1.3.2. Without this process, it would be difficult to observe dust in the Universe. Another powerful tool is line absorption against a background ionizing source. If one knows the intrinsic shape of the spectrum, it is possible to detect the presence of matter and its properties, e.g. abundance of metals in stellar atmospheres or gas in the line-of-sight of a quasar. The metals absorb photons at specific wavelengths and the shape of the absorption line profile contains information about the abundance and kinematics of the absorbing material. By studying absorption, is it possible to gain information about gas, which is often too diffuse to be detected in emission. This is discussed more in Sect. 1.3.4.

Photoionization is the process of an atom getting ionized by the absorption of a photon. For hydrogen this looks like

$$\mathrm{HI} + \gamma \rightarrow \mathrm{p} + \mathrm{e}\,,$$

where HI is neutral hydrogen, p is a proton and e is an electron. The common notation for neutral hydrogen in astrophysics is denoted by HI, HII is singly ionized hydrogen (which is just a proton) and molecular hydrogen is written as H_2. There are four main mechanisms for the excitation of gas; photoionization from stars, photoionization from AGNs, photoionization by X-ray photons emitted by shocked hot gas, as well as ionization by collisions. Ionization (as well as sublimation and dissociation) through particle collisions is distinguished from photoionization and called collisional ionization.

1.2.3 Emission: electronic transitions

Emission through electronic transitions is when an electron in an atom or molecule changes its quantum energy state from a higher level to a lower level by the emission of a photon. This is typically in the ultraviolet (UV) and visible but also in the mid-IR (MIR) to far-IR (FIR) wavelength regions.

Recombination lines occur when a free electron in ionized gas is captured and recombines with an atom. For hydrogen ions, the process is

$$\mathrm{p} + \mathrm{e} \rightarrow \mathrm{HI} + \gamma\,.$$

After the recombination, the atom will likely be in an excited state and the electron will cascade down to the ground state, emitting a range of photons as the electron transitions to less excited states. The brightest recombination lines in high-z galaxies are typically from hydrogen and helium. For hydrogen, these are the Lyman and the Balmer series. In the Lyman series the electron transitions from n$\geq$2 to n=1 (where n is the principal quantum number), with rest frame emission lines in the UV. In the Balmer series, the electron transitions from n$\geq$3 to n=2, with rest frame emission lines in the optical. In astrophysics, the transitions are commonly denoted by the Greek alphabet $\alpha, \beta, \gamma, \delta$,..., with increasing steps. Lyα (n=2$\rightarrow$1) and Hα (n=3$\rightarrow$2) are the first transitions for the Lyman and Balmer series, respectively. Lyα is a very useful line for the study of ionized gas in high-z galaxies, as they are redshifted to optical wavelengths in the observed frame.

Forbidden lines arise when an electron jumps from a upper energy level to a lower lower energy level in neutral or ionized atoms, but where the transitions have a very low transition probability compared to permitted transitions. They are called forbidden, because they are not allowed according to the selection rules of electronic transitions, often because they contain a spin-flip of the electron. They rarely occur under normal conditions here on Earth. That is because the densities are high and collisions between atoms will carry away the energy before the electronic transition can occur.

Forbidden lines only occur in low-density gas $\sim$10–10^5 cm^{-3} in the interstellar medium and disappear above a certain critical density. Collisions are rare events in low-density gas and de-excitations via emitting forbidden-line photons are therefore possible, and are observed as spectral lines. Forbidden lines are denoted by square brackets, such as the [C I] lines of atomic carbon. Semi-forbidden lines are similar to forbidden lines. The transition probability is higher, but still low compared to permitted transitions. They are denoted with a single bracket, such as C III]. The line ratios of forbidden lines contain important information about the gas, e.g. abundance of the emitting gas, temperatures, density and ionization status.

Hyperfine structure lines occur when an atom changes state between two hyperfine levels, meaning the electron changes its spin. The spin-flip transition will change the spin between the electron and the spin of the nucleus from parallel to antiparallel and emit a photon, which will be detected as a spectral line. The most famous example in astrophysics is the 21 cm hydrogen line. The transition is highly forbidden. The excited state has a mean life time of around 10 million years. It is thus a transition that is very unlikely to occur in a laboratory here on Earth, but is commonly observed in interstellar hydrogen clouds and is used to study neutral hydrogen.

1.2.4 Emission: rotational and vibrational transitions

Molecules that have a permanent nonzero electric dipole moment are called polar molecules. They can change their electric dipole moment via the emission of a photon, by either a change of rotational or vibrational status, or both at the same time.

Rotational lines occur for asymmetric molecules (e.g. CO), when they change their rotational state. The change in rotational energy is quantized and only occurs at specific frequencies and results in the emission of microwave wavelengths. The permitted transitions for rotations are given by $\Delta J = \pm 1$, according to the selection rule for angular momentum. In astrophysics, the common notation for e.g CO $J = 1 \rightarrow 0$ is CO(1–0).

Vibrational lines occur, just like rotational lines, in polar molecules. Vibrations are stretching the molecule's internal bonds and can change the electric dipole moment, which leads to a possible emission of photons, typically at infrared (IR) wavelengths. A change of the vibrational state is often accompanied by a change of the rotational state and is then called a **rotational-vibrational transition**. It creates a cascade of lines at slightly different energies, since the rotational energy is low compared to the vibrational. These lines are also seen in the mainly in the infrared.

1.2.5 Radiative transfer

The radiation from a source can be described by its specific intensity, I_ν, which is conserved along a ray traveling through free space. However, as described in the previous sections, when space is not empty, the radiation will interact with the matter and can be absorption and scattered. How the specific intensity changes as it passes through a medium can be described by the radiative transfer equation including absorption and emission processes (without scattering),

$$\frac{\mathrm{d}I_\nu}{\mathrm{d}s} = -\alpha_\nu I_\nu + j_\nu, \tag{1.4}$$

where ds is the length of the path through the medium, α_ν is the absorption coefficient and j_ν is the emission coefficient of the medium. If we introduce the optical depth $\mathrm{d}\tau_\nu = \alpha_\nu \mathrm{d}s$, it is possible to express the radiative transfer equation as

$$\frac{\mathrm{d}I_\nu}{\mathrm{d}\tau_\nu} = -I_\nu + S_\nu, \tag{1.5}$$

where

$$S_\nu \equiv \frac{j_\nu}{\alpha_\nu} \tag{1.6}$$

is called the source function. In order to express the radiative transfer equation in its integral form, some manipulations need to be done. First, we reorganize (1.5) and multiply by e^{τ_ν},

$$\begin{aligned} e^{\tau_\nu}\mathrm{d}I_\nu + e^{\tau_\nu}I_\nu\mathrm{d}\tau_\nu &= e^{\tau_\nu}S_\nu\mathrm{d}\tau_\nu \\ \mathrm{d}(e^{\tau_\nu}I_\nu) &= e^{\tau_\nu}S_\nu\mathrm{d}\tau_\nu\ . \end{aligned} \tag{1.7}$$

We then integrate, with the starting point $\tau_\nu = 0$ and with an initial specific intensity $I_\nu(0)$,

$$\begin{aligned} \int_{I_\nu(0)}^{I_\nu} \mathrm{d}(e^{\tau_\nu}I_\nu) &= \int_0^{\tau_\nu} e^{\tau'}S_\nu d\tau' \\ e^{\tau_\nu}I_\nu - e^0 I_\nu(0) &= \int_0^{\tau_\nu} e^{\tau'}S_\nu\mathrm{d}\tau' \\ e^{\tau_\nu}I_\nu = I_\nu(0) &+ \int_0^{\tau_\nu} e^{\tau'}S_\nu\mathrm{d}\tau' \end{aligned} \tag{1.8}$$

As a last step, multiplying with $e^{-\tau_\nu}$ yields

$$I_\nu(\tau_\nu) = I_\nu(0)e^{-\tau_\nu} + \int_0^{\tau_\nu} e^{-(\tau_\nu-\tau')}S_\nu\mathrm{d}\tau'\ , \tag{1.9}$$

which gives the radiative transfer equation in its integral form. It can be simplified under the assumption that the source function S_ν is constant along the line-of-sight,

$$I_\nu(\tau_\nu) = I_\nu(0)e^{-\tau_\nu} + S_\nu(1 - e^{-\tau_\nu})\ . \tag{1.10}$$

The first term on the right hand side describes the amount of the intrinsic radiation that is absorbed by the medium. The second term is the gain of specific intensity through emission from the medium, that is, photons added to the radiation along the line-of-sight.

Opacity

Opacity is the combined effect of scattering and absorption, that describes how "difficult" it is for radiation to pass through a medium. Opacity is measured in optical depth. The infinitesimal increase in optical depth along a line of sight at frequency ν is given by

$$\mathrm{d}\tau_\nu = \alpha_\nu\mathrm{d}s = \sigma_\nu n\mathrm{d}s\ , \tag{1.11}$$

which is a dimensionless parameter introduced in the section above. The optical depth can also be described in terms of the effective cross section (σ_ν) and the number density (n), which might give a more intuitive feeling for it. The cross section is a measure of how likely it is for the radiation to interact with a particle and the number density is a measure of how many particles there are to interact with. Consider a medium (typically a cloud of gas) which is either dense and/or has a high cross section. Radiation traveling though it will more likely interact with the gas particles. The chance of absorbing or scattering the radiation is high. The optical depth is measure of how opaque the gas cloud is to radiation at a certain frequency and is integrated over the size (s) of the cloud,

$$\tau_\nu = \int_0^s d\tau_\nu. \tag{1.12}$$

The optical depth τ_ν is an important property and contributes to determining how a ray of light is affected while passing through a medium. In a case of very high optical depths (the gas is optically thick),

$$\tau_\nu \gg 1 \quad \Longrightarrow \quad I_\nu = S_\nu,$$

which means that an observer only sees the emission from the outermost layer of the medium (S_ν) and the initial signal ($I_\nu(0)$) is completely absorbed by the medium. At the other end, if the optical depth is very low (the gas is optically thin), it is possible to use the Taylor expansion of e^x, which gives,

$$\tau_\nu \ll 1 \quad \Longrightarrow \quad I_\nu = I_\nu(0)(1 - \tau_\nu) + S_\nu \tau_\nu.$$

In this case, the observer sees both the initial signal attenuated by a factor of $(1 - \tau_\nu)$, and the emission from the medium itself, lowered by a factor of τ_ν.

When opacity is due to dust it is called extinction. This is a very important aspect of astrophysics since the dust not only attenuates the light, but dust grains also give rise to spontaneous emission after being heated through photon absorption. Dust radiative transfer will be discussed in further detail in section 1.3.2.

1.3 Galaxy components

Galaxies are gravitationally bound systems of stars, gas, dust, stellar remnants and dark matter. It is also believed that every massive galaxy hosts a super massive black hole (SMBH) in its center (Kormendy & Ho 2013). Dynamically, most of the mass appears to be in the form of dark matter. Its presence has been inferred e.g. from the flattening of galaxy rotation curves at large radii. Stars are fundamental building blocks and emit most of the light we observe from galaxies. The gas within the galaxy is the fuel for further star formation and black hole growth. Dust only makes up $\sim$0.1% of the mass of a Milky Way type galaxy. Nevertheless, it is a very important component. It efficiently absorbs stellar radiation (affecting the observed emission of a galaxy). It also provides a mechanism for the efficient cooling of gas. The space between galaxies is filled with the intergalactic medium (IGM). The IGM is thought to be a large gas reservoir that fuels the galaxy with new gas through accretion processes. This would enable stars to form during longer time periods, than if the galaxy would only consume the gas already residing in it. Galaxies are structures that formed very early in the Universe, with recent observed candidate galaxies that formed only $\sim$0.5 Gyrs after the Big Bang (Oesch et al. 2016, z=11.09) and (Hashimoto et al. 2018, z=9.1). Galaxies vary in size, shape, gas content and activity. Historically, they have been classified as spirals, elliptical or irregular galaxies, depending on their morphology (Hubble 1926). There are many other ways to classify galaxies, e.g. depending on the rate at which they form stars, or the activity of the SMBH in the center or if they are especially bright in certain wavelength bands. Galaxies can be very bright and they are used to probe the most distant Universe. Through studying galaxies at different epochs, we gained some of the most constraining information we have about the evolution of the Universe. In order to gain as much information as possible, it is important to understand each of the components that contributes to the radiation we detect from distant galaxies.

1.3.1 Stellar population

Stars are born in dense molecular clouds that fragment and gravitationally collapse. When the density inside the collapsing cloud is sufficiently high, hydrogen starts to transform into helium through nuclear fusion. The characteristics of stars and their evolution is that it depend on their initial mass. The more massive the star, the hotter its surface. The relationship between surface temperature and total luminosity of the stars is typically illustrated in a Hertzsprung–Russell diagram. Most stars lie on the so called main sequence of stars in the diagram. Low mass (0.08–0.45 $M_\odot$, type M) stars are small, red in color and burn hydrogen much slower, with a life time of $\sim$100 Gyr. High mass (10-50 $M_\odot$, types O and B) stars, are blue, large and have a short life time of about 10-100 Myr. Because of the short lifespan of massive stars, they are used as traces of ongoing star-formation in galaxies. Ongoing star-formation is typically seen in spiral galaxies, where the spiral arms appear more blue then the other parts of the galaxy. Low mass stars have a very long expected lifetime, longer then the age of the Universe, which is 13.77 Gyr (Planck Collaboration et al. 2016). Therefore, red low mass stars still exist in galaxies that have long since stopped forming new stars and are said to be dead.

Stars are also responsible for the chemical evolution of galaxies. Heavier elements are produced via fusion at their centers. The elements replenish the surrounding interstellar medium (ISM), when stars eject material through winds or through supernova explosions. The enrichment of the ISM has important effects of the efficiency of further star formation, as more metal rich gas cools faster then pristine gas. By studying the radiation emitted by stars and attenuated by gas in a galaxy, we can infer information about the current and past star formation activity as well as the physical condition of the ISM.

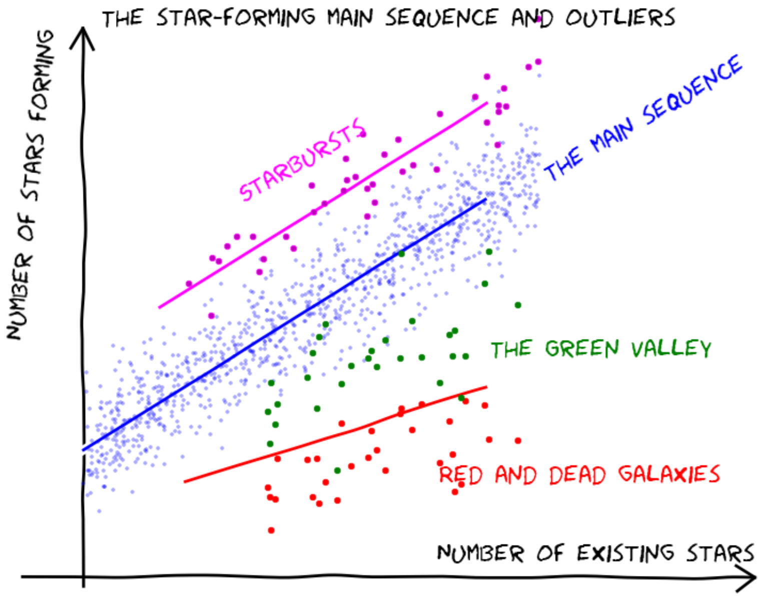

FIGURE 1.4: The main sequences of star forming galaxies with the four main classes of galaxies based on their location in the star-formation rate (SFR) vs stellar mass ($M_{\star}$) plane. Credit: Harry Ferguson

Main sequence of star-forming galaxies

Similarly to the main sequence of stars, galaxies have also been empirically shown to have a tight correlation between their star formation rate (SFR) and stellar mass ($M_{\star}$). This relation is known as the main sequence (MS) of star-forming galaxies. More massive galaxies form more stars than less massive galaxies. The observations of star-forming galaxies form an almost linear relationship with a slope of approximately 1 and with a scatter of only 0.3 dex (e.g., Brinchmann et al. 2004; Noeske et al. 2007; Elbaz et al. 2007). Deviations from a linear slope have also been reported. At high stellar masses the slope flattens off (e.g Whitaker et al. 2014; Schreiber et al. 2015). The MS relationship is observed both in the local Universe and at high-z (e.g., Speagle et al. 2014; Santini et al. 2017, out to $z \sim 6$), where the SFR increases with redshift. For a fixed stellar mass, the SFR at z=2 is larger by a factor of $\sim$4 ($\sim$30) relative to similar galaxies at z=1 (z=0) (Daddi et al. 2007). A reason for the higher rate of star formation in the early Universe may be that larger amounts of gas were available. Tacconi et al. (2010) find in a study of molecular gas, that the average gas fraction at $z \sim 1.2$ ($z \sim 2.3$) was 44% (34%), three to ten times higher than in local massive spiral galaxies.

The main sequence can be used to classify different types or groups of galaxies with respect to their location in comparison to the normal star-forming galaxies (see Fig. 1.4). Galaxies that are above the sequence by 3 times the scatter, or a factor of 10, are called "starburst" galaxies (Rodighiero et al. 2011), and are forming stars at an elevated rate. If the galaxies fall below the MS, then they are classified as "red and dead" (also "quenched" or "quiescent"). They are the "red sequence" and are not forming many stars. Galaxies that lie in between the MS and the red sequence are sometimes referred to as the "green valley", galaxies that are thought to be in the process of shutting down their star formation.

Starbursts may be driven by major mergers where strong dissipation in the gas cause it to fall deeper in the potential well or drives strong compression. This would lead to an increased star formation efficiency (Daddi et al. 2010b). In cosmological simulations it has been argued that the combined mechanisms of gas accretion from the IGM and supernovae driving outflows are both needed for the galaxy to remain in balance, necessary in order to stay on the MS. The enrichment from supernovae and accretion of pristine gas seems to also keep the level of metallicities in agreement with observations (Finlator & Davé 2008; Davé et al. 2011). AGN feedback is hypothesized to be an important driver for the evolution of galaxies from the blue MS to the red sequence. Schawinski et al. (2007) observed at low redshifts, $0.05 < z < 0.1$, that galaxies selected as star-forming fall on the MS, but galaxies with AGNs are located considerably closer to the red sequence. They interpret this as AGN feedback, driving the evolutionary sequence from star-forming to quiescent at recent epochs. AGNs selected in different ways (radio, X-ray and IR), have shown similar trends: Radio AGNs seem to be falling on the red sequence, X-ray AGNs cluster in the green valley, and IR AGNs begin slightly bluer, but are still off the MS. This has been interpreted as follows. After the AGN turns on, star formation is quenched and the AGN shifts from being radiatively efficient, meaning bright in optical and IR, to being radiatively inefficient, meaning bright in radio frequencies (Hickox et al. 2009).

1.3.2 Dust

Dust is an important part of astrophysics. Its extinction obscures radiation and must be corrected for in observations. Dust also seems to play an important role in galaxy evolution. Interstellar dust has several effects that substantiate its importance (Draine 2011):

- Interstellar extinction: dust absorbs and scatters radiation. The degree varies, shorter wavelengths are generally more extincted.
- Thermal emission: Dust absorbs radiation and heats up. It re-emits radiation in the IR to sub-mm.
- Depletion of elements: Dust binds certain elements into solid grains and “removes" them from the gas, which changes the observed abundances.
- Effecting the gas chemistry: Dust acts as catalyst for H_2, molecules can form on the surface of the grains.
- Allow cooling: In dense regions, dust can act as a cooling mechanism for gas. It absorbs energy from the gas through collisions and radiates it away.

In the following subsections, the extinction and thermal emission are discussed in detail.

Extinction

Opacity due to dust particles is called extinction. Dust can scatter and absorb photons. Its efficiency in doing so depends on its grain size, its chemical composition and the presence of magnetic fields, which can align the dust grains. The extinction is wavelength dependent and dust is more efficient at absorbing UV and optical photons than IR photons. Star light appears more red after being extincted by dust, as the blue light is absorbed and scattered to a higher degree than the red light. This effect is aptly named “reddening”. The dimming of light due to interstellar dust was likely first documented in Barnard (1907, 1910), who showed that some stars appear to be dimmed by an absorbing medium. Figure 1.5 shows an example of the effect of extinction in different photometric bands. At the center of the molecular cloud, the visible light is nearly completely absorbed. At the edges of the cloud, the light is dimmed and reddened. In the near-IR Ks-band, the light is less affected and the cloud is thus more transparent at longer wavelengths.

Nowadays, the attenuation of dust has been studied extensively and the effects of dust have been characterized in detail. This is done, e.g., by studying different sight-lines and comparing

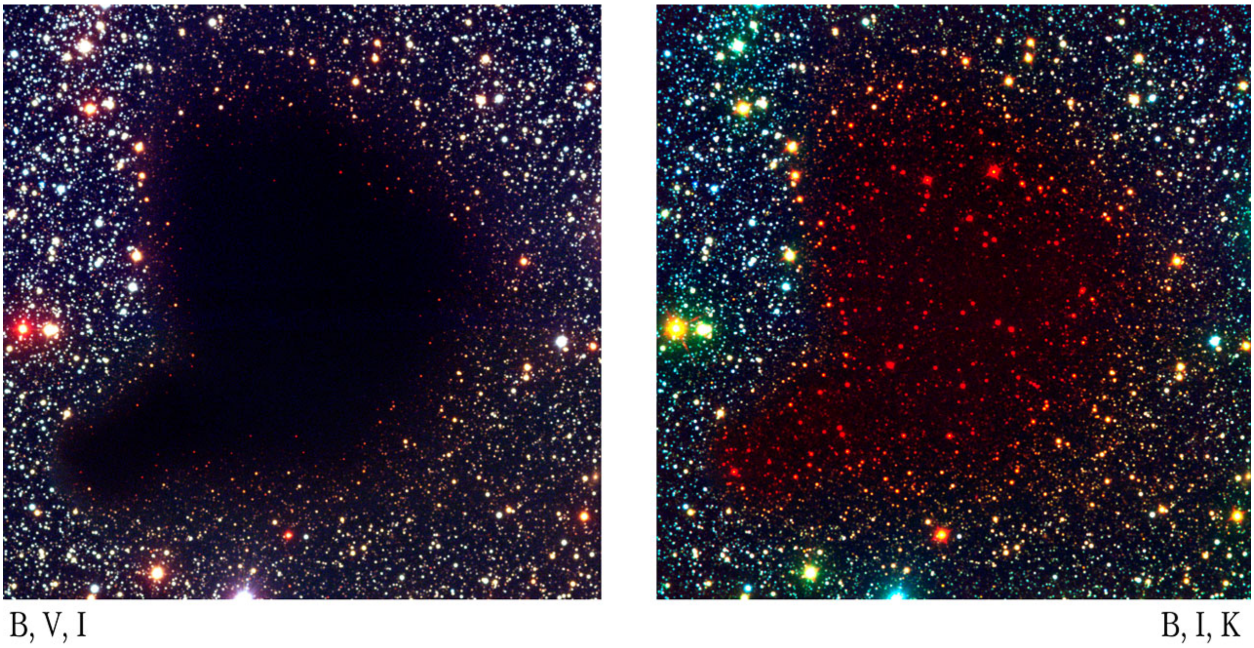

FIGURE 1.5: Two color composite images of Barnard 68, a molecular cloud located at a distance of ~130 pc, showing the effect of dust attenuation and reddening of stellar radiation at different wavelengths. *Left:* image composed of three optical filters, B-band 0.44 μm (blue), V-band 0.55 μm (green) and I-band 0.90 μm (red). *Right:* in false color B-band 0.44 μm (blue), I-band 0.85 μm (green) and near-IR Ks-band 2.16 μm (red). Credit: ESO/press release eso0102.

the light from standard candles, stars of which we know the intrinsic spectrum, to that of light from similar stars, attenuated by dust. The extinction at wavelength λ is defined as

$$\frac{A_\lambda}{\mathrm{mag}} = -2.5 \log_{10}\left[\frac{I_\lambda}{I_\lambda(0)}\right], \tag{1.13}$$

where $I_\lambda(0)$ is the intrinsic light and I_λ is the light attenuated by dust. The extinction, A_λ, can also be expressed in terms of optical depth, τ_λ. The attenuated light is described by $I_\lambda = I_\lambda(0)e^{-\tau_\lambda}$, as shown in section 1.2.5,

$$\frac{A_\lambda}{\mathrm{mag}} = -2.5 \log_{10}(e^{-\tau_\lambda}) = -2.5 \frac{(-\tau_\lambda)}{\log(10)} = 1.086\, \tau_\lambda \,. \tag{1.14}$$

The amount of extinction varies from different line-of-sights and the slope of the extinction is often characterized by

$$R_V \equiv \frac{A_V}{A_B - A_V} \equiv \frac{A_V}{E(B-V)} \,, \tag{1.15}$$

where A_B (A_V) is the extinction in the 0.44 μm B-band (0.55 μm V-band) and $E(B-V)$ is the reddening. Figure 1.6 shows the wavelength dependent extinction relative to the extinction at the visible V-band (A_λ/A_V), as a function of the inverse wavelength (λ^{-1}), for the Milky Way. The average value of R_V is approximately 3.1 (Draine 2011). Besides having a steep rise in extinction towards the far-UV, there is also a broad absorption "bump" at 2175 Å. The origin of the bump is still not known exactly. It has been postulated to arise from either aromatic carbon particles (e.g., Draine 1989; Duley & Seahra 1998) or possibly polycyclic aromatic hydrocarbons (PAHs, see e.g., Joblin et al. 1992; Li & Draine 2001; Siebenmorgen et al. 2014).

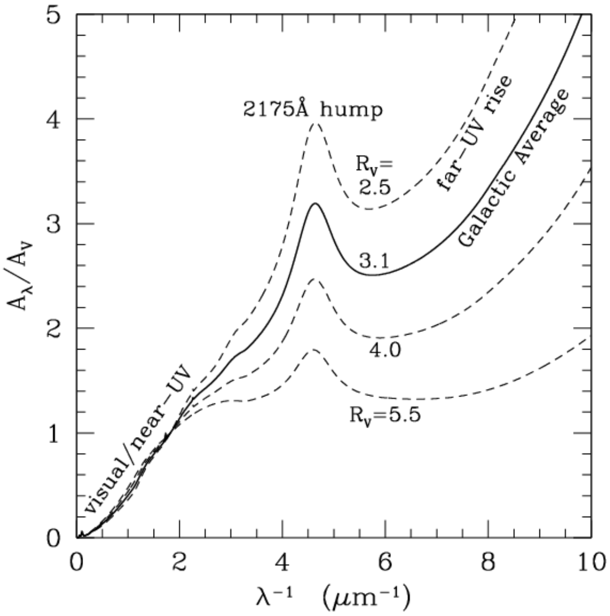

FIGURE 1.6: The extinction curve of the Milky Way for different degrees of reddening, R_V=2.5, 3.1, 4.0 and 5.5. Apart from the rise towards the ultraviolet, the extinction increases around the 2175 Å bump. Image reprinted from (Li & Mann 2012).

Dust emission

Dust emission is an important diagnostic, and provides additional information about the structure and chemical composition of regions which might not be detectable otherwise. Figure 1.7 exemplary shows the different looks of a spiral galaxy observed in optical and infrared light. The dust is heated by the young stars which then re-emits the absorbed light mainly in the mid- and far-IR. Dust is very efficient at absorbing starlight and in dense regions, dust can completely absorb the light, leaving what looks like dark streams or patches (Fig. 1.7, *top panel*). Observing objects in dust emission can thus provide a information about the structure and distribution of gas, as well as information about the underlying stellar population.

The emission from dust depends on the gain size and chemical composition. Since it is not possible to collect a sample of interstellar dust and analyze it in a laboratory, we rely on remote observations in order to characterize the properties of dust. The only exceptions to this is the first sample return mission Stardust, which collected particles in the solar system and returned them to Earth in 2006, and the Voyager 1 spacecraft, which in 2012 left the heliopause and entered the ISM and are still sending data back to Earth. The exact chemical composition and the gain size distribution of interstellar dust are still not well constrained. One way to gain further insight is by studying the depletion of elements in the diffuse interstellar medium through absorption-line spectroscopy. This method indicates which elements are likely to be incorporated in dust grains (see, e.g., De Cia et al. 2016). This predicts that C, Mg, Si and Fe are the main components of interstellar dust. The direct emission of heated dust has been studied over a large wavelength range in the Milky Way (e.g., Wright et al. 1991; Arendt et al. 1998). This puts constraints on the general shape of the spectral energy distribution (SED) of dust in the diffuse interstellar medium. Extensive modeling efforts have been made, trying to reproduce the observed SED of dust. The modeling uses theoretical descriptions of the interaction of light and dust grains in radiative transfer calculations (e.g., Li & Draine 2001; Popescu et al. 2011; Siebenmorgen et al. 2014). In this field, the dust is characterized by size and composition, and a dust mix contains different gain sizes and sometimes additional molecules. The are three main contributors needed to reproduce the observed dust SED (see also Fig. 1.8). 1) Thermal emission from large grains accounts for the far-IR

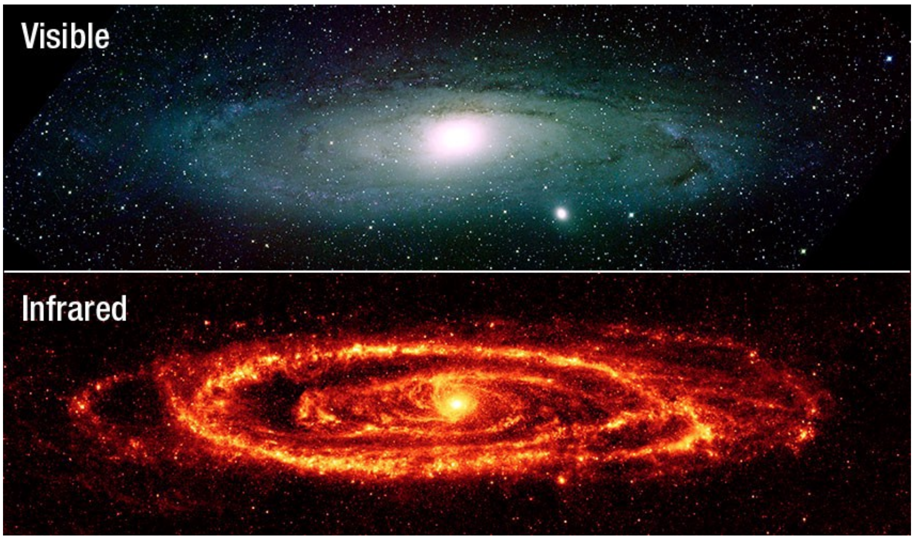

FIGURE 1.7: Two different views of M31, Andromeda, in visible light originating from stars and in infrared light (24 μm, in false color) from dust emission. In the optical, the bulge dominates. The spiral arms are more distinct in the infrared image. This illustrates the advantages of multi-wavelength astronomy. Credit: NASA/JPL-Caltech/Univ. of Ariz., visible: NOAO, infrared: *Spitzer*.

peak. 2) Very small grains become extremeley hot and explain the emission at shorter wavelengths. 3) PAHs, essentially big molecules explain observed diffuse emission bands at 5-10 μm.

1.3.3 Interstellar Medium

The interstellar medium (ISM) is the gas and dust that exists in between stars within a galaxy. This is matter from which new stars are formed from. The ISM consist mainly of hydrogen ($\sim 71\,\%$) and helium ($\sim 27\,\%$) from the primordial nucleosynthesis and all other elements heavier then helium, refereed to as metals, contribute only $\sim 1\,\%$ of the total mass (Draine 2011). Dust only makes up a tiny fraction ($\sim 0.1\,\%$) of the ISM. Metals are produced in stars when they burn hydrogen and helium to heavy elements up to iron. Through supernova explosions, these elements are ejected into the ISM, slowly increasing its amount of metals. The chemical evolution of the ISM reflects the star-formation history. The chemical evolution of the ISM in turn constrains the potential for further star formation and black hole growth, as gas is the fuel for both. Even though heavier elements only make up a small fraction of the total mass, they are vital for the chemistry, ionization state and temperature of the gas. The ISM is a multi-phase medium with the following main phases (Draine 2011):

- Cold dense gas: H_2, T=10–50 K, $n_{\rm H} \sim 10^3$–$10^6\,{\rm cm}^{-3}$
- Cool neutral gas: HI, T$\sim 10^2$ K, $n_{\rm H} \sim 10^1\,{\rm cm}^{-3}$
- Warm neutral gas: HI, T $\sim$ a few10^3 K, $n_{\rm H} \sim 0.6\,{\rm cm}^{-3}$
- Warm ionized gas: HII, T$\sim 10^4$ K, $n_{\rm H} \sim 0.2$–$0.6\,{\rm cm}^{-3}$
- Hot ionized gas: HII, T$> 10^{5.5}$ K, $n_{\rm H} \sim 10^{-3}\,{\rm cm}^{-3}$.

By mass, most of the gas is in atomic or molecular hydrogen. By volume, ionized gas makes up most of the galaxy.

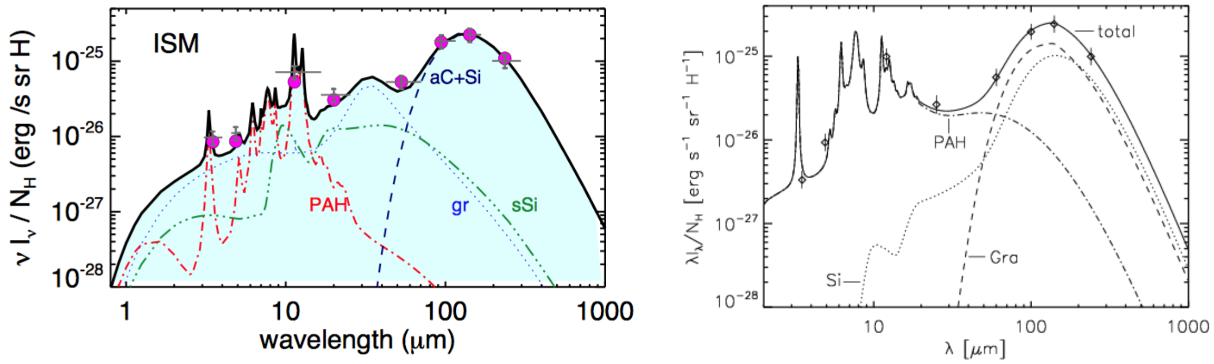

FIGURE 1.8: Modeled spectral energy distribution of dust compared to COBE data (Arendt et al. 1998) of observed infrared emission per H nucleus from dust heated by the average starlight background in the Milky Way. *Left:* dust model consisting of large silicates (Si), amorphous carbon (aC), small silicates (sSi), graphite (gr) and PAHs. Reprinted from (Siebenmorgen et al. 2014). *Right:* model SED composition are from silicate (Si, dotted line), grains (Gra, dashed line) and PAHs (dashed-dotted line). Reprinted from (Popescu et al. 2011)

Molecular gas

Molecular gas plays an important role in the ISM, as dense cores of molecular clouds are the birth places of stars. Molecular hydrogen, H_2, is the dominating element and H_2 are catalyzed on the surface of dust grains. Molecular hydrogen has a binding energy of 11.2 eV and can be dissociated by UV photons. So it needs to be shielded against the interstellar radiation field (ISRF) in order to exist. This is done by either dust grains or through self-shielding. In the outer layers of molecular clouds H_2 is photodissociated and destroyed. At column densities of $\sim 10^{20}\,\mathrm{cm}^{-1}$, photoexcitation transitions become optically thick. This prevents the UV photons from penetrating deep into the cloud. The outer H_2 molecules shield the inner H_2 molecules from the radiation, the H_2 becomes self-shielding. H_2 is a symmetric molecule and lacks a permanent electric dipole moment. It thus has a large spacing between its rotational energy levels (Draine 2011). The molecular gas is in general too cool to populate even the lowest rotational level. It therefore does not emit any spectral lines that are easy to observe. Instead, other molecules are used as tracers. Carbon monoxide (CO) is the second most abundant molecule and is commonly used as a tracer for H_2.

CO has a binding energy of 11.1 eV and needs to be shielded against the ISRF just like H_2. This is also done by self-shielding and the the build up of CO is very similar to H_2, CO is also destroyed in the outer regions. CO is a polar molecule with a permanent electric dipole moment. This leads to a closer spacing of the rotational energy levels. The lowest excited level is populated at even only at a few K, easily reached even in cold molecular clouds. The three rotational transitions with the lowest energies are ^{12}CO(1–0)=115.27 GHz, ^{12}CO(2–1)=230.53 GHz, and ^{12}CO(3–2)=345.79 GHz. The atmospheric transmission at these wavelengths is good, they can be observed with ground based telescopes. At high redshifts, higher rotational transitions are also shifted to observable wavelengths and are important diagnostics to study cold gas. The different rotational transitions have increasingly high excitation energies, making it more difficult to populate the higher-J levels. The required physical conditions of the gas are different and the high rotational transitions occur in denser gas. The different rotational transitions thus probe different regions. The lowest level CO(1–0) traces the diffuse and extended molecular gas and is a better tracer of the total amount of molecular gas than the high rotational transitions.

To convert the CO mass to H_2 mass, one has to assume a conversion factor, usually expressed as X_{CO} or α_{CO}, to transform observed CO luminosity to molecular gas mass,

$$M_{\mathrm{H}_2} = \alpha_{\mathrm{CO}} L'_{\mathrm{CO}}. \tag{1.16}$$

The utility of this relation has been well established observationally (e.g., Young & Scoville 1991; Solomon et al. 1997). The choice of conversion factor is very important and it has been shown to vary with environments. α_{CO} depend strongly on the abundance of metals and dust, since they will shield the clouds from the ISRF, and lower metallicity will lead to dissociation of CO deeper into the could. α_{CO} also seems to be decreasing for higher SFRD (e.g Strong et al. 2004; Sandstrom et al. 2013), and also to decrease closer to the center of spiral galaxies. It is important to consider this, especially for high-z star forming galaxies, where the environments may vary significantly from the Milky Way. It is typical to use a bimodal CO-to-H_2 factor for starburst galaxies and mergers ($\alpha_{CO} \sim 0.8$) and normal star-forming galaxies ($\alpha_{CO} \sim 4$, Milky Way type).

Recent studied have found that CO is effectively destroyed by cosmic rays (Bisbas et al. 2015; Papadopoulos et al. 2018) but leaves H_2 intact, changing the CO/H_2 ration for star forming galaxies in the Universe. Due to this, [C I] has been postulated as a more robust tracer for molecular gas, even though the tracing capability of [C I] decreases for low metallicities (Papadopoulos et al. 2004; Glover et al. 2015). [C I] has two fine structure lines [C I](1–0) and [C I](2–1), which both are optically thin and have a lower optical depth than CO, tracing larger column-densities. If both the upper and lower transitions are observed, it is possible to constrain the temperature and column density of carbon. [C I](1–0) and [C I](2–1) have critical densities of $\sim 400\,\mathrm{cm}^{-3}$ and $\sim 10^3\,\mathrm{cm}^{-3}$, respectively (similar to CO(1–0) and CO(2–1)), so they probe the same gas phase as CO. They can be excited even in the outermost diffuse regions. All of this makes [C I] to a good candidate for tracing H_2.

Neutral gas

Neutral gas makes up a significant fraction of the local interstellar medium ($\sim 40\%$, Draine 2011). It constitutes mainly of atomic gas, with HI being the most abundant element. Neutral hydrogen is observed in emission from the forbidden spin-flip transition 21 cm line or in 21 cm line absorption against a radio continuum. Another method to probe neutral gas is to observe absorption line profiles in optical and UV lines. The 21 cm (1.420 GHz) line was first observed by Ewen & Purcell (1951). Since then maps of neutral hydrogen have been made, revealing for the first time the spiral structure of the Milky Way. It is possible to calculate the relative speed of each arm from the Doppler shift of the lines of individual clouds. Rotation curves of spiral galaxies can be constructed from the speeds of the clouds. In case there is a radio continuum background source, HI can be observed in absorption. It traces the cool components of the neutral gas. Unlike the 21 cm emission, 21 cm absorption can also be detected at high redshift since the absorption strength only depend on column density and background flux. For example, radio emission from jets produced by AGNs allow the cold neutral gas of the host galaxy to be observed in absorption.

Neutral HI gas also gives rise to absorption features in lines such as ionized Lyα emission by absorption and/or scattering. This provides an additional tool to study the spacial extent of neutral gas, as the absorbing region can be constrained. The absorption line profiles themselves provide direct information about properties of the absorbing neutral gas, e.g. dynamics and morphologies.

Warm ionized gas

Ionized gas contains hydrogen gas that has been photoionized by high energy photons (HII). The main mechanism for ionization in the local interstellar medium is by young hot stars, typically massive O-stars. If dense gas clouds are ionized around a star or collection of stars, the region is the called a HII-region. It is normally the molecular gas cloud from which the stars were born and has now been completely ionized. Extended low-density regions of ionized gas, referred to as warm ionized gas, contain much more total mass. The warm ionized gas can also be excited by AGNs, X-ray photons from shocked gas, and by collisions. It is traced by recombination or forbidden (semi-forbidden) collisionally excited lines and provides a tool to study the physical conditions of the gas. The relative intensity of different emission lines can shed light on the ionization mechanism, as well as the abundance, the density and the temperature of the gas. From line profiles it is also possible to get kinematic information about the gas. The intrinsic width of a line depends on the **natural broadening**, where the lifetime of an excited state and the uncertainty of its energy is connected via the uncertainty principle. A shorter lifetime will have a larger uncertainty in energy and thus give rise to a broader emission line. The width of a line also changes due to the local conditions of the gas. **Thermal Doppler broadening** arises from the fact that the emitting gas has a distribution of velocities and the emitted photons will be blue- or red-shifted depending on the relative velocity to the observer. A higher temperature of the gas results in a broader spectral line. **Impact pressure broadening** (or collisional broadening) depends on both the density and the temperature of the gas and occurs when the emitting particle collides with other particles, which interrupts the emission process. This shortens its lifetime and increases the uncertainty in the emitted energy, which broadens the line just like natural broadening. The combined effect of theses two mechanisms for broadening yields a Voigt profile. Emission lines can be shifted with respect to each other or to the systemic redshift of the source. The shift can provide information about the motion of the emitting gas. This can be used to show that there are multiple gas clouds and also trace outflows of gas.

Hot ionized gas

The hot ionized sometime refereed to coronal gas (because of similarities with the hot solar corona) is very diffuse and has a large filling factor ($\sim$ 50% Draine 2011). The gas is thought to be heated by shocks from supernovae explosions. The high temperature gas is collisionally excited and can be highly ionized, with main cooling through line like C IV, [O IV] and [O IV], for gas of T>10^5 K (Gnat & Sternberg 2007; Oppenheimer & Schaye 2013). In the presence of an AGN, the gas can also be photoionized from the central SMBH or shock ionized by the radio jets propagating though the inter stellar medium.

1.3.4 Circumgalactic medium

The circumgalactic medium (CGM), is the gas that fills halos surrounding galaxies. It can be defined as the gas which is outside the disks or ISM of the galaxy, but inside their virial radius. However, there is no precise definition of when the gas passes through one of these boundaries. So the CGM is a term for the halo gas between the ISM and the intergalactic medium (IGM). The CGM has in recent years gained importance as a tool for understanding galaxy evolution. It is now believed that the CGM plays a role in regulating the gas flows into and out of galaxies, since the gas then has to pass though the CGM. Understanding the CGM can shed light on the accretion of intergalactic gas as a fuel for star formation and black hole growth. The CGM also regulates the gas supply, which might be very important for quenching galaxies. It is also a place for recycling gas, as outflows from the galaxy will be injected into the CGM. For a recent excellent review about the CGM, see Tumlinson et al. (2017).

Ways to detect the CGM

The CGM is very diffuse, $n_{\rm H} \gtrsim 10^{-2}$ (Tumlinson et al. 2017), which makes observations of it a challenge. One of the main ways to probe the CGM is through absorption lines. They are seen either against a bright background source (e.g. quasars), or against the light from the galaxy itself. Either method requires the estimation of the intrinsic continuum of the background source, to detect departures from the estimated continuum. The second general method for observing the CGM is by detecting the CGM in emission. Emission lines have gained importance in the last few years, as new sensitive instruments are becoming available, e.g. MUSE at the Very Large Telescope, PCWI at the Palomar Observatory and KCWI at the Keck II telescope. Absorption line studies with bright background sources have the advantages that they are sensitive to low column densities and are independent of the redshift and the apparent luminosity of the host galaxy. A disadvantage on the other hand is that they are typically limited to one sight-line per galaxy. They only provide projected measurements of gas surface densities. Metal absorption lines provide a powerful tool to probe the gas content in the Universe. They have been observed in massive surveys looking at ion lines like [Mg II] (e.g., Quider et al. 2011; Zhu & Ménard 2013) and at high-z (e.g, Matejek & Simcoe 2012). Other studies containing $\sim$1000 galaxies have put constraints on the size and content of the CGM tracing lines as HI, [O IV], Lyα, [N V], C IV, [C III] and [Si IV] (e.g., Adelberger et al. 2005; Rudie et al. 2012; Turner et al. 2014). It is also possible to stack very faint signals to get mean properties of the absorbing gas. The result no longer contains any kinematic information though. These types of studies have revealed large amounts of dust on scales from 20 kpc to a few Mpc around galaxies. They relate the reddening of background quasars to the CGM of foreground galaxies (Ménard et al. 2010; Peek et al. 2015). Studies using the galaxy's own light as the background source are able to trace outflows and inflows. Outflows around star-forming galaxies have been seen in several lines, e.g. [N I] (Martin 2005), [Mg II] (Bordoloi et al. 2011), [Fe II] and [Mg II] (Kornei et al. 2012; Rubin et al. 2014) and in far-UV absorption lines like [Si II], [C II], [Si II], [Si IV] and [N II] (Heckman et al. 2015).

Detection of the CGM in emission rather than in absorption can constrain the density profile, morphology and physical extent of the gas more directly. The first components of the halo gas of the Milky Way were detected in neutral hydrogen (HI), and are referred to as high-velocity clouds. The entire sky has been mapped in a HI survey (Kalberla et al. 2005) and HI has also been observed in other galaxies. Emission lines in the optical and UV trace ionized gas and probe the CGM, as they can map the morphology and kinematics of the gas (Martin 2005; Cantalupo et al. 2014). The hot halo gas has a low surface brightness but can be observed in X-ray emission (e.g., Anderson et al. 2016).

Properties of the CGM

The CGM is multi-phased, meaning it has been observed in neutral, molecular, and ionized gas. The ionization potential energy of the ions spans an order of magnitude. The CGM has a complex kinematic structure, as determined form observations of the same absorption line feature having multiple components with different velocities and linewidths. The CGM is hotter than the ISM and has different definitions of the temperature of different phases. For cold CGM, T=10^{4-5} K, for warm T=10^{5-7} K and for hot T>10^{7} K (Werk et al. 2014). The CGM has been observed in extended ($\sim$80 kpc) Lyα emission around individual galaxies (e.g., Prescott et al. 2015; Erb et al. 2018). It has also recently been shown that a large fraction of star-forming galaxies at redshifts $3 < z < 6$ have extended halos (Wisotzki et al. 2016; Leclercq et al. 2017). Cantalupo et al. (2014) present a giant Lyα structure (460 kpc) around a z $\sim$2.3 quasar, including a cosmic web filament. Other large scale ($\sim$300 kpc) Lyα emissions have sub-structures that show signs of coherent kinematics and are interpreted as being accreted onto a central massive halo (Arrigoni Battaia et al. 2018). Filament structures have also been observed in very diffuse optical emission (Vernet et al. 2017). The ionized gas shows large scale structures indicating streams and filaments connected to the CGM. They are a way to supply the galaxy with gas. Besides the complex structure seen in ionized emission, the CGM can also have metal enriched cold gas on large scales ($\sim$160 kpc), as has been observed through absorption (Prochaska et al. 2014). Additional support for this has come from the detection of large reservoirs of molecular gas detected in CO and [C I] (Emonts et al. 2018). There is also evidence that the large amount of molecular gas can fuel the in-situ star-formation in the CGM observed in the spiderweb galaxy (Emonts et al. 2016). A large scale ($\sim$250 kpc) system of several CO and continuum thermal emission sources (with SFR$\sim$30-120 $M_\odot$ yr^{-1}) has been observed around a quasar. It is interpreted as clumpy accreting streams which have in-situ star formation, enriching the gas even before it is accreted onto the central galaxy (Ginolfi et al. 2017). All of these observations provide support and constraints for large scale cosmological simulations, as we are now starting to detect these extended structures, hypothesized to fuel galaxies via accretion of IGM gas passing through the CGM.

1.4 High-z Radio Galaxies

High-redshift radio galaxies (HzRGs) are some of the largest, most massive and most luminous galaxies in the Universe. They are a rare type of galaxy and as indicated by the name, HzRGs have a bright radio component (radio-loud). It is thought to be powered by accretion of material onto the SMBH in the center of the galaxy. The real start of radio galaxy astronomy came when Baade & Minkowski (1954) discovered that the spectrum of a galaxy studied by Seyfert (1943) is associated with the radio source Cygnus A. In the beginning of the 1960s, the first quasar was discovered (Schmidt 1963) and it was shown that radio sources vary with cosmic epoch. This observation contradicted the "Steady State" cosmology. Also during the 1960s, it was suggested that the source powering quasars was the accretion of gas onto a massive object (Salpeter 1964). During the 1970s, large efforts were made to find higher redshift radio galaxies. They were observed out to $z \sim 1$ (Spinrad & Bahcall 1976; Spinrad et al. 1977; Smith & Spinrad 1980). At this point they were still not considered to be important objects in the general scheme of galaxy evolution, and the radio source and optical host where usually studied separately. During the 1980s and 1990s, optical photometric plates were replaced by CCDs. This enabled the discovery of radio galaxies at much greater redshifts, highest at $z = 5.2$ (van Breugel et al. 1999). Since then, other types of galaxies have been observed at much higher redshifts and it took almost 20 years to find a radio galaxy with an even higher redshift, namely $z = 5.7$ (Saxena et al. 2018). With the increase of resolution, it was also shown that the radio sources are aligned with the optical part of the host galaxy. The idea that they must be interacting with each other became more popular and radio galaxies gained importance in the field of galaxy evolution. Especially after the empirical evidence for a correlation between the mass of the black hole and the velocity dispersion of the host galaxy was found, AGNs became in general more important observational targets for galaxy evolution studies.

1.4.1 Active Galactic Nuclei

Super massive black holes (SMBHs) are thought to reside in every massive galaxy (Kormendy & Ho 2013). When a SMBH ($> 10^6$ $M_\odot$) accretes matter, the object releases a large amount of energy and is referred to as an active galactic nuclei (AGN). The galaxy features then an addition source of energy, completely unrelated to the nuclear fusion of its stars. Most SMBHs are not active and it is thought that powerful AGNs have a short life time, 10^6–10^8 yrs (Martini 2004) and that SMBHs may go through periods of activity. The enormous release of energy by AGNs are thought to play an important role in galaxy evolution. The energy is enough to drive out the gas from the galaxy and heat up the surrounding CGM, preventing the halo gas from cooling down. This is hypothesized to shuts down the of fuel to the galaxy, as discussed in section 1.3.4 and 1.1.2. Due to the release of large amounts of energy, AGNs are often bright across a wide wavelength range, making them visible out to high redshifts.

Unification model of AGNs

Since the discovery of galaxies hosting AGNs, a zoo of different AGNs has emerged, showing different signatures. In an attempt to understand all the different galaxies being observed, Antonucci (1993); Urry & Padovani (1995) suggested a radical simplification of our idea of AGNs. They proposed that the large differences in appearance of observed quantities are mostly due to the viewing angle. Besides the viewing angle, the radio loudness and whether jets are present or not are the main properties which determine the appearance of AGNs (see Fig. 1.9).

In this scheme of unification, the AGN is seen as an axial structure with the central black hole (BH) in the middle. The BH is surrounded by an accretion disk of dust and gas $\sim$100 AU, radiating across the full electromagnetic spectrum. The accretion disk is thought to be the origin

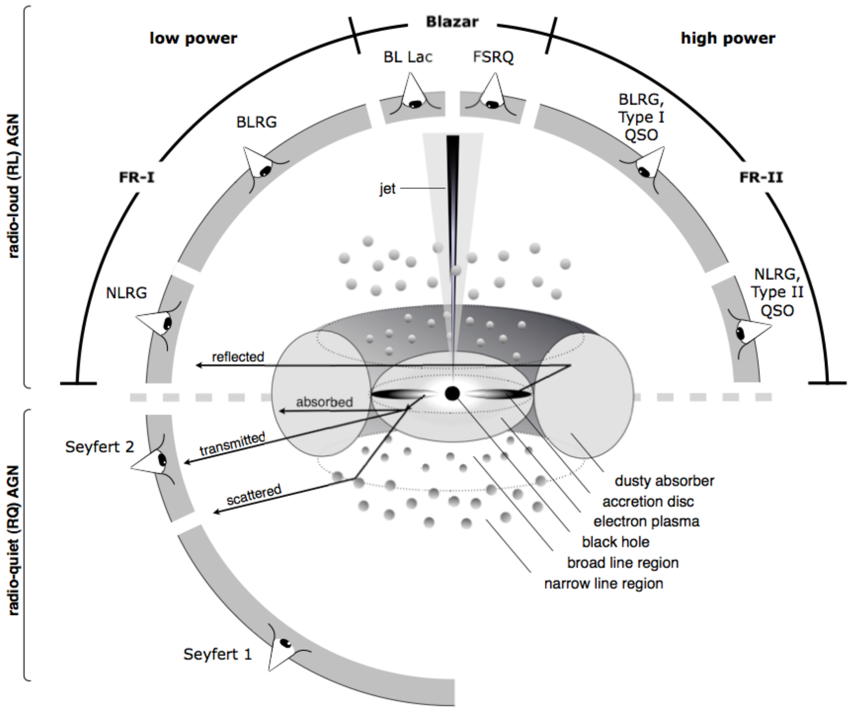

FIGURE 1.9: The unification model of AGNs. The galaxy properties depend mainly on the viewing angle, whether or not jets are present and the power of the radio emission. Reprinted from (Beckmann & Shrader 2012).

of the observed X-ray emission, via inverse Compton scattering of the photons to X-ray energies. This forms a corona, or atmosphere, above the inner accretion disk, but the exact shape and size is still unknown. The accretion disk is thought to be surrounded by an absorbing torus of dust and the emission from the inner parts can only escape along the axis of the structure.

Gas extending from the SMBH to the inner wall of the dusty torus is refereed to as a broad line region (BLR) observed in broad ($\gtrsim$1000 km s^{-1}) optical emission lines. The lines are broad because the emitting material is moving around the black hole at high speeds, causing Doppler-broadening. The gas is photoionized and heated by the radiation from the accretion disk. This region is important for understanding the AGN, because the motion is governed by the properties of the central source. Also, the gas scatters UV photons from the underlying continuum. Changes in the BLR thus indirectly show changes of the central source. The BLR is not visible if the galaxy is viewed edge-on, because of the dust torus.

Further out from the center, at $\sim 10^4$ AU, there is cool low density gas that emits narrow optical emission lines (a few 100 km s^{-1}). The narrow line region (NLR) is the only part that can be resolved using optical telescopes. It is possible to some extent to do kinematic studies and map the gas. From the intensity ratio between pairs of forbidden lines it is possible to measure the electron density and temperature of the NLR. As the NLR extends above (and below) the plane of the dust, it can often be observed even when we are seeing the object edge-on.

If the SMBH is radio loud, then it is associated with jets that are launched from the central region. These can be of varying power and size and greatly effect the appearance of the object. It is assumed that these jets are orthogonal to the equatorial plane of the torus and within the ionization cone. If a galaxy is observed face-on and the jet is facing the observer, which is looking down directly through the beam, the objects are called Blazars. They subdivide into BL Lacertae objects (BL Lac) that have a variable brightness, and flat-spectrum radio quasars (FSRQ). If we observe a radio-loud galaxy edge-on (the side of the jets are seen as they propagate outwards), the

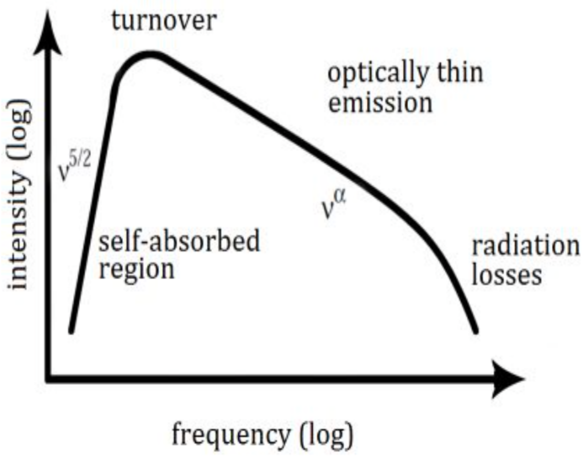

FIGURE 1.10: Generic synchrotron spectrum from a galaxy hosting an AGN. Credit: SAO

object is called radio galaxy. If the radio has high power the subclass is Fanaroff-Riley class II (FR-II) or if the radio source is weak, Fanaroff-Riley class I (FR-I)s. AGNs are also sometimes referred to as type 1 (have BLR and NLR, almost face-on) or type 2 (only NLR, edge-on), depending on the viewing angle. If the source is radio-quiet (has no jets), then the AGN is refereed to as Seyfert I (face-on, BLR and NLR) or Seyfert II (edge-on, only NLR).

1.4.2 Properties of HzRGs

High-z radio galaxies are often defined as z$\gtrsim$2 and having radio luminosity at 500 MHz rest frame frequency of $L_{500\mathrm{MHz}} > 10^{27}\,\mathrm{W\,Hz^{-1}}$. As suggested by their name, radio galaxies are characterized by their powerful radio emission. The emission is often in the form of jets with a visible two-lobed structure centered around a compact component at the center of the host galaxy. The jets are spatially resolvable from the ground, unlike quasars. HzRGs are among the most massive ($M_\star > 10^{11} M_\odot$, Seymour et al. 2007; De Breuck et al. 2010) and luminous galaxies in the Universe. Besides having a large stellar mass, they also contain a large amount of hot X-ray emitting gas ($\sim 10^{12}$ $M_\odot$; e.g., Miley 1980), UV/optical line-emitting warm gas (10^{8-9} $M_\odot$; e.g., Osterbrock & Ferland 2006), molecular gas (10^{11} $M_\odot$; e.g., Downes et al. 1993) and dust (10^{8-9} $M_\odot$; e.g., Reuland et al. 2004). While the AGN outshines the host galaxy in quasars, in HzRGs, both the AGN and the host galaxy can be observed, also due to the favorable orientation. This and the fact that all important components of a galaxy are luminous in the same object, makes distant radio galaxies unique laboratories for probing the early Universe.

1.4.3 Synchrotron emission

The radio emission associated with galaxies originate from synchrotron radiation. Synchrotron radiation is a type of non-thermal radiation emitted by relativistic charged particles (usually electrons) that spiral through a magnetic field. Since the electrons are constantly changing their direction (spiraling motion) they are actually accelerated and emit photons. The radiation produced in this manner has a characteristic polarization perpendicular to the plane of the magnetic field. This has been shown to be consistent with observations of highly polarized radio emission. The spectrum of synchrotron emission is a result of the emission spectra of all individual electrons. The emitted energy does not only depend on the magnetic field, but also on the energy of the electrons themselves. The spectrum has a power-law shape connected to the energy distribution of the seed electrons (Fig. 1.10). The spectrum is characterized by a peak at the critical frequency (ν_c), with a rapid decline to lower frequencies, where it is optically thick and dominated by synchrotron self-absorption, leading to a 5/2 power-law spectrum. In the optically thin regime, the slope of the emission is described by the spectral index (α), $S_\nu \approx \nu^\alpha$. HzRGs typically have a spectral index of $-1 < \alpha < 0$. The principal processes for energy loss are "aging" of electrons (high- energy electrons, emitting at the highest frequencies, lose energy more quickly), inverse Compton (IC) and adiabatic loss. The first two of these effects tend to steepen the observed spectrum, causing an exponential cut-off at high frequencies in the absence of continuous injection. IC scattering (either from synchrotron seed photons or CMB photons) results in emission at much higher frequencies and is typically observed in the soft X-rays. For the spectral index to remain constant over a large frequency range, continuous injection of relativistic particles is needed.

Galaxies with powerful radio emission is usually observed to have two main radio components; a compact flat-spectrum component and an extended steep-spectrum component. The extended component is typically seen as a double-lobed structure, centered at the compact component (aligned with the host galaxy). The core-to-lobe flux ratio is usually used to measure orientation, the angle between the jet direction and the line-of-sight (Orr & Browne 1982). Sources with a high ratio are core-dominated (a flat-spectrum; FSRQ) and with a low ratio they are lobe-dominated (a steep-spectrum; radio galaxies). The radio emission of galaxies are described by four main parts:

- **Core** is the compact flat spectrum component aligned with the nucleus of the radio galaxy or quasar. Typically unresolved at $\geq$0.1 arcsec.
- **Jets** are linear collimated structures connecting the core with the outer extended lobe structure. They jet may be visible as a coherent line, with knots and/or only part of inferred path between the core and lobes is visible.
- **Hotspots** are the bright knots located at the outer ends of the lobes and are thought to be the working surface where the jets meets the ambient medium, creating strong shocks. The spectral index of the hotspot is typically flatter then that of the lobe it resides in.
- **Lobes** are the extended steep spectrum component powered by the jets and are a result of the interaction between the jets and the surrounding medium.

z-α correlation

There is an observed correlation between the steepening of the radio spectral index and the identified redshift of the host galaxy (Tielens et al. 1979; Blumenthal & Miley 1979). It has been shown that steep-spectra are on average at grater distances and from more luminous sources than normal spectra. This rule has proven to be one of the most reliable techniques to find high-z radio galaxies. The true nature of the z-α correlation is still not completely understood, and there are three different suggested explanations. The main one is motivated via a simple connection between the K-correction and the shape of the optically thin regime of the synchrotron spectra, which has a concave shape due to radiation losses. The observed spectral index determined from two fixed observed frequencies will sample a steeper part of the radio spectrum at high-z than at low-z, because the radiative losses increase for higher frequencies. However, this alone cannot be the explanation, as several HzRGs show no concave curvature at the observed frequencies. Klamer et al. (2006) showed that $\sim$90% of their sample of 37 radio galaxies show a straight slope (without any curvature) between 0.8–18 GHz. The second explanation for the observed z-α correlation comes as a result of the connection of luminosity and spectral index together with the strong Malmquist bias in flux density limited surveys. For the source to be detected, it needs to be powerful enough to be brighter than the flux limit, which leads to the L-α relationship. The source requires a higher emissivity and stronger magnetic fields, which leads to more rapid synchrotron losses and thus a steeper radio spectrum (Krolik & Chen 1991; Blundell et al. 1999). The third explanation is that the steepening of the radio spectral index at high redshifts is due to an environmental effect (Klamer et al. 2006). This is motivated by high-z galaxies being on average located in a denser environments. The electrons in the jets are working against the medium, causing them to decrease in velocity, and thus steepening the spectrum. This would result in both a z-α and L-α relationship. The only drawback is that the ambient medium around HzRGs seems to be rather clumpy and not uniform. This poses a potential problem since the difference between the spectral index of the two lobes within the same source is often small. For the spectral index to remain similar for both lobes, the two jets have to work against similar medium.

Radio size and age

Radio sources grow in size as they get older and the collimated jets launched by the central engine expand outwards into the surrounding medium. Their size can therefore be used to estimate how long a radio source has been active, or the elapsed time since it was last active. The size itself gives an indication of the timescale of the activity. A better estimation is achieved if the environment through which the jets are propagating is considered. Some of the most extended radio source are a few Mpc in projected size (Ishwara-Chandra & Saikia 1999). These source have been interpreted as either being very old and/or being located in underdense environments compared to smaller sources. Mack et al. (1998) found the spectral ages of these giant radio sources to not be more than 4×10^7 yrs which is the typical age of normal sized radio galaxies (e.g., Klein et al. 1995). This favors the picture that a low density ambient medium enables the radio sources to become very extended.

There are two different age estimates for radio sources. The first is based on the time scale for transport of energy from the nucleus out to the hotspots. The estimated jet speed is 0.1 c (Ishwara-Chandra & Saikia 1999) and the jet lengths are the projected distances between the lobes and the core. The second method is based on the lifetime of the radiating electrons, which are affected by both synchrotron and inverse-Compton losses. This is the spectral age and can be estimated through multi frequency observations (Alexander & Leahy 1987; Leahy et al. 1989; Harwood et al. 2013). The source can be visible well after the supply of energy to the outer lobes has ceased, so the two timescales can differ from each other.

The morphology of the radio emission can in certain cases also be used to constrain the age of the nuclear activity. AGNs are thought to be active for limited periods of time but may go through periods of activity. Double-lobed radio sources provide a direct observational constraint of this. Double-lobed radio sources have two pairs of lobes aligned along the same axis, and with a common radio core. The pair of lobes are interpreted as being produced at two different periods of AGN activity. Schoenmakers et al. (2000) estimated the time of the interruption in AGN activity to a few Myr.

1.4.4 Sample selection

All the sources presented in this thesis have been selected is a similar manner, and are effected by certain selection effects. In the search for high-z the $z - \alpha$ correlation was used to identify candidate HzRGs (with steep α) from large number of radio sources (Roettgering et al. 1994; Blundell et al. 1998; De Breuck et al. 2000). These were then compared to wide-field optical and NIR survey to find a host galaxy counterpart, using optical CCDs in the 1990s (e.g., Roettgering et al. 1995; McCarthy et al. 1996) and later with K-band imaging (De Breuck et al. 2002). When the position of the host galaxy had been located to arcsec resolution, follow up spectroscopic observations were made to identify the redshift of the HzRGs. Spectroscopic redshift confirmation is very expensive in terms of telescope time in general, but especially because HzRGs are scattered across the sky and cannot be grouped together. The spectroscopic confirmations were made using lines like Lyα, He II, C IV and C III] and are effected by the so-called "redshift desert" region of $1.2 < z < 1.8$ (Cruz et al. 2006). This mean that the lines fall in a wavelength range not covered by optical instruments. For very high redshift these lines also fall outside the range. The sample is redshift biased since it is difficult to get complete spectroscopic redshift confirmation and galaxies in the redshift desert and at high redshift are underrepresented. Another bias may arise from the fact that sources which does not show strong emission lines (i.e. galaxy containing large amount of dust) would also be "missing" since spectroscopic observations would not detect any lines. Another bias for this particular sample of radio galaxies arise from the initial selection criteria. A steep spectral index might mean we are biasing our sample towards galaxies residing in denser environments which are thought to makes the radio lobes brighter and steeper.

1.5 Galaxy spectral energy distribution fitting

The spectral energy distribution (SED) of a galaxy is the combined light from all sources of radiation within a galaxy after is has been passed through the ISM. Basically all physical properties of a galaxy alter the shape of the SED. The main factors are the stellar population, dust mass and grain size distribution, abundance of metals, radiation field and presence of an AGN. The basic principle of SED fitting is to extract physical values by fitting modeled spectra to the observed SED. From this, quantities such as the stellar mass, star formation rate, star formation history, metallicity, dust properties and the stellar initial mass function (IMF), can be constrained.

The observations of light from a galaxy can be divided into two types, photometric and spectroscopic. Photometric data are measurements where the radiation is summed over a certain wavelength range, by integrating the flux through a filter. Spectroscopic data are observed with a spectrograph which provide detailed information as a function of wavelength. Spectroscopic observations are very useful and can provide very constraining information about an object, but they are very time consuming. Because of this, high-z studies often rely on photometric measurements instead. One of the strengths of SED fitting is that even though galaxies are observed mainly through broad-band photometric filters, the modeled spectra can still be constrained to determined physical properties of the source.

As have already been discussed, the light at different wavelengths typically probe different underlying physical processes. The UV-optical is mainly due to young massive stars, in the red and NIR the older population peaks. The mid to FIR is usually dominated by dust emission and the radio originates from synchrotron emission. If the galaxy host an AGN, it can contribute to both the optical and IR, as well as in X-ray and radio emission. Depending on what scientific question you want to answer, you will most likely study different wavelength ranges of the electromagnetic spectrum of a galaxy.

In this thesis I am interested in constraining the SFR and the luminosity of the AGN. I do this by disentangling the IR emission from dust heated by the stellar population and the AGN. I will thus mainly focus on the IR to radio part of the spectrum. Still, I will briefly discuss SED fitting for galaxies in general, the available codes, their limitations and the motivation why I during my thesis made yet another code.

1.5.1 The basics

There two main ingredients needed to preform SED fitting are empirical or theoretical models, and a fitting routine to finds the most likely solution by comparing the model predicted fluxes to the observed quantity. These two components are combined into a SED fitting code. The algorithm used for fitting and the models vary from one code to another, depending on the intended use of the SED fitting code.

Models

Depending on what you are studying, the models can vary in complexity and be motivated by both empirical and theoretical aspects. The models are either in the form of templates or analytic models. A main part of the modeling effort in galaxy evolution has been made in describing the spectra of a collection of stars, referred to as a simple stellar population (SSP). This is the combined emission from stars born at the same time. It is determined by 3 main parts: 1) the individual spectra of each star; 2) the evolutionary tracks of stars of different masses known as isochrones, which specify the position in the Hertzsprung-Russell diagram for stars with a common age and metallicity; 3) the IMF, which describes the how many stars of a certain mass are born (Salpeter 1955; Kroupa 2001; Chabrier 2003). SSPs (e.g, Fioc & Rocca-Volmerange 1997; Bruzual & Charlot 2003; Maraston 1998) are alone not enough to describe the combined emission of a galaxy, you need to create composite stellar populations (CSPs). They require two additional steps; 1) consider the star formation history and from that construct SSPs with a range of ages; 2) take into account the chemical evolution and include stars with a range of metallicities. To get a total SED of your galaxy you also need to take into account the attenuation of CSPs by dust and also include the re-emitted radiation by heated dust. These are the main components needed to build up the SED for normal galaxies in the range UV to FIR (Fig. 1.11). These models are usually provided in SED fitting codes as large libraries, containing templates of pre-modeled galaxy spectra. Libraries are created by varying the star formation history, metallicity and dust abundance. If you have data to constrain the whole wavelength range, you will in principle be able to infer quantities such as stellar mass, dust mass, dust temperature and/or star formation history, as long as your models are representative of the object in question.

Another approach to SED fitting is to use analytic models to describe the observed SED. This does not require large libraries of templates. However, this approach is not applicable to all galaxy components, since the emission is often too complicated to be modeled with a simple analytic model. It is for example not uncommon to model the emission of dust in the far-IR with a simple modified black body or the radio emission from synchrotron radiation as a power-law with an exponential cut off (the point where radiation losses starts effecting the spectral index). In this case the number of free parameters is easy to control.

To expand SED fitting to also include active galaxies, the emission from the AGN must also be modeled and added as an additional component. Again, this can either be in the form of empirical/theoretical templates or analytic models to describe the general shape of the SED without fine details.

Fitting routines

Whether you have a set of generated templates or analytic models, you need to fit these to the observed data points. This can be done in different manors, but the main idea is to use an algorithm that finds the most likely solution between the modeled and observed data. In the beginning of SED fitting the algorithms were relatively simple, such as chi-square statistic. This is based on minimizing the χ^2 parameter (often refereed to as the goodness of the fit) which is a sum of the differences between the modeled and observed flux in a set of photometric band.

$$\chi^2 = \sum_{i}^{n} \frac{(O_i - E_i)^2}{E_i}, \tag{1.17}$$

Where $i = 1, ...n$ number of photometric bands, O_i is the observed flux in the ith band and E_i the expected flux calculated from a give model. In recent years it has become more popular to use Bayesian statistics. In this framework the the prior beliefs together with the likelihood function are combined to construct a posterior belief distribution, this is given by Bayes' theorem,

$$P(M|D) = \frac{P(D|M)P(M)}{P(D)} \tag{1.18}$$

where $P(M|D)$ is the posterior distribution after providing the observed data D. The P(M) is the prior probability distribution, or prior belief of the model M before obtaining the data. $P(D|M)$ is the likelihood function, so how likely it is that model M is describing the observed data. And $P(D)$ is the model evidence.

The amount of available data usually puts a tight constraint on how complicated models you can reasonably fit to your data. This is something one should keep that in mind when working with SED fitting. It is easy to over interpret results from SED fitting. This is because even if you have a only a few observed data points, you might be able to fit a model to them and estimate

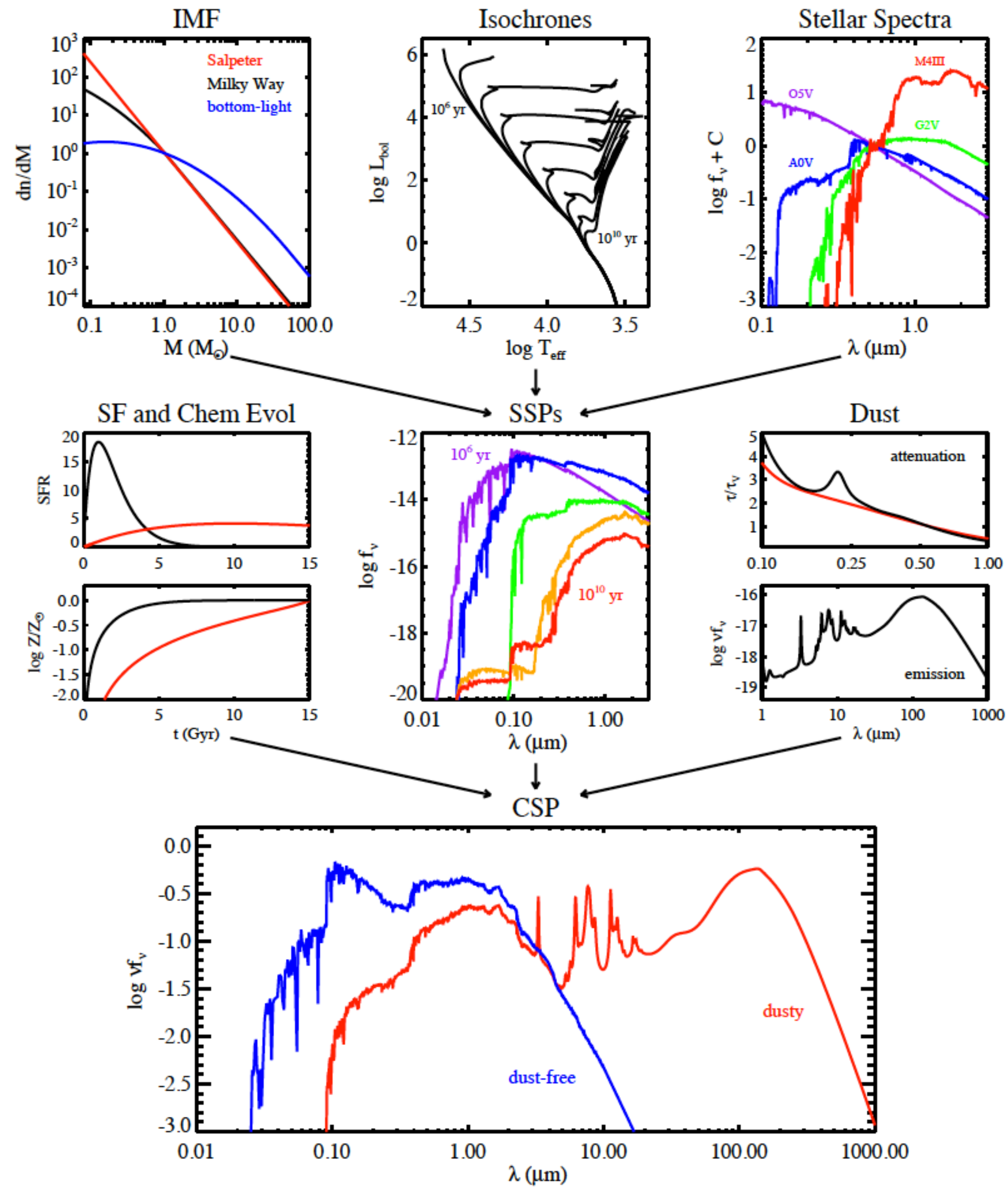

FIGURE 1.11: Overview of the main components needed to crate the emission from normal galaxies in the wavelength range UV to FIR. Reprinted from (Conroy 2013)

several physical quantities, but for which you might actually not have data to constrain them properly. A rule of thumb is to not ever have more free parameters then number of data points.

1.5.2 Available galaxy SED fitting codes

The first software to fit SED of high-z galaxies were made for the paper Sawicki & Yee (1998) and was later developed into the code SEDfit (Sawicki 2012). It can be used to estimate photometric redshifts and for fitting galaxies in optical to NIR. Following this, several other complete SED fitting codes (including both models and fitting routines) have been produced. MAGPHYS is a self-contained package to interpret galaxy SED in the range UV-FIR (da Cunha et al. 2008). It has also been updated to cover high-z galaxies including also radio emission (with fixed spectral index) but does not include any AGN component (da Cunha et al. 2015). CIGALE is a galaxy evolution SED fitting tool operating in the Far-UV to FIR. It includes AGN templates and can disentangle the IR dust emission components caused by stellar and AGN radiation (Noll et al. 2009). DecompIR is a IR specialized code focused on the decomposition of dust emission heated by stellar and AGN radiation (Mullaney et al. 2011). AGNfitter operates in the UV to sub-mm and includes four components: stellar population, dust emission heated by stars, an accretion disk and a torus of AGN heated dust (Calistro Rivera et al. 2016). Another code which will soon become public is PÉGASE.3 a galaxy evolution SED fitting code in UV to sub-mm wavelengths (Fioc et al. in prep). This list of codes is not complete, but highlights some of the most popular ones. There exist many others, some specified to more specific tasks. At the start of my PhD thesis there where no publicly available code that could disentangle dust emission heated by AGN and stellar radiation as well as including synchrotron radiation in the IR to sub-mm.

1.5.3 The increasing complexity with high resolution data

All of the above mentioned codes have been developed to study galaxy evolution. Since this is a huge topic in itself, each code focuses on different aspects and there is no universal code that can be applied to all galaxies. One typical common limitation of photometric SED fitting codes is that they often assume that the flux measure in all bands originate from the same source. This might not seem like a problem, if you have reliable astrometry you should be able to ensure that your observed flux comes from the same galaxy. Now, the problem lies in the fact that photometric data is often very inhomogeneous, in order to cover a wide wavelength rage. The data set is often a combination of space based telescopes (e.g. *Hubble*, *Herschel* and *Spitzer*), ground based facilities, single dish and/or interferometric data. The resolution is different depending on the wavelength and the aperture size (Table. 1.1). For a single dish telescope the angular resolution (θ) is give by the Rayleigh criterion of a circular aperture,

$$\theta = 1.22\,\frac{\lambda}{D} \tag{1.19}$$

where λ is the wavelength of the observed radiation and D is the diameter of the dish aperture. For extra galactic SED fitting the limitation in angular resolution is most prominent in the FIR (the peak of thermal dust emission). This is because the FIR is mainly probed with *Herschel*, a space telescope where the dish size is limited and results in a large beam size. The peak of the dust emission is thus not alway well constrained since several sources can fit within one beam and contribute to the observed flux. When for example complementary ALMA observation is available it has been shown that one or more extra source can be located within one *Herschel* beam. These additional sources can for example be merging galaxies, star-formation regions in the CGM, or synchrotron emission. The spatial resolution add new information about the system and should preferably be included in SED fitting. If you know for example that you are actually looking at two galaxies instead of just one (which is would look like with *Herschel*), fitting a single galaxy template

Telescope/instrument	wavelength [μm]	aperture [m]	angular resolution [arcsec]
Hubble/WFC3	0.2–1.7	2.4	0.02–0.15
Spitzer/IRAC	3–8	0.85	1–2
Herschel/PACS	90–155	3.5	5–9
Herschel/SPIRE	240–480	3.5	15-30
APEX/LABOCA	870	12	18.6
ALMA/band6	1300	19–558*	0.4
ALMA/band3	3200	15–600*	1.5

TABLE 1.1: Example of the wide range in resolution for a selection of instruments. (*) the range in baselines, the resolution of ALMA depend on the configuration.

to all your photometric data points may no longer be justifiable. Now, if you only observe multiple components in you ALMA data, it might be clear what the physical origin of the different sources are. This is where multi-wavelength observations might break degeneracies. But this requires a flexible SED fitting routine, able to handle multiple components in the photometric bands with high enough resolution to resolve individual components, and fit the combined expected flux from the individual models in the photometric which does not resolve any structure.

FIGURE 1.12: Inspection of the ALMA high site in 2016 by the author and CDB.

1.6 Telescope-instrument

The data presented in this thesis are obtained mainly by using the ALMA telescope operating in the mm/sub-mm and by using the MUSE instrument installed on the Very Large Telescope operating in the optical wavelength range.

1.6.1 ALMA

The Atacama Large Millimeter/submillimeter Array (ALMA) telescope is as given by the name, an array of antennas and observes light between infrared and radio waves. It is situated on the 5000 m high plateau Chajnantor, in northern Chile. The array consists of 66 individual antennas which work together via a technique called interferometry, which combines the signal from each antenna and combine them to reconstruct an image. This technique makes it possible to obtain high-precision images without constructing enormous single dish telescopes, since the distance between antenna pair acts as the dish size of an interferometer. The 66 ALMA antennas can be arranged in different configurations with the maximum distance varying between 150 m to 16 km. This flexibility allows ALMA to observe with different resolutions and study structures of different spatial extent. ALMA also has an extension called Atacama Compact Array (ACA) which is an additional array of smaller (7 m, the standard antennas are 12 m) telescopes in a more compact configuration, sensitive to very extended structures. ALMA currently offers observations in eight different wavelength bands, covering most part of the range 0.3–3.3 mm (Fig. 1.13).

1.6.2 MUSE

The multi-unit spectroscopic explorer (MUSE) is an instrument installed on UT4 at the Very Large Telescope (VLT). The telescope is part of the Paranal Observatory situated at a height of 2635 m in the Atacama desert in northern Chile. MUSE is an optical wide-field integral field spectrograph, meaning it is an instrument that combines spectrographic and imaging capabilities. It has a field of view of 1×1 arcmin, with a sampling of 0.2×0.2 arcsec spaxels. The field is divided into 24 sub-fields which are fed into 24 integral field units. It has an spectral range of 0.465–0.93 μm and produces a cube where each plane is an image and each pixel is a spectrum.

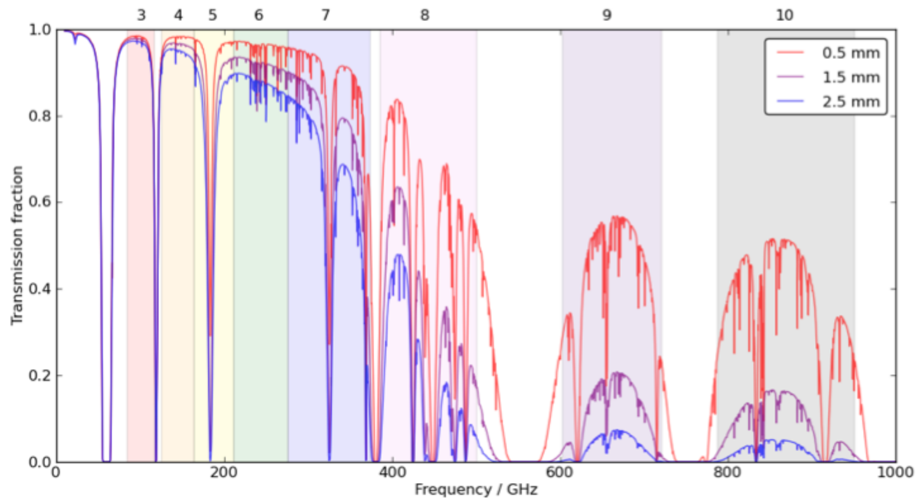

FIGURE 1.13: Atmospheric transmission as a function of wavelength, given for three different column densities of percipitable water vapour (PWV). Credit: ALMA European arc

1.7 Outline

In this thesis, I present new constraints on the star formation rate of HzRGs by including additional ALMA data at $\lambda \sim 1$ mm to previous photometric LABOCA, *Herschel* and *Spitzer* measurements. The star formation rates are estimated through SED fitting. In order to make use of the spatial information provided by the high resolution deep ALMA data in fitting, I developed a new SED fitting code, Mr-Moose. I also explore the environment around one individual HzRG, in molecular and ionized gas by combining ALMA and MUSE 3D data cubes.

Chapter 2

Chapter 2 presents the new SED fitting tool Mr-Moose (Multi-resolution and multi-object/origin spectral energy distribution fitting procedure). This is a flexible fitting routine that can be used to simultaneously fit multiple components depending on the geometry and complexity of the source. In its current version, it only includes the feature where the user can define analytic models to describe the observed SED. The code is not limited to a fixed wavelength range, it is instead the analytic models that determines over which range they are applicable. The code is meant to be fully adaptable in the choice of the number free/fixed parameter. The code also handles data points which are reported as upper limits in a continuous way when the goodness of the fit is evaluated. Mr-Moose is open source and have been made publicly available[1].

The code and paper

For the code, I developed the main framework of the code, the way the input files are read, inclusion of filters, the adaptive inclusion of analytic models and the simultaneous fitting of multiple components. The code was then made publicly available by my collaborator Guillaume Drouart, who also included functions to automatically generate images of the fitting procedure as well as making it possible to have different redshift for different components. The paper was mainly written by my collaborator who is the first author, by all rights. All the functions of the code and creation of figures utilized in Chapter 3 were developed by me.

[1] https://github.com/gdrouart/MrMoose

Chapter 3

Chapter 3 presents the observations, data reduction, analysis/discussion of ALMA band 6 or band 3 data obtained for 25 HzRGs at $1 < z < 5.2$. The continuum images show a more complicated picture of the sub-mm than expected, where the thermal dust emission might be contaminated by multiple dust sources and/or synchrotron emission. This was the main motivation for creating Mr-Moose. By the means of SED fitting it is possible to disentangle the FIR emission into AGN and star-formation heated dust as well as synchrotron. This together with many non-detections in the ALMA band reveals much lower star formation rates than previously estimated for HzRGs, suggesting they are on their way of being quenched.

The paper

For the paper I have reduced all ALMA data (except for one source 4C 23.56), produced all the plots and carried out the analysis and discussion. The ATCA data was reduced by a collaborator. I have written the paper, with contribution from my collaborators i.e. §3.5 and §3.6.

Chapter 4

Chapter 4 presents a study of the gas around the HzRG 4C 19.71 at $z = 3.59$, using ALMA [C I](1–0) and MUSE rest frame UV emission lines Lyα, C IV and He II. The observations, data reduction and analysis reveals an extended structure of diffuse ionized gas, roughly following the ionization cone. Extended multi-phase quiescent CGM gas is detected in [C I](2–1) and C IV with very narrow line widths. We present simple Cloudy modeling, which shows that the line ratios are consistent with a PDR in the CGM ionized by the AGN. But since we are limited to low signal-to-noise and few emission lines, the modeling results are not conclusive, but we illustrate the power of probing the gas with multi-wavelength observations

The paper

For the paper I have reduced the ALMA and MUSE data, done the analysis and produced all the plots (except Fig. 4.5). I have written the paper with the contribution from collaborators i.e. §4.4.3. The cloudy modeling was done my MDH.

Chapter 2

Mr-Moose: An advanced SED-fitting tool for heterogeneous multi-wavelength datasets

MNRAS 477, 4981–5000 (2018)

G. Drouart[1] and T. Falkendal[2,3]

[1]International Centre for Radio Astronomy Research, Curtin University, 1 Turner Avenue, Bentley, Western Australia 6102, Australia, [2]European Southern Observatory, Karl Schwarzschild Straße 2, 85748 Garching bei München, Germany, [3]Institut d'Astrophysique de Paris, 98bis boulevard Arago, 75014 Paris, France

Abstract

We present the public release of Mr-Moose, a fitting procedure that is able to perform multi-wavelength and multi-object spectral energy distribution (SED) fitting in a Bayesian framework. This procedure is able to handle a large variety of cases, from an isolated source to blended multi-component sources from an heterogeneous dataset (i.e. a range of observation sensitivities and spectral/spatial resolutions). Furthermore, Mr-Moose handles upper-limits during the fitting process in a continuous way allowing models to be gradually less probable as upper limits are approached. The aim is to propose a simple-to-use, yet highly-versatile fitting tool for handling increasing source complexity when combining multi-wavelength datasets with fully customisable filter/model databases. The complete control of the user is one advantage, which avoids the traditional problems related to the "black box" effect, where parameter or model tunings are impossible and can lead to overfitting and/or over-interpretation of the results. Also, while a basic knowledge of Python and statistics is required, the code aims to be sufficiently user-friendly for non-experts. We demonstrate the procedure on three cases: two artificially-generated datasets and a previous result from the literature. In particular, the most complex case (inspired by a real source, combining *Herschel*, ALMA and VLA data) in the context of extragalactic SED fitting, makes Mr-Moose a particularly-attractive SED fitting tool when dealing with partially blended sources, without the need for data deconvolution.

2.1 Introduction

Confronting observations and models of our Universe is the very core of any fitting procedure. However, the fitting process faces an increasing number of challenges to adapt and compare the wide variety of models and observations. From the modelling side, generations of large libraries of highly non-linear physical processes allow for a more accurate description of the complexity of the physical processes at work in the sources. From the observer's side, new instruments and facilities continue to push further resolution — both spectrally and spatially — and sensitivity over the electromagnetic spectrum. The principle of fitting appears at the frontiers of these two sides and interfacing these two aspects optimally is crucial. How to obtain maximal information from the data (which can vary a lot on quality and quantity) and compare it to the most optimal models available? By optimal here, we define the model which will represent data with the most fidelity or complexity without going in the regime of "overfitting", where degeneracies between parameters dominate, and therefore, no meaningful constraints can be extracted from the dataset (usually keeping in mind the Ockham razor principle). This optimal regime can be quantified thanks to the Bayes theorem, where likelihood of different models can be compared to find the relative likelihood probability of one model compared to another. The particular case of spectral energy distribution fitting is an old problem and can be traced as far as the 1960s (e.g., Tinsley 1968). This technique has seen a considerable development starting at the end of the twentieth century and is now widely used in most fields of Astrophysics: from stars in our Galaxy to very distant galaxies during the epoch of reionisation.

As data throughout the electromagnetic spectrum became readily available, more and more complex models were developed, such as PEGASE (Fioc & Rocca-Volmerange 1997), Maraston (1998), *Starburst99* (Leitherer et al. 1999), Bruzual & Charlot (2003), MAPPINGS III (Groves et al. 2004) to predict galaxy emission and Pier & Krolik (1992); Hönig et al. (2006); Fritz et al. (2006); Nenkova et al. (2008); Stalevski et al. (2012); Siebenmorgen et al. (2015) for AGN emission to name the most widely used. Note that these codes do not contain any fitting routines, their main intent being to provide the user with a vast library of templates exploring a large, often non-linear parameter space. As a result, SED fitting techniques remained primitive, mainly using minimising algorithms and regression such as least-square or chi-square minimisation. Since 2000, we have seen a rise of tools implementing more sophisticated statistical frameworks in order to explore degeneracies in the increasing complexity of the SED fitting. It is important here to distinguish the two complementary aspects of SED fitting: the models used to predict the SED given a set of parameters and assumptions (Conroy 2013, for a recent review) and the algorithm used to estimate the parameters on data (the fitting itself, see Sharma 2017, for a review on the different available algorithms). During the last decade, these two aspects were often combined to provide users off-the-shelf SED fitting procedures with a varying wavelength range: Magphys (da Cunha et al. 2008) for galaxy evolution in the UV-FIR range, BayesClumpy (Asensio Ramos & Ramos Almeida 2009) for AGN torus fitting in the UV-FIR range, CIGALE (Noll et al. 2009) for galaxy evolution with AGN implementation in the UV-FIR range, BRATS (Harwood et al. 2013) specialised for multi-radio frequency fitting in resolved sources, SEDfit (Sawicki 2012) for galaxy evolution in optical/NIR implementing spatially resolved sources, SEDeblend (MacKenzie et al. 2016) for SED fitting in the context of lensed source with FIR observations, AGNFitter (Calistro Rivera et al. 2016) focusing on the AGN component in the UV-FIR range, etc. to name the most widely used in extragalactic astronomy[1].

In an extragalactic context, most of these codes such as Magphys, CIGALE, BayesClumpy or AGNFitter, rely on a relatively strong assumption: all the emission comes from a single unresolved source and cross-identification at different wavelength is trivial. This simplification, while being necessary to enable the interpretation of extended multi-wavelength coverage (typically from UV to FIR) and to make use of the numerous source catalogues available in literature, is also one of their most important shortcomings in the advent of high resolution imaging across the electromagnetic spectrum. Indeed, as the wavelength range increases, resolution and sensitivity change drastically, and the assumption of the single source is no longer valid. Also, the other codes such as BRATS, SEDeblend or SEDfit are specialised in relatively short wavelength range and/or very specific applications: BRATS for spectral index mapping in radio, SEDeblend for lensed sources

[1] see also `http://www.sedfitting.org/Fitting.html` for a more exhaustive listing.

in the FIR domain and SEDfit in the optical/NIR domain for resolved galaxies. None of the aforementioned codes present the possibility to fit partially resolved sources, from NIR to radio.

To cite a more specific example as presented in Gullberg et al. (2016a): fitting simultaneously *Spitzer*(3-160 μm Werner et al. 2004), *Herschel*(70-500 μm Pilbratt et al. 2010), ALMA(100-700 GHz) and VLA data for distant, partially resolved galaxies, illustrates exactly this point. One one hand, the resolution of *Herschel* does not allow to properly disentangle different spatial components (blending) but provides five data-points in spectral space, particularly covering the thermal dust IR peak of the SED. One the other hand, ALMA is particularly suited to answer to the question of the spatial location, at the cost of smaller spectral coverage. Also the heating sources of the dust emitting at 70 μm and 3 mm is different (AGN or young stars) but is linked through the total energy emitted and their location. The same type of reasoning can be applied to the AGN radio emission (ν <100 GHz, from the VLA for instance), often unresolved at low frequency and presenting multi-components at higher frequencies (core, jets, hot-spots and lobes). In the case of radio galaxies, these last two aspects are even co-existing for a single source. Therefore, as these observations are complementary, each providing valuable constraints spectrally and spatially on different overlapping components (some with non-detections), why not combining all information together? This is where Mr-Moose intervenes, providing a framework to simultaneously combine spatial and spectral information into a single fitting routine. The paper is organised as follows: we explain the methodology and structure of the code as well as the description of the input and output files in § 2.2. § 2.3 presents three examples of application of Mr-Moose. In § 2.4, we discuss the limitations and future developments and finally conclude in § 2.5.

2.2 Design and structure of Mr-Moose

Mr-Moose stands for Multi-resolution and multi-object/origin spectral energy distribution fitting procedure. The philosophy when designing Mr-Moose was to provide a tool for SED fitting, sufficiently simple to be used by non-SED fitting experts, yet sufficiently versatile to handle as many cases as possible, particularly in the context of multi-wavelength samples. The main drivers for the design are:

1. to handle data with a large span of resolutions to combine interferometer/single-dish observations,
2. to deal with upper limits consistently, allowing a fit with gradually decreasing probability when approaching an upper-limit rather than an arbitrary cut at 3σ,
3. to treat the fitting in a bayesian framework to provide asymmetric uncertainties on parameters and to identify easily degeneracies as well as comparing different model combinations,
4. to allow a wide variety of models as input, analytic models for this first release and/or libraries for non-linear models in future updates.

Mr-Moose is written in `Python` 2.7, developed in PyCharm Community Edition and complies to the PEP8 writing standard. It relies as much as possible on already existing packages (see full list in Appendix) to further increase robustness. The code was designed to be user friendly but not user opaque. A large (and necessary) control of the data, model and fit setting inputs is allowed to test the reliability of the output and therefore avoid the "black-box" effect. However, the code aims to be sufficiently simple to be used with a minimal statistical and computational knowledge. We first present the core of the fitting procedure, the maximum likelihood estimation and review the inputs and outputs files. Table 2.1 summarises the different file extensions used in Mr-Moose. We also report a simplified flowchart of the code structure in Figure 2.1 and refer the user to a more detailed flowchart in the GitHub repository[2].

[2]`https://github.com/gdrouart/MrMoose`

Extension	Use	Description
.fit	input	file containing the settings for the fit.
.dat	input	file containing the data.
.mod	input	model file containing the function, parameters and their considered range
.fil	input	filter files, containing the transmission curves
.sav	output	file containing the information from the fit, saved for future use, and storing the settings for the fit
.sed	output	file containing the flux per frequency (in Hz) of the best fit for all components of the SED in unit of erg $s^{-1}cm^{-2}Hz^{-1}$
.pdf	output	output files containing the plots
.fits	output	modelisation of the source(s) in each filter from the .dat file
.py	...	Mr-Moose files containing the procedures.

TABLE 2.1: Summary of the convention for the file extensions, as used in Mr-Moose

2.2.1 The maximum likelihood estimation in Mr-Moose

The code working in a bayesian framework, likelihood calculation is central in identifying the most representative models to the data and providing marginalised probability density functions for each parameter in order to estimate uncertainties. Following the Bayes theorem written in terms relevant for SED fitting, the probability of a model M given the data D can be written as:

$$P(M|D) = \frac{P(M) * P(D|M)}{P(D)}, \tag{2.1}$$

where P(M | D) is the posterior distribution (the probability of M *after* observing D), P(M) is the prior probability (the probability of M *before* observing D), P(D | M) is the likelihood (the probability of observing D given M), and P(D) is the model evidence (a measure of how well the model M predicts the data D and can be considered as a normalisation factor to the problem, often non-trivial to estimate). Therefore, $P(M|D)$ is the final parameter distribution (that we are looking for) and $P(D|M)$ is likelihood to be determined and to maximise (or minimise given our estimator, a slightly modified version of the goodness-of-fit). This maximum likelihood (abbreviated P onwards) corresponds to the product of all probabilities of the model given the data and can be written as:

$$P \propto \prod_i P_i \prod_j P_j, \tag{2.2}$$

with *i* the detections and *j* the upper limits. We stress that the prior on the model parameters (set to uniform, corresponding to an uninformative prior in Mr-Moose version 1). Each individual probability distribution, respectively for detection and upper limit (following a normal distribution), are defined as follows:

$$P_i \propto \exp\left[-\frac{1}{2}\left(\frac{S_i^{data} - S_i^{model}}{\sigma_i}\right)^2\right]\Delta S_i, \tag{2.3}$$

$$P_j \propto \int_{-\infty}^{S_{lim,j}^{data}} \exp\left[-\frac{1}{2}\left(\frac{S_j - S_j^{model}}{\sigma_j}\right)^2\right] dS_j, \tag{2.4}$$

where S_i^{data} is the measured flux and σ_i, its standard deviation, S_i^{model} is the predicted flux, all in filter *i* for a detection and *j* for a non-detection. Note the ΔS_i as being the data offset from the true value of S_i^{data}, infinitesimally small in the case of detection, and dS_j referring to the integrated flux probability (S_j) to the detection threshold $S_{lim,j}^{data}$ (see Appendix 1, their Fig. 6, Sawicki 2012, for a graphical representation). Taking the logarithm of Eq. 2.2 and injecting Eq. 2.3 and 2.4, we obtain:

$$\begin{aligned} P \propto & -\frac{1}{2}\sum_i \left(\frac{S_i^{data} - S_i^{model}}{\sigma_i}\right)^2 + \sum_i \ln\Delta S_i \\ & + \sum_j \ln \int_{-\infty}^{S_{lim,j}^{data}} \exp\left[-\frac{1}{2}\left(\frac{S_j - S_j^{model}}{\sigma_j}\right)^2\right] dS_j, \end{aligned} \tag{2.5}$$

The second term of the right-hand side of the equation being constant, maximising the probability, P, corresponds to minimising the following estimator:

$$\begin{aligned} \chi^2 = & \sum_i \left(\frac{S_i^{data} - S_i^{model}}{\sigma_i}\right)^2 \\ & - 2\sum_j ln \left\{\sqrt{\frac{\pi}{2}}\sigma_j \left[1 + \text{erf}\left(\frac{S_{lim,j}^{data} - S_j^{model}}{\sqrt{2}\sigma_j}\right)\right]\right\}. \end{aligned} \tag{2.6}$$

We apply a change of expression of the third term of Eq. 2.5 making use of the error function, *erf*, for computational convenience (see Appendix A of Sawicki (2012) for details). In practice, the error function tends to infinity quickly but gradually after a threshold point (the upper limit) calculated by the user as the local noise level in the original image, in the corresponding filter (the same image at a given filter/frequency can provide a combination of detections and upper limits if the location of components are known). This χ^2 is only slightly different when including the upper limits into the calculation. We note that in the case when no upper limit is provided, the second term is null, and therefore the equation corresponds to the classical χ^2 definition. In order to explore the parameter space and minimises the χ^2 (equivalent to maximising the posterior probability), we make use of the `emcee` python package (Foreman-Mackey et al. 2013), allowing a choice of different samplers to probe the parameter space.

The `emcee` package follows the classic Markov chain Monte Carlo (MCMC) approach, consisting of randomly moving walkers exploring the parameter space. The main goal is to sample of the posterior probability density function of the parameters with a sufficiently high number of independent realisations. This is the best compromise between a brute force approach where each solution of the parameter space is calculated for a given grid and a standard least-square minimisation where only the best solution is provided (which can be a local minima). This approach also presents the advantage to estimate uncertainties on the model parameters, even with non-normal distributions thanks to the exploration the parameter space, but without the computing cost (increasing exponentially with the number of parameters). To explore and reach convergence on the best solution, the main idea of a MCMC approach is to set a walker in the parameter space, moving randomly with a given step size. For each new position, the likelihood function is evaluated, and the step is accepted if the probability is higher than the previous position. Hence the walker moves slowly towards the best solution which maximise the likelihood function. Several algorithms are available, the most famous being the Metropolis-Hasting (M-H) algorithm. However, this algorithm can fail to converge quickly when the convergence parameters are not optimally tuned and the parameter space presents strong non-linear behavior (in particular if the step length is not optimised for the problem). New algorithms were developed to answer these caveats, reducing significantly the converging time. In particular, `emcee` uses affine-invariant transformations (Foreman-Mackey et al. 2013; Goodman & Weare 2010) to sample the parameter space, using a

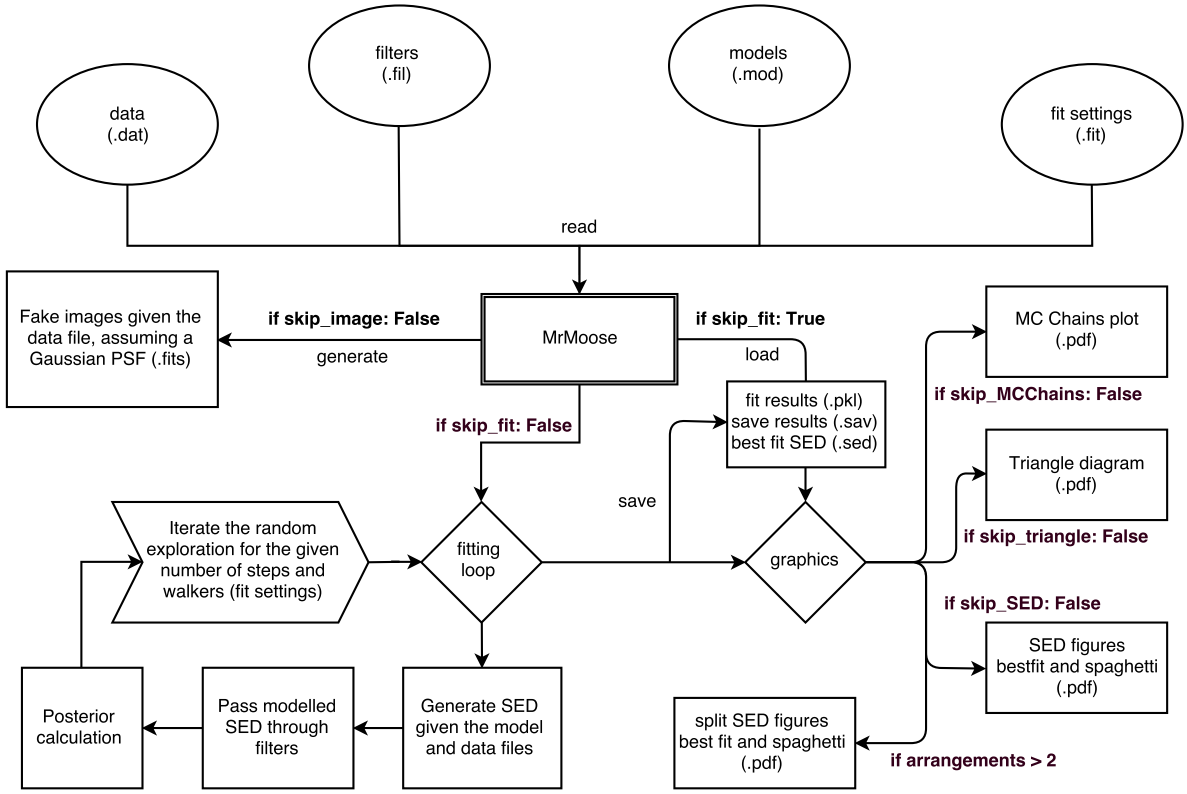

FIGURE 2.1: Flow chart of Mr-Moose.

stretch move based on the other walker positions. This presents the advantages of being less sensitive to strongly correlated parameters allowing a minimum loss of performance and therefore a quicker convergence. Also, this algorithm enables two valuable simplifications compared to the standard M-H: (i) the performance of the code is basically relying on two parameters: a, a gain parameter and n, the number of walkers and (ii) the possible parallelisation, splitting the chains into complementary sub-ensembles to predict iteratively the next walker moves, enabling even larger performance gains for specific problems. We refer the reader to Foreman-Mackey et al. (2013) for more details on the algorithm.

2.2.2 Inputs

Mr-Moose requires four input files: a data-file, a model-file, a setting-file, and the filter database each containing the necessary information to perform the fit (see Table 2.1).

Data file

The data-file requires the most attention in its design as it will set up the number of arrangements (the various data/model combination). The Mr-Moose procedure doesn't check for inconsistency in the data, and is the responsibility of the user to provide reliable or relevant photometric points (well calibrated and corrected for any photometric effects). To help with this step, corresponding images will be generated for each reported filter in the data file (see § 2.2.3). Multi-wavelength SED fitting is particularly challenging in this regard, therefore specific care should be taken in order to have consistent data throughout the fitting range (blending, filtering of scale/flux by interferometers, instruments corrections, aperture effects, absolute calibration uncertainties) by adding

Name of columns	Type	Purposes/Notes
Filter	string	filter name. It should match exactly the name of a filter in the database (case sensitive), without the extension (***.fil), necessary to calculate the model flux during the fitting (§ 2.2.2)
lambda0	float	central wavelength of the filter
RA	string	right ascension of the source in the 00h00m00.0s format - used only in the .fits generation
Dec	string	declination of the source in the 00d00m00.0s format - used only in the .fits generation
resolution	float	resolution of the instrument in arcsec - used only in the .fits generation
det_type	string	indicate if the reported value is a detection or an upper limit
flux	float	observed flux in the given filter
flux_error	float	uncertainty on the flux for the given filter
arrangement	integer	the number of the arrangement
component	string	the name of the arrangement (will be used for the spilt plot)
component_number	list of integer	the list of models to fit for this data point (separated with a semi-column)

TABLE 2.2: Structure of the .dat file. We provide here an example

extra models/arrangements if necessary. However, we stress that starting with a simple case and gradually complexifying the fitting is usually a rewarding approach. Table 2.2 summarises the data-file organisation.

Model file

The model-file contains the information of the parameters from the combination of the models to fit on the data. Table 2.3 shows the format of the model file. The function name is referring to the function to be called during the fit and therefore should match exactly the name of the user defined function (case sensitive). The function is to be defined in the `models.py` file. Ideally, it should be sufficiently well designed to avoid a drop in execution time as each model is executed at each step for each walker by avoiding as much as possible loops, conditions or function calls. The code already provides some functions, developed and tested for specific applications and examples (Gilli et al. 2014; Falkendal et al. 2018; Drouart & Falkendal 2018). We provide here a description of the models provided with the release of Mr-Moose:

- BB_law: a black body model directly called from the `astropy` package (Astropy Collaboration et al. 2013)

$$S_\nu = N\frac{2h\nu^3/c^2}{\exp(h\nu/kT)-1}, \tag{2.7}$$

  where S_ν is the flux in erg s^{-1} cm^{-2} Hz^{-1}, N the normalisation to the data (relatively complex term containing the scaling to the data and the solid angle covered by the source with the small angular size source simplification, depending on each instrument for unresolved sources see[3] for more details), ν the frequency in Hz, h the Planck constant, k the Boltzmann constant, T the temperature in K, c the speed of light.

- AGN_law: an empirical AGN model designed to fit the IR AGN component

$$S_\nu = N\left(\frac{\nu_{cut}}{\nu_{obs}}\right)^{-\alpha}\exp\left(-\frac{\nu_{cut}}{\nu_{obs}}\right), \tag{2.8}$$

[3] `https://casper.berkeley.edu/astrobaki/index.php/Single_Dish_Basics`

Name		
#		
function_name	number of parameter (n)	
first parameter	min value	max value
second parameter	min value	max value
⋮	⋮	⋮
n parameter	min value	max value
#		

TABLE 2.3: Structure of the .mod file. It consists of series of blocs, to be repeated as many time as necessary to add the models to be fitted on the data. We present an example in § 2.3.1 and § 2.3.2. It is to be noted that the name of the parameters should be expressed in latex syntax if the user requires the parameter to be written in latex format in the plot (particularly the triangle plot).

where ν_{cut} the cutoff frequency, α the spectra index, ν_{obs} the observed frequency in Hz

- sync_law: a single power law model, common form to represent synchrotron emission in radio and is defined as:
$$S_\nu = N\nu^\alpha, \tag{2.9}$$
- a modified black body function as used in Gilli et al. (2014) for example #3 (see § 2.3.3),
$$S_\nu = NB_\nu(T)\left(1 - \exp\left[-\left(\frac{\nu}{\nu_0}\right)^\beta\right]\right), \tag{2.10}$$
where B_ν is the blackbody function defined previously (as BB_law), β the dust emissivity and ν_0 the frequency where the dust emission enters the optically thick regime ($\tau = (\nu/\nu_0)^\beta$ =1).

Each model exists in two versions, the standard where an array of frequency, an array with the parameter and the redshift value is provided and a version with redshift as a free parameter by simply adding the `_z` at the end of the function (see examples in the Mr-Moose repository) and by changing the `all_same_redshift` and providing the relevant redshift array (one redshift value per component). Note that when the redshift is a free parameter, the inputs are slightly different with only an array of frequency and an array for the parameters. We refer the user to the examples available in the repository. The library of models will increase in future updates depending on the need, we refer to the user manual for an up-to-date library of available models. We remind that the package `astropy` (Astropy Collaboration et al. 2013) provides a large library of the most commonly used function in astronomy. Also, we suggest to design the model with parameters spanning a large range in log-scale (such as normalisation factors, as done in the examples in this paper), making sure the corresponding function is making the adequate transformation to calculate flux. The initial position of the walkers are set following the `emcee` documentation: a Gaussian ball of walkers, centred on the median of the parameter interval. This has important consequences and should be taken into account when defining this interval (see § 2.4).

Setting file

The setting file (see full structure in Table 2.4) contains the parameters for Mr-Moose to perform the fit such as the number of walkers (*nwalkers*), the number of steps (*nsteps*), the limit (*nsteps_cut*) at which the chains should be used to plot the results (the limit from which convergence of the fit is reached). We provide examples with typical numbers. For more information, we invite the user to read the recommendations from the `emcee` documentation. In a nutshell: the more walkers and steps, the better. However a balance has to be found to keep the code executable on a machine. From experience, one effective strategy consists to run some first blind tests to have a feeling of the likely requirements for the number of walkers and the number of steps. For relatively simple case, we advice to start with 200 walkers and run for 500 steps, with a cut at 400 (*nwalkers*=200, *nsteps*=500 and *nsteps_cut*=400). This first run will probe the parameter space with 20 000 points ((*nsteps-nsteps_cut*) $\times$ *nwalkers*) and gives an indication of how many steps might be required to reach convergence. For a larger the number of parameters, a larger number of walkers and steps is required to explore more thoroughly the parameter space (see example 1 versus example 2).

Filter database

The filter database is essential in the fitting routine as allowing to predict the flux of a given combination of components at a given wavelength. For each step, the average flux of the model is calculated through the transmission curve of the filter given in the data file. This transmission curve represents the response of a telescope for a constant incident flux (in the frequency space) for a given frequency range. The convolution of the incident flux with the telescope response is important as any large variation in the SED within a spectral window can bias the estimated flux, for instance in the case of an emission line or a strong gradient within the averaged frequency range. This effect is particularly strong in optical and NIR where the telescope response varies significantly from filter to filter. During the fitting, we therefore calculate for each filter, the corresponding telescope response convoluted with the modelled source with the following equation:

$$S_i = \frac{\int_{\nu_{min}}^{\nu_{max}} S_\nu^{model} t_\nu d\nu}{\int_{\nu_{min}}^{\nu_{max}} t_\nu d\nu} \tag{2.11}$$

where S_i the averaged flux for a given filter i, ν the frequency, S_ν^{model} the flux of the model and t_ν the transmission curve. Each of the filter used in the data file must be present in the database, or the code will fail to execute. Addition of new filters is easy, a simple text file with two columns, frequency and corresponding transmission can be added in the filters folder. For optical and NIR, given the large amount of filters used in astronomy, we point the reader to Asiago Database on Photometric Systems[4] to add the relevant filters for a specific analysis (Fiorucci & Munari 2003). For other wavelength, we refer the user to each instrument user manual to provide the relevant transmission curve. In the case of radio telescopes (ALMA, VLA, ATCA, etc), the bandpass calibration corrects for any effect, therefore the telescope response can be approximated as a gate function centred on the observed frequency and covered by the correlators (which can be discontinuous, depending on the configuration required to the science case)[5].

2.2.3 Outputs

Mr-Moose produces series of outputs, containing different information (see Table 2.1). The outputs can be divided in two parts: the supporting files (".fits", ".pkl", ".sav", ".sed") and the result files (".pdf"). We focus first on the support files and their contents, allowing to dig further in the interpretation if necessary and allow for an easy reproduction of a given fitting. We designed Mr-Moose to allow users familiar with the `emcee` package to use their custom tools from the ".pkl". However, Mr-Moose comes also with plotting functions to display results in order to interpret the result from the fit. There are several graphs ".pdf" file generated by the procedure: chain convergence, triangle and SED plots. These plots works "in unison" to understand the results of the fitting. Any unexpected behaviours in these plots should bring suspicion on the inputs, would it be data, model used, arrangements defined or the settings of the fitting procedure.

[4] `http://ulisse.pd.astro.it/Astro/ADPS/`

[5] two functions in the `mm_utilities.py` can be found to generate these gate filters

Parameter	Type	Purposes/Notes
source_file	string	the source file path where the data are to be read
all_same_redshift	boolean	keyword to allow for the redshift of the components to be a free parameter
redshift	float array	the redshift of each component in the system
model_file	string	the model file where the parameters of the models and their range are selected (the parameters to fit)
nwalkers	integer	the number of walkers for the fit (should be typical more than 100, emcee documentation advice at least twice the number of free parameters). It play a role on the speed at which the chain converges, so usually the more the better (in the limit of the computer memory).
nsteps	integer	the number of steps for each walkers to perform (can vary widely from 200 to several thousand base on the complexity of the problem)
nsteps_cut	integer	should be smaller than *nsteps*, it represents the number of steps to ignore when drawing the probability density function of the parameters (it depends mainly on convergence time and the number of walkers as it require to select a sufficiently large number of points to populate the parameter space after convergence.
percentiles	float array	the percentile of the distribution to be returned (used in the plots to show max intervals). Must be odd-dimensioned and all numbers in the range $0 \leq$*percentiles*≤ 1. The default values are chosen to represent probability density functions which are not normal, excluding the 10% outliers.
skip_imaging	boolean	skip the creation of the data file in images
skip_fit	boolean	skip the fitting
skip_MCChains	boolean	skip the generation of the MC-Chains plot
skip_triangle	boolean	skip the generation of the triangle plot
skip_SED	boolean	skip the generation of the SED plots
unit_obs	string	unit of the wavelength/frequency provided in the .dat file
unit_flux	string	unit of the flux provided in the .dat file

TABLE 2.4: Structure of the .fit file. In order, the columns refer to the name of the variable as expressed in the code, its type and its purpose.

Supporting files: chains, SED, fitting and fits files

The ".fits" files are generated following the data provided in the ".dat" file. For each filter, the procedure generates an image in the FITS format (commonly used in astronomy Wells et al. 1981), containing all the components associated with this filter, making use of the RA, Dec and resolution values provided in the ".dat" file. The procedure creates a unresolved source, assuming a Gaussian point spread function of full width at half maximum provided as the resolution parameter, at the given position (RA, Dec). This allow to check that the combination of the data file are correctly assigned by direct comparison with the original images, if available. We note that the pixel size is fixed to a fifth of the resolution parameter.

A ".pkl" file, contains the object from the `emcee` procedure saved making use of the `cPickle` function from the `pathos` package allowing a serialisation, necessary in case of parallelised use. No modifications are implemented from the original `emcee` sampler, and as such, `emcee`-familiar users can make use of this output into custom graphical tools. This file contains the complete chain for each walker and other diagnostics provided by the `emcee` package.

The ".sav" file contains the information from the fitting, including the setting file and the model structures, modified during the fitting and storing the final results in a YAML format. The file contains the final percentiles for each parameter, the best fit value, the name and path of the output files generated by the procedure.

A ".sed" file is created reporting each component of the models from the global best fit. The first column is the frequency in Hz, the following columns reports the flux in $\mathrm{erg\,s^{-1}\,cm^{-2}\,Hz^{-1}}$.

Result files: Convergence, Triangle and SED plots

The convergence plot shows the walkers exploration of the parameter space for each iteration of the procedure for each parameter. This plot helps to identify when convergence is reached, therefore to which value to set the *nsteps_cut* parameter to be used by the triangle and SED plots. When is convergence reached? The walkers should oscillate at given values in all windows simultaneously, revealing that they converged into the minimum of the parameter space. Note that several minima can co-exist, therefore the walkers can be split between several values, but as long as the chains are stable around these values (for several hundreds steps), convergence can be considered as reached. However, with the increasing complexity of larger parameter spaces, some walkers can be "stuck": i.e. moving erratically, very slowly or not moving at all. Therefore including these walkers in the subsequent plots would bias any interpretation of the probability density distribution. We report for completeness these "stuck" walkers in the convergence plot (with a different colour coding) as a check of the fitting (see § 2.3). These "stuck" walkers will be ignored in the triangle, and SED plots. We filter these out extracting only the chains from the sampler with a high acceptance fraction (meaning that walkers are effectively "walking"). The default value for this threshold of selection in Mr-Moose is set to half of the average acceptance fraction value of all chains (AAF value, for instance if AAF = 0.6, the threshold is defined as 0.3 and all chains below are ignored in the following steps). We report both the AAF along with the fraction of walkers filtered out with this cut (SW) in the convergence plot. For specific cases, where the default cut is not optimal, Mr-Moose allows to set a manual value (see README). As a guide, AAF should be in the 0.2-0.5 range and the stuck walkers fraction relatively low. For better details, we report the reader to the `emcee` documentation. Briefly, in the case of AAF and SW values being extremes, three solutions are to increase the number of walkers (*nwalkers*), to better define the initial parameter values through the parameter interval (see § 2.4) or to simply increase the number of steps (*nsteps*).

The triangle plot shows several pieces of information from the fit making use of the `corner` package. It basically uses all information contained by the selected walkers in the chain after the convergence value (*nsteps_cut*) provided in the setting-file. It presents two types of plot: 2D

Name	Purposes/Notes
triangle_plot	probability density functions for each parameter and by pair. This plot is particularly efficient to reveal degeneracies between parameters (banana shape) or unconstrained parameters by the fit (no single peak in the probability density function)
MCChains_plot	values of parameters at each step for each walker. This plot is particularly useful to show when convergence is reached, used to calculate all the quantities displayed in other plots
SED_fnu_plot	plot in units of frequency and flux of all the data and models on the same graphical window. While relevant for few components or arrangements, this plot becomes rapidly too complex for multi-component case
SED_fnu_splitplot	split plot in unit of frequency and flux for each arrangement defined in the data file
SED_fnu_spaghettitplot	plot showing all the possible parameter values on the SED after convergence (at each step for each walker). This plot translates the triangle plot on the data, showing how constrained the model is compared to the data.
SED_fnu_splitspaghettitplot	equivalent to the SED_fnu_splitplot but for the spaghetti style
SED_file	file storing the SED of each component as plotted in the SED_fnu plot
sampler_file	file storing the chains of the fitting.
save_struct	file storing the details of the fit for future references and reproducibility, save the fit settings dictionnary

TABLE 2.5: List of the output files and their use.

paired-parameter plots and marginalised distribution for each parameter in a form of a triangle. The 2D plots shows the probability density functions by reporting each step of each walker for the projected parameters. Additional contours are also added, representing an alternative version of the dot-representation, with contour values being at the 25%, 50% and 75% of the maximal value of the corresponding marginalised distribution. We stress that these contours do not correspond to the percentiles of the distribution, obtained by cumulative integration of the probability density function. Along the diagonal, the marginalised distributions of each parameter are presented by histograms. The percentile values defined in the setting-file are also reported. We recommend the use of a sightly different version of the seven-figure summary (L. 1920), omitting the two extremes, minimum and maximum values of the distribution as particularly sensitive to outliers and "stuck" walkers, therefore 10%, 25%, 50%, 75% and 90%. They usually present a good summary of different type of distributions (as it is expected to deviate substantially from normal distributions) although should not prevent to carefully check each distribution visually to identify problems. This triangle diagram is particularly helpful to (i) reveal any degeneracies among parameters (ii) reveal if parameters are constrained, and how well, given the dataset.

The SED plots show the fit of each arrangement on the data, the final results of the models and data combination. The final number of generated plot changes, depending on the complexity of the source considered. First, the SED is coming in two versions, a best fit and a "spaghetti" version. The former shows the best overall fit to the data, each colour corresponding to one model (the maximum likelihood reached in the chains). The latter shows all the solutions provided by each walkers at each step after the convergence cut (same than the triangle plot). This is particularly useful to see how good the models are constrained with the data in combination with the triangle and convergence plots. We choose this representation over a shaded area representation to better visualise the constraints from the data and to better highlight the different solution in case of the presence of several minima. For sources with several arrangements, split versions of the SED will also be produced to ease interpretation (see examples in § 2.3) with colour coding of the models conserved over the windows.

Name	parameter	true value	fit value
sync_law	N	-22*	$-21.85^{+0.14}_{-0.15}$
	α	-1	$-1.02^{+0.02}_{-0.02}$

TABLE 2.6: Components and parameters of example #1. * value in logarithmic scale. The uncertainties quoted are the 25 and 75 percentiles.

2.3 Examples

In order to demonstrate Mr-Moose capabilities, we focus here on three specific extragalactic examples which where used to build this procedure (the code is provided with several examples with increasing complexity, we focus here on the artificial ones produced by the file `example_1.py` and `example_6.py`) as well as a previous result from literature. For the sake of simplicity, we will refer to them as example #1, #2 and #3, respectively. The first is a simple case of fitting, with only one model onto a dataset, here synchrotron emission from a radio source in the 74 MHz-8.4 GHz range. The second case is much more complex: we here aim to disentangle the contribution of various components, spatially non-collocated and originating from different physical processes. We take the example of a powerful radio galaxy and a star forming galaxy companion with separate emission from the lobes (of synchrotron origin), the dust heated by star formation and the dust heated by AGN, in the 8 μm-1.4 GHz wavelength range. The third example cover a real dataset published in Gilli et al. (2014), fitting a modified black body in the 70 μm-3 mm range to reproduce dust emission of a distant quasar, demonstrating the useful addition of upper-limits in the fitting process.

2.3.1 Example #1: single source, single component

This example is the simplest fitting imaginable for Mr-Moose, consisting of a single law on a given dataset. Although of limited interest, it allows us to familiarise with the code. We benchmark Mr-Moose by generating a fake source and trying to recover these original parameters.

Fake source and input files

To generate a fake source data-points, we assume a single, unresolved source at $z = 0$ emitting a single synchrotron law represented by the model `sync_law` with α=-1 and $\log_{10}N$=-22 (to recover a source with flux at Jy-level) where α is the slope and N the normalisation (in log-scale). We generate five single points passing this SED through the filters from the filter library and assign a given signal-to-noise ratio (here SNR=5 for all points). We simulate further observation uncertainties by adding a random gaussian noise with a standard deviation corresponding to the provided SNR value. In practice, the code adds (or subtracts) flux to each datapoint, not following exactly the original synchrotron law defined previously. By adding this extra noise the chance of recovering the exact parameter values decreases, this perfectly illustrates the real case of observations, where each point is drawn from a distribution. This fake data-file (Listing A.9) is, along with the setting-file (Listing A.6) and the model-file (Listing A.1), generated from the `example_1.py` procedure (provided with Mr-Moose). These files are therefore fed into Mr-Moose to perform the SED fitting.

Output files and results

The code generates the output files previously described (see § 2.2). We focus on the four ".pdf" plots: the convergence plot (Fig. 2.2), the triangle plot (Fig. 2.3) and two SED plots (in unit of F_ν, Fig. 2.4).

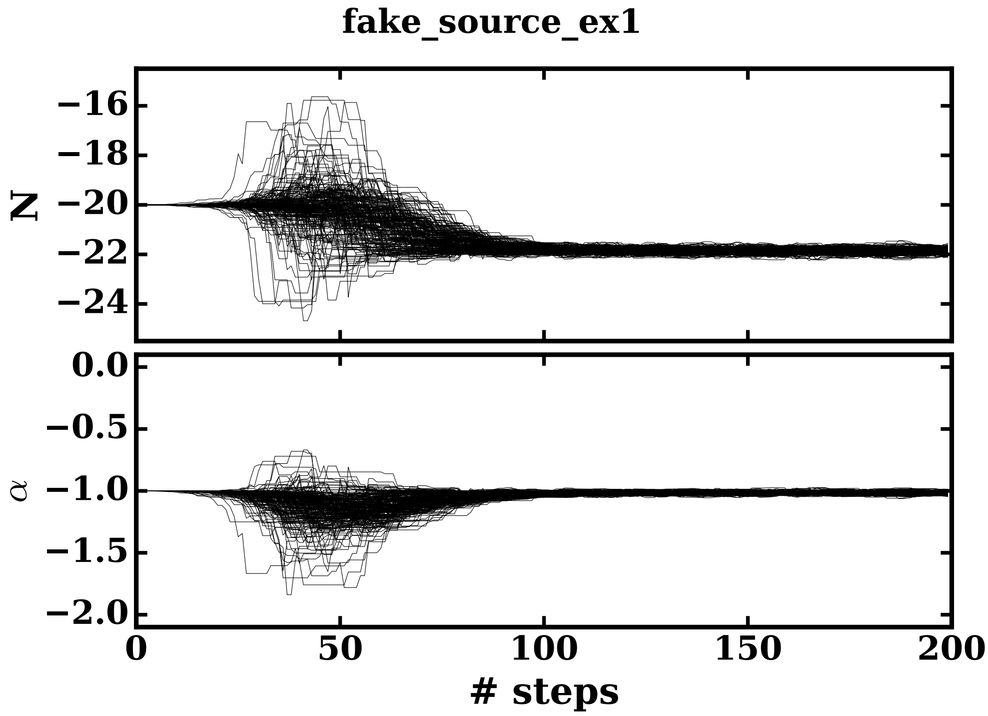

FIGURE 2.2: MC-Chains for each parameter for the given number of steps for example #1. Note the convergence reached roughly after step #100

The MC-Chains plot (Fig. 2.2) shows here a quick convergence (reached roughly at the #100 step). We define *nsteps_cut*=180, and apply it to the subsequent plots (triangle and SEDs).

The triangle plot (Fig. 2.3) is the classical plot to represent multi-parameter space: plotting the distribution of parameters in pairs with the marginalised distribution of each parameter on the hypotenuse of the the triangle. Along this diagonal, the marginalised distribution for each parameter is a histogram. The dashed lines are the percentiles provided in the setting-file, here 10%, 25%, 50%, 75% and 90% (provided by the user in the setting-file), as recommended in § 2.2. The parameters are well constrained in a small area of the parameter space. It is interesting to note that even if the two marginalised distributions show relatively Gaussian-like distributions, the 2D projection is far from being a symmetric cloud. The contours correspond here to 25%, 50% and 75% from the maximal value of the marginal distributions. Overall, we note that the input parameter are recovered within the uncertainty interval (remembering we added extra noise to the data, see Table 2.6).

As presented in § 2.2, the code generates two version of the SED to visualise convergence and the effect of uncertainties: the best fit and the "spaghetti" version allows to visualise the how well the data constrain the parameters of the model. Fig. 2.4 shows that the power-law parameters are well constrained with only a small scatter of the model in the data-points.

2.3.2 Example #2: multi-sources, multi-components

For the second example, we aim to demonstrate the application of Mr-Moose to a much more realistic situation where the total emission received is a complex combination of several blended sources at different wavelengths by using all the variations and freedom allowed by Mr-Moose. This fake system is adapted from a real science case, see Gullberg et al. (2016b). In the following

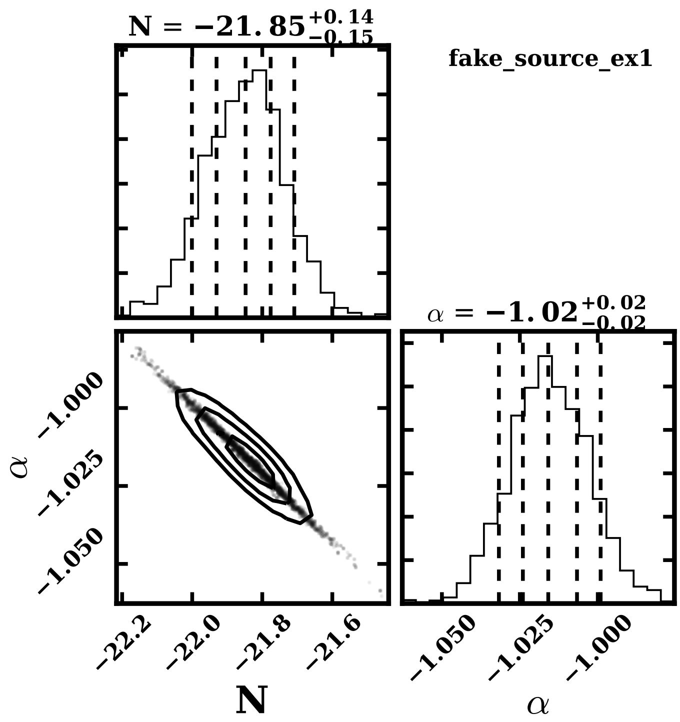

FIGURE 2.3: Triangle diagram for example #1. The diagonal represents the marginalised probability distribution. The vertical dashed line correspond to the 10%, 25%, 50%, 75% and 90% percentiles of the distribution. The 50% percentile parameter along the 25% and 75% percentile values are reported in Table 2.6. The other diagram represents the 2D projection of the parameter space on the corresponding parameters on the abscissa and ordinate axes. The contours represents the density distribution at 75%, 50% and 25% of the maximum parameter value .

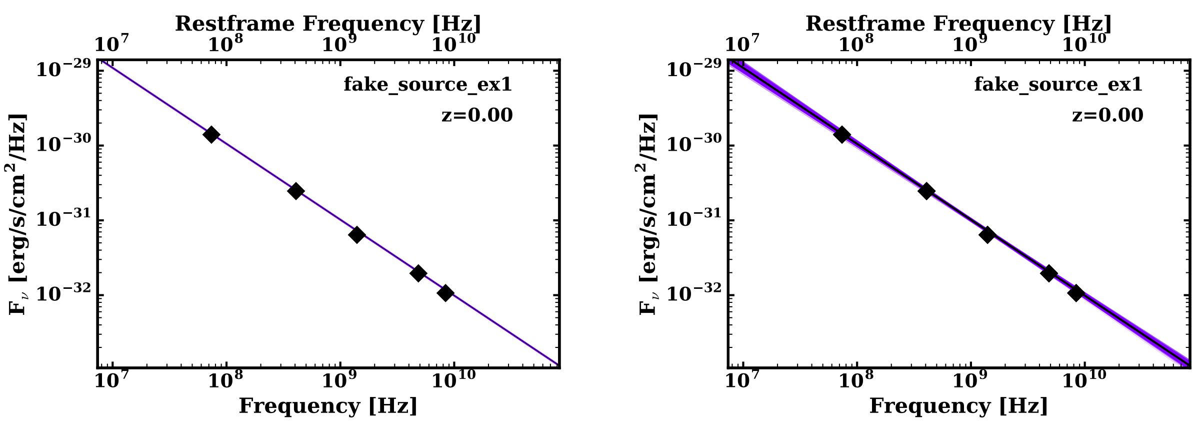

FIGURE 2.4: SEDs for example #1. Note that the uncertainties are plotted but are smaller than the datapoints, diamonds being detections. *left:* best fit plot. The plain black line is the sum of the different components in each arrangement. *right* "spaghetti" plot. The best fit here is reported as the black plain line for each component (defined in the .dat file). The shaded area is the sum of each model representation after convergence (values of the parameters at each step of each walker).

Name	parameter	true value	fit value
AGN_law	$N_{\rm AGN}$	-32*	$-31.94^{+0.08}_{-0.09}$
	$\alpha_{\rm AGN}$	-2	$-2.04^{+0.13}_{-0.12}$
BB_law(1)	$N_{\rm BB1}$	-22*	$-21.75^{+0.29}_{-0.22}$
	T_1	40	$42.98^{+13.30}_{-14.82}$
BB_law(2)	$N_{\rm BB2}$	-22*	$-21.74^{+0.30}_{-0.18}$
	T_2	60	$45.51^{+9.71}_{-16.63}$
sync_law(1)	$N_{\rm s1}$	-22*	$-21.64^{+0.93}_{-0.87}$
	$\alpha_{\rm s1}$	-1	$-1.06^{+0.09}_{-0.10}$
sync_law(2)	$N_{\rm s2}$	-22*	$21.88^{+0.91}_{-0.87}$
	$\alpha_{\rm s2}$	-1.2	$-1.03^{+0.09}_{-0.10}$

TABLE 2.7: Components and parameters of example #2. *All normalisation values are logarithmic values. The quoted uncertainties are the 25 and 75 percentiles.

paragraph and Fig. 2.5, we summarise this complex source consisting of two galaxies, one powerful radio galaxy with two bright radio lobes (FRII type, Fanaroff & Riley 1974) and a star-forming companion galaxy.

Fake source and input files

The following characteristics and assumptions are used to define this system:

- The radio galaxy is composed of an AGN, a host galaxy and is star-forming
- The AGN is radio-loud presenting a FRII morphology (two bright radio lobes)
- The companion is star-forming and without AGN
- The SED coverage covers the 8 μm-1.4 GHz range with various resolutions and detections as the result of the different facilities used for observations.

Fig. 2.6 presents the observations, each image generated by Mr-Moose before the fitting. To further precise, the IR SED do not differentiate the two galaxies due to the lack of resolution and is constituted of three components: the cold dust from both the companion and the host and the AGN hosted in the radio galaxy. We also note that the 350 μm, 500 μm and 870 μm are only upper limits and therefore, the sum of these three components cannot largely exceed these values. The synchrotron emission is constituted of two lobes, partially blended with the radio galaxy itself and with the companion or unresolved at the lowest radio frequency. Also, the synchrotron and dust emission are equally contributing at certain frequencies (here 230 GHz).

We have a total of 14 observations in the 8 μm-1.4 GHz range, with 17 photometric data-points. The total number of components is therefore five, one AGN dust component, two cold dust component (one the radio galaxy, one of the companion galaxy assuming that the cold dust component originates from young stars) and two synchrotron emissions (originating from each lobe). This corresponds to ten free parameters, summarised in Table 2.7. Given the combination of resolution, sensitivity, frequency coverage, photometry and components, we can define seven arrangements of the data/models, used to generate the fake data-file and model-file.

1. Dust/AGN: combination of the dust emission from the companion and the radio galaxy, itself consisting of the AGN and cold dust components *Spitzer*, *Herschel* and LABOCA (Siringo et al. 2009):

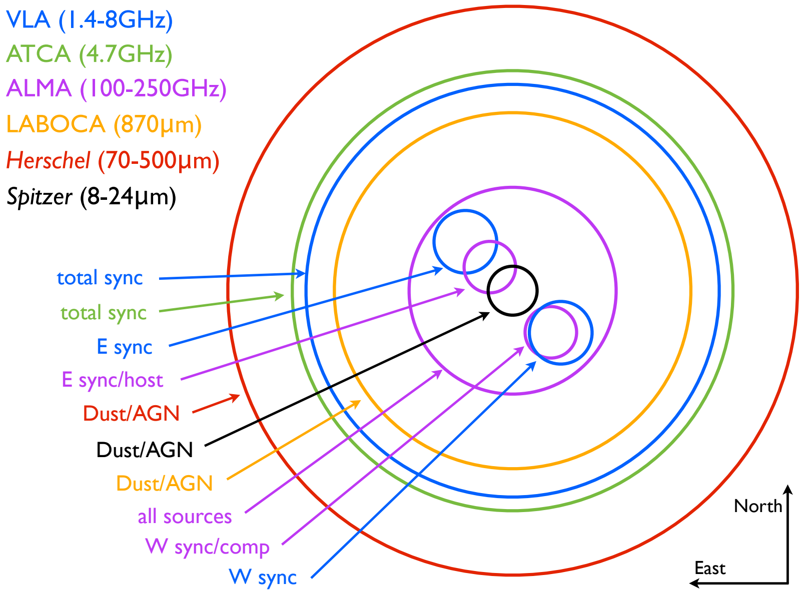

FIGURE 2.5: Scheme of the combination of observations at different wavelengths from the data file to illustrate the considered example. The circle sizes are relative to the resolution of the observation but not to scale (see Fig. 2.6). Note that *Herschel*, LABOCA, one ALMA, one VLA and ATCA observations are not resolving the different components. From bigger to small circles: *Herschel*, ATCA, VLA, LABOCA, ALMA, double circles are VLA and ALMA(closer to center), and in the center *Spitzer*.

2. W sync/comp (western synchrotron, companion): partially resolved at 229 GHz, combination of synchrotron and cold dust emission (ALMA Band 6, 7.5 GHz bandwidth)

3. E sync/host (eastern synchrotron, host galaxy): partially resolved at 245 GHz, combination of synchrotron and cold dust emission (ALMA Band 6, 7.5 GHz bandwidth)

4. total sync (total synchrotron): unresolved radio emission at 1.4 GHz, 4.7 GHz 102 GHz (VLA, ATCA and ALMA Band 3 at 50 MHz, 2 GHz and 7.5 GHz bandwidth, respectively)

5. W sync: only resolved at 4.8 GHz and 8.4 GHz (VLA, C and X bands, with 50 MHz bandwidth)

6. E sync: only resolved at 4.8 GHz and 8.4 GHz (VLA, C and X bands, with 50 MHz bandwidth)

7. total emission: combination of all components at 102 GHz (ALMA Band 3, with 7.5 GHz bandwidth)

We generate the fake files using the fake source procedure provided with Mr-Moose, generating, summing and passing the different combination through the adequate filters, in the same fashion presented in § 2.3.1. Table 2.7 lists the values of each parameter and Fig. 2.6 the images corresponding to each filter from the data-file. We choose *nwalkers*=400 to make sure to have a sufficiently large number of walkers exploring the parameter space and a deliberately (too) large number of steps (*nsteps*=3500) to ensure convergence is reached.

Output files

The code generates the output files previously described in § 2.2. Given the higher number of arrangements, two new SED files are generated (compared to example 1), presenting a split version

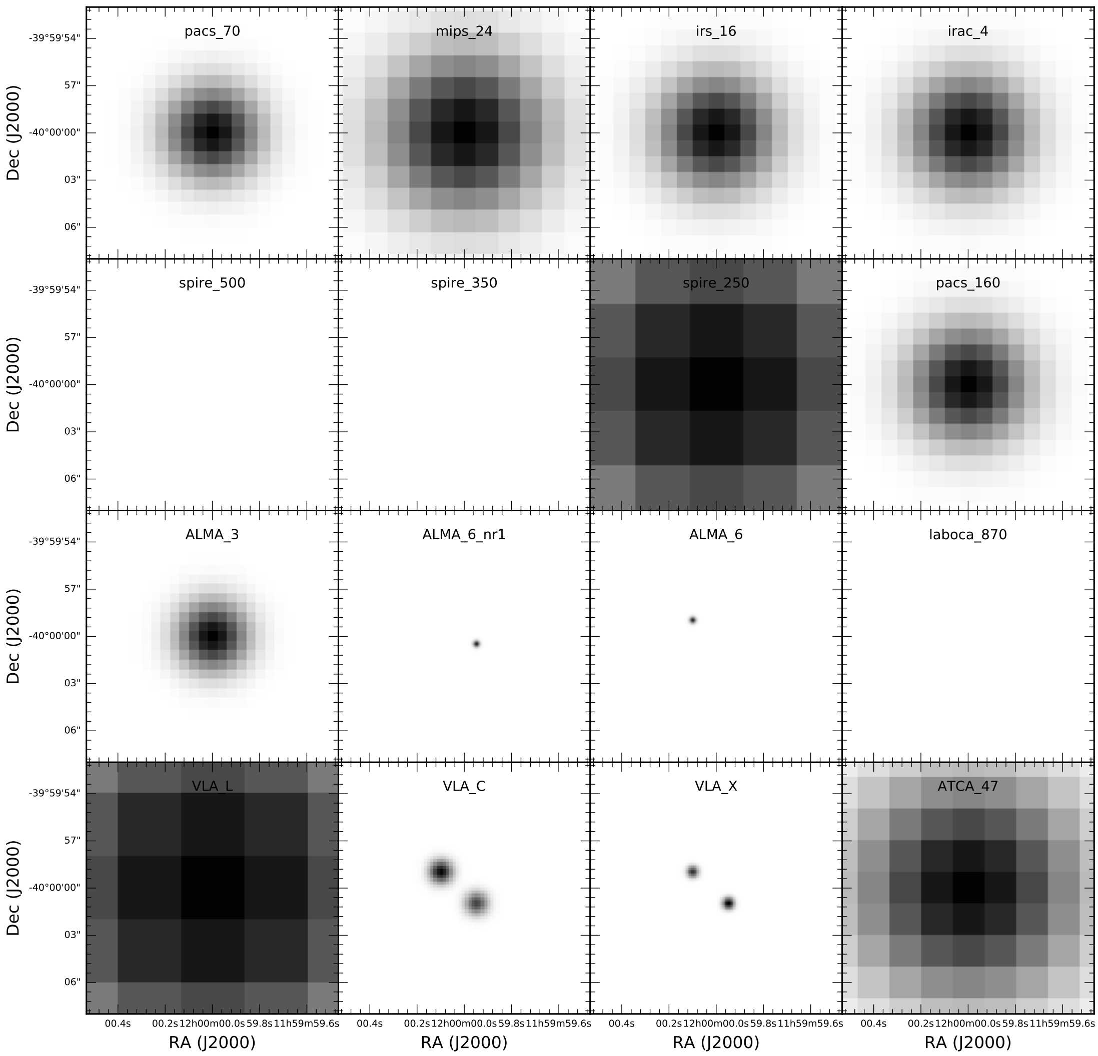

FIGURE 2.6: Images generated from the information contained data file assuming a Gaussian point spread function, all images scaled to the same coordinates. Frequency is decreasing toward the right and the top. Note that no sources are detected in *spire_350, spire_500 and laboca_870* images, while VLA_X and VLA_C present two components. North is top and East is left on all images.

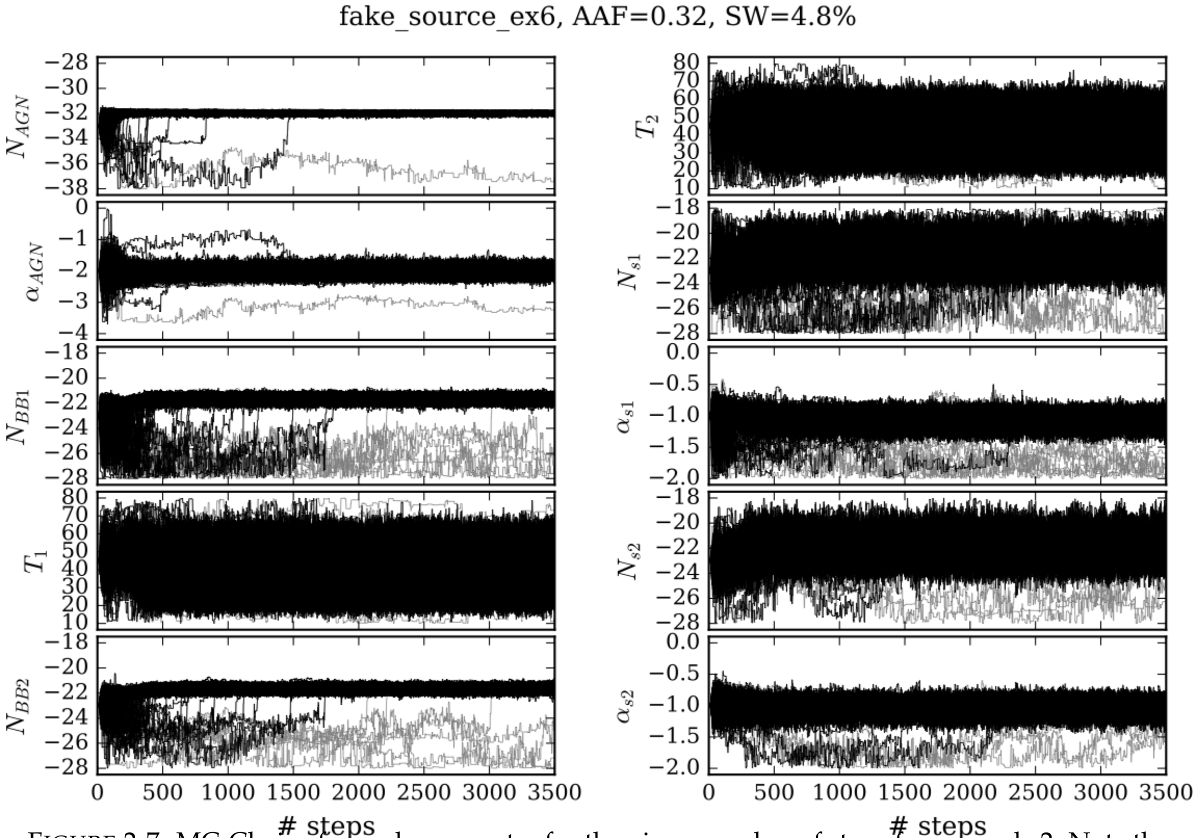

FIGURE 2.7: MC-Chains for each parameter for the given number of steps for example 2. Note the convergence reached roughly after 1000 steps. The grey lines are the "stuck" walkers, excluded from further analysis (see § 2.3.2 and Fig. 2.8).

of the total SED. Indeed, when dealing with complex system, presenting emission from different origins, over-plotting everything on the same SED makes interpretation difficult. Therefore, MrMoose provides split SEDs, with the same scale and range for each arrangement (seven in this example) with color coding each model component. We describe here the results from the convergence plot (Fig. 2.7), the triangle plot (Fig. 2.9) and finally finish by the SEDs (Fig. 2.10-2.11).

Fig. 2.7 shows the chains of walkers, where convergence is reached roughly after 1000 steps. With more attention, one notices each parameter converges at different times, the first ones being the most constrained parameter such as $N_{\rm AGN}$ or $\alpha_{\rm AGN}$ (compared to $N_{\rm BB1}$). Also from this plot, it is clear that the dust temperature cannot be further constrained without extra information. We deliberately chose a larger number of steps to ensure we would not miss a long convergence trend. The grey chains corresponds to flagged walkers, below the acceptance fraction threshold discussed in § 2.2. In this particular example, the default AAF threshold value does not filter out some isolated walkers which did not converge even after this large number of steps. This is probably due to the increasing complexity of the parameter space, where several local minima coexist. We therefore set a manual acceptance fraction threshold at 0.23. We choose this value because it filters out the low-end tail of the distribution of the acceptance fraction values (see Fig. 2.8) corresponding to the isolated walkers in the parameter space (see the bottom of the $N_{\rm BB2}$ chains, at roughly step #1000). To plot the following SEDs and triangle diagram, we set the limit *nsteps_cut*=3450. A much lower cut, such as 3000, is possible but would clutter the following diagrams and given our 400 walkers, this still represents 20000 points to sample our distributions.

Fig. 2.9 provides us with information on the parameters. Looking at the histogram on the diagonal, we can see that most parameters are relatively well constrained, within the original values,

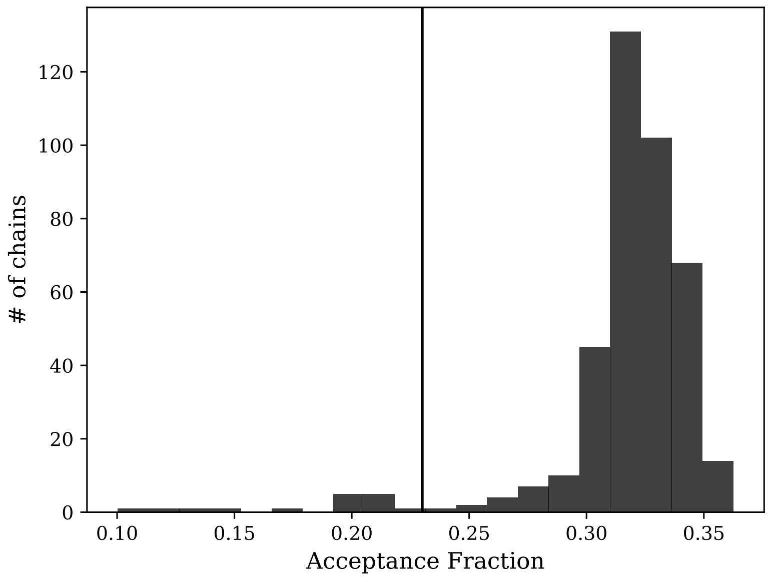

FIGURE 2.8: Histogram of the acceptance fraction of the 400 chains. Note the cut at 0.23, chains under this values are reported in grey in Fig. 2.7, which are the "stuck walkers" (see text § 2.3.2).

except for the temperature of the cold dust components, especially T_1 (This will be particularly obvious in the SED plot). We also see that the increasing complexity of the system, contours are very useful to highlight "banana" shapes more clearly. This is a perfect demonstration of how Mr-Moose provides reliable results, in the ambiguous case of a lack of data.

Fig. 2.10 and Fig. 2.11 respectively show the single and the split SEDs for the best fit and "spaghetti" visualisations. In these case, overplotting all information on a single SED is very confusing (see Fig. 2.10). While, we keep this figure for its pedagogic value, we prefer to focus on the split version of SED to interpret the fitting (see Fig. 2.11). On the top panel (best-fit visualisation), the procedure proposes a really good fitting. When incorporating the uncertainties on the parameters, in the bottom panel (spaghetti visualisation), we see that the superposition of the different components explain the degeneracies observed in Fig. 2.9. The large variation of the temperature allows for a large variation of the normalisation and, in turns, a different setup and relative contribution of each component. This is a perfect illustration that (i) a simple value of minimum χ^2 fit is limited as not providing a fair view of the fitting, (ii) extra-information on the relative contribution of the different components is necessary to better constrain the fit (iii) even a sophisticated fitting approach does not preclude to high-quality data and a careful examination of the source.

2.3.3 Example #3: real dataset

We finally run Mr-Moose on a published dataset to ensure the code is able to recover previous results. We take the example from Gilli et al. (2014) as photometry and parameter results are reported in the publication and allow for a direct comparison. Briefly, the data, a combination of ALMA and *Herschel* observations with upper limits and detections, are used to fit a modified black body component (reported in § 2.2.2), in order to access the dust properties of a z=4.75 quasar. We run the code in two configurations a and b: one with only the detected filters and a second adding the upper limits to the fit. For both configurations we set β=2 and ν_0=1.5 $\times 10^{12}$ Hz as in the original publication. We list the files in the Appendix and run the procedure twice. We

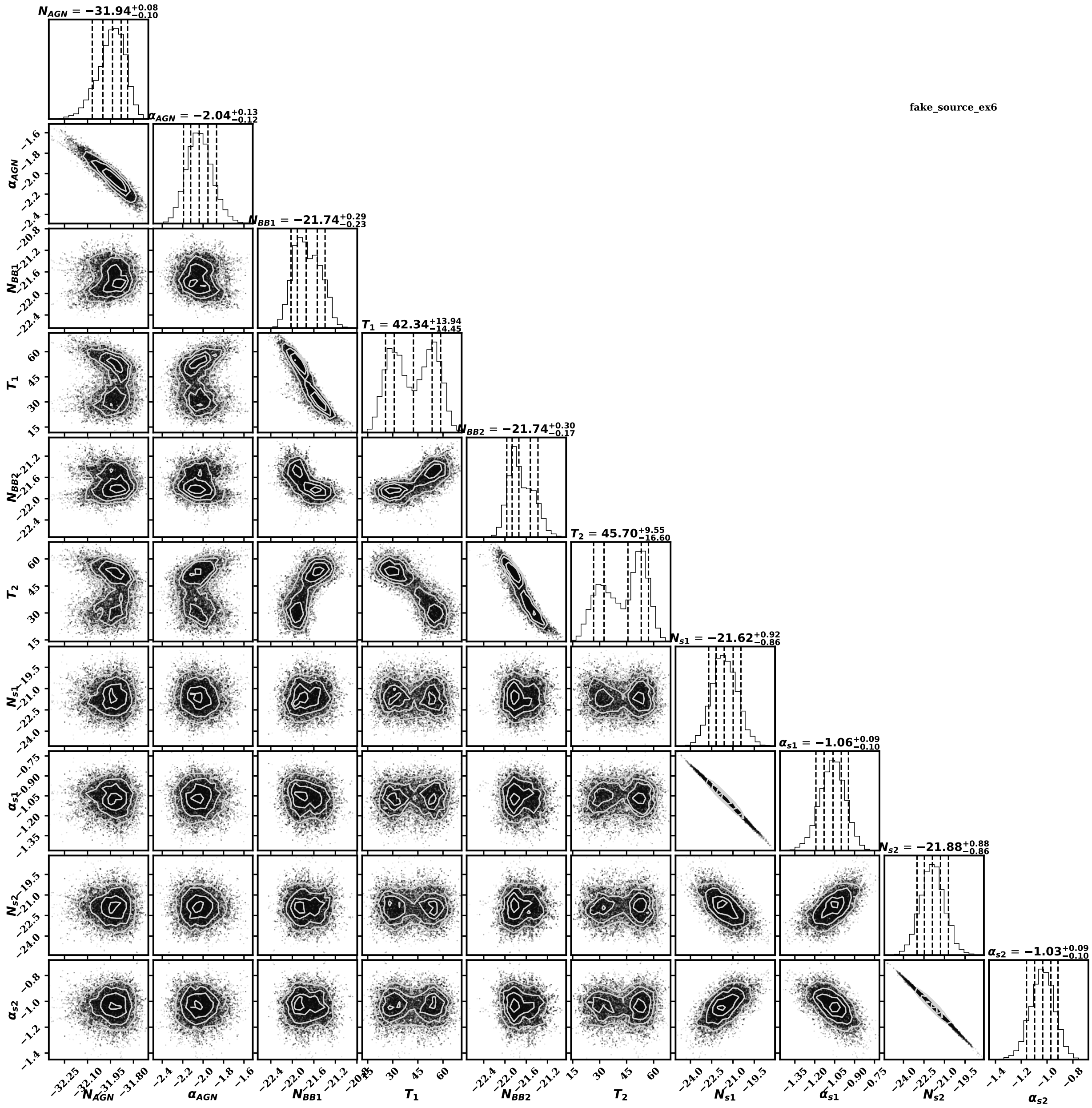

FIGURE 2.9: Triangle diagram for example #2. The diagonal represents the marginalised probability distribution. The vertical dashed line correspond to the 10%, 25%, 50%, 75% and 90% percentiles of the distribution. The 50% percentile parameter along the 25% and 75% percentile values are reported in Table 2.7.The other diagrams represent the 2D projection of the parameter space on the corresponding parameters on the abscissa and ordinate axes. The contours represents the 75%, 50% and 25% of the maximum parameter value.

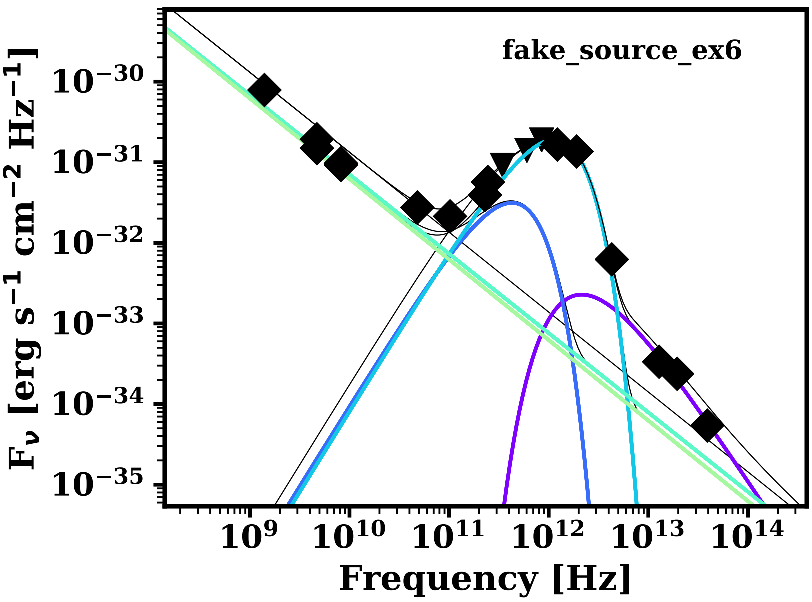

FIGURE 2.10: Total SED for each arrangement of data and models plot in a single figure. Coloured lines refer to the different models and the black lines are the total of all components in each arrangement. This figure is reported for pedagogic purposes only as, given the increasing complexity of the system, a split SED is much clearer to disentangle the various contribution of the components to the data (see Fig. 2.11).

focus only on recovering the temperature parameter as the other parameters are derived either from the best fit temperature or directly from observed fluxes.

For the case of detection only *(a)*, the temperature is recovered within the uncertainties of the quoted value in the original paper (see Table 2.8, Fig. 2.12, Fig. 2.13 and Fig. 2.14). Note also the asymmetrical uncertainties when having the information from parameter space exploration. The uncertainties provided by Mr-Moose are different, referring to the 25% and 75% of the distribution when the value quoted in Gilli et al. (2014) is likely the standard 1σ symmetric uncertainty assuming a normal distribution.

When including upper limits *(b)*, the result differs with a slightly lower temperature and uncertainties. This is probably due to the inclusion of upper limits as continuous data with decreasing probability as defined in Eq. 2.6 (note also how the model is able to converge above the upper limits, which are represented as 1σ in Fig. 2.14, bottom right rather than the 3σ in Fig. 2, Gilli et al. (2014). This is a good demonstration of how constraining upper limits can add valuable information when performing SED fitting. As mentioned in the original paper, we would like to stress that the uncertainties reported here are mainly fit uncertainties: they only represent the combined user knowledge on the uncertainties given in the data file.

For a more general comment, these statistical uncertainties do not incorporate any systematic uncertainties (which can dominate in certain cases). This is a very common problem in SED fitting, the final uncertainties obtained are limited to the systematic uncertainties associated to the assumed model to represent the data or from the data themselves. We add this word of caution for user non-familiar with SED fitting as these effects are often more subtle (but can be larger than the statistical uncertainties!) and usually hidden in the model choice and/or data. In this particular case, only a full comparison between a range of models (e.g. the common problem of IMF in stellar population fitting) and a complete data processing uncertainties (e.g. bad calibration or sky subtraction) assessment can answer this particular question.

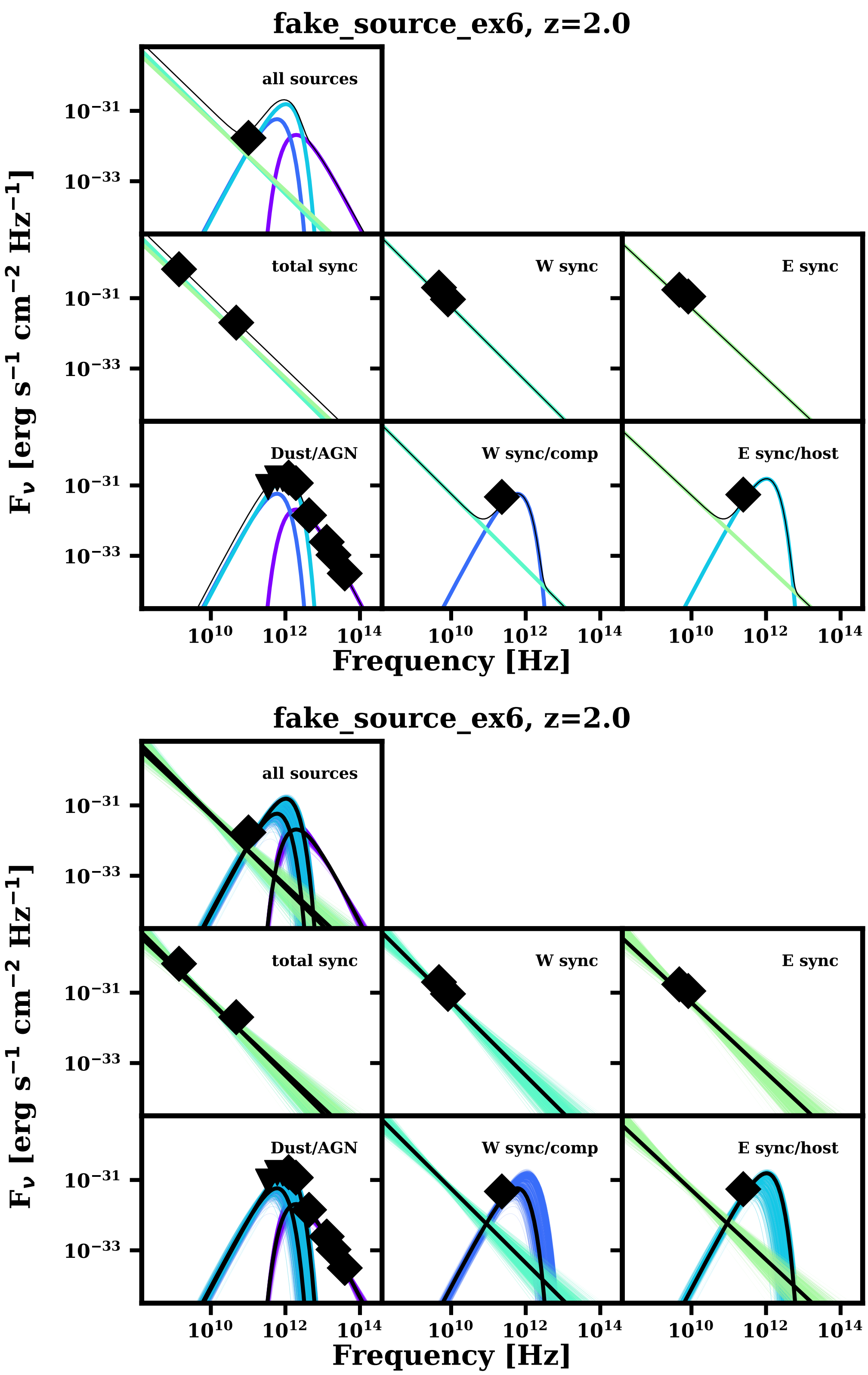

FIGURE 2.11: SEDs for example #2, split into subplots to illustrate each arrangement. Note that the uncertainties are plotted but are smaller than the datapoints. Diamonds are detections while downward triangle are upper limits. *top:* best fit plot. The plain black line is the sum of the different components in each arrangement. *bottom* "spaghetti" plot. The best fit here is reported as the black plain line for each component (defined in the .dat file). The colours refer to each model component, consistently between each subplot.

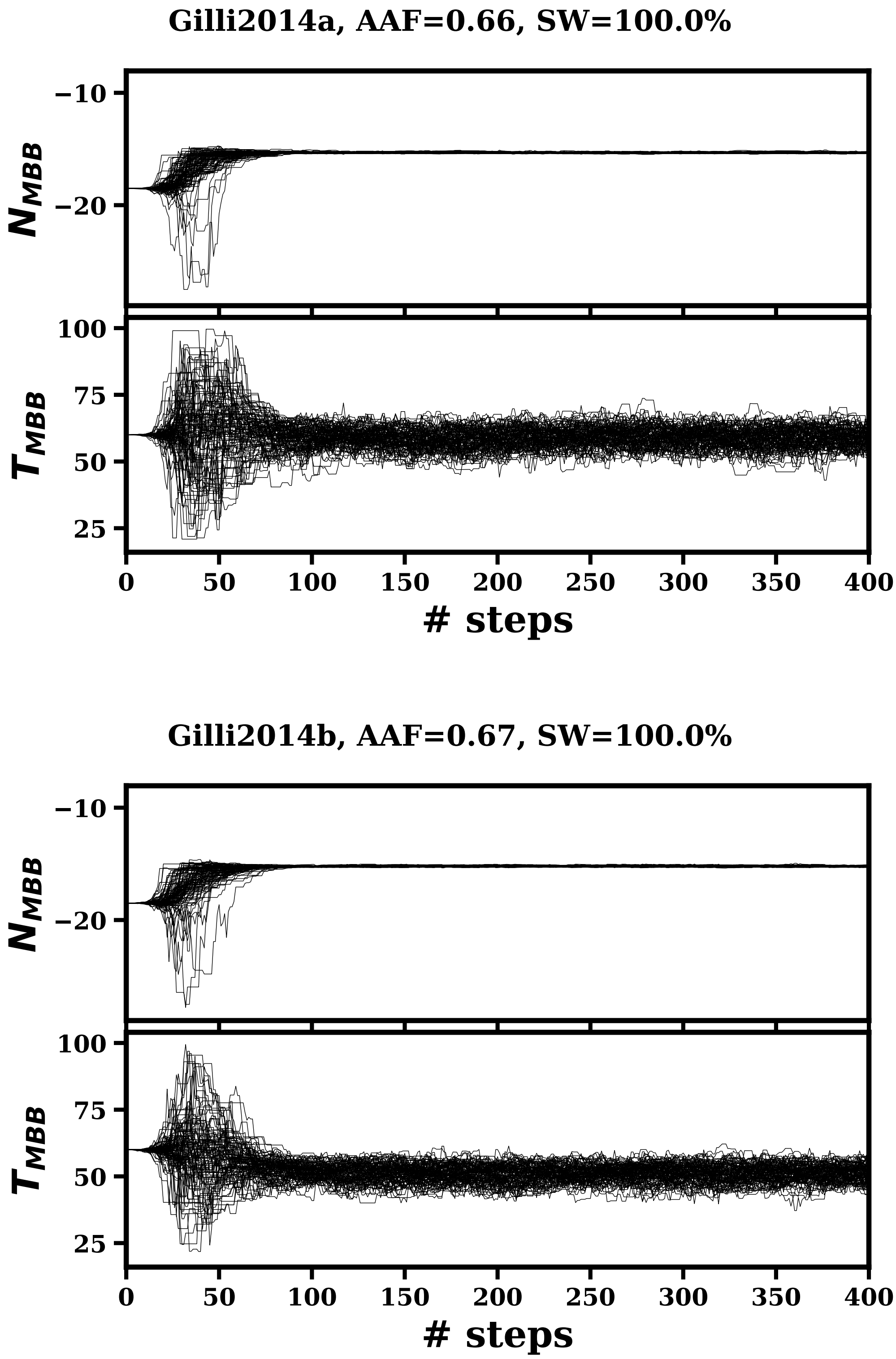

FIGURE 2.12: MC-Chains for example #3. Note the convergence after roughly 100 steps. *Top*: detections only*(a)*. *Bottom:* detections and upper limits*(b)*.

Name	parameter	Gilli2014+	config *a*	config *b*
MBB	N	n/a	-15.33$^{+0.05}_{-0.04}$	-15.22$^{+0.05}_{-0.04}$
	T[K]	58.5$^{+5.8}_{-5.8}$	59.14$^{+3.61}_{-4.06}$	51.08$^{+3.01}_{-3.23}$

TABLE 2.8: Components and parameters of example #3. * value in logarithmic scale. The uncertainties quoted are the 25 and 75 percentiles. See § 2.3.3 for the details about configurations *a* and *b*.

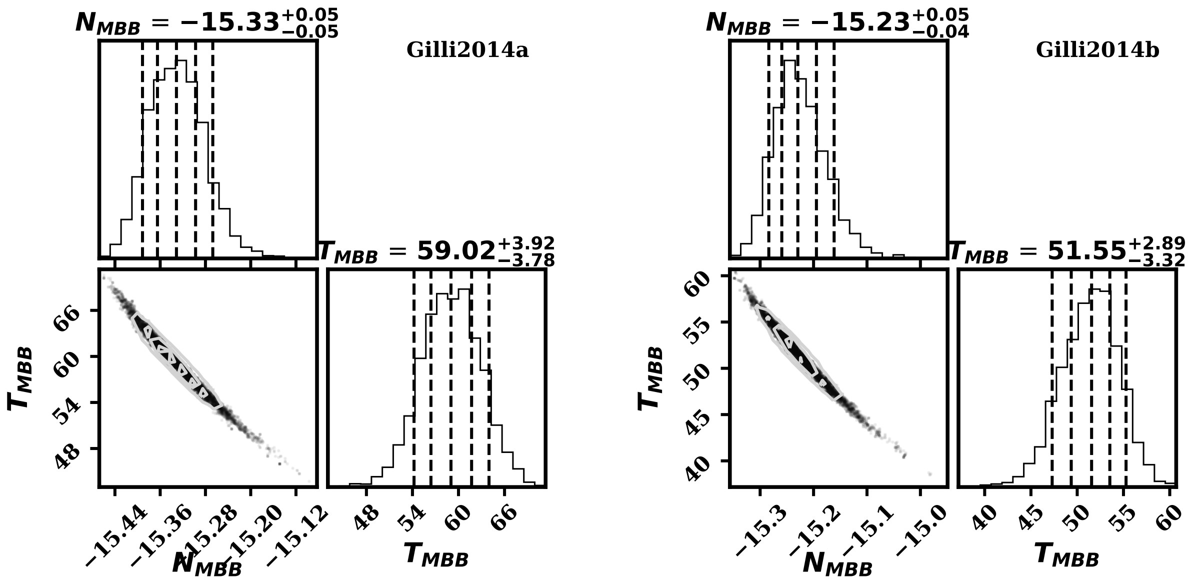

FIGURE 2.13: Triangle diagram for example #3. *Top*: detections only *(a)*. *Bottom:* detections and upper limits *(b)*. The diagonal represents the marginalised probability distribution. The vertical dashed line correspond to the 10%, 25%, 50%, 75% and 90% percentiles of the distribution. The 50% percentile parameter along the 25% and 75% percentile values are reported in Table 2.8. The other diagram represents the 2D projection of the parameter space on the corresponding parameters on the abscissa and ordinate axes. The contours represents the 75%, 50% and 25% of the maximum parameter value .

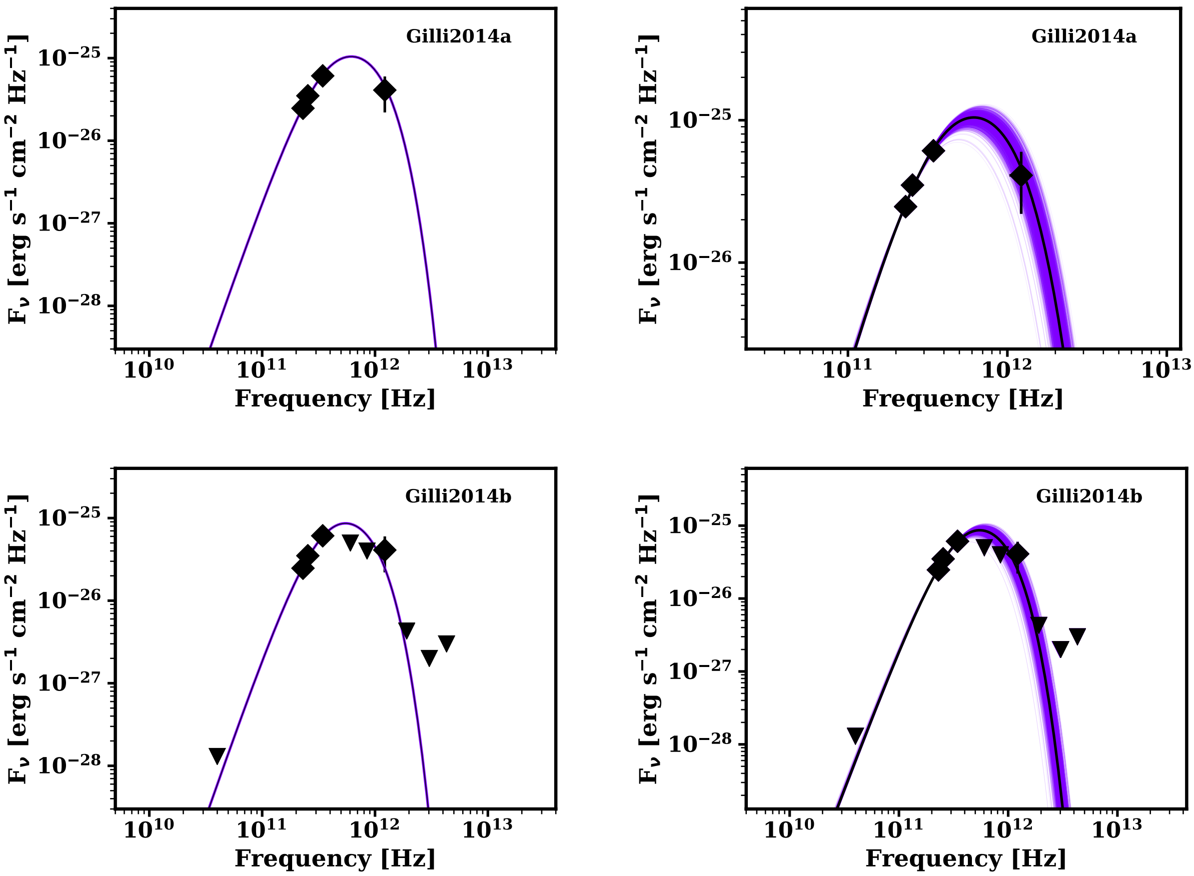

FIGURE 2.14: SEDs for example #3. *Top*: detections only*(a)*. *Bottom:* detections and upper limits*(b)*. *Left:* Best fit plot. *Right:* Spaghetti plot. The diamonds are the detections and the triangles are the 1σ upper limits. Note that the fitting can converge above the upper limits to a certain extent.

TABLE 2.9: Execution time for different configurations of Mr-Moose. All times reported are approximate time when executed on a relatively recent laptop (here for a laptop with a (3.1GHz Intel core i7 and 16GB DDR3 memory)).

Examples	*nwalkers*	*nsteps*	# of parameters	Time
# 1	200	200	2	~2 min
# 2	400	3500	10	~24 h
# 3a	200	400	2	~5 min
# 3b	200	400	2	~10 min

2.4 Known limitations and future developments

At the publication of this paper, the code will be available online on the GitHub platform at the following url: `https://github.com/gdrouart/MrMoose`, under a GPLv3 license (allowing re-use and modifications, see `License.txt` in Mr-Moose folder). While Mr-Moose is under continuous development and will see periodic upgrades, the code also knows some limitations. We list some of the most important ones and refer the reader to the README for a more exhaustive list of all known issues/limitations.

- The execution time is highly dependent on the complexity of the configuration: the most parameters/components/arrangements, the longer the time for the fitting to converge. Typical execution times are from couple of minutes to several hours (see Table 2.9) for a reasonably recent machine. More particularly, it assumes that the user defined models are as efficient as possible because these models are called at each iteration for each walker and is therefore the bottleneck of the code. Large number of walkers and steps can lead to significantly larger files, slowing the process. Even if Mr-Moose is designed to run in one step, we recommend to split the run in several steps, first generate the images only to check your data-file, hence a second run to perform the fit and a third to generate the ".pdf" files (by changing the keywords values in the setting file).

- Choosing initial values close to the "true" values is important, otherwise the code will take a long time to converge (if converging at all). This choice of initial guess is particularly important when including upper limits. By design, when the parameter values produce a model above an upper limit, the likelihood is very quickly set to infinity due to the error function (see § 2.2). Therefore a slight underestimation of parameters is preferable, particularly on any normalisation parameters (to keep the second term of the χ^2 in Eq. 2.6 close to null at the beginning). We remind that the initialisation of the walkers is made following the `emcee` recommendation: a Gaussian "ball" of walkers centred on the median value of the interval parameters.

- The code provides two levels of parallelisation (multi-core processing) for the calculation of the likelihood: the parallelisation on one source and the parallelisation on a sample of sources. The former tends to deteriorate the performance, most likely due to the large overheads when the likelihood is relatively simple (see `emcee` documentation). The second is only applicable on a sample of sources and therefore is much more efficient in reducing fitting time of an entire sample, using one core per source (Mr-Moose is provided with the wrapper `herd.py` to parallelise on sample). However, specific care should be taken to avoid running out of memory as the number of positions to store scales with the number of steps and walkers (and the number of sources to fit simultaneously).

We list here some of the future features, already planned:

- allowing for a wider range of priors: in the current version, only uniform priors are incorporated. We plan to add a variety of priors in order to increase the fidelity of prior knowledge into the fitting procedure. This will also solve the initial parameter value limitations mentioned previously.

- a migration to Python 3 is planned (when upgraded, all further developments will be applied to the Python 3 in priority)
- implementing the use of discrete models such as sophisticated AGN models or galaxy evolution models. This step requires the implementation of a methodology where the samplers can explore a (partially) discrete parameter space. Several solutions are considered (SED interpolation, brute force, branch-and-bound methods, nesting, etc). Its implementation is beyond the scope of this paper, it will be the object of a major update of Mr-Moose.

2.5 Conclusion

We presented a new fitting tool allowing the user to fit SEDs for a variety of source configuration from relatively simple to complex source configuration in a bayesian framework using the `emcee` package. The code, highly customisable, allows a wide range of configurations between data and models, with the aim to stay user-friendly. The code consistently handles upper limits along with detections, each data point being calculated through the filter database, also managed and defined by the user. The large flexibility on creating models/data/filters makes this code virtually adaptable to any case, independently of wavelengths, instruments/telescopes combinations or science cases, providing a robust tool to interpret increasingly complex multi-wavelength datasets. In particular, the code appears ideally suited (but not limited) to fit a combination of *Spitzer*, *Herschel*, ALMA and JVLA dataset, and/or in the presence of constraining upper limits in the data even in the case of a single unresolved source.

Acknowledgements

GD would like to thanks Steven Murray for insightful discussions on Bayesian inference and the Curtin PyClub for useful programming tips. We also thank Matt Lehnert, Carlos De Breuck, Joel Vernet and Nick Seymour for advices and help in the conception of this code. GD acknowledges the ESO Scientific Visitor Programme in supporting the development of this code.

Chapter 3

On the road to quenching massive galaxies: ALMA observations of powerful high redshift radio galaxies

A&A, in press

Theresa Falkendal [1,2] Carlos De Breuck[1], Matthew D. Lehnert[2], Guillaume Drouart[3], Joël Vernet[1], Bjorn Emonts[4],Minju Lee[5,6] Nicole P.H. Nesvadba[7] Nick Seymour[3] Matthieu Béthermin[8], Sthabile Kolwa[1], Bitten Gullberg[9] and Dominika Wylezalek[1,10]

[1]European Southern Observatory, Karl-Schwarzchild-Str. 2, 85748 Garching, Germany, [2]Sorbonne Université, CNRS UMR 7095, Institut d'Astrophysique de Paris, 98bis bvd Arago, 75014, Paris, France [3] International Center for Radio Astronomy Research, Curtin University, Perth WA 6845, Australia, [4] National Radio Astronomy Observatory, 520 Edgemont Rd, Charlottesville, VA 22903, USA, [5]Department of Astronomy, The University of Tokyo, 7-3-1 Hongo, Bunkyo-ku, Tokyo 133-0033, Japan, [6] National Observatory of Japan, 2-21-1 Osawa, Mitaka, Tokyo 181-0015, Japan, [7] Institut d'Astrophysique Spatiale, CNRS, Université Paris Sud, 91405 Orsay France, [8] Aix-Marseille Univ., CNRS, LAM, Laboratoire d'Astrophysique de Marseille, 13013 Marseille, France, [9] Centre for Extragalactic Astronomy, Department of Physics, Durham University, South Road, Durham DH1 3LE, UK, [10] Department of Physics and Astronomy, Johns Hopkins University, Bloomberg center, 3400 N. Charles St, Baltimore, MD, 21218, USA

Abstract

We present 0.3″ (band 6) and 1.5″ (band 3) ALMA observations of the (sub)millimeter dust continuum emission for 25 radio galaxies at $1 < z < 5.2$. Our survey reaches a rms flux density of $\sim$50 μJy in band 6 (200-250 GHz) and $\sim$20 μJy in band 3 (100-130 GHz). This is an order-of-magnitude deeper than single-dish 850 μm observations, and reaches fluxes where synchrotron and thermal dust emission are expected to be of the same order-of-magnitude. Combining our sensitive ALMA observations with low-resolution radio data from ATCA, higher resolution VLA data, and infrared photometry from *Herschel* and *Spitzer*, we disentangle the synchrotron and thermal dust emission. We determine the star-formation rates and AGN infrared luminosities using our newly developed Multi-resolution and multi-object/origin spectral energy distribution fitting code (Mr-Moose). We find that synchrotron emission contributes substantially at $\lambda \sim$1 mm. Through our sensitive flux limits and accounting for a contribution from synchrotron emission in the mm, we revise downward the median star-formation rate by a factor of 7 compared to previous estimates based solely on *Herschel* and *Spitzer* data. The hosts of these radio-loud AGN appear predominantly below the main sequence of star-forming galaxies, indicating that the star formation in many of the host galaxies has been quenched. Future growth of the host galaxies

without substantial black hole mass growth will be needed to bring these objects on the local relation between the supermassive black holes and their host galaxies. Given the mismatch in the timescales of any star formation that took place in the host galaxies and lifetime of the AGN, we hypothesize that a key role is played by star formation in depleting the gas before the action of the powerful radio jets quickly drives out the remaining gas. This positive feedback loop of efficient star formation rapidly consuming the gas coupled to the action of the radio jets in removing the residual gas is how massive galaxies are rapidly quenched.

3.1 Introduction

The connection between active galactic nuclei (AGN), their host galaxies and environments has been one of the central questions in extra-galactic astrophysics for over 30 years (Balick & Heckman 1982). This contemporary debate centers around two predominant issues concerning the influence of AGN on their environment: Is their influence "positive" or "negative", meaning do they either increase or decrease the star-formation efficiency of their hosts? How do super-massive black holes (SMBHs) regulate their own growth? These two questions are intertwined. When the SMBH is active, it may well regulate its own growth while also enhancing or inhibiting the stellar or baryonic mass growth of its host. The empirical, approximately linear relationship between the mass of SMBH and both galaxy bulge mass and the velocity dispersion (e.g., Magorrian et al. 1998; Gebhardt et al. 2000; Ferrarese & Merritt 2000; Häring & Rix 2004), suggests that the growth of these two components is concomitant along the observed relationship. However, it is not clear if this relation is causal or if it simply reveals a connection between galaxy-galaxy mergers and that the growth of galaxy components are limited asymptotically (central limit theorem, e.g., Peng 2007; Jahnke & Macciò 2011).

SMBHs and host galaxies share several properties. Both SMBHs and galaxies have exponential cut-offs at the high mass end of their co-moving space densities (e.g., Shankar et al. 2009; Ilbert et al. 2013; Kelly & Shen 2013). Both the population of SMBHs and galaxies also exhibit mass downsizing whereby the oldest, in the case of galaxies, and the most massive of SMBHs grew early and rapidly (e.g., Thomas et al. 2005, 2010; Merloni & Heinz 2008). However, there is a mismatch in both the shape and co-moving number density between galaxies and dark matter halos, especially at the low and high mass ends of these functions (Benson et al. 2003). Because powerful AGN can have a mechanical and radiative energy output similar to or exceeding that of the binding energy of a massive galaxy and dark matter halo, AGN are thought to play a key role in regulating the baryonic growth of galaxies. Both observations and simulations have suggested that there may be a positive trend between the mean black hole accretion rate and star-formation rate (SFR; e.g., Delvecchio et al. 2015; McAlpine et al. 2017), while the mean SFR as a function of black hole accretion rate shows no correlation for low luminosity sources (e.g., Stanley et al. 2015; McAlpine et al. 2017). One should be cautious when interpreting both theoretical and observational results in the definition of what exactly AGN feedback is and how AGN affect their host galaxies to explain the properties of an ensemble of galaxies (Scholtz et al. 2018). The strength and nature of AGN feedback – the cycle whereby the SMBH regulates both its own growth and that of its host – depends on galaxy mass and morphology. For example, the most massive elliptical galaxies are generally metal-rich and old, while less massive lenticular galaxies, which make up the bulk of the early-type galaxy population, have star formation histories that lasts significantly longer (Thomas et al. 2005, 2010; Emsellem et al. 2011; Krajnović et al. 2011). Clearly, if AGN feedback plays a crucial role in shaping the ensemble of galaxies, its impact on massive dispersion dominated galaxies must result in somewhat different characteristics in these galaxies compared to rotationally-dominated, predominately less massive lenticular galaxies.

To gain a deeper understanding about how the growth of host galaxy and the SMBH are intertwined, it is important to study the characteristics of the star formation occurring in the host galaxies of actively fueled black holes. Within this context, powerful radio galaxies generally, and high-redshift radio galaxies (HzRGs) in particular, are important test beds of our ideas on the physics underlying AGN feedback. At almost all redshifts, powerful radio-loud AGN are hosted by galaxies that are among the most massive (Bithell & Rees 1990; Lehnert et al. 1992; van Breugel et al. 1998; Rocca-Volmerange et al. 2004; Best et al. 2005). Since we know that at low redshift the star formation history of many of these galaxies was brief, but intense (e.g., Thomas et al. 2005; Tadhunter et al. 2011), and they lie at the exponential high mass tail of the stellar mass distribution (e.g., Seymour et al. 2007; Ilbert et al. 2013), if AGN play an important role in shaping massive galaxies, it is in these galaxies that this must be most evident. Most importantly, HzRGs, are luminous sources not only in the radio, but also throughout the mid-infrared (MIR) and sub-mm continuum. This generally implies that they have high rates of star-formation (Archibald et al. 2001; Reuland et al. 2003a), and a rapid accretion onto the SMBH. Due to the fact that the broad line region and rest-frame ultraviolet-optical continuum emission from their accretion disks is obscured, we can observe their stellar emission (Seymour et al. 2007; De Breuck et al. 2010). All of these arguments make HzRGs important targets for understanding the complex relationship between AGN and massive galaxies.

The substantial mechanical and radiative AGN luminosity and apparently significant star-formation rates of HzRGs leads to a quandary. If AGN feedback effectively suppresses black hole and galaxy growth, why do the host galaxies of AGN grow so rapidly (mass doubling times of $\sim$0.1-1 Gyr, Drouart et al. 2014)? This is the "coordination problem", the apparent contradiction which is a paradoxical situation where the strongest phase of energy and momentum injection into the interstellar medium of the host galaxy by the AGN is not co-concomitant with strong suppression of star formation (see e.g., Drouart et al. 2014, 2016). Models predict an offset between the fueling of the AGN and the suppression of star formation because the timescales for fueling the AGN is substantially shorter than the star-formation timescale within the host. Could the impact of AGN feedback be to increase the star formation efficiency in galaxies (i.e., "positive feedback"; Silk 2013; Kalfountzou et al. 2017)?

The bulk of the bolometric output of HzRGs is emitted in the infrared (IR; e.g., Miley & De Breuck 2008). Both AGN and star-formation (SF, dust heated by stars) contribute energy to the dust continuum spectral energy distribution; the AGN heats the dust to warm temperatures ($T \gtrsim 60$ K) emitting in the MIR, while the SF generally heats the dust to lower temperatures ($T \lesssim 60$ K) and emits mainly in the far-infrared (FIR). The *Herschel* space telescope provided an opportunity to cover both sides of the peak of thermal emission allowing us to disentangle the dust components heated by AGN and SF. In our *Herschel* radio galaxy evolution (HeRGÉ) project, we constrained spectral energy distributions (SEDs) for a sample of 70 radio galaxies at $1 < z < 5.2$ (Drouart et al. 2014). While this led to substantially improved estimates of the SFR, one limitation of *Herschel* data are their low spatial resolution (e.g., 36" at 500 μm). As shown by several arcsecond resolution follow-up observations, the dust continuum emission often splits into several components, which are not necessarily coincident with the AGN host galaxy (De Breuck et al. 2005; Ivison et al. 2008, 2012; Nesvadba et al. 2009; Emonts et al. 2014; Gullberg et al. 2016b). Sub-arcsecond resolution imaging is therefore essential to separate the star formation occurring in the AGN host galaxies from that occurring in the nearby companion galaxies. We have therefore started a large systematic follow-up program of our HeRGÉ sample with the Atacama Large Millimeter Array (ALMA).

As HzRGs are, by selection, the brightest radio sources at each redshift, synchrotron radiation may make a substantial contribution at (sub)mm wavelengths. This was already discussed by Archibald et al. (2001), who concluded the 850 μm, fluxes of three sources in their sample of 47 may be dominated by synchrotron emission. However, to make such an assessment, one has to assume that the sub-mm fluxes are a straight power-law extrapolation of the radio SED. While one may expect the spectra to steepen at high frequencies due to aging of high energy electrons, there are also suggestions that the SEDs in at least some HzRGs remain a power law with a constant exponent even at the highest observed radio and/or mm frequencies (Klamer et al. 2006).

The high sensitivity of ALMA also allows us to reach flux density levels more than an order-of-magnitude fainter than previous single-dish observations with LABOCA/SCUBA. Reaching such depths implies that we may reach flux density levels of the extrapolated synchrotron emission in most of the sources in our sample. It is therefore essential to disentangle the thermal dust and synchrotron components. To achieve this, we adopt two strategies: (1) multi-frequency photometry covering the range $10 < \nu_{\rm obs} < 200$ GHz, and (2) spatially resolving the radio core and lobes. For this first strategy, we combine our ALMA data with 7 mm and 3 mm observations from the Australia Telescope Compact Array (ATCA; Emonts et al. 2014). For the second strategy, we use the available radio maps from the Very Large Array (VLA; Carilli et al. 1997; Pentericci et al. 2000; De Breuck et al. 2010), which have similar spatial resolution as our ALMA data. A more detailed study of the physics of the high-frequency synchrotron emission is deferred to a forthcoming paper. For now, we simply consider the possibility that synchrotron component will impact our (sub)mm observations and our estimates of the SFRs of the AGN host galaxy.

The three main SED components, synchrotron emission, AGN and SF heated thermal dust emission constitute the SEDs of HzRGs. Because each component potentially makes a significant contribution to the over all SED, it requires an analysis of photometry covering an order-of-magnitude range in spatial scales – sub arcsecond to 10s of arc seconds. To this end, we developed the **M**ulti-**r**esolution and **M**ulti-**o**bject/**o**rigin Spectral **e**nergy distribution fitting procedure MrMoose (Drouart & Falkendal 2018). This versatile code allows us to isolate the SF heated dust emission $L_{\rm SF}^{\rm IR}$ from the two spectrally adjacent components – the AGN heated dust component at higher frequencies and the synchrotron emission at lower frequencies. We revise the $L_{\rm SF}^{\rm IR}$ downwards by a factor of many compared to previous *Herschel* determinations.

This paper is structured as follows: after introducing the sample and observations in §2, we briefly describe our fitting code in §3. The overall results are described in §4, with detailed descriptions of each individual source given in the appendix. We discuss the implications of our results in §5, and summarize our conclusions in §6.

3.2 Observations and data reduction

3.2.1 Sample

Our sample consists of 25 HzRGs over the redshift range $1<z<5.2$. This is a subsample of the parent HeRGÉ sample of 70 HzRG, a project dedicated to observed HzRGs, with *Herschel* (described in detail in Seymour et al. 2007; De Breuck et al. 2010). To summarize, the parent samples sources were selected to have luminosities at rest-frame 3 GHz greater than 10^{26} W Hz^{-1} and have ultra-steep radio spectra (α=-1.0; $S_\nu \propto \nu^\alpha$, at $\nu_{\rm obs} \sim 1.4$ GHz). The parent sample has complete 12-band 3.6 to 850 μm photometry from *Spitzer*, *Herschel* and SCUBA/LABOCA (De Breuck et al. 2010; Drouart et al. 2014). The subsample of 25 sources observed with ALMA were chosen to be easily observable by ALMA, i.e., the southern part of the parent sample and were grouped in such a way that multiple sources share a phase calibrator to minimize the overheads to the extent possible.

3.2.2 ALMA Observations

ALMA Cycle 2 band 6 (and band 4 for source TN J2007-1316) observations were carried out from June 2014 to September 2015 (Table 3.1). We used four 1.875 GHz spectral windows, tuned to cover molecular lines at the specific redshift of each source (McMullin et al. 2007). The data was calibrated in CASA (Common Astronomy Software Application) with the supplied calibration script (with exception of MRC 2224-273, for which the provided script was changed to correctly compensate for different averaging factor in one of the spectral windows). Since a significant fraction of our sources have a low SNR, we decided to optimize the sensitivity by using natural weighting to construct images. For all sources, except TN J2007-1316, atmospheric absorption noise was present in observations, therefore we excluded the affected channels from the final images. The settings used in our data reduction were: cell size of 0.06 arcsec (roughly 5 times smaller than the beam size), barycentric reference frame (BARY), and the mode 'mfs' (multi-frequency synthesis emulation). For the brightest source MRC 0114-211, a phase self-calibration was done which decreased the RMS noise in the final image from 87 μJy to 59 μJy.

The ALMA Cycle 3 band 3 (and band 4 for source MRC 0943-242) observations were conducted from March 2016 to September 2016 (Table 3.1). We used four 1.875 GHz spectral windows tuned to include the [C I](1–0) line in one of the side bands. Just as for the Cycle 2 observations the data were calibrated in CASA with the calibration scripts provided by the observatory and the continuum maps were produced in the same way, i.e., natural weighting, cell size of 0.28 arcsec, BARY and mode mfs, to be consistent over the whole sample.

For the source, 4C 23.56, we use the ALMA band 3 and 6 continuum data presented in Lee et al. (2017). Please see Lee et al. (2017) for details of the observations and data reduction.

3.2.3 ATCA 7 mm and 3 mm data

The ATCA observations of 7 mm continuum in some of the sources were conducted over $2009 - 2013$. These continuum data were part of a survey to search for cold molecular CO(1–0) gas in high redshift radio galaxies (Emonts et al. 2014). The data were obtained using the compact hybrid H75, H168 and H214 array configurations, with maximum baselines of 89, 192 and 247 m, respectively. This resulted in synthesized beams ranging from roughly $6-13$ arcsec. We used the Compact Array Broadband Backend (CABB; Wilson et al. 2011) with an effective 2 GHz bandpass and 1 MHz channels, centered on the redshifted CO(1–0) line ($32-48$ GHz; Emonts et al. 2014). The data were calibrated using the software package, MIRIAD (Sault et al. 1995). The observing and data reduction strategy, as well as the basic data products, were previously described in Emonts et al. (2011b) and Emonts et al. (2014). For MRC 0943-242, we also used the ATCA 3 mm ATCA/CABB system on March 21 2012 in the H168 array configurations and on September 30 and Oct 1 2012 in the H214 array configuration to obtain an upper limit of the radio continuum at 88.2 GHz. This frequency corresponds to the redshifted CO(3-2) line, which was not detected in our observations. We used PKS 1253-055 (March) and PKS 0537-441 (Sept/Oct) for bandpass calibration, PKS 0919-260 for frequency gain calibration, and Mars (March) and Uranus (Sept/Oct) to set the absolute flux levels. The total on-source integration time was 5.1 hrs. We used a standard observing and data reduction strategy to calibrate these 3 mm data, matching the strategy of the 7 mm data. The resulting synthesized beam of these 3 mm data is $2.4'' \times 1.9''$ (PA 82°) after robust +1 weighting (Briggs 1995). The rms noise level of these 3 mm data are 0.3 mJy,beam^{-1}.

3.3 Mr-Moose

Mr-Moose is a new SED fitting code, developed with the goal of being able to handle multi-resolution photometric data that have multiple spatially-resolved detections in the same photometric band. The specific motivation for developing this new code is to be able to make full use of the information contained in deep and high resolution ALMA data. When combining ALMA and radio interferometric (such as JVLA and ATCA) data with previous low resolution data (such as *Herschel* or *Spitzer*) where the beam is too large to resolve individual components, one needs a SED fitting tool able to handle multiple components in order to make full use of the interferometric data which often contain multiple resolved components. Mr-Moose[1] is open source and the current version operates in MIR to radio wavelengths (Drouart & Falkendal 2018). The code relies on simple analytic models to describe the underlying physical processes. It is up to the user to

[1]https://github.com/gdrouart/MrMoose

Name	ALMA band	RMS [μJybeam]	Beam size [arcsec]	Antennas	Central frequency [GHz]	Integration time [minutes]	Observations date
MRC 0037-258	6	57	0.26×0.22	42	230	6	2014-08-28
MRC 0114-211	6	59	0.27×0.22	42	230	6	2014-08-28
TN J0121+1320	3	12	1.57×1.19	36	102	183	2016-04-17
				36		78	2016-04-17
MRC 0152-209	6	58	0.39×0.32	34	245	7	2014-08-28
				35		7	2014-07-21
MRC 0156-252	6	50	0.39×0.32	34	245	7	2014-08-28
				35		7	2014-07-21
TN J0205+2242	3	17	1.87×1.37	36	97	86	2016-03-08
				36		121	2016-04-17
MRC 0211-256	6	52	0.39×0.32	34	245	7	2014-08-28
				35		7	2014-07-21
TXS 0211-122	6	51	0.47×0.25	36	250	5	2014-09-01
MRC 0251-273	6	55	0.61×0.44	35	231	3	2015-06-13
MRC 0324-228	6	52	0.57×043	35	231	3	2015-06-13
MRC 0350-279	6	56	0.42×0.28	34	245	4	2014-08-28
MRC 0406-244	6	65	0.41×0.28	34	245	4	2014-08-28
PKS 0529-549	6	45	0.42×0.2	34	233	5	2014-09-02
TN J0924-2201	6	79	0.68×0.58	36	243	2	2014-04-28
MRC 0943-242	4	13	1.61×1.03	42	133	146	2016-03-06
				34		4	2015-09-26
MRC 0943-242	6	61	0.47×0.38	36	243	2	2014-04-28
				37		3	2015-06-12
				34		4	2015-09-26
MRC 1017-220	6	67	0.48×0.36	36	243	2	2014-04-28
				37		3	2015-06-12
4C 03.24	3	18	1.92×1.46	42	102	101	2016-03-06
TN J1338+1942	3	12	1.72×1.36	43	92	39	2016-04-16
TN J2007-1316	4	44	0.44×0.34	43	150	3	2015-06-29
MRC 2025-218	6	46	0.29×0.26	39	232	3	2015-07-19
				34		3	2014-08-18
MRC 2048-272	6	45	0.27×0.25	39	232	3	2015-07-19
				34		3	2014-08-18
MRC 2104-242	6	43	0.27×0.27	39	232	3	2015-07-19
				34		3	2014-08-18
4C 23.56[1]	3	16	0.87×0.60	43	106	61	2015-06-30
4C 23.56[1]	6	81	0.78×0.68	25	265	4	2014-04-25
4C 19.71	3	13	1.76×1.59	36	103	141	2016-03-06
MRC 2224-273	6	72	0.41×0.39	33	251	4	2014-07-28

TABLE 3.1: Details about the ALMA observations. Several sources were observed more than once because the first observation did not meet the requested sensitivity and/or resolution. The additional data were included in the final reduction when they improved the signal-to-noise of the resulting image. [1]The ALMA are from Lee et al. (2017), see that study for details concerning the reduction and observations.

Model name	degree of freedom	Free parameters	Fixed parameters
AGN heated dust	2	N_{AGN}, γ [0,6],	λ_{cut}=33 μm
SF heated dust	2	N_{BB}, T [20,70K]	ν_0=1.5 GHz, β=2.5
Synchrotron	2	N_{sync}, α [-4,0]	...

TABLE 3.2: List of the free parameters in our models and their allowed ranges. N_{AGN} is the normalization of the AGN power law with slope, γ, and rest-frame cut-off wavelength, λ_{cut}. The λ_{cut} is fixed for all galaxies except 4C 23.56. We choose this particular galaxy to fit this parameter because it is AGN-dominated (see Fig. 3.1). N_{BB} is the normalization of the modified black body of temperature, T. N_{sync} is the normalization of the synchrotron power-law with slope α.

define which data point should be fitted to which analytic models. Each photometric data point can be associated to any number of models and combinations of different models. It therefore *only* requires the user to make educated guesses about the underlying physical processes responsible for the observed flux and does not require the user to select only one possible choice. The code fits simultaneously all pre-selected analytic models and uses Bayesian statistics to find the most likely solution given the set of observed fluxes. The Bayesian, Monte Carlo Markov Chain (MCMC) approach provides marginalized posterior probability density functions (PDF) for each of the free parameters.

In this paper, we model the MIR through radio spectral energy distributions with three components: a component representing dust heated by an AGN which we model as a power law with a slope, γ, and an exponential cut-off at ν_{cut} (3.1); a component representing dust heated by the young stellar population of the host galaxy or companion which we model as a modified black body (3.2); and a component representing synchrotron emission which we modeled as a simple power law with constant slope, α, with no cut-off at high frequencies (3.3). Table 3.2 summarizes the allowed range and the number of free parameters in the three different models.

3.3.1 Analytic models

In this paper, simple analytic models are used to fit each component of the SED, instead of, using a (perhaps more realistic) physical models because of the limited number of data points available. As is often the case for high-redshift studies, we are limited to broad band photometric data. So even though this sample of galaxies has been observed with *Herschel*, *Spitzer*, LABOCA, and now ALMA, we are still limited to $\sim$10 data points in the infrared. To properly constrain more complex models, more data points are needed. We therefore rely on less complicated, but empirically justifiable models, to fit the data in a statistically robust way and to prevent the temptation to over-interpret the physical processes underpinnings of our results (e.g., the characteristics of the AGN torus which may be responsible for reprocessing the emission from the accretion disk).

AGN model

The IR-luminosity of the source is modeled following the study of Casey (2012). The mid- and far-infrared SEDs are fitted with a combination of a simple power law with a low frequency exponential cut-off and a single temperature modified black body. These two simple models represents the dust heated by both the AGN and star-formation in the galaxy respectively. However, in this paper, the two models to describe the AGN and SF component are de-coupled and normalized individually to fit the photometry. The functional form of the dust heated by the AGN is,

$$S_{AGN} = N_{AGN}\ \nu^{-\gamma}\ e^{-(\nu_{cut}/\nu)^2}, \tag{3.1}$$

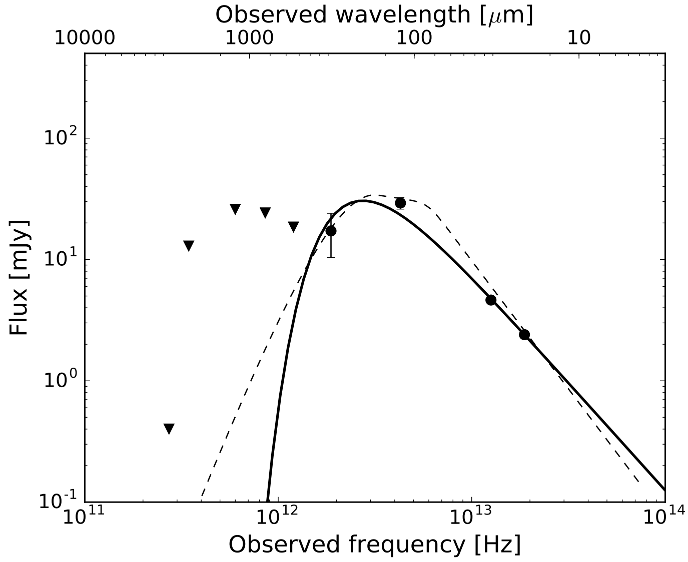

FIGURE 3.1: The best fit of the SED of 4C 23.56 when assuming that the AGN is solely responsible for the mid-infrared emission and allowing $\lambda_{\rm cut}$ to be an additional free parameter. The black solid line shows the best fit with $\lambda_{\rm cut} = 33^{+3}_{-3}$ μm. The dashed line is the best fit AGN model used in Drouart et al. (2014) which itself is the average AGN used in the DecompIR SED fitting code (Mullaney et al. 2011). See Table A.23 for details about the photometric data.

where $\nu_{\rm cut}$ is the rest-frame frequency of the exponential cut-off of the power law. The shape at longer wavelengths of the heated dust by AGN is not well constrained because cold dust emission often completely dominates at longer wavelengths making it very difficult to determine the actual shape of the AGN emission. Therefore, we use a simple exponential with a fixed rest-frame cut-off wavelength/frequency at $\lambda_{\rm cut}$ =33 μm or $\nu_{\rm cut}$=9.085 THz. This value was determined by letting $\lambda_{\rm cut}$ be a free parameter for one galaxy and finding the best fit value. The mid-infrared emission of 4C 23.56 appears to predominately due to warm dust emission from its AGN and the far-infrared emission is very faint suggesting that it has a very low star formation rate. Within our sample, this makes 4C 23.56 the most obviously suitable choice for determining $\lambda_{\rm cut}$ for this sample of HzRGs. Fig. 3.1 shows the best fit with $\lambda_{\rm cut}$ as a free parameter. The chosen model for the warm dust used in this paper has also been adopted in other studies. For example, Younger et al. (2009) found good agreement when fitting the IR emission of luminous high-redshift galaxies with a modified black body paired with a power law component at short wavelengths.

Star-formation model

The far-infrared emission from dust heated by star-formation is fitted by a simple single temperature modified black body (i.e., a "graybody"),

$$S_{\rm BB} = N_{\rm BB}\left(1 - e^{-(\nu/\nu_0)^\beta}\right)\ B_\nu\left(\nu, \mathrm{T}\right), \tag{3.2}$$

where $B_\nu(\nu, \mathrm{T})$ is a black body (BB) distribution, ν_0 is the critical frequency where the source becomes optically thin (assumed to be fixed at $\nu_0 = 1.5$ THz; Conley et al. 2011) and β is the emissivity, which we fixed at $\beta = 2.5$. The value of the emissivity depends on the characteristics of the dust grain size, composition, distribution and how efficiently the grains re-emit the absorbed energy. It is common to assume a β in the range 1-2 (Hildebrand 1983) but values of up to 2.5 at sub-mm wavelengths have been found in the integrated SEDs of galaxies (Galametz et al. 2012; Cortese et al. 2012). A value of $\beta = 2.5$ has been adopted in this paper. This is justified because sources with both LABOCA and ALMA detections in the submm have SEDs that are better fit with

β=2.5 compared to models with $\beta \sim 1.5 - 2$. Whether or not this is physical is a difficult question to answer since we do not know the precise composition of the dust grains in these sources. Also, the emission from dust in galaxies is most likely a combination of regions with different temperatures and mixtures of grain size distributions and compositions. This means that when a single modified black body is fitted to the total dust emission from a galaxy the estimated value of beta is affected by these different effects which may result in an increase in β.

Synchrotron model

The synchrotron emission is fitted with a single power law,

$$S_{\rm sync} = N_{\rm sync}\ \nu^{\alpha}, \tag{3.3}$$

with a constant slope α. Such a simple representation is perhaps not a physical model in that it does not include the possibility of a steepening or cut-off due to the aging of the electron populations. At which frequency this happens is not constrained with the data we have available for most of the sources. Therefore, it is important to realize that with this simple power law, we are fitting the maximum possible contribution from synchrotron to the radio and mm frequencies. For the sources with a good photometric data coverage in the high radio frequencies (i.e., $>$10 GHz), there is no evidence for a high frequency cut-off or steeping, in agreement with previous work (Klamer et al. 2006; Emonts et al. 2011b).

3.3.2 Fitting procedure

Mr-Moose fits a pre-selected number of models to the rest-frame photometry of a galaxy. To do this, it uses Bayesian parameter estimation to find posterior distributions of the free parameters which are determined based on the prior distribution (uniform) and the likelihood function. Mr-Moose uses the Monte Carlo Markov Chain (MCMC) core provided in the Python package, *Emcee* (Foreman-Mackey et al. 2013). The best fit model is determined by minimizing the likelihood (χ^2); a parameter of the goodness of the fit, calculated by comparing the observed data with the model values for the combination of all models at the same time for each photometric band. The parameter space is explored by “walkers” taking random steps. Each walker makes a chain of random steps with each new step being only dependent on the previous step in the sequence. The new value of a parameter after each step is accepted if the χ^2 is lower than the likelihood of the previous step in the chain, or rejected if it is higher, in which case, the previous value is retained. The process continues resulting in a random walk. The parameter space is thus explored during these "walks" and from the combination of the chain of each individual walker, posterior probability density functions (PDF) are estimated. These PDFs are used to find the best fit values and the uncertainties of each parameter.

The likelihood function, χ^2, is calculated as described in Sawicki (2012). One particular aspect of calculating the likelihood function in this way, is to emphasize that it treats upper limits in a continuous way. There is no sharp upper cut to the allowed value of the modeled data can be for data points reported as upper limits. The upper limits are included in a continuous way, and the modeled value can also go above the 3σ upper limit of the observed data, but in that case the χ^2 increases rapidly when the model starts to over predict the flux of the upper limit. In the case where all of the observed photometric data are detections, the likelihood function reduces to the classical expression of χ^2. We refer the reader to the *Appendix: The maximum likelihood formalism for SED fitting with upper limits* in (Sawicki 2012) for details about the derivation of the maximum-likelihood. We also refer the reader to the paper (Drouart & Falkendal 2018) for a more detailed description of Mr-Moose.

3.3.3 Setting up the SED for fitting

For each source, input files need to be specified individually. This is necessary because the code can fit a large number of possible models to each data set. Depending on the complexity of the source, if there are several individual resolved components, the user can launch the code with any number of models adapted to the specific nature of each source. If all the photometric data is unresolved then the multi-component part of the code is not applicable and only a single combination of synchrotron emission, modified black body and power-law component is needed.

It is up to the user to assign which data point belongs to which model or set of models, and thus, requires some knowledge of the source properties and what underling processes contribute to the observed flux. The code is not made to be applied blindly to a large sample of galaxies. Even though the process of assigning analytic models to each photometric data point may sound subjective, we actually let the code decide between multiple models as illustrated in Table 3.3. In case of doubt, we provide the code with many flexible options. For the sources with spatially-separated detections in the same band, it is easy to connect them to corresponding detections at other frequencies. To show how the set up is done, we take MRC 0114-211 as an example. This source has unresolved *Spitzer* IRS through to LABOCA data, resolved ALMA band 6 data with two spatially resolved continuum components, unresolved ALMA band 3, ATCA and VLA L data and resolved VLA C- and X-band data with two resolved components. The two radio components coincide with the two detections in ALMA. The FIR data are unresolved and it is unclear if this is the combined flux from the two individual sources detected in ALMA or just the flux from the host galaxy with no contribution from the companion. For the two detections in ALMA it is unclear if these are two thermal dust emitting objects or the high frequency end of the synchrotron emission. The unresolved radio data is the total flux from both synchrotron components. In this situation, since we cannot decide what is the nature of the two ALMA components and therefore allow contributions to their flux from both synchrotron emission and the modified black body model. We refer the reader to the full list of components and how they are assigned to various models which is shown in Table 3.3. The code then determines what contributes to each component, not the astrophysicist.

The best fit is determined by minimizing χ^2, which is calculated by fitting models to each spatial and photometric data point. The MCMC attempts to find the most likely solution considering all the data at the same time. For example, as we already outlined, in the case of MRC 0114-211, two black bodies and two synchrotron models were assigned to the spatially resolved ALMA band 6 data points and what came out of the fitting procedure is that the eastern component is consistent with being dominated by synchrotron emission and the western is dominated by thermal dust emission from the host galaxy (Sect. A.3 and Table 3.3).

3.4 Results of the SED fitting with MrMoose

Combining *Spitzer*, *Herschel*, SCUBA/LABOCA, ALMA, ATCA and VLA data, we fit the FIR–radio SED with Mr-Moose to derive the IR luminosities of both the SF and AGN components in our sources. Importantly, we are able to disentangle the contribution of synchrotron at $\sim$1 mm, which can otherwise masquerade as thermal dust emission. The contribution of synchrotron to the long wavelength thermal dust emission, if not well-constrained, can lead to a general overestimate of L_{SF}^{IR} and thus the SFR (see also Archibald et al. 2001). The focus of this paper is to disentangle the emission of cold (assumed to be heated by young stars) and warm (assumed to be heated by the AGN) dust emission from individual components and to separate the emission from nearby objects and radio hot spots/lobes by identifying independent emission components. We did not include the *Spitzer* IRAC bands since these can be dominated by stellar photospheric emission and emission from PAH bands. No models for photospheric emission from stars are included in the version of the SED fitting code, Mr-Moose, we used in this paper.

Photometric band	Assigned model	Fitted model
IRS (16 μm)	AGN, BB1, BB2	AGN
MIPS (24 μm)	AGN, BB1, BB2	AGN
PACS (70 μm)	AGN, BB1, BB2	AGN, BB2
PACS (160 μm)	AGN, BB1, BB2	AGN, BB2
SPIRE (250 μm)	AGN, BB1, BB2	AGN, BB2
SPIRE (350 μm)	AGN, BB1, BB2	BB2
SPIRE (500 μm)	AGN, BB1, BB2	BB2
LABOCA (870 μm)	AGN, BB1, BB2	BB2
ALMA 6 east comp.	BB1, Sync2	Sync2
ALMA 6 west comp.	BB2, Sync1	BB2
ALMA 3	BB1, BB2, Sync1, Sync2	Sync1, Sync2
ATCA (7mm)	Sync1, Sync2	Sync1, Sync2
VLA X west comp.	Sync2	Sync2
VLA X east comp.	Sync1	Sync1
VLA C west comp.	Sync2	Sync2
VLA C east comp.	Sync1	Sync1
VLA L	Sync1, Sync2	Sync1, Sync2

TABLE 3.3: The list of models assigned component to each photometric band for MRC 0114-211. The last column lists the model components that dominate each band as determined through SED fitting with Mr-Moose. Models that contribute less than 1% to the total flux in a particular band for the best fitting model are not listed.

3.4.1 SF and AGN IR luminosities

From our well-sampled SEDs we estimate the total IR luminosity of the AGN and SF component (L^{IR}_{AGN} and L^{IR}_{SF}). We estimate the total IR luminosity as the integrated flux density over rest-frame 8-1000 μm continuum emission. The flux densities are derived from the best fit of the analytic models, (3.1) and (3.2) for the AGN and SF component respectively. To determine the total integrated luminosity, the analytic models need to be well constrained. For several sources, this is not the case for the SF component. Either because there are only upper limits in the FIR and ALMA bands (e.g., Fig. A.31), the measured ALMA flux is not consistent with originating from pure dust emission (e.g., Fig. A.13) or there is only one detection in the FIR (e.g., Fig. A.40) which is not enough to constrain a model with two free parameters. In these cases, only an upper limit of L^{IR}_{SF} can be estimated. This is done by scaling a modified BB (with fixed $\beta = 2.5$ and T=50 K) to the ALMA data point.

The estimated upper limit of the L^{IR}_{SF} is dependent on the exact values of β and T that are assumed. A flatter slope, $\beta = 1.5 - 2$, will lower the inferred IR luminosity. Assuming a higher (or lower) temperature then 50 K for a fixed β will increase (or decrease) the integrated IR luminosity. We illustrate these dependencies in Fig. 3.4. In our sample, eight sources are not detected in our ALMA data: TN J0205+2242, MRC 0324-228, MRC 0350-279, TN J2007-1316, MRC 2025-218, MRC 2048-272, MRC 2104-242 and 4C 23.56. Four sources have ALMA fluxes which are consistent with being dominated by synchrotron emission: MRC 0037-258, MRC 0152-209, MRC 0406-244 and MRC 1017-220. The SFR for these sources are determined by scaling a modified BB to the ALMA detection and are thus very conservative upper limits (i.e., they could be much lower).

In the case of only upper-limits in the MIR, it is not possible to constrain the AGN contribution to the SED. This is the case for four sources: TN J0121+1320, TN J0205+2242, TN J0924-2201 and MRC 2048-272. For these four galaxies, L^{IR}_{AGN} is given as a upper-limit and have been estimated by scaling the analytic AGN model, (3.1), to the *Spitzer* IRS 16 μm upper-limit with a fixed slope

TABLE 3.4: Characteristics of the sources

Name	Position		ALMA	Flux	RMS
	R.A.(J2000.0)	Dec.(J2000.0)	band	[mJy]	[μJy/beam]
MRC 0037-258	00:39:56.44	−25:34:31.00	6	0.36 ±0.08	57
TN J0121+1320	01:21:42.73	+13:20:58.00	3	0.19 ±0.01	12
MRC 0156-252(N)	01:58:33.66	−24:59:31.01	6	0.97 ±0.58	49
MRC 0156-252(S)	01:58:33.45	−24:59:32.12	6	0.63 ±0.39	50
TN J0205+2242	02:05:10.69	+22:42:50.40	3	<0.05	17
MRC 0211-256	02:13:30.53	−25:25:20.81	6	0.67 ±0.09	52
TXS 0211-211	02:14:17.38	−11:58:46.89	6	0.31 ±0.08	51
MRC 251-273	02:53:16.68	−27:09:11.94	6	0.35 ±0.07	55
MRC 0324-228	03:27:04:54	−22:39:42.10	6	<0.21	52
MRC 0350-279	03:52:51.60	−27:49:22.60	6	<0.19	56
MRC 0406-244	04:08:51.48	−24:18:16.47	6	0.50 ±0.10	65
TN J0924-2201	09:24:19.90	−22:01:42.30	6	0.88 ±0.70	79
MRC 0943-242(Y)	09:45:32.77	−24.28.49.29	6	0.84±0.40	61
MRC 0943-242(O)	09:45:32.22	−24.28.55.06	6	2.46 ±0.15	61
MRC 0943-242(T)	09:45:32.39	−24.28.54.05	6	1.33 ±0.12	61
MRC 0943-242(F)	09:45:32.44	−24.28.52.55	6	0.42±0.96	61
MRC 1017-220	10:19:49.02	−22.19.59.86	6	0.52 ±0.11	67
4C 03.24(S)	12:45:38.36	+03:23:20.70	3	0.71±0.14	11
4C 03.24(H)	12:45:38.36	+03:23:20.70	3	0.08±0.07	11
TN J1338+1942	13:38:25.98	+19:42:31.00	3	0.18±0.09	10
TN J2007-1316	20:07:53.26	−13:16:43.60	4	<0.25	44
MRC 2025-218	20:27:59.48	−21:40:56.90	6	<0.12	46
MRC 2048-272	20:51:03.59	−27:03:02.50	6	<0.17	45
MRC 2104-242	21:06:58.28	−24:05:09.10	6	<0.12	43
4C 23.56	21:07:14.84	+23.31.44.91	3	0.23±0.05	16
4C 23.56	21:07:14.84	+23.31.44.91	6	<0.4	81
4C 19.71(H)	21:44:07.45	+19:29:14.60	3	0.07±0.05	13
4C 19.71(N)	21:44:07.49	+19.29.18.99	3	0.29±0.53	13
4C 19.71(S)	21:44:07.53	+19.29.10.78	3	0.11±0.05	13
MRC 2224-273	22:27:43.28	−27.05.01.67	6	0.22±0.06	58
Multiple components*					
MRC 0114-211(S)	01:16:51.40	−20.52.06.98	6	9.82 ±0.38	87
MRC 0114-211(N)	01:16:51.44	−20.52.06.96	6	2.21 ±0.31	87
MRC 0152-209(S)	01:54:55.76	−20.40.26.96	6	2.30 ±0.10	58
MRC 0152-209(N)	01:54:55.74	−20.40.26.59	6	1.75 ±0.13	58
PKS 0529-549(E)	05:30:25.53	−54.54.23.30	6	0.37± 0.07	46
PKS 0529-549(W)	05:30:25.44	−54.54.23.21	6	1.33 ±0.16	46

Integrated fluxes are determined over regions where the signal has a significance $>1.5\sigma$. Upper limits are 3σ above the noise at the IRAC position of each source over an area of one ALMA beam. The noise for each source is estimated by measuring the root-mean-square of the pixels in the non-primary beam corrected images. The peak flux is the deconvolved value from a single Gaussian fit. The signal-to-noise estimates are from the image and do not include the uncertainties in the flux calibration. The characteristics of various components of MRC 0943-242 are indicated as "Y" for Yggdrasil, "T" for Thor, "O" for Odin, and "F" for Freja (see Gullberg et al. 2016a, for details). Other notations are "N" for the northern component, "H" indicating the host galaxy, "S" for the southern component, "E" for the eastern component, and "W" for the western component.
* Sources with multiple components for which the individual components are not robustly separated in the ALMA continuum images. The flux of these sources is deblended by fitting 2 Gaussian profiles using CASA 4.5.0. The flux is determined by integrating the fit, peak values are deconvolved with the beam, the position is the flux center of the fit, and noise level is estimated from the RMS of the uncorrected primary beam image. For MRC 0152-209, the flux in the ALMA continuum data is divided between a northern and southern component (see Emonts et al. 2015b, for details).

TABLE 3.5: Integrated AGN and SF luminosities.

Name	redshift	L^{IR}_{AGN} [10^{12} $L_\odot$]	L^{IR}_{SF} [10^{12} $L_\odot$][1]	SFR [$M_\odot$ yr^{-1}]	LAS [arcsec]	size* [kpc]	Stellar mass [$\log(M_*/M_\odot)$]	Temp. [K]	L^{IR}_{SF} / L^{IR}_{SB}**
MRC 0037-258	1.100	$0.93^{+0.10}_{-0.06}$	<2.17	<249	27.6[a]	231.7	11.56[g]	uncons.	...
MRC 0114-211	1.410	$2.00^{+0.05}_{-0.04}$	$1.09^{+0.28}_{-0.28}$	126	<2[a]	<17	11.39[g]	40^{+1}_{-13}	0.47
TN J0121+1320	3.516	<2.67	$5.43^{+2.32}_{-2.11}$	626	0.3[b]	2.2	11.02[g]	53^{+9}_{-9}	0.72
MRC 0152-209 (H)	1.920	$9.57^{+1.30}_{-1.06}$	$15.82^{+1.85}_{-2.36}$	1817	2.2[c]	19.0	11.76[g]	69^{+4}_{-4}	0.89
MRC 0152-209 (C)	1.920	...	$0.94^{+0.88}_{-0.42}$	108	...	...	...	28^{+7}_{-5}	...
MRC 0156-252	2.016	$10.08^{+1.54}_{-1.58}$	<1.99	<228	8.3[d]	71.2	12.05[g]	uncons.	...
TN J0205+2242	3.506	<2.70	<0.74	<84	2.7[b]	20.2	10.82[g]	uncons.	...
MRC 0211-256	1.300	$0.61^{+0.02}_{-0.08}$	$1.02^{+0.18}_{-0.15}$	117	2.4[a]	20.6	<11.54[g]	36^{+4}_{-4}	0.57
TXS 0211-122	2.340	$10.75^{+0.98}_{-0.70}$	$0.71^{+0.89}_{-0.55}$	81	17.0[d]	142.5	<11.16[g]	53^{+17}_{-21}	>0.16
MRC 0251-273	3.160	$9.98^{+2.95}_{-2.74}$	$0.69^{+1.05}_{-0.52}$	79	3.9[a]	30.3	10.96[g]	47^{+19}_{-19}	>0.11
MRC 0324-228	1.894	$7.76^{+0.82}_{-0.70}$	<0.86	<98	9.6[a]	81.1	10.7(8)[f]	uncons.	<0.15
MRC 0350-279	1.900	$0.66^{+0.24}_{-0.10}$	<0.77	<88	1.2[a]	10.4	<11.00[g]	uncons.	...
MRC 0406-244	2.427	$9.40^{+1.41}_{-1.26}$	<1.63	<186	10.0[d]	83.2	11.1(3)[f]	uncons.	<0.22
PKS 0529-549	2.575	$5.88^{+0.83}_{-0.83}$	$8.86^{+1.66}_{-1.50}$	1018	3[i]	24.7	11.46[g]	66^{+5}_{-4}	0.84
TN J0924-2201	5.195	<14.98	$1.00^{+1.34}_{-0.71}$	142	1.2[b]	7.6	11.10[g]	uncons.	>0.23
MRC 0943-242 (H)	2.923	$6.39^{+1.57}_{-1.35}$	$0.36^{+0.23}_{-0.29}$	41	3.9[d]	31.0	11.3(4)[f]	52^{+18}_{-22}	0.03
MRC 0943-242 (C)	2.923	...	$6.49^{+1.41}_{-1.94}$	747	...	...	...	42^{+3}_{-4}	...
MRC 1017-220	1.768	$2.01^{+0.24}_{-0.09}$	<1.75	<201	<0.2[c]	<1.7	<11.70[g]	uncons.	...
4C 03.24	3.570	$16.48^{+3.23}_{-4.04}$	$1.23^{+2.08}_{-1.13}$	142	6.0[e]	44.7	<11.27[g]	59^{+15}_{-20}	0.26
TN J1338+1942	4.110	$11.24^{+3.84}_{-2.83}$	$4.02^{+2.6}_{-1.63}$	461	5.2[c]	36.6	11.04[g]	46^{+9}_{-9}	0.59
TN J2007-1316	3.840	$5.13^{+1.35}_{-0.60}$	$2.19^{+2.33}_{-1.63}$	251	3.5[b]	25.3	11.9(0)[f]	59^{+14}_{17}	0.35
MRC 2025-218	2.630	$1.16^{+0.75}_{-0.24}$	<0.36	<41	5.1[d]	41.7	<11.62[g]	uncons.	...
MRC 2048-272	2.060	<0.18	<0.65	<74	6.8[c]	58.2	11.47[g]	uncons.	...
MRC 2104-242	2.491	$9.56^{+1.52}_{-1.58}$	<0.38	<43	23.7[c]	196.2	11.0(0.6)[f]	uncons.	<0.07
4C 23.56	2.483	$27.58^{+1.60}_{-1.24}$	<0.49	<56	53.0[d]	439.1	<11.59[g]	uncons.	...
4C 19.71	3.592	$10.91^{+6.47}_{-3.74}$	$0.74^{+1.52}_{-0.55}$	84	23.3[d]	172.0	<11.13[g]	44^{+24}_{-17}	0.17
MRC 2224-273	1.679	$1.70^{+0.37}_{-0.15}$	$1.21^{+0.72}_{-0.55}$	138	<0.2[a]	<1.7	11.41[g]	61^{+11}_{-12}	0.55

L^{IR}_{AGN} is the integrated AGN luminosity. L^{IR}_{SF} is the integrated SF luminosity over the wavelengths 8–1000 μm in the rest-frame assuming $\beta = 2.5$ (§ 3.4.1). Upper-limits in L^{IR}_{SF} were estimated assuming $\beta = 2.5$ and T=50 K (Sec. 3.4.1). The star-formation rates, SFR, are calculated from the L^{IR}_{SF} via the conversion given in Kennicutt (1998b) but we scaled these values from the original Salpeter IMF assumed in Kennicutt (1998b) to a Kroupa IMF by dividing by a factor of 1.5. LAS is the largest angular size of the radio source as given in the references indicated by the superscript: [a]Kapahi et al. (1998), [b]De Breuck et al. (2000), [c]Pentericci et al. (2000), [d]Carilli et al. (1997), [e]van Ojik et al. (1996), [i]size extracted from original map. (*) The physical size of radio source at 1.4 GHz (LAS) at the given redshift. The stellar masses are taken from the studies indicated by the superscript: [g]De Breuck et al. (2010), [f]Drouart et al. (2016). Both of these studies use a Kroupa 2001 IMF. Some values of the stellar mass have two estimates. The value in the parentheses replaces the last digits to give the alternative value (see § 3.4.5). For example, the possible stellar masses for MRC 2104-242 are $\log(M_*/M_\odot)$=11.0 or 10.6. (**) The difference between the total luminosity of heated dust by star-formation, L^{IR}_{SF} (this paper) and the total luminosity of dust heated by starbursts L^{IR}_{SB} (Drouart et al. 2014). Two of sources contain additional sources in the ALMA images and for these two sources, we indicate the host galaxy and companions as "H" and "C", respectively.

of γ=2. The best fit values and upper-limits of L^{IR}_{AGN} and L^{IR}_{SF} are given in Table 3.5.

3.4.2 Calculating uncertainties of the integrated IR luminosity

The estimated total integrated luminosity results from our fitting the SEDs. Each combination of the parameters affects the total infrared luminosity in a unique way. There are degeneracies between parameters, meaning that several combinations of parameters can give the same integrated luminosity. Therefore the standard uncertainty estimates, such as quadratically summing the uncertainties for the luminosities of each individual component, is not an accurate reflection of the true uncertainty. In order to estimate accurately the total luminosity and its associated uncertainty, we performed an after-the-fit post-processing calculation. Because each Monte Carlo chain contains all the required information about each fitted parameter, we build the marginalized distribution for the integrated luminosity for each step and each walker after convergence by integrating the model in the defined wavelength limits (8-1000 μm in the rest-frame in our case). From this distribution we are therefore able to derive the percentile values that are listed in Table 3.5.

3.4.3 High frequency synchrotron

The synchrotron emission is modeled by assuming a power-law with a constant slope without any steepening or cut-off at high frequencies. This means that we are estimating the maximal possible contribution from individual synchrotron components out to frequencies where the low frequency tail of the cold dust emission and synchrotron possibly overlap. Through the use of already published VLA L, C and X-band data (Carilli et al. 1997; Kapahi et al. 1998; Condon et al. 1998; Pentericci et al. 2000; De Breuck et al. 2010; Broderick et al. 2007) as well as ATCA 7 mm and ALMA band 3 for a subset of our sample, we were able to determine whether or not the detections in ALMA are likely to be the high frequency extrapolation of the synchrotron emission or low frequency thermal emission from dust.

There are in total 13 individually resolved detections in 10 ALMA maps which have been found though the SED fitting procedure to most likely be dominated by synchrotron emission. For four sources, MRC 0037-258, MRC 0156-252 (both components), MRC 0406-244, and MRC 1017-220, the total ALMA flux is consistent with being dominated by synchrotron emission. For these sources their L^{IR}_{SF} and SFR are only given as upper limits (Figs. 3.4, 3.5, 3.6, and 3.8). In two sources, MRC 0114-211 and PKS 0529-549, one out of two ALMA components are dominated by synchrotron emission and the other detection appears dominated by thermal dust emission. For three sources, MRC 0943-242, 4C 23.56 and 4C 19.71, both the synchrotron lobes and host galaxies are detected in ALMA band 3 or 4. The best fit of these sources is consistent with the lobes being dominated by synchrotron emission. The detections of the host galaxies for MRC 0943-242 and 4C 19.71 are consistent with thermal dust emission, while for 4C 23.56, the modified black body component is completely unconstrained.

3.4.4 IR luminosity model comparison

The IR luminosities were calculated by integrating the flux density of the two analytic models used in this analysis (see Eqs. 3.1 and 3.2). This procedure differs from the previous SED fitting work on the parent sample where starburst templates and an average AGN model were used to fit the SED (Drouart et al. 2014). To investigate how these different approaches may influence our results, we now make a direct comparison of our results with those of Drouart et al..

The study of Drouart et al. used the AGN model implemented in DecompIR (see Fig. 3.1; Mullaney et al. 2011) The simple empirically motivated model implemented in this paper does not deviate much from the average AGN model of Mullaney et al. (2011). A direct comparison

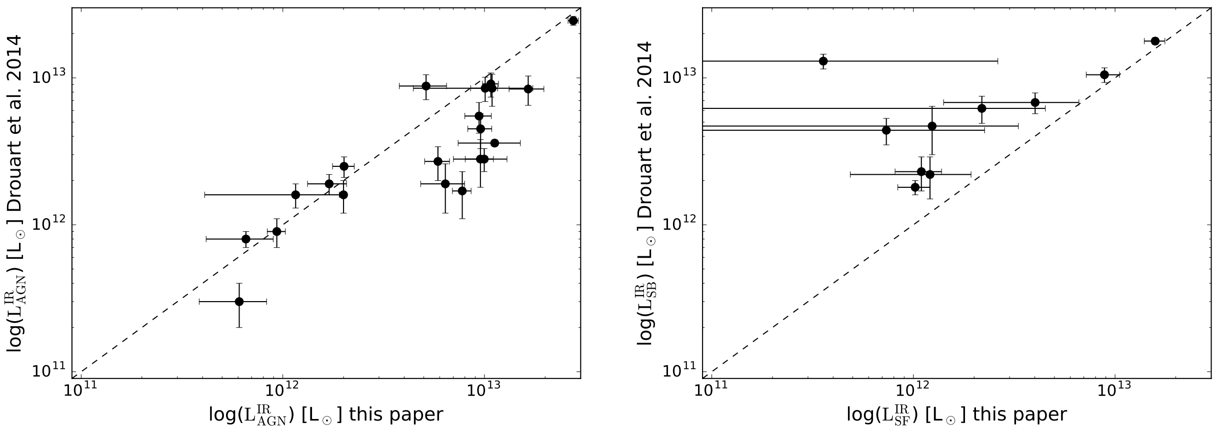

FIGURE 3.2: A comparison of the integrated IR AGN and SF luminosities computed in this paper compared to the results of Drouart et al. (2014). *(top)* A comparison between the infrared luminosity of the AGN and *(bottom)* a comparison between the infrared luminosity of the starburst or star forming component. In both panels, the dashed line is the one-to-one relationship between luminosities.

of the total integrated AGN luminosities (Fig. 3.2), L^{IR}_{AGN} suggests a modest, ∼20%, offset in the median of L^{IR}_{AGN} in between the two approaches.

Quality	Number	L^{IR}_{SF}/L^{IR}_{SB}
Constrained L^{IR}	11	0.49
L^{IR}_{SF} upper limit	3	<0.15
L^{IR}_{SB} upper limit	3	>0.17
All sources	17	∼0.38

TABLE 3.6: The average ratio of IR luminosities of this paper (denoted as L^{IR}_{SF}) and those from (Drouart et al. 2014, denoted as L^{IR}_{SB}). The ratio is given for three cases: the L^{IR} estimated for sources with detections in both ALMA and Herschel and thus the infrared luminosities are constrained in both studies (Constrained L^{IR}); when the infrared luminosity is given as an upper limit in this paper but is given as a detection in Drouart et al. (L^{IR}_{SF} upper limit); and where L^{IR} for the source is constrained but L^{IR}_{SB} is an upper limit in Drouart et al. (L^{IR}_{SB} upper limit).

We compare the star-forming models in this paper and those from Drouart et al. The differences are predominately due to having data in the rest-frame submm which is more sensitive, has higher spatial resolution, and covers a wider wavelength range. As can be seen from the SED shapes of the starburst/star-forming components, they differ both in the presence of PAH features in the Drouart et al. models, and sometimes in the overall shape depending on which starburst template is used (Fig. 3.3). The PAH features do not contribute significantly to the total integrated L^{IR}_{SF}. However, in general when it comes to SED fitting, the choice of template can change the integrated L^{IR} by up to a factor of 4, as mentioned in Sect 4.4 of Drouart et al. (2014). The factor of 4 is estimated in the case one cannot discriminate between the most extreme starburst templates. Even in the less extreme case, there is still a factor of ∼2 between the sets of templates that are consistent with the same data points. The SED parameters that influence this difference include the assumed dust temperature, opacity and emissivity (see also Fig. 8 of Casey et al. 2018, who show how different templates can give the same integrated IR luminosity). The bottom right panel of figure 3.3 illustrates the importance of having at least one sensitive measurement on the

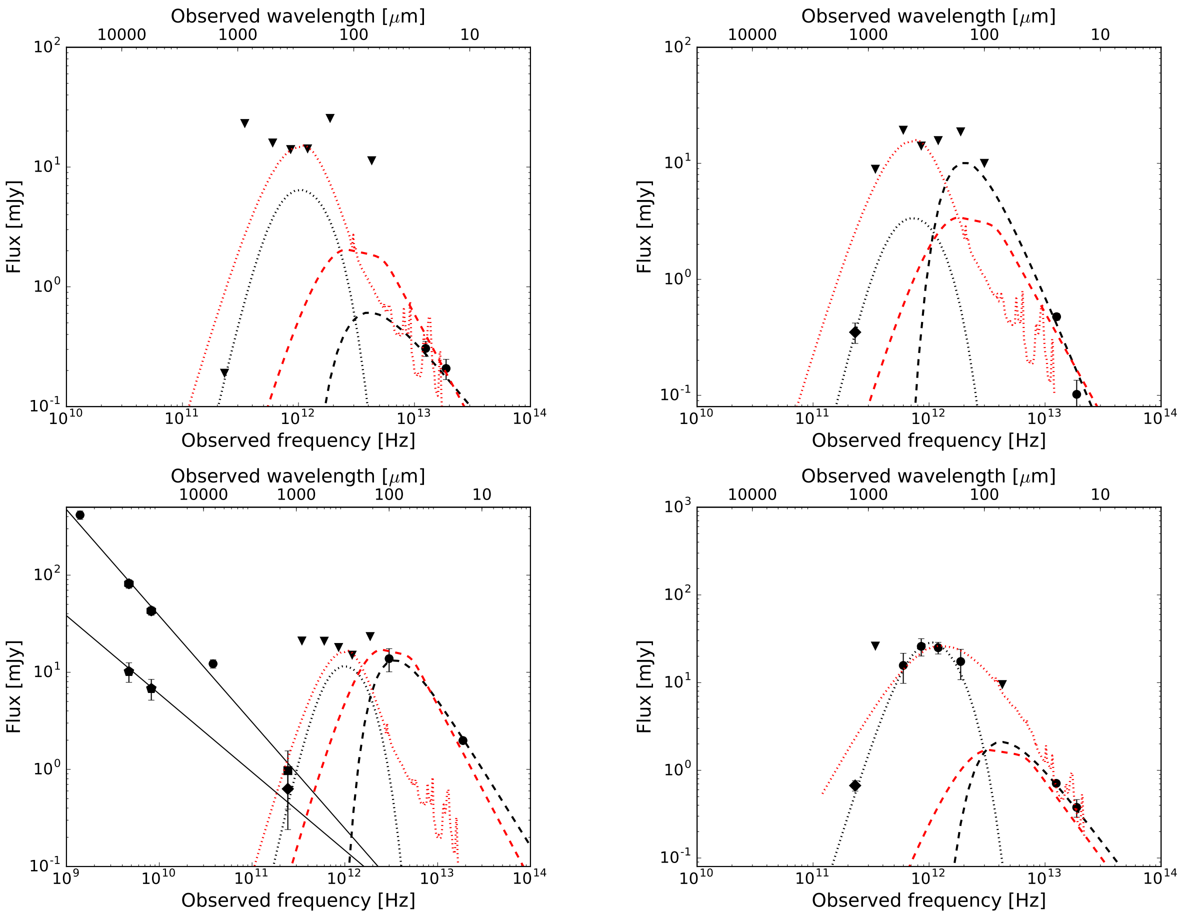

FIGURE 3.3: Model comparison between the SF and AGN models of this paper and Drouart et al. (2014) for galaxies MRC 0350-279 *(top left)*, MRC 0251-273 *(top right)*, MRC 0156-252 *(bottom left)* and MRC 0211-256 *(bottom right)*. In each plot, the black solid lines represent the synchrotron emission, dotted lines indicate the FIR thermal emission due to star-formation, and dash-dotted indicates the best-fit MIR emission due to the AGN as determined from the best fits to the photometry for each galaxy. The red lines with the same styles represent the same components as fitted in Drouart et al. A synchrotron power-law was not fit in the analysis of Drouart et al.

Rayleigh-Jeans side of the emission peak, even when there are multiple detections near the peak of the SED. In this HzRG MRC 0211-256, the observed ALMA band 6 flux is 10× lower than the predicted flux in the Drouart et al. (2014) model.

We identify four general categories where the SED fits lead to significant differences in L_{SF}^{IR}, between the two studies: (1) only upper limits in the FIR; (2) one detected ALMA component and upper limits in the rest of the FIR bands; (3) two spatially resolved detections in the ALMA bands; and (4) when the FIR consists mainly of detections. It is clear that there are cases where the differences are not significant (e.g. MRC 0156-252). However, in some cases, isolating a subcomponent in high resolution, 0.3″, sensitive ALMA imaging leads to a significantly lower L_{SF}^{IR} which simply is not possible using only the low-resolution *Herschel* data (e.g. MRC 0251-273). There are also cases where significantly deeper ALMA data ($\gtrsim$10× deeper than any previous submm/mm observations) still does not detect any emission (e.g. MRC 0350-279). Accordingly, our limits on L_{SF}^{IR} are also much more stringent, but formally still consistent with the shallower upper limits of Drouart et al. Furthermore, we also include a more robust extrapolation of the synchrotron component due to now including the ALMA and ATCA ∼90 GHz data.

As mentioned above, it is important to note that the choice of template can change the L_{SF}^{IR}, by ∼2 even with good photometric coverage of the peak of the thermal dust emission. In our sample, six sources have ≥3 FIR detections from *Herschel* and LABOCA. Out of these six, three have good agreement in the infrared luminosity, having ratios of 0.72–0.89, with Drouart et al.. One is an ALMA source with multiple components, MRC 0943-242, which explains the large difference in L_{SF}^{IR}. Only two sources, MRC 0211-256 and 4C 03.24, have poor agreement due to differences between a modified black body and the starburst templates used in Drouart et al. (2014). Considering that Drouart et al. found a potential difference of ∼2 within the templates used in their study, it is to be expected that we are finding a factor of 2–3 difference compared to their results for a few of our sources, especially when we also include an additional ALMA data point that constrains the Rayleigh-Jeans side of the emission peak.

Quantitatively, we find that our estimated far-infrared luminosities of the component due to star formation are only a fraction of those found by Drouart et al. (Fig 3.2 and Tab. 3.6). If we only include detections, we find that our estimates of L_{SF}^{IR} are only ∼50% of those estimated in Drouart et al. If we also include detections and upper limits of L_{SF}^{IR} in either of the two papers, then our estimates are only ∼40% of those in Drouart et al., (Table 3.3). We discuss the implications of these significantly lower L_{SF}^{IR} in Sects. 3.5 and 3.6. If we compare all the sources together and estimate the median IR luminosity including upper limits of the overlapping 25 sources in both studies, we find our IR luminosities are a factor ∼7 lower.[2]

3.4.5 Notes on the Stellar Masses

Given the importance of stellar masses in our analysis, we briefly discuss the nature of the mass estimates we are utilizing. All stellar masses used in this paper are based on those estimated in Seymour et al. (2007); De Breuck et al. (2010); Drouart et al. (2016). Our stellar masses are based on 6-band *Spitzer* photometry covering 3.6–24 μm, augmented with near-IR imaging. The AGN in our sample may contribute flux to the optical to mid-IR photometry used to determine the stellar masses. AGN emission contributes from both direct and scattered continuum (dominating at $\lambda_{\rm rest} < 1\mu$m), and dust emission from the torus (dominating at $\lambda_{\rm rest} > 5\mu$m). Our sample is composed of Type-2 AGN where the direct AGN contribution is obscured by the dusty torus. One exception, MRC 2025-218, has a SED which is consistent with AGN-dominated continuum emission and thus, although it is detected in the photometry used to estimate masses, we assume its stellar mass is an upper limit. *Spitzer* photometry used in Seymour et al. (2007) and De Breuck et al. (2010) allowed them to extrapolate the hot dust emission from the AGN down to rest-frame

[2]For this comparison, we used a Kaplan-Meier estimator (Feigelson & Nelson 1985).

1–2 μm where the old stellar population peaks. The stellar masses of objects where this hot dust contribution *may* dominate are conservatively listed as upper limits.

In the remaining objects, De Breuck et al. (2010) derived the stellar masses assuming a maximally old stellar population. While such estimates are reasonable, they may slightly over-estimate the masses (for a detailed discussion, see Seymour et al. 2007). To remedy this, Drouart et al. (2016) combined the *Spitzer* data with existing optical and near-IR photometry on a sub-sample to perform a multi-component SED fitting through population synthesis. In cases of overlap, we use the stellar masses derived by Drouart et al. (2016). The paper from which each mass estimate is taken is indicated in Table 3.5.

3.5 Relationship between radio galaxies and their supermassive black holes

We can now compare the relative growth rates of both galaxies and their central supermassive black holes, using estimates of the star-formation rates and the mass accretion rates, respectively. Such an investigation addresses the question of how galaxies and black holes evolved to the black hole mass-bulge mass relation we observe locally (Magorrian et al. 1998; Gebhardt et al. 2000; Ferrarese & Merritt 2000; Häring & Rix 2004). We have already discussed this issue for radio galaxies in Drouart et al. (2014), so we only briefly highlight how our results reinforce the conclusions of that paper. The differences between our approach and the one of Drouart et al. (2014) are detailed in Section 3.4.4. Other than these differences, we follow the analysis of Drouart et al. quite closely, e.g., we use the same conversion factors between IR luminosities and SFR and AGN accretion rates, and a very similar SED to determine the AGN luminosities (see Fig. 3.1 and 3.2 for a direct comparison).

3.5.1 Determining growth rates of star-formation and SMBH

To estimate the star formation rates of galaxies, we use the conversion factor from Kennicutt (1998b):

$$\mathrm{SFR} = 1.72 \times 10^{-10} \times \mathrm{L}_{\mathrm{SF}}^{\mathrm{IR}}, \tag{3.4}$$

using a Salpeter (1955) IMF. For consistency when comparing the SFR with stellar masses from Drouart et al. (2014) and De Breuck et al. (2010), we divide these estimates by a factor of 1.5 to convert from a Salpeter IMF to a Kroupa IMF. Our new data and fitting have resulted in significantly lower star-formation rate estimates for some sources compared to Drouart et al.. If we only consider the 25 sources in common, the median star-formation rate as estimated by Drouart et al. is 760 $\mathrm{M}_{\odot}.\mathrm{yr}^{-1}$. The SFR for our sample span from about 40 to $\sim$2000 $\mathrm{M}_{\odot}.\mathrm{yr}^{-1}$ with a median[3] value of 110 $\mathrm{M}_{\odot}.\mathrm{yr}^{-1}$ (Table 3.5). Our star-formation rates are 7 times lower than previously estimated by Drouart et al. for the same sources.

To convert $\mathrm{L}_{\mathrm{AGN}}^{\mathrm{IR}}$ to black hole accretion rate $\dot{\mathrm{M}}_{\mathrm{BH}}^{\mathrm{acc}}$, we follow Drouart et al. (2014):

$$\kappa_{\mathrm{AGN}}^{\mathrm{Bol}} \times \mathrm{L}_{\mathrm{AGN}}^{\mathrm{IR}} = \epsilon \dot{\mathrm{M}}_{\mathrm{BH}}^{\mathrm{acc}} c^2, \tag{3.5}$$

where the efficiency factor $\epsilon = 0.1$ and the bolometric correction factor $\kappa_{\mathrm{AGN}}^{\mathrm{Bol}} = 6$. We refer to Drouart et al. (2014) for a more detailed discussion. A large fraction of the sample lies above the one-to-one line between the $\mathrm{L}_{\mathrm{SF}}^{\mathrm{IR}}$ and $\mathrm{L}_{\mathrm{AGN}}^{\mathrm{IR}}$, showing that the FIR emission from the SF component is generally much weaker than the luminosity of the AGN. This is consistent with other samples of powerful AGN (e.g., Netzer et al. 2014, 2016; Stanley et al. 2015)

[3]the medians were estimated using a Kaplan-Meier estimator (Feigelson & Nelson 1985).

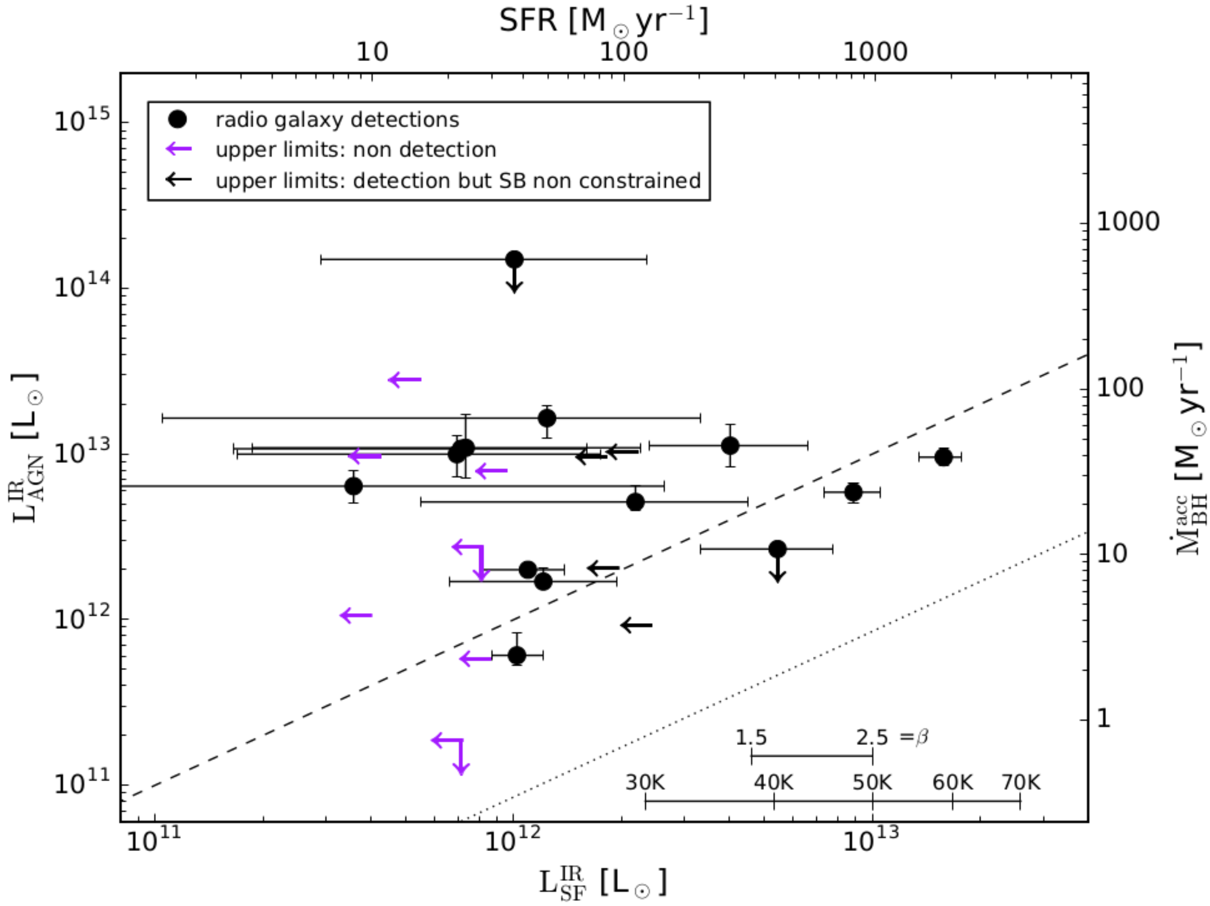

FIGURE 3.4: The estimated AGN luminosity, L^{IR}_{AGN}, versus the SF luminosity, L^{IR}_{SF}. The dashed black line indicates the values where $L^{IR}_{AGN} = L^{IR}_{SF}$, while the dotted black line indicates parallel growth of the stellar mass and black hole mass, $\dot{M}^{acc}_{BH}$=0.002×SFR. Filled black circles are galaxies detected with ALMA and with constrained SF and AGN luminosity estimates. Purple arrows are sources with upper limit in the ALMA band. The upper limits of L^{IR}_{SF} are approximated by scaling a modified black body to the 3-σ upper limit estimated assuming β=2.5 and T=50 K. We note that we assumed β=2.5 for all of our fits and 50 K is approximately the medium temperature of our best fits (Table 3.5). Black arrows indicate galaxies which are detected in ALMA but where the observed ALMA flux(es) are consistent with an extrapolation of the lower frequency synchrotron emission implying little or no contribution from thermal dust emission. We indicate with bars in the lower right corner of the plot, how the upper limits of the L^{IR}_{SF} would shift if one of the fixed parameters, β or T, are changed with respect to our assumed values of $\beta = 2.5$ and T=50 K.

3.5.2 Relative growth rates of galaxies and SMBHs

What are the relative growth rates of the stellar and black hole mass? To make this comparison, we simply scale the IR luminosities of each component as just described. If the galaxies evolve along the local relation, we would expect the accretion rate, $\dot{M}_{\rm BH}^{\rm acc}$, to be about $\sim$0.2% of the SFR (we chose 0.2% to be consistent with Drouart et al. and is within the uncertainty of estimates in the literature at the time; see Kormendy & Ho 2013). Of course, there are many assumptions that must be made in order to use these relations and one should be aware that the empirical relation is really between integrated IR luminosities, $L_{\rm SF}^{\rm IR}$ and $L_{\rm AGN}^{\rm IR}$, with scaling factors. Nevertheless, we find that our sample lies more than an order of magnitude above the local parallel growth relation of 0.2% (Fig. 3.4). This suggests that the black holes can become overly massive relative to their host galaxies if the accretion time spans the same time scale as the star formation. In fact, given that the host galaxies are already massive, it is likely that this implies that the SMBHs are overly massive at the epoch they are observed.

In Drouart et al. (2014), we argued that for the growth of the host galaxy and SMBH to ultimately be consistent with the local relation, the on-going star formation would have to last about a factor of 8 longer than the observed level AGN activity. Shifting $L_{\rm SF}^{\rm IR}$ downwards by about a factor of 7, now implies that the star formation must last over a factor of 50 longer. If the lifetime of the radio loud phase is $\sim$25 Myrs (Martini & Weinberg 2001; Schmidt et al. 2017), this would suggest that the star formation has to last more than a Gyr. Since we predominately have upper limits for the star formation rates of the majority of the galaxies, this appears unlikely. There is evidence at high redshift that perhaps SMBHs are already overly massive compared to their host galaxies, where overly massive means that they do not have the local value of the black hole mass to spheroidal mass ratio (e.g., Nesvadba et al. 2011; Wang et al. 2013; Willott et al. 2015; Trakhtenbrot et al. 2015; Shao et al. 2017; Vayner et al. 2017, but see Willott et al. 2017). Thus, the time required for the stellar mass to "catch up" to the mass of the SMBH is actually much longer than we have estimated here. Our new results therefore exacerbate the problem already discussed in Drouart et al. that it appears difficult for the mass ratio of the SMBH and the spheroidal component of the radio galaxies to fall on the local relation through star formation. We caution however that the average black hole accretion rates over longer time scales of star formation are not well constrained by the relatively instantaneous estimates provided here and in Drouart et al. (Hickox et al. 2014; Stanley et al. 2015; Volonteri et al. 2015b).

3.5.3 Keeping up with rapid SMBH growth

The host galaxies of HzRGs need to catch up with the growth of the SMBH, as they appear to be already overly massive. In order to end up on the local mass relationship, the stellar component needs to grow through a mechanism that does not fuel substantially the supermassive black hole. In the following sections, we discuss the possibility of growth by mergers as a way to explain how the sample of high-z galaxies in our study can evolve on to the local relationship.

Growth through major mergers

High redshift powerful radio galaxies like the ones studied here are found in environments which are over-dense (e.g., Wylezalek et al. 2013; Hatch et al. 2014; Dannerbauer et al. 2014; Cooke et al. 2015, 2016; Noirot et al. 2016, 2018). In such environments, mergers are likely an important mode of galaxy growth. However, a few caveats must be kept in mind when considering galaxy mergers as the mechanism allowing galaxies and SMBHs of powerful radio galaxies to evolve onto the local mass relation. The first requirement is that mergers do not bring substantial amounts of gas to grow the SMBH significantly compared to the mass of the accreted stars. Major mergers, which may increase the stellar mass considerably, would have to be gas poor galaxies as major mergers can carry gas efficiently to small scales (kpc-scales) through dissipation which may lead to significant black hole growth. Generally, massive galaxies at high redshift, those that would constitute major mergers for radio galaxies, are gas-rich (e.g., Bolatto et al. 2015; Noble et al. 2017; Emonts et al. 2018). So unless massive galaxies within the over-dense environments of radio galaxies are particularly gas poor (see e.g., Emonts et al. 2014; Lee et al. 2017; Dannerbauer et al. 2017; Emonts et al. 2018) then major mergers do not appear to be particularly favored for growing the stellar content of radio galaxies. Having said that, the quenching time of moderately massive galaxies in clusters is likely a small fraction of the Hubble time (e.g., Muzzin et al. 2012; Foltz et al. 2018) but with reduced efficiency with increasing redshift (Nantais et al. 2016, 2017). The second significant problem with major mergers as the driver of the stellar growth is that the merging galaxy likely also contains a supermassive black hole. In the early universe, the merger partner may have a black hole that is massive relative to the mass of its host (e.g., Willott et al. 2015). After the merger has advanced to the coalescence stage of the merger, which occurs in a few dynamical times of the most massive galaxy, the black holes will merge in less than a Hubble time ($\lesssim$1 Gyr for $M_{\star}\sim10^{11}$ $M_{\odot}$, which is approximately the stellar masses of our galaxies; Berczik et al. 2006; Merritt et al. 2007) A final, but perhaps less important limitation in such a picture is that the relative velocities of the merging galaxies should be relatively low, of-order the internal dynamical velocity of the stars in the most massive galaxy. Thus, relative low speed encounters are favored for efficient merging. In the over-densities surrounding the high redshift radio galaxies, the dispersion of the most massive galaxies in the potential appears to be high (Kuiper et al. 2011; Noirot et al. 2018).

Growth through minor mergers

Minor mergers may be an effective way to allow the mass of old stellar populations to grow in massive galaxies without fueling significant SMBH growth. There are several pieces of evidence that suggest hypothesizing that minor mergers contributed significantly to the stellar mass growth of massive galaxies. High resolution imaging suggests that there may be low mass galaxies in the surroundings of some radio galaxies (Miley et al. 2006; Seymour et al. 2012). So the potential merging sources are close at hand. Beyond just the necessary association of low mass galaxies, there are a number of lines of evidence that support the notion that massive early-type galaxies grew substantially through minor mergers. Some of these are: *(1)* the size evolution of massive galaxies in the early Universe to the present may be driven principally through minor mergers (e.g., Daddi et al. 2005; van Dokkum et al. 2008; Delaye et al. 2014; Vulcani et al. 2016; Hill et al. 2017); *(2)* the change in the mass and luminosity function of galaxies with redshift and as a function of environment (e.g., Ilbert et al. 2013; Sarron et al. 2017); *(3)* the elemental abundance ratios, abundance gradients, and age gradients in the outer regions of local massive spheroids are consistent with accreting galaxies with a range of masses, perhaps predominately low mass, which had their star formation truncated early in their growth (Huang et al. 2013; Greene et al. 2013; Barbosa et al. 2016); and *(4)* the mass of massive early-type galaxies grew by about a factor of 4 over the last $\sim$10 Gyr (e.g., van Dokkum et al. 2010; Ilbert et al. 2013).

Interestingly, Hill et al. (2017) identified the epoch at which the stellar growth of very massive galaxies, $M_{\star}\gtrsim10^{11.5}$ $M_{\odot}$, transition from growing substantially through star formation to one where mergers dominate the stellar mass growth. This is at the low redshift end of the objects in our study but is overall consistent with the quenching we observe. Moreover, at the average redshift we are observing our sample, they also find a factor of 3 increase in the stellar mass, which again is similar to what is needed to close the gap between the mass of the supermassive black holes and the host galaxies (see also van Dokkum et al. 2010; Vulcani et al. 2016). Both the fossil record in nearby massive galaxies and their *in situ* evolution suggest that minor mergers played a role in their stellar mass growth and physical properties (e.g., Greene et al. 2013; Hilz et al. 2013; Laporte et al. 2013; Hirschmann et al. 2015).

A comparison with BCGs and X-ray-selected AGNs

Radio galaxies lie in over-densities and have been suggested to be progenitors of brightest cluster galaxies (BCGs; Hatch et al. 2014), a more relevant comparison is not with the general properties of massive galaxies but the stellar mass growth of BCGs. Statistical samples of BCGs are limited to redshifts lower than about 1 which is lower than the median redshift of our sample, z∼2.4. Results from these studies suggest that BCG typically grew by about a factor of 2 over the last 8-10 Gyrs (Aragon-Salamanca et al. 1998; Bellstedt et al. 2016). Overall, these growth rates are consistent with semi-analytic models which indicate that, since about z∼1-1.5, BCGs grew by about a factor of 2-4 (De Lucia & Blaizot 2007; Tonini et al. 2012). However, any theoretical result explaining the growth of BCGs is sensitive to the treatment of dynamical friction and tidal stripping through galaxy-galaxy interactions as galaxies move through the cluster potential (e.g., Shankar et al. 2015). We conclude that if some of the galaxies in our sample are destined to become BCGs, then our overall current understanding of the stellar growth of these massive clusters galaxies is consistent with closing the difference in relative masses of the supermassive blackholes and their host galaxies.

Other samples, such as X-ray selected AGN, show a range of relative growth rates of SMBH and host galaxies. Some studies, like those that select star forming galaxies and then investigate their black hole accretion rates (using amount of X-ray emission observed above that expected that due to galaxy stellar populations) and SFR, find that black holes and galaxies are growing in lock-step (e.g, Delvecchio et al. 2015). Similarly, some studies of X-ray selected AGN with a wide range of AGN bolometric luminosities that black holes and galaxies grow in lock-step (z∼2, e.g., Mullaney et al. 2012). But such results are not found universally. Netzer et al. (2016), again for an X-ray selected sample of AGN, but now at somewhat higher redshifts than previous studies, find that SMBHs are growing more rapidly on average than their hosts. Cisternas et al. (2011) find that there is no evolution in the black hole-to-galaxy mass ratio out to z∼1, except perhaps for high mass black holes where black holes are overly massive relative to their host galaxies. Could the variety of results be simply due to the mass of both the galaxy and the SMBH (Cisternas et al. 2011)?

3.6 SFR and Main Sequence Comparison: On the road to quenching

The main sequence of star-forming galaxies – the empirical relation between the star-formation rate and stellar mass with a slope of approximately 1 and a scatter of about a factor of 2 – has been studied extensively both theoretically and observationally (the MS, e.g., Brinchmann et al. 2004; Noeske et al. 2007; Elbaz et al. 2007; Daddi et al. 2007; Santini et al. 2009, 2017; Peng et al. 2010; Whitaker et al. 2012; Stark et al. 2013; Speagle et al. 2014; Lehnert et al. 2015; Davé et al. 2016; Lee et al. 2018; López Fernández et al. 2018; Davidzon et al. 2018). The relation is observed over a wide redshift range, z∼0-7, and its normalization increases with increasing redshift. The MS has often been parameterized as a simple power-law but there has also been evidence that the MS flattens at higher stellar masses (e.g, Whitaker et al. 2014; Lee et al. 2015; Tasca et al. 2015; Schreiber et al. 2015; Tomczak et al. 2016; Lee et al. 2018). The slope of the MS and the turnover mass in the case of a flattening MS depend on the sample selection, redshift range and the technique used to determine the stellar mass and SFR. The estimated turnover stellar mass is $\sim 10^{10}$-$10^{10.5}$ $M_\odot$ (e.g., Schreiber et al. 2015). The MS can be used to study and classify galaxies according to their relative SFR, where large deviation from the MS suggests that galaxies are "starbursts" if they lie above the MS, or quenched, if they fall below the MS. The definition of whether a galaxy is a starburst or is quenched varies in literature, but is often taken as either offset by more than 3 times the scatter or a factor of 10 above or below the mean relation (e.g., Rodighiero et al. 2011). We now compare our sample of HzRG with the MS and discuss what the implications are now

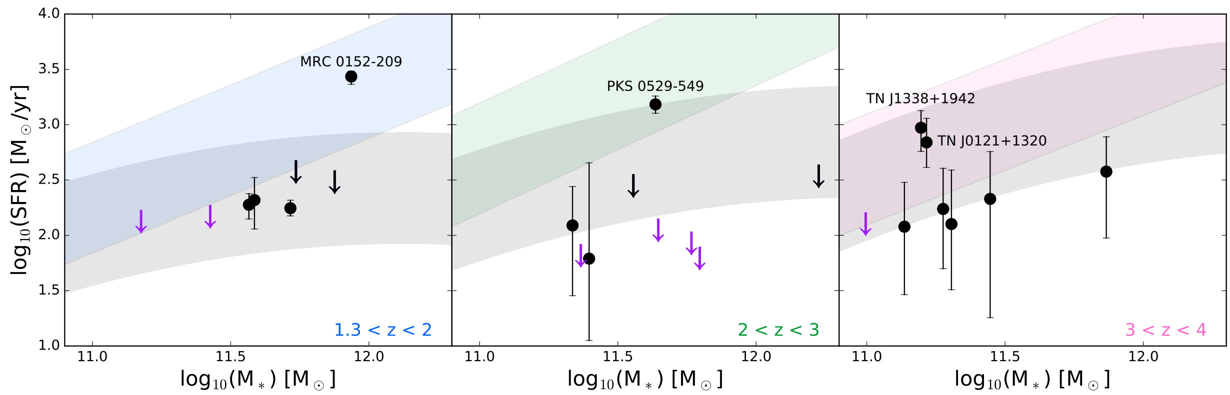

FIGURE 3.5: Relationship between the SFR and stellar mass for different redshift bins. The colored shaded regions shows the MS of (Santini et al. 2017) for each respective redshift bins with a 0.3 dex scatter around the MS. The gray shaded regions shows the MS with a 0.3 dex scatter from Schreiber et al. (2015), with a turnover at higher stellar masses. Our stellar masses have been scaled from a Kroupa to a Salpeter IMF to be consistent with the IMF used to make the MS in this comparison. In the highest redshift bin, $3 < z < 4$, two sources, TN J1338+1942 and TNJ0924-2201, have been added to the right most panel despite having redshifts outside of the range used to construct the MS (z=4.110 and 5.195 respectively). Given the redshift dependence on the normalization of the MS, these galaxies may lie relatively lower in comparison with the mean relation of a MS derived using galaxies over a more appropriate, higher redshift range (see Fig. 3.6).

that we include spatially-resolved FIR ALMA data and account for possible contamination from synchrotron emission.

3.6.1 Comparison with the MS and impact of submm spatial resolution

Our sample of radio galaxies has a wide range of relative SFR compared to galaxies which lie along the MS (Fig. 3.5; Schreiber et al. 2015; Santini et al. 2017). Unfortunately, the number of possible MS parameters such as slope, zero-point, and whether or not the MS was fitted with a turnover at high stellar masses makes a direct comparison with our results challenging. To make matters worse, there are additional potential differences in the methods and wavelength range used to estimate stellar masses and SFR, the range of stellar masses studied, and, for consistency with the broad redshift range of our sample, the redshift range that any individual study covered. For example, Santini et al. (2017) redshift span of $1.3 < z < 6$ and stellar mass range,$\sim 10^{7.5}$-10^{11}M$_{\odot}$. Our masses are generally higher than their upper mass limit. Schreiber et al. (2015) span stellar masses from $\sim 10^{9}$ to $10^{11.3}$ M$_{\odot}$, which makes their mass range comparable to the radio galaxies in our sample. Unfortunately, their redshift range is rather limited, $0.5 \leq z \leq 2.5$, for making a robust comparison with our sample difficult. Of course, these limitations are purely observational depending on the depth and area covered by the surveys from which these results are derived. Our HzRG sample consists of the rarest, most massive galaxies selected from all sky radio surveys. HzRGs thus allows us to extend MS studies to the most massive end of the galaxy mass distribution, and as now discussed, our comparison suggests that the HzRGs in our sample fall either on or below the star-forming MS (Fig. 3.5).

We first compare our results with the MS from Schreiber et al. (2015) (gray regions in Fig. 3.5), covering $0.5 < z < 4$ and for M$_*$=$10^{11.33}$ M$_{\odot}$, close to the mean stellar mass of $10^{11.35}$ M$_{\odot}$ of our sample. In comparison to Schreiber et al. (2015), who fits a turnover in the MS at high stellar masses, we find 2 sources lie above, 14 sources lie within the 0.3 dex scatter of the MS, and 9 lie below the MS. We note however, that 3 of the sources that lie along the MS have only upper limits in their estimated SFR. In addition, 2 sources have uncertainties in their SFR estimate, which give them a significant probability of lying below the MS. All of these sources could well lie below the MS. Thus, in comparison with the results of Schreiber et al. (2015), we find that the galaxies in our sample generally fall below the main sequence.

Since Schreiber et al. fit their data in the SFR-stellar mass plane with a function that has a turnover, comparing our results with a study that does not allow for such a turnover, may result in a change in how we characterize our results. We therefore also compare our results with the MS from Santini et al. (2017), which does not include such a turnover (colored regions in Fig. 3.5). We again find that our HzRG sample significantly lies below the MS. None of our sources lie above the MS of Santini et al. (2017), 6 sources lie along the MS, 5 sources lie at at the lower ± 0.3 dex boundary, and 6 sources lie below. The remaining 7 sources have upper limits in SFR, and may well lie below the MS of Santini et al. (2017). At any rate, the comparison with both Schreiber et al. (2015) and Santini et al. (2017) suggest that many of our sample galaxies lie below the MS and are consistent with being quenched.

Three out of the four galaxies with the highest SFR in our sample and which lie on or above the MS, TN J0121+1320, MRC 0152-209, PKS 0529-549, and TN J1338-1942, have morphological features in the ALMA continuum suggesting that perhaps they might be mergers (we indicate these four sources by name in Fig. 3.5 to highlight the fact that they are high in the SFR-stellar mass plane compared to the other galaxies in our sample). The Dragonfly galaxy, MRC 0152-209, has two clearly interacting mm components. Indeed, for this source there is strong evidence that the dynamics of this system are consistent with a strong interaction of 3 components with significant mass transfer between them (Emonts et al. 2015b,a). Both TN J0121+1320 and PKS 0529-549 have elongated shapes which are different from the synthesized beam, which in analogy with the Dragonfly galaxy, is consistent with them being mergers. We would need (sub-)mm line kinematics and continuum morphology at higher resolution to know definitively whether or not they are mergers. TN J1338-1942 is unresolved in our data and, within this criterion, is not consistent with being a merger.

We can also compare the sSFR our sample with that of the ensemble of star-forming galaxies as a function of redshift (Fig. 3.6). Just as with our comparison with main sequences at various redshifts, we find that a large fraction of our sample falls below the main sequence and its evolution. To be conservative, we made this comparison with the MS evolution estimated in Schreiber et al. (2015), which includes a turnover in their fitting of the MS. Even though the galaxies are massive and lie above the mass at which the turnover starts and the MS flattens, our galaxies generally lie below. Of course, if we used main sequences that do not allow for a turnover in the stellar mass-SFR relation, then the difference between our sources and the evolution of the MS at constant mass would be even more dramatic. We note that since the slope of the MS is about 1 and if there is no flattening in the MS at high stellar masses, then the exact mass used for comparison with the radio galaxies is not particularly important.

Our results are different from previous studies. In previous studies massive high redshift radio galaxies have often been associated with high BH accretion rate combined with high SFR because they are extremely luminous in both the mid-IR (Ogle et al. 2006; Seymour et al. 2007; De Breuck et al. 2010) and the sub-mm (Archibald et al. 2001; Reuland et al. 2003a; Stevens et al. 2003). Not surprisingly given the sensitive upper limits or finding that synchrotron emission may dominate the emission at mm wavelengths, our star formation rate estimates are lower than those found by other studies. On the other hand, our results on the AGN-heated dust luminosity are consistent with previous studies, which is not surprising given that we are using the same or similar data. Our finding that HzRGs fall mainly along or below the MS is therefore new. Most of the sources lying below the MS relation are non-detections in the ALMA band, and often not detected in the SPIRE bands either. These galaxies have very low SFR and are an order-of-magnitude weaker then what was previously estimated. These galaxies are not star forming, they are on their way to being quenched.

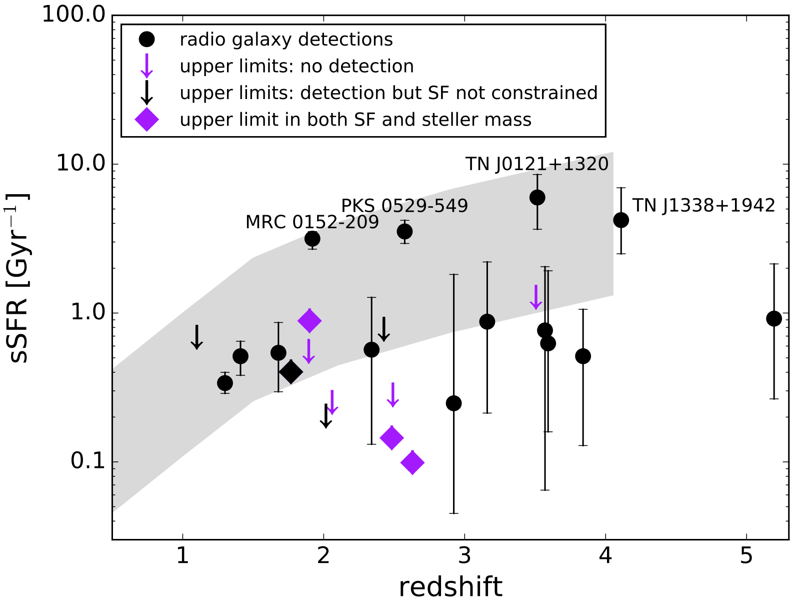

FIGURE 3.6: Specific star formation rate, sSFR (Gyr^{-1}), as a function of redshift. The black filled circles, black arrows and purple arrows represent the radio galaxies of our sample that are detected, detected but with unconstrained SF component and undetected with ALMA, respectively. The diamonds indicate sources which have both upper limits on the stellar mass and the SFR. The shaded region shows the galaxy main sequence (adapted from Schreiber et al. 2015) for $M_*=10^{11.33}$ $M_\odot$. We only indicate the redshift range $0.5 < z < 4$ in the shaded region as z=4 is the redshift limit of the objects studied in Schreiber et al.. We do not extrapolate to higher redshifts (Stark et al. 2013).

3.6.2 Comparison with X-ray selected high redshift AGNs

Naturally, given the importance of understanding the relation between the growth of the stellar population of galaxies and the influence of AGN, it is useful to compare our results for the star-formation rates of powerful high redshift radio galaxies with those of other types AGN. Within the perspective of the overall population of AGN, it is not clear exactly what the role of the AGN is in quenching the star formation. We find that many of our sources do not currently have significant star formation. Our upper limits, constraining the median SFR to be ~100 $M_\odot$.yr^{-1}, are also consistent with little or no star formation, especially for those sources with upper limits in the *Herschel* bands and (likely) only synchrotron emission in the mm. As we already discussed, the typical lifetime of AGN is of-order a few 10 Myrs. The IR and sub-mm thermal dust emission probes star formation, past and present, over timescales of 100 Myrs or more (i.e., comparable to a few internal dynamical times of the galaxies; Lehnert & Heckman 1996; Boquien et al. 2014, 2016). These differing timescales implies that unless the AGN are significantly longer lived than we currently understand them to be, the luminous or mechanical output from AGN is unlikely to be the sole mechanism for shutting down star formation in these galaxies.

We can perhaps understand this by comparing the results of studies of the AGN influence on the star formation within their hosts. In Fig. 3.7, we show such a comparison focusing on X-ray selected AGN from various studies (based on a similar figure in Netzer et al. 2016, but see also Rosario et al. 2012; Stanley et al. 2015, 2017 for earlier or different renditions of the same plot). Our galaxies lie at the upper end of the distribution of AGN luminosities and their total infrared luminosities are dominated by the emission from the AGN they host. Generically, our host galaxies are forming stars at a much lower rate on average than the X-ray selected AGN, at least for those that have well determined star formation rates. Netzer et al. (2016) found that if they stacked the X-ray selected AGN without detections in the infrared results in a much lower mean IR luminosity due to young stars. This stacked luminosity and the implied SFR is comparable to our sample. These final results may suggest that the key parameter in the difference in differential growth rates of actively fueled SMBHs is in fact is the luminosity of the AGN. All of our sources and those of Netzer et al. are among the most luminous at their respective redshifts.

Such an hypothesis would explain a wide range of results. If we focus on studies that sample a wide range of AGN bolometric or IR luminosities and estimated SFRs, the evidence points to both the AGN and galaxies growing in lock step (Mullaney et al. 2012; Rovilos et al. 2012; Delvecchio et al. 2015) and there is generally no widespread evidence for quenching (e.g., Harrison et al. 2012; Rosario et al. 2013; Stanley et al. 2017). However, one has to be cautious in these simple relations between galaxies being on the main sequence and the impact of AGN on their star formation rates. The effect of AGN on star formation rates may be subtle and may also influence the control sample of galaxies without active black holes. Scholtz et al. (2018) make the interesting point that the star-formation rate distribution at constant mass of galaxies with or without AGN is similar, and this result actually agrees with simulations. They suggest that the agreement between AGN and non-AGN in lying on the same relation in the SFR-stellar mass plane is because the impact of AGN is evident in both samples, and it is this effect that is driving the slope of decreasing sSFR with increasing mass (see also Mainieri et al. 2011). So the effect of AGN feedback is subtle, broadening distributions and not necessarily correlating with AGN power/luminosity as might be naively expected. In a study similar to ours, Mullaney et al. (2015) used ALMA observations of X-ray selected AGN, finding that the estimated SFRs were lower relative to previous findings. This reduction lead to AGN hosts having a different distribution than the star forming galaxy population, meaning the AGN population of star forming galaxies had a broader, and perhaps even offset distribution of star formation rates (Rovilos et al. 2012; Rosario et al. 2015).

3.6.3 A significant synchrotron contribution in submm

Our high resolution ALMA data allowed us to do component separation such that the contribution of synchrotron to the mm emission is now clear, originating from radio lobes and the nuclei. For 9 out of 25 sources, the best-fit SEDs of specific spatial components are consistent with a power-law extrapolation from radio frequencies. These spatial components are likely dominated by synchrotron emission. The total flux of 5 galaxies, not just the lobes, are associated with pure synchrotron emission and are consistent with no contribution from thermal dust emission. For 2 host galaxies, which have two spatially-resolved emission components in the ALMA band, the majority of the mm-flux is due synchrotron with only a minor contribution from thermal dust emission.

It is surprising to find our high frequency data is consistent with an extrapolation of the synchrotron intensities in the radio (Jaffe & Perola 1973; Carilli et al. 1991; Blundell et al. 2006). The energy loss though aging of the electrons and inverse Compton scattering should steepen the observed spectrum at higher frequencies. But what we see in a few sources is that the synchrotron spectrum continues straight out to high frequencies (e.g., Gopal-Krishna et al. 2001). One possible explanation is that the electrons are continuously accelerated within the lobes, perhaps through strong oblique shocks (e.g., Summerlin & Baring 2012). The details and analdysis of the radio spectra including ALMA synchrotron detections will be presented in a subsequent study.

3.6.4 Star formation and radio source sizes

The spatial separation of the emission from the radio lobes – the projected distance between the two lobes or between the core and lobes – can provide useful constraints on the nature of the AGN. The separation, if the sources expand at constant velocity, can be used as a proxy for the age of the radio source (e.g., Carilli et al. 1991). Larger sources correspond to older sources. A possible test

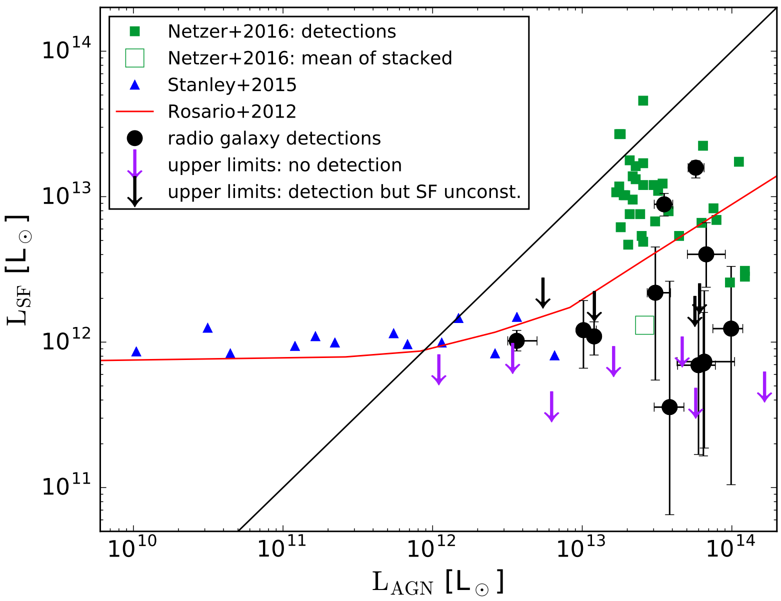

FIGURE 3.7: Comparison of our results in the L_{SF}–L_{AGN} plane to other studies. L^{IR}_{AGN} for our sample is scaled by a factor 6 to estimate the bolometric luminosity. Black circles indicate sources detected with ALMA. Black downward pointing arrows indicate sources detected in ALMA where the sub-mm flux is consistent with being dominated by synchrotron emission. Purple downward pointing arrows indicate sources not detected with ALMA. The X-ray selected sources from Netzer et al. (2016) detected with *Herschel* over the redshift range z=2-3.5 are indicated with green squares; the large open green square is the SFR of the undetected sources which were stacked to estimate their median SFR. Blue triangles indicate X-ray selected sources from Stanley et al. (2015) over the redshift range, $1.8<z<2.1$. The red line is the fit from Rosario et al. (2012) to the mean relation for AGNs over the redshift range $1.5<z<2.5$ scaled up by a factor of 2 (see Netzer et al. 2016, for details). We indicate when the luminosity due to star formation equals that of the AGN with a black solid line.

of a scenario where the AGN is the agent driving the quenching of star formation is that galaxies with the lowest star formation rates have the largest radio sources. In fact, we do see a possible trend between the largest angular size of a radio source and the predominance of upper limits to the star formation rates (Fig. 3.8). This trend is robust in the sense that high significance estimates of the SFR all appear below largest angular sizes of $\sim$3 arcsec. At the typical redshifts of our sources, this corresponds to approximately 10-15 kpc in radius, or about the expected extent of the interstellar medium of a massive galaxy. We do not have a sufficient number of sources or sensitive enough upper-limits to say that there is a correlation. Such a correlation would be interesting, as it would support a simple model of propagating jets that may enhance star formation when they are still confined within the host galaxy, but then quickly preventing further star formation after they break out.

Timescale arguments may also complicate the comparison between radio size and SFR. The duration of AGN activity is thought be around 10^7 to 10^8 yrs (e.g., Martini & Weinberg 2001; Hopkins et al. 2005; Schmidt et al. 2017). The star formation likely lasts much longer. Other than observing a proclivity for the upper-limits in the SFR to be associated with radio sources larger than the host galaxy proper, it may not be that surprising that we do not see a very clear correlation. There are several factors that may influence the rate at which radio jets expand into the surrounding media. Perhaps the most important is the environment into which the jets are expanding. For jets which propagate outwards into denser environments, the radio source may be confined and can either simply expand more slowly, or can decelerate (Shabala et al. 2017). There may not be a simple linear relationship for individual sources and they may not all take the same amount of time to reach the same size. There are also of course projection and beaming effects to consider. Since we observe a wide range of SFRs, radio morphologies, and lobe asymmetries in this sample (De Breuck et al. 2010), it is likely that the characteristics of the surrounding environments of the individual radio sources play a significant role in determining the scatter in this relation. Moreover, given that the star formation is expected to occur on time scales longer than the duration of the AGN activity perhaps not seeing a clear cut correlation is not unexpected, regardless of the processes that can influence radio source sizes and morphologies. Other effects may play a role since the galaxies in our sample with high SFRs, have morphologies consistent with being mergers (Sect. 3.6).

3.7 Possible interpretation of our results

Our interpretation of our results is that: *(i)* the quenching we observe for the majority of the sample is naturally explained by our galaxies predominately being at the high mass end of the galaxy population (Ilbert et al. 2013) and having very massive SMBHs (Nesvadba et al. 2011). We know that such galaxies in the local universe must be quenched rapidly and soon after their most substantial period of growth (e.g., Thomas et al. 2005, 2010). They also likely grew subsequently, after they are quenched, through the accretion of relatively low mass, likely gas-poor galaxies (e.g., Greene et al. 2013). Thus, we can say that their quenching is mainly a result of the fact that they are already massive only a few Gyrs after the Big Bang; and, *(ii)* given the fact that some of galaxies in the sample of high redshift radio galaxies have intense star formation and young stars (Dey et al. 1997, Man et al. 2018, in prep.), it is likely that star formation played a key role in quenching the host galaxies of distant radio galaxies. This is a natural conclusion, given that the AGN are likely only luminous for 10s of Myrs (Schmidt et al. 2017), which is generally shorter than we would expect bursts of star formation to last. Other samples of AGN with lower host masses have substantial outflows (e.g., Harrison et al. 2016), and are not generally quenched.

It is difficult to isolate the impact of mass and environment on the rate and timing of quenching. Mass quenching is more important at earlier times in the evolution of galaxies and may be more important in denser regions (e.g., Peng et al. 2010; Muzzin et al. 2012; Lee et al. 2015; Darvish

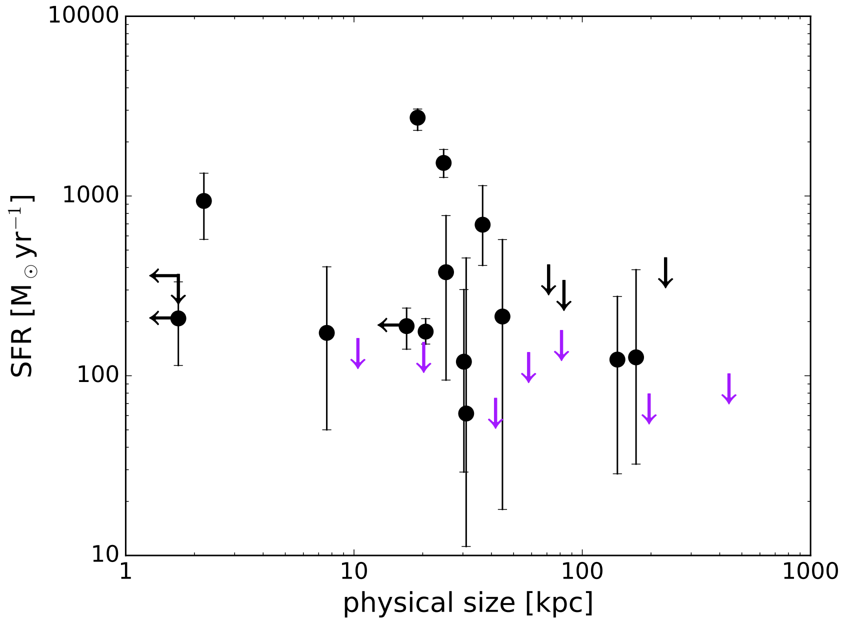

FIGURE 3.8: Star formation rate, SFR in $M_\odot.yr^{-1}$, versus the projected physical size of the radio emission in kpc, calculated using the largest angular size (LAS) of the radio emission at 1.4 GHz (De Breuck et al. 2010). Black filled circles are detections, black arrows detections but with unconstrained SF component and purple arrows non-detections (see text for details).

et al. 2016; Kawinwanichakij et al. 2017; Darvish et al. 2018). And in the case of powerful radio galaxies, which lie in over-dense environments, both gas-rich and gas-poor mergers likely play an important role in both the growth of the stellar mass and the black holes. Volonteri et al. (2015a) suggest that in the merger phase, the AGN dominates the bolometric luminosity but the accretion can be very stochastic (see also Gabor & Bournaud 2013; DeGraf et al. 2017). It appears that the galaxies in our sample with the highest star-formation rates all host very powerful AGN, and are potentially all advanced mergers, consistent with this picture. In fact, PKS 0529-549, which has one of the highest SFRs of all the galaxies in our sample, has a modest gas fraction of about 15%, a high star-formation efficiency (SFR/molecular gas mass), and has been transforming its gas into stars rapidly (Man et al., in prep.). The star formation efficiencies in the other radio galaxies with high SFRs also appear extreme (10-100 Gyr^{-1}; Man et al.). But of course, that does not explain our results in themselves. Dubois et al. (2015), in a study using numerical simulations of the relative growth of SMBHs and their host galaxies, found that star formation may regulate the black hole accretion rate. During the most rapid, gas-rich phase of the growth of massive galaxies, it may be that a larger fraction of the gas in the ISM is not available to fuel the SMBHs, but is consumed via star formation (see DeGraf et al. 2017). As the gas fractions decline, the relative power of the AGN compared to that of the star formation increases, resulting in an increased star formation efficiency. Concomitantly, the increased star formation rate can then disperse the dense gas making it easier for the jets to drive vigorous and efficient outflows (Nesvadba et al. 2006, 2017).

So we suggest that mass is the primary difference in the characteristics of our sample of galaxies compared to other samples of AGN (see also Mainieri et al. 2011; Stanley et al. 2017). This difference makes it then much easier for the AGN to dominate the bolometric output as the SMBHs in massive galaxies may be "overly" massive for their host masses. Even relatively low accretion rates would lead to powerful AGN emission. The mechanical and radiative output from the young massive stars, heats the interstellar medium, changes its phase distribution, and puffs it up. In such a state, the coupling between the mechanical energy of the jet and heated and expanded interstellar medium of the galaxy, would be high (Biernacki & Teyssier 2018). This leads to a positive feedback loop at the end of the most rapid growth phase of massive galaxies where the residual gas of star formation is rapidly removed through the action of the AGN, leading to the rapid session of star-formation. The galaxy is on the road to being quenched.

3.8 Conclusions

With 0.3″ resolution mm ALMA data, and utilizing the new SED fitting tool, MrMoose, we have estimated L^{IR}_{SF} and L^{IR}_{AGN}. We have disentangled the IR luminosity into components heated by the stellar populations and that heated by the luminous AGN that reside in these host galaxies. With our deep ALMA observations, we reach depths at which we expect the thermal dust and synchrotron contributions to the mm emission to be of the same order-of-magnitude. This high sensitivity is the reason why it is essential to disentangle both spectrally and spatially the contribution from the high frequency synchrotron emission at (sub-)mm wavelengths. From a study of 25 powerful high redshift radio galaxies, our main conclusions are:

- We find that the SFRs are lower than previously estimated, having a median which is ∼7 times lower (cf. Drouart et al. 2014). This is a result of having deep ALMA data enabling us to estimate robust upper limits, to disentangle several emission components, and determine if the mm emission represents the high frequency end of the power-law extrapolation of the radio emission. We interpret any flux density estimate that is consistent with the power-law extension from the radio to the (sub-)mm as synchrotron emission, and not as dust heated by young stars.

- Unlike many studies of high redshift AGN, we find that a large fraction of our sources do not lie within the scatter of the relation between the stellar mass and the star-formation rate of star forming galaxies (the "main sequence"). Since the deviation of the radio galaxies with upper limits does not meet the general criterion for quenched galaxies, we interpret such galaxies as being "on their way to being quenched".

- Finding lower star formation rates generally exacerbates the problem of differential growth between the black hole and the host galaxy discussed by Drouart et al. (2014). This favors a scenario where the host galaxies ultimately grow by dissipationless merging which adds additional stellar mass without increasing significantly the mass of the black hole. We find that at the typical specific star-formation rates we estimate for the host galaxies, the host galaxy needs ∼50 times longer than the time over which the SMBH is active to "catch up" to having the local ratio of black hole mass to stellar mass.

- There is no clear relation between the radio size and SFR, although we note that the upper limits on the star formation rate tend to be in sources where the LAS is larger than ∼3 arcseconds. However, given that the star formation is expected to occur on time scales of the same order or longer than the duration of the AGN activity (10^7 to 10^8 yrs) perhaps not finding a clear cut correlation is not completely surprising even if the radio jets are driving the quenching we observe.

From these results, we suggest that mass is the primary difference in the characteristics of our sample of galaxies compared to other samples of AGN. The host galaxies of our sample of radio galaxies are generally more massive and likely harbor high mass black holes than AGN selected using other methods. Hosting more massive black holes means that it is also easier for the AGN to dominate the bolometric output of the galaxy, even if it forming stars vigorously. In order to comprehend how the host galaxies are quenching so rapidly, we hypothesize a positive feedback loop between the AGN and star formation. The star formation leads to rapid gas depletion and its intense energy input heats the remaining gas allowing the interaction between the gas and jets to be efficient. The AGN then blows away the residual gas at the end of the star formation episode. It is in this way perhaps that the host galaxies of powerful high redshift radio galaxies are "on the road to being quenched".

Acknowledgements

M.D.L. wishes to thank the ESO visitors program for its continued support and Marta Volonteri and Gary Mamon for fascinating discussions. T.F. acknowledges financial support from ESO and INSU/CNRS for this work. T.F., C. De B. and M. D. L. thank Joe Silk for interesting suggestions and analysis and an anonymous referee for their constructive criticisms and suggestions. BG acknowledge support from the ERC Advanced Programme DUSTYGAL (321334) and STFC (ST/P0000541/1). This paper makes use of the following ALMA data: ADS/JAO.ALMA#2012.1.00039.S, ADS/JAO.ALMA#2013.1.00521.S, ADS/JAO.ALMA#2015.1.00530.S, and ADS/JAO.ALMA#2012.1.00242.S. ALMA is a partnership of ESO (representing its member states), NSF (USA) and NINS (Japan), together with NRC (Canada), NSC and ASIAA (Taiwan), and KASI (Republic of Korea), in cooperation with the Republic of Chile. The Joint ALMA Observatory is operated by ESO, AUI/NRAO and NAOJ. The Australia Telescope is funded by the Commonwealth of Australia for operation as a National Facility managed by CSIRO. The authors wish to express their sincerest thank you to the staff of the CSIRO for their assistance in conducting these observations and the program committee for their generous allocation of time and continuing support for our research. The National Radio Astronomy Observatory is a facility of the National Science Foundation operated under cooperative agreement by Associated Universities, Inc.

Chapter 4

ALMA and MUSE reveal a quiescent multi-phase halo probing the CGM around the z$\simeq$3.6 radio galaxy 4C 19.71

To be submitted to A&A

Abstract

We present VLT/MUSE imaging spectroscopy of rest frame UV emission lines and ALMA observations of the [C I] $^3P_1$-$^3P_0$ emission line, probing both the ionized and diffuse molecular medium around the radio galaxy, 4C19.71, at z$\simeq$3.6. The radio galaxy has extended Lyα emission over a region $\sim$100 kpc in size preferentially oriented along the axis of the radio jet. Faint Lyα emission extends beyond the southern hot spot. We find even more extended C IV emission over a region of $\sim$150 kpc in size where the most distant extension which lies $\sim$40 kpc beyond the north radio lobe and has narrow line widths FWHM$\sim$180 km s^{-1} and a small relative velocity offset Δv$\sim$130 km s^{-1} from the systemic redshift of the radio galaxy. [C I] is detected in the same region with FWHM$\sim$100 km s^{-1} and Δv$\sim$5 km s^{-1}. We interpret this as evidence of quiescent multi-phase gas residing within the halo at a projected distance of $\sim$75 kpc from the host galaxy. To test this hypothesis, we performed photo-ionization/photo-dissociated region modeling with the code Cloudy which suggest that the [C I]/C IV $\lambda\lambda$1548,1551 and C IV $\lambda\lambda$1548,1551/He II ratios are consistent with a PDR/ionization front in the circum-galactic medium likely energized by photons from the AGN. This modeling is consistent with a relatively low metallicity, log [Z/Z$_\odot$]~ -1.5 to -2, and diffuse ionization with an ionization parameter (proportional to the ratio of the photon number density and gas density), log U~ -3. Our observations have limited signal-to-noise ratios and contain few diagnostic emission lines so our modeling results are only suggestive, but doing this analysis allows us to illustrate the potential quantitative power for understanding the physical characteristics of the circum-galactic gas with multi-wavelength integral field observations of halos hosting active galactic nuclei.

4.1 Introduction

The circum-galactic medium (CGM) has in recent years gained importance for galaxy evolution, since it is believed to control the gas supply of the galaxy. It is the place where gas from the galaxy is recycled and where new gas is accreted through streams from the intergalactic medium. The CGM is very diffuse and challenging to observe, especially in direct emission. New instruments such as MUSE, PCWI and KCWI made advances towards observing the spatial extent of the CGM in emission from ionized gas. Extended Lyα haloes have recently been observed with MUSE around a large fraction of star-forming galaxies at redshifts 3$\leq$z$\leq$6 in the Hubble Deep Field South (Wisotzki et al. 2016; Leclercq et al. 2017). Extended Lyα haloes have also shown kinematic signs suggesting large-scale rotation of accreting material (Prescott et al. 2015) and a filamentary structure (Cantalupo et al. 2014). Arrigoni Battaia et al. (2018) observed an enormous Lyα nebula around a radio-quiet quasar at z=3.164 with MUSE, spanning $\sim$300 kpc and showing accretion of substructures onto the host quasar. With MUSE it is now possible to characterize the physical properties of the CGM around galaxies. Observations have shown spectacular extended ionized regions around quasars and star-forming galaxies.

High-redshift radio galaxies (HzRGs) have also been shown to be embedded in extended gaseous halos, often reaching out to >100 kpc from the nucleus (e.g. van Ojik et al. 1997; Reuland et al. 2003b; Swinbank et al. 2015). They are detected in strong emission lines from Lyα to Hα. HzRGs are among the most massive $M_{\star}>10^{11}M_{\odot}$ (Seymour et al. 2007; De Breuck et al. 2010) and luminous galaxies in the Universe. They have high AGN accretion and star-formation rates (SFRs), as well as bright and steep synchrotron spectra (Archibald et al. 2001; Reuland et al. 2003a; Drouart et al. 2014). This makes HzRGs unique markers of massive galaxies. Together with their edge-on orientation, they provide the only test beds to study the growth of both the host and the AGN in situ, as well as the interaction of the radio jet with the surrounding CGM. In MRC 0316-257, low surface brightness Lyα emission has been identified, with arc-like morphologies arising at 150–250 kpc from the core. These structures have been interpreted as inflows along filaments (Vernet et al. 2017, see also Gullberg et al. 2016a for another source similarly interpreted). Previously, long slit spectroscopy of HzRGs had shown very extended low surface brightness Lyα halos (in some cases also seen in C IV, He II and [N V]; Villar-Martín et al. 2003), showing that quiescent ionized gas exists beyond the radio lobes.

The CGM around HzRGs can also contain large extended, $\sim$70-100 kpc, reservoirs of molecular gas which has been detected in [C I] $^3P_1$-$^3P_0$, CO(1–0), CO(4–3), and H2O (Emonts et al. 2016; Gullberg et al. 2016b; Emonts et al. 2018). The amount of molecular gas estimated from these observations showed that it is sufficient to fuel the in-situ star formation taking place in the CGM and in fact, the properties of the CGM are such that it falls along the relationship between the star-formation rate and molecular gas mass surface densities (the "Schmidt-Kennicutt relation" Emonts et al. 2016). Molecular gas on even larger scales ($\sim$250 kpc) has been interpreted as the denser regions of accretion streams feeding the central massive galaxies. Ongoing star formation in the streams enriches the gas even before it is accreted (Ginolfi et al. 2017). Circum-galactic molecular gas around other AGN has been interpreted as due to outflows (Cicone et al. 2015). These observations support the view that the CGM is in part metal-rich and dense and provide a link between cold halo gas and in-situ star formation. Molecular gas has also been detected $\sim$90 kpc away from the host galaxy, but without any optical or dust continuum counterpart (Gullberg et al. 2016a). The region contains dynamically quiet gas with a relatively low velocity offset and could potentially be explained as being part of an accretion flow. Gullberg et al. (2016a) also note that the nuclear molecular gas is very narrow and dynamically quiescent, compared to the typical broad optical/UV emission line gas seen close to the AGN.

The classical low-J CO emission lines have proven to be good tracers of diffuse, low density molecular gas. It has been suggested that [C I] can be a equally good tracer, complementing the other lines (Papadopoulos et al. 2004). The [C I] lines have similar critical densities as the lower rotational transitions of CO, and trace the same diffuse gas. But unlike the optically thick CO lines, [C I] is optically thin and therefore probes higher column densities than CO (Papadopoulos et al. 2004). Due to the low critical density, [C I] does not probe the most dense gas, but is a good tracer of the diffuse gas. Recent studies have also brought up the possible issue that CO in star-forming galaxies might be effectively destroyed by cosmic rays, while leaving H_2 intact (Bisbas et al. 2015, 2017). This suggests that [C I] might be a more reliable H_2 tracer in environments of star-forming galaxies, AGNs and near synchrotron emitting galaxies (Papadopoulos et al. 2018).

4C19.71 is a massive, double-lobed, steep-spectrum, FR-II type HzRG with X-ray emission seen at both the core and hot spots over an extent of $\sim$ 60 kpc (Smail et al. 2012). The galaxy has extended [O III] line emission spanning from the host out to both the lobes (Armus et al. 1998).

The large size of the emission of 66 kpc×16 kpc is unusual compared to radio galaxies at $z \sim 2$ (Nesvadba et al. 2017). The galaxy has bright extended Lyα, C IV and He II halos of the size of $\sim$ 120 kpc observed with long slit spectroscopy (Maxfield et al. 2002). 4C19.71 is a unique galaxy, bright across a wide wavelength range and the face-on orientation as well as luminous AGN provide a testbed to study the gas within the galaxy, the interaction of the radio jets as the expand outwards and the properties of the halo gas.

Throughout the paper we assume a flat Λ cold dark matter (ΛCDM) cosmology with $H_0 = 67.8$ km s^{-1},Mpc^{-1}, $\Omega_{\rm M}$=0.308 and Ω_Λ=0.692 (Planck Collaboration et al. 2016), which implies a scale of 7.427 kpc arcsec^{-1} at $z = 3.59$.

4.2 Data

4.2.1 ALMA Observations

The Atacama Large Millimeter/submillimeter Array (ALMA) cycle 3 observations in Band 3 were carried out on UT 2016 March 6, with 38 min on-source integration and 38 operating antennas. The four 3.875 GHz wide bands were tuned to include the [C I] $^3P_1$-$^3P_0$ (hereafter [C I](1–0)) and ^{13}CO $J = 4 \rightarrow 3$ lines, covering 94.6–98.4 GHz and 106.5–110.3 GHz. We calibrated the data with the Common Astronomy Software Applications (CASA) using the observatory supplied calibration script. The data cube and moment 0 maps were also produced using CASA. A natural weighting (robust parameter of 2) was applied since the data has low signal-to-noise. This results in a continuum image with synthesized beam 1.8"×1.9" and a RMS of 14 μJy. To produce the cube and look for [C I](1–0) ($\nu_{\rm rest}$=492.16 GHz) and ^{13}CO(4–3) ($\nu_{\rm rest}$=440.77 GHz) emission lines, we binned the data to 50 km/s which resulted in an RMS noise of 0.3 mJy. To create the moment–0 maps, we first subtracted the continuum in the uv-plane by fitting a first-order polynomial over all the spectral window (but excluding the channels where the [C I](1–0) and ^{13}CO(4–3) emission were expected to lie). We then collapse the cube over the frequency range 107.21–107.27 GHz and 96.007–96.067 GHz for the [C I](1–0) and ^{13}CO(4–3) moment–0 maps respectively, resulting in line-only continuum-free images.

4.2.2 MUSE Observations

Multi Unit Spectroscopic Explorer (MUSE) observations on VLT/UT4 were carried out during four nights between 7th of June 2016 to 2nd of September 2016, with a total of five hours on source integration time, with an average seeing of ∼1.2". The data were taken in five sets of two 30 min exposures rotated 90 degrees with respect to each other, resulting in a total of 10 exposures. We reduced the data using the MUSE instrument pipeline version 1.6.2. First, we prepossessed the data with the standard settings to produce a calibrated and sky subtracted combined data cube. But due to strong skylines which were not optimally subtracted and created artifacts in the cube, especially the [OI] skyline which lies at the redshifted wavelength of Lyα emission in 4C19.71, we decided to re-process the cube. To overcome the problems with the previous reduction, we reduced each exposures individually without sky subtraction and put them on the same spatial and spectral coordinate grid, by providing the first exposure (astrometry corrected) as the OUTPUT_WCS argument for the other nine exposures. Then we sky subtracted each exposure by using ZAP 2.0 (the Zurich Atmosphere Purge Soto et al. 2016). Finally, we merged all 10 individual 30 min exposures into one combined cube using the python package MPDAF 2.5 (muse python data analysis framework) developed by the MUSE Consortium[1].

Moment–0 maps were created by subtracting the continuum emission by fitting a first order polynomial to the red and blue side of each emission line and the collapsing the cube over

[1]https://mpdaf.readthedocs.io/en/stable/credits.html

λ_{obs}=5581.64–5584.14 Å, λ_{obs}=7100.39–7102.89 Å, λ_{obs}=7525.39–7535.39 Å and λ_{obs}=8739.14–8756.64 Å for Lyα, C IV, He II and C III], respectively.

4.2.3 Previous Supporting Observations

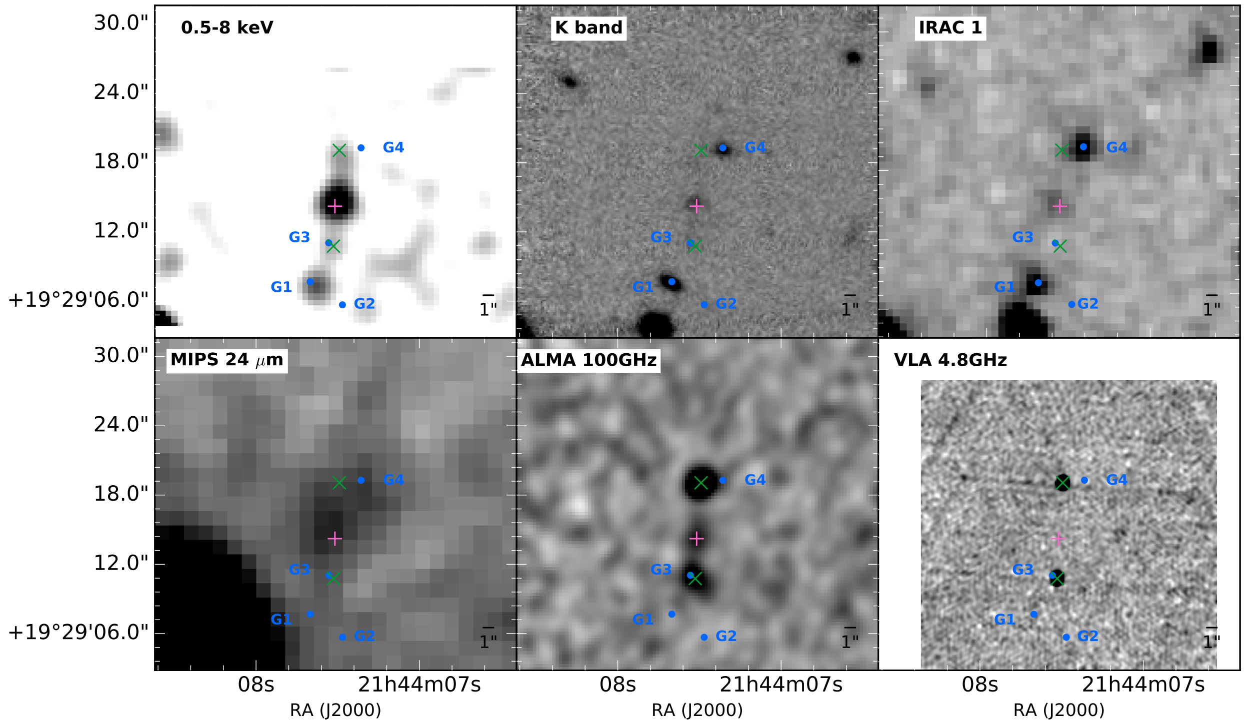

FIGURE 4.1: Six views around 4C19.71 from previous publications. *Top left:* smoothed 0.5–8 keV *Chandra* images Smail et al. (2012); *top center:*; K-band 2.0–2.45 μm (Armus et al. 1998); *top left:* IRAC 3.6 μm (Seymour et al. 2007); *bottom left:* MIPS 24 μm (De Breuck et al. 2010); *bottom center:* ALMA band 3 continuum of 94.6–98.4 GHz and 106.5–110.3 GHz (Falkendal et al. 2018); *bottom right:* VLA band C 4.8 GHz (Pentericci et al. 2000). Pink plus indicate the center of the host galaxy determined from the peak of the thermal dust emission of the ALMA band 3 continuum image. Green crosses indicated the hot sport of the two radio lobes. The blue filled circles show the location of four foreground galaxies around 4C19.71. For details about coordinates and redshifts of the sources in the field see table A.26. The unmarked continuum sources in the different images are stars.

4C19.71 has an extensive set of previous observations, spanning from X-ray to radio frequencies (Fig. 4.1). 4C19.71 was observed with *Chandra* showing weak X-ray emission on $\sim$ 60 kpc scales extending from the host galaxy and in the direction of the two radio lobes (see Smail et al. 2012, for details about the data reduction). The two radio lobes are also detected in very weak X-ray emission. With the Keck near-infrared camera 4C19.71 was observed in K-band and detecting [O III] 5007 Å through the narrow-band 2.284–2.311 μm filter, finding line emission on 74×9 kpc extending out towards the radio jets (Armus et al. 1998). 4C19.71 was also part of a large *Spitzer* and *Herschel* survey of 70 HzRGs $1 < z < 5.2$ (see Seymour et al. 2007; De Breuck et al. 2010; Drouart et al. 2014, for details about the data reduction) observed with the Infrared Array Camera (IRAC), the Infrared Spectrograph (IRS), the Multiband Imaging Photometer (MIPS) on *Spitzer*, the Photodetector Array Camera and Spectrometer (PACS) and the Spectral And Photometric Image

Receiver (SPIRE) on *Herschel*. The IRAC 3.6 μm, 4.5 μm and MIPS 24 μm show continuum emission at the location of the host galaxy. 4C19.71 have also been observed at radio wavelengths with the Very Large Array (VLA) bands C, X and L (Pentericci et al. 2000; Reuland et al. 2003a). Bands C and X show a clear and quite symmetric double lobe structure, but the core is not detected in any of the VLA bands. Through SED fitting the stellar mass has been estimated to be log ($M_\star$ / $M_\odot$)=11.13 (De Breuck et al. 2010) and the SFR=84 $M_\odot$ yr^{-1} (Drouart et al. 2014; Falkendal et al. 2018). The K-band image shown in figure 4.1 is publicly available[2] but does not have an astrometric solution. We use AIPS (Astronomical Image Processing System) and the task XTRAN to determine the coordinate transformation between image pixels and the RA and Dec of reference stars. We use Gaia DR2 (Gaia Collaboration et al. 2018) to retrieve the coordinates of the 5 brightest stars in the field and via XTRAN we obtained a new K-band image with corrected astrometry.

4.3 Results

Combining ALMA (sub)-mm observations with MUSE optical observations reveals extended line emission at larger scale around 4C19.71 than previously observed. Figure 4.1 shows X-ray 0.5–8 keV continuum, K-band, IRAC 3.6 μm, MIPS 24 μm, ALMA 100 GHz continuum and VLA 4.8 GHz images of 4C19.71. The AGN at the host galaxy is detected in all of these wavelength bands, except with the VLA, which only detects two synchrotron lobes extending towards the north and south. 4C19.71 is also bright in Lyα and the narrow band image shows bright emission at the position of host galaxy extending out towards both the northern and southern radio lobes (Fig. 4.2). Weak Lyα emission is also detected south of the southern lobe (region C, Fig. 4.3). Similar morphological structure is also seen in C IV, He II and C III] (Fig. 4.2). The general structure and extent of the ionized gas is in agreement with previous long-slit spectroscopy observations (Maxfield et al. 2002). [C I](1–0) line emission have been detected at the host galaxy (region B, Fig. 4.3) and 9 arcsec ($\sim$75 kpc) north of the source (region A, Fig. 4.3). This extended [C I](1–0) emission coincides with weak C IV observed with MUSE (Fig. 4.2). Region A is not detectable in any continuum emission, with a 3σ-upper limit of 0.4 μJy. Weak C IV is also detected south of the source (region B) showing similar velocity dispersion and velocity offset as the emission from region A. Figure 4.3 shows the three different regions from which the emission line spectra are extracted; A: north of the northern radio lobe, B: the core where the AGN reside and C: south of the southern radio lobe. We will in the following discuss each of these results in detail.

4.3.1 Molecular emission lines

We searched for [C I](1–0) and ^{13}CO(4–3) lines in the ALMA cube by binning to different velocity widths and stepping through to find source. Due to the low signal-to-noise, we did not bin the cube further than 50 km s^{-1}. We found two [C I](1–0) detections, one in region B, at the position of the host galaxy coinciding with the K-and, IRAC 3.6 μm and 4.5 μm, and IRS 16 μm and the ALMA thermal dust component of the host (Fig. 4.1) and one detection in region A. From the moment-0 map of the [C I](1–0) emission (summed over $\nu_{\rm obs}$=107.21–107.27 GHz of the *uv* continuum subtracted cube, Fig. 4.2) we define the boundaries of the two [C I](1–0) regions (cyan regions in Fig. 4.3). We extract the spectra from region B (*uv* continuum subtracted ALMA cube), region A (non-*uv* continuum subtracted ALMA cube) and from region C (non-*uv* continuum subtracted ALMA cube) to show the noise spectra. The ^{13}CO(4–3) line is not detected with ALMA. A moment-0 map of the ^{13}CO(4–3) non-detection was constructed with the same width as the [C I](1–0) moment-0 map ($\nu_{\rm obs}$=96.007–96.067 GHz) and centered at $\nu_{\rm obs}$=96.037 GHz assuming the systemic redshift.

[2] http://www.eso.org/ cdebreuc/shzrg/

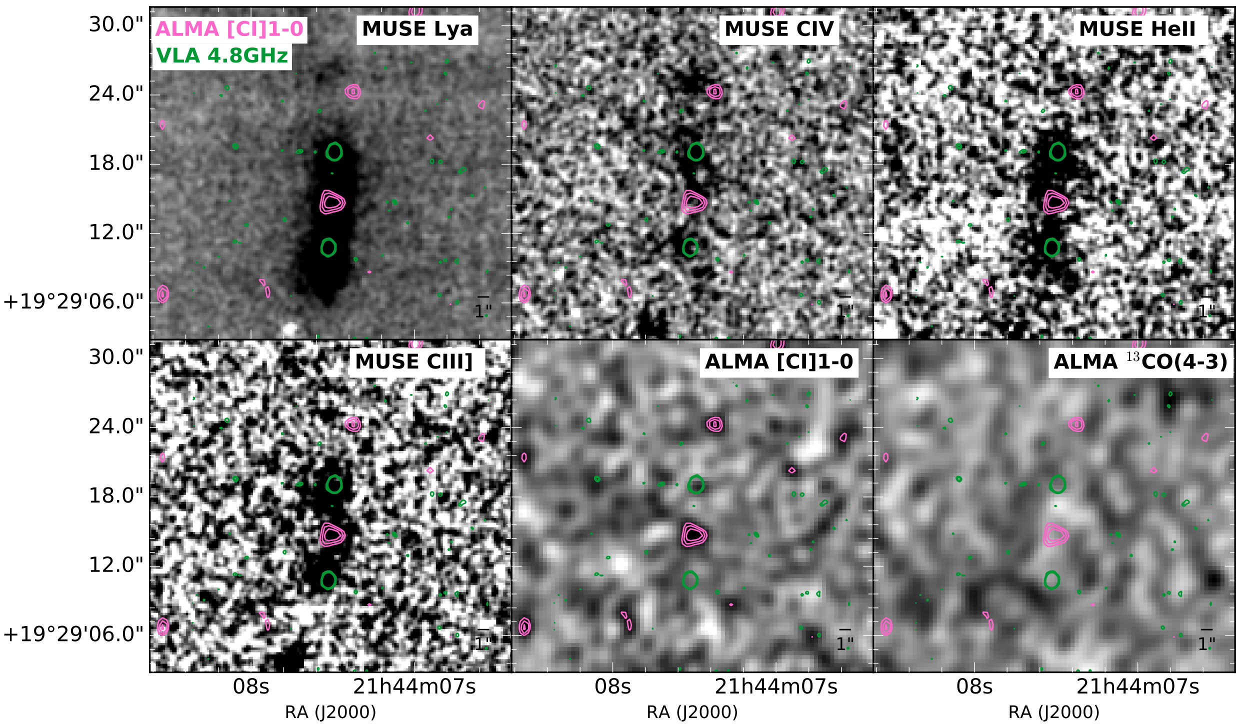

FIGURE 4.2: Six narrow band images of 4C19.71. *Top left:* Lyα (λ_{obs}=5581.64–5584.14 Å); *top center:* C IV 1548.2 Å (λ_{obs}=7100.39–7102.89 Å); *top right:* He II (λ_{obs}=7525.39–7535.39 Å); *bottom left* C III] (λ_{obs}=8739.14–8756.64 Å); *bottom center:* [C I](1–0) (107.21–107.27 GHz) from the continuum subtracted cube. *bottom right:* ^{13}CO(4–3) (96.007–96.067 GHz) from continuum subtracted cube. MUSE moment-0 maps are smoothed with a Gaussian filter of size 7×7 pixels. Pink contours is overlaid [C I](1–0) line emission (levels at 2.5σ, 3σ and 3.5σ, σ = 29 mJy). Green contours is overlaid VLA band C (levels at 3σ, $\sqrt{2} \times 3\sigma$, $3\sqrt{2} \times 3\sigma$ and $5\sqrt{2} \times 3\sigma$, $\sigma = 45\,\mu$m.)

We fit both [C I](1–0) lines with a simple Gaussian profile to estimate the integrated line flux, line width and velocity offset. We use non-linear least square method to fit a Gaussian function to the spectrum using the rms=0.3 mJy as one sigma error of the flux. The reported errors is the square root of the variance, one sigma, of the parameter estimate for the Gaussian fit. We use the [C I](1–0) line at the core (region B) to determine the systemic redshift ($z_{\rm sys}$=3.5895) of the host galaxy, and the fit yields a FWHM of 87±23 km s^{-1} and a frequency integrated flux of 0.40±0.15 10^{-18} erg cm^{-2} s^{-1}. The extended detection in region A is only shifted ∼5 km s^{-1} from the [C I](1–0) at the core, has a FWHM of 108±54 km s^{-1} and a frequency integrated flux of 0.19±0.12 10^{-18} erg cm^{-2} s^{-1}. Figure 4.4 shows the spectra of the two detected [C I](1–0) lines with the best fit model, as well as a pure noise spectra extracted from region C. Figure 4.4 also shown the noise spectra of the ^{13}CO(4–3) line at the location of the host galaxy (region B). Table 4.2 lists the fitted parameters.

The optically thin ^{13}CO lines are intrinsically faint (line ratio ^{12}CO/^{13}CO∼20–40 and [C I](1–0)/^{12}CO(4–3)∼0.6 (Alaghband-Zadeh et al. 2013; Bothwell et al. 2017)), and have only been detected in a few high-z galaxies (Henkel et al. 2010; Danielson et al. 2013; Spilker et al. 2014; Zhang et al. 2018). Our non-detection of ^{13}CO(4–3) is to be expected and will not be discussed any further.

4.3.2 Ionized gas

The MUSE spectrum revels an extended structure of ionized gas around 4C19.71. Overall, the spectrum is consistent with the previous long-slit spectroscopy observations done by Maxfield et al. (2002), but now with full spatial information over the large (1×1 arcmin) MUSE field. What is observed with MUSE and not seen in previous studies are narrow and very faint extended gas, extending far beyond the radio lobes (Fig. 4.2), region A and C (Fig. 4.3) detected in C IV. At the host galaxy, region B, strong Lyα, C IV and He II emission is detected and the extracted spectra indicate that at least one absorber is present. Furthermore, the Lyα and He II are only marginally detected in the extended regions A and C. This is due to the intrinsic faintness of the gas and the fact that 4C19.71 is at a very unfortunate redshift. Both the Lyα and He II spectra is severely effected by skyline subtraction residuals. The very strong [OI] ($\lambda_{\rm rest}$=5577.338 Å) skyline falls right on top of our redshifted Lyα emission and the He II emission is affected by three different skylines. In figure 4.4 the affected velocity channels are highlighted in yellow. This means that the weak emission from region A and C are very uncertain and that it is also difficult to fit a line profile to the emission from region B. Under better redshift circumstances, it is often possible to use the non-resonant He II line to determine the velocity shift and width of the emission line. This information can then be used to determine the systemic redshift and act as a template to determine absorption line profiles in the Lyα and C IV emission (under the assumption that all lines originate from the same gas). In the case of 4C19.71, instead we rely on the [C I](1–0) line to determine the systemic redshift and it is beyond the scope of this paper to characterize the absorbers in region B.

C IV is on the other hand not affected by the pretense of skylines and this means the emission line is intact and we can fit the line. The detection of C IV also make possible to do a direct comparison with the [C I] line detected with ALMA. This is something new and important for modeling since it provides information about the same species in different ionizing state. Furthermore, even though the Lyα and He II emission is unreliable, we can still give an estimate on the strength of the emission and determine flux ratios between then different lines. This is important for photoionization modeling where flux ratios between different atoms and ionization populations provide direct constraints on the physical state of the gas.

The C IV $\lambda\lambda$1548,1551 doublet show narrow line widths. Both from region A and C, where the faint C IV emission has line widths narrow enough to spectrally resolve the doublet. The C IV doublets are fitted with a simple double Gaussian profile to estimate the integrated line flux, line width and velocity offset. We use non-linear least square method to fit a double Gaussian function to the spectrum using the extracted variance spectrum as flux error. The reported errors is the square root of the variance, one sigma, of the parameter estimate for the Gaussian fit. For the double Gaussian we fixed the 1548:1550 ratio to the theoretical ratio of 2:1 (e.g., Flower et al. 1979; Nussbaumer & Schild 1981), the width of the two lines are set to be the same and the center of the blue component (λ1548.2 Å) is a free parameter with the center of the red component (λ1550.8 Å) fixed to a 2.6 Å shift with respect to the blue line. Best fit for the extracted spectrum of region A yields a FWHM of 179±27 km s^{-1}, blueshifted by $\sim$-133 km s^{-1} (centered at the blue component) from the systemic redshift and the doublet has a wavelength integrated flux of 11.00±2.10 $\times$ 10^{-18} erg cm^{-2} s^{-1}. The extracted spectra from region C show a similar line profile, with a FWHM of 264±48 km s^{-1}, blueshifted $\sim$-35 km s^{-1} and with a wavelength integrated flux density of 8.70±2.16 $\times$ 10^{-18} erg cm^{-2} s^{-1}. Figure 4.4 show the best fit for region A and B and table 4.2 lists the line properties.

To estimate the Lyα λ1215.7 Å integrated line flux, we integrate the velocity bins not affected by skyline subtraction residuals, instead off fitting a line profile to the emission line. For region A and C, only the blue and red wings of the emission lines are present in the spectrum. We integrated the flux over the channels containing the blue and red wings and this yields a lower limit for both the regions. In order to guide the eye, a Gaussian line profile have been fitted to the Lyα spectrum of region A and C, by letting the width and center vary within the error margin of the fitted C IV and excluding the channels strongly affected by skylines (red dashed line, Fig 4.3). The blue side of the Lyα emission from region B is affected by at least one absorber (see Fig 4.3). The red side appears to be more intact and it is prominent that the line must be much broader than in region A and C. From only the red side of the line, we estimate the width to be FWHM$\gtrsim$1000 km s^{-1}. We estimate the lower limit of the integrate line flux of region B, by only integrating over the channels containing the red side of the line.

The He II λ1640.4 Å emission from region A and C is estimated by comparing modeled line profiles to the extracted spectra. For the modeled line, we fix the line width and velocity offset to that of the C IV form each respective region. We plot the corresponding modeled line profiles for He II/C IV line flux ratios 1:2, 1:1, 2:1 and 3:1 (see green, blue, cyan and purple dashed-lines respectively, in figure 4.4). If we can only trust the channels unaffected by strong skylines, then this gives that the He II spectrum of region A is consistent with a 1:2 to 2:1 ratio and region C is consistent with a 2:1 to 3:1 ratio. Which means that the He II is brighter than C IV in region C.

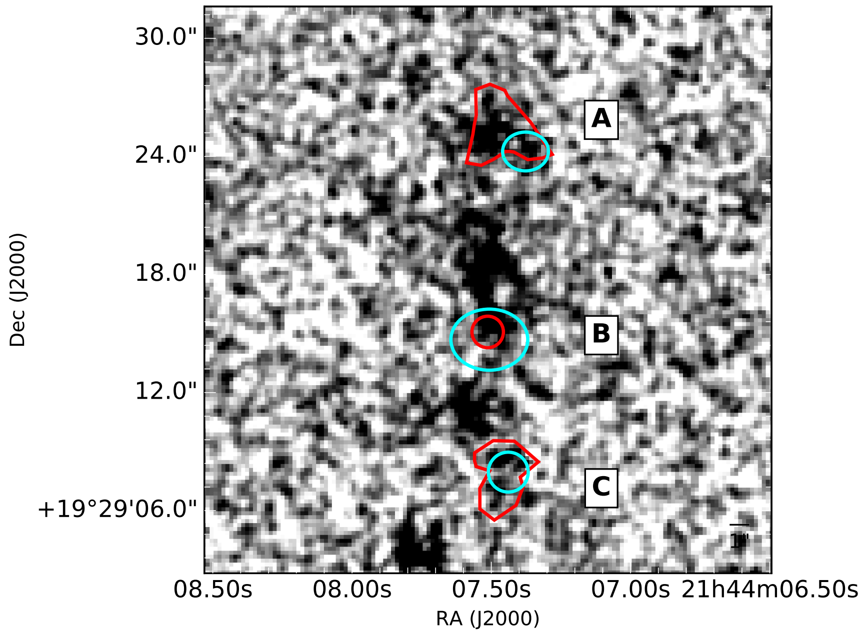

FIGURE 4.3: Greyscale images of C IV emission in 4C19.71. The regions bound by red lines are positions of the spectra extracted from the MUSE cube, determined from the C IV narrow band image. The regions bound by cyan lines indicate the position of the extracted [C I] spectra from the ALMA cube, defined from the [C I] mom-0 map to maximize the S/N. The north [C I] detection is unresolved and extracted by a beam size. The extracted spectra are shown in figure 4.4. The three main regions where the spectrum is extracted are indicated by the A: north of the northern radio lobe, B: host galaxy and core where the AGN reside and C: south of the southern radio lobe.

4.3.3 Gas masses and star formation efficiency

The molecular gas mass (M_{H_2}) is usually traced by rotational CO transitions and is a well-established technique (e.g. Dickman et al. 1986; Elmegreen 1989) used both in the local Universe (e.g, Young & Scoville 1991; Downes & Solomon 1998) and at higher redshift (e.g. Frayer et al. 1998; Omont et al. 1996; Emonts et al. 2016). Papadopoulos et al. (2004) shows that there is a small scatter in the [C I]/CO luminosity ratio. This suggests that the two atomic carbon [C I] fine structure lines [C I]$^3P_2 \rightarrow ^3P_1$ and [C I]$^3P_1 \rightarrow ^3P_0$ may also be used to estimate the molecular gas mass. [C I](1–0) and [C I](2–1) have critical densities $\sim$500 cm^{-3} and $\sim$1000 cm^{-3} respectively, comparable to that of CO(1–0) so they probe the same phase of the gas, and are good tracers of diffuse molecular gas. But in contrast to the ^{12}CO lines, the [C I] lines are optically thin, and may therefore be a

Property	Value	Reference
Ra(J2000), Dec (J2000)	21:44:7.45, +19:29:14.60	
Ra(°), Dec(°)	326.03104, 19.48739	
Systemic redshift (z_{sys})	3.5895	This work §4.3.1
Stellar mass ($M_\star$)	$10^{11.13} M_\odot$	De Breuck et al. (2010)
Molecular mass* (M_{H_2})	$3.06 \pm 1.11 \times 10^{10}\, M_\odot$	This work §4.3.3
Ionized mass (M_{HII})	$>1.65 \times 10^7\, M_\odot$	This work §4.3.3
Infrared luminosity ($L_{IR} \equiv L_{8-1000\mu m}$)	$0.74^{+1.52}_{-0.55} \times 10^{12}\, L_\odot$	Falkendal et al. (2018)
Star formation rate (SFR)	$84^{+172}_{-62}\, M_\odot\, yr^{-1}$	Falkendal et al. (2018)
Star formation efficiency (SFE)	$2.74^{+5.57}_{-0.99}\, Gyr^{-1}$	This work §4.3.3
Depletion time scale (τ_{dep})	$0.36^{+1.08}_{-0.18}\, Gyr$	This work §4.3.3
Gas fraction (f_{gas})	0.19 ± 0.07	This work §4.4.1
SFR surface density ($\log\Sigma_{SFR}$)	$-0.87\, M_\odot, kpc^{-1}$	This work §4.4.1
Gas surface density ($\log\Sigma_{gas}$)	$1.69\, M_\odot, pc^{-1}$	This work §4.4.1

TABLE 4.1: Properties of the host galaxy 4C 19.71 (MG 2144+1928). The systemic redshift is calculated from the detected [C I] line at the nucleus. The SFR is calculated from the L_{IR}, via the conversion given in Kennicutt (1998b) but scaled to a Kroupa IMF by dividing by a factor of 1.5 since the stellar mass is calculated for a Kroupa IMF in De Breuck et al. (2010). (*) the molecular mass estimated from the [C I] line is likely tracing more extended gas then only being confined within the galaxy disk. This means our estimate is more like an upper limit in the possible molecular gas content of the host galaxy alone, see §4.4.2 for a more detailed discussion.

ALMA							
Line	ν_{rest} GHz	ν_{obs} GHz	Δv $km\,s^{-1}$	peak flux mJy	SdV $Jy\,km\,s^{-1}$	Line flux $10^{-18}\,erg\,cm^{-2}\,s^{-1}$	FWHM $km\,s^{-1}$
North							
[C I]	492.2	107.24	5±23	0.47±0.20	0.05±0.03	0.19±0.12	108±54
Core							
[C I]	492.2	107.23	0	1.21±0.29	0.11±0.04	0.40±0.15	87±23
MUSE							
Line	λ_{rest} Å	λ_{obs} Å	Δv $km\,s^{-1}$	peak flux $10^{-20}\,erg\,cm^{-2}\,s^{-1}\,Å^{-1}$	Line flux $10^{-16}\,erg\,cm^{-2}\,s^{-1}\,Å^{-1}\,km\,s^{-1}$	Line flux $10^{-18}\,erg\,cm^{-2}\,s^{-1}$	FWHM $km\,s^{-1}$
North							
Lyα*	1215.7	~5577	~-133	>280	>5.8	>13.7	~179
C IV	1548.2 (1550.8)	7102.32	-133±14	138.1±18.2	4.64±0.93	11.00±2.10	179±27
He II**	1640.4	~7525	~-133	70–176	2.3–9.3	5.5–22	~179
Core							
Lyα*	1215.7	...	...	~600	>44.0	>104.3	$\gtrsim$1000
South							
Lyα*	1640.4	~5578	~-35	>1000	>26.6	>63.0	~264
C IV	1548.2 (1550.8)	7104.66	-35±25	80.2±13.7	3.67±0.91	8.70±2.16	264±48
He II**	1640.4	~7527	~-35	160.4–240	7.3–11.0	17.4–26.1	~264

TABLE 4.2: Line fluxes of the C IV doublet for the south and north detection and [C I](1–0) for the core and north detection. The line fluxes are given both in velocity integrated and frequency- (ALMA line) or wavelength-integrated (MUSE). For the MUSE lines the reported FWHM is deconvolved with the instrument resolution of $\sim$110 $km\,s^{-1}$ at $\sim$1550 Å. (*) The flux of the Lyα emission is estimated by integrating over the bins where the complete line should be, for the northern and southern extension we only have signal in the wings of the line. At the core the blue side is completely absorbed and sky subtracted away, so we give the flux as an lower limit by integrating the red side only. The integrated flux is thus a lower limit since we are missing part of the line. (**) the He II line is severely effected by skyline subtraction and cannot be fitted by any line profile. Instead the integrated flux is estimated by scaling a Gaussian with the same with and velocity offset as the C IV line and for flux rations He II/C IV= 0.5, 1 and 2 for the north extension and He II/C IV= 2 and 3 for the south extension, see Fig. 4.4.

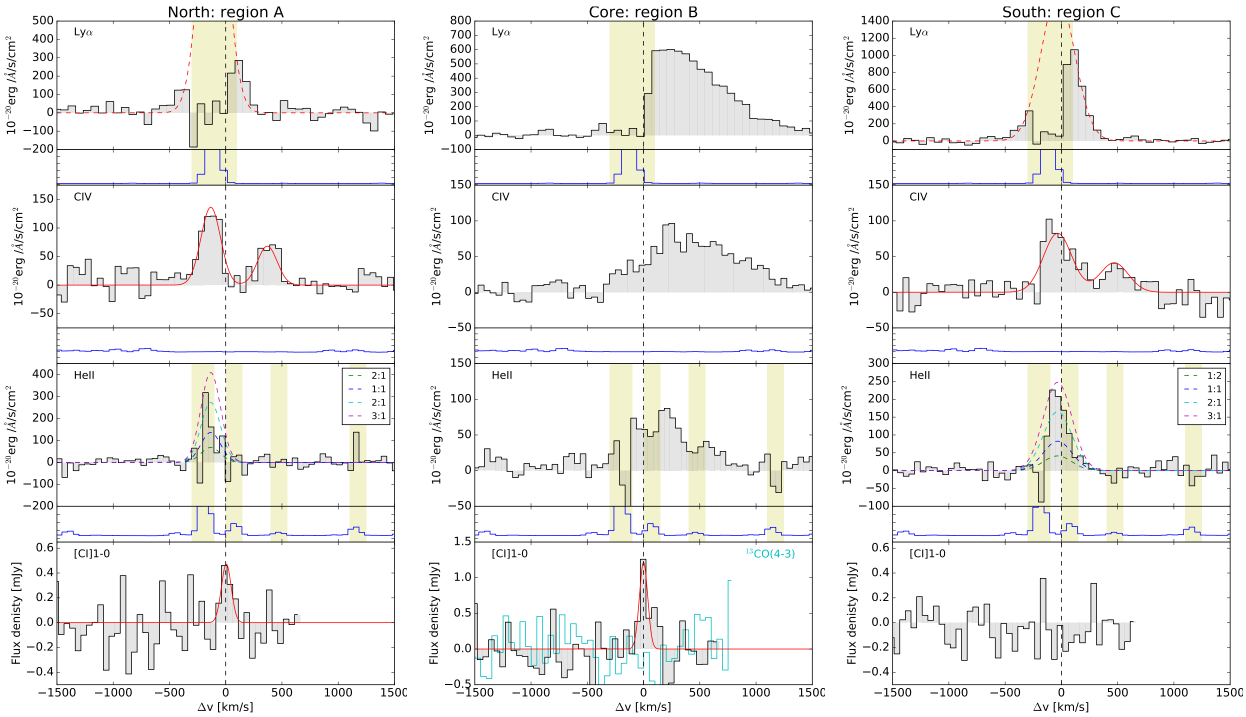

FIGURE 4.4: Extracted spectra of three different regions, as seen in Fig. 4.3. Left to right: North, Core and South. Top to bottom: Lyα, C IV, and He II from the MUSE cube and [C I] from the ALMA cube. The x-axes of the spectra are velocity relative to the systemic redshift, measured from the [C I] line at the core, zero indicated in dashed black. The y-axes are flux densities. Lower panels of Lyα, C IV, and He II: skyline spectra. Yellow shaded regions: wavelength channels strongly affected by the skyline subtraction. Red lines: fitted line profiles, for details see Sec. 4.3.1 and Sec. 4.3.2. Dashed blue, green, cyan and magenta lines: theoretical He II lines if width and centering were the same as the C IV line and the flux ratio He II/C IV was 0.5, 1, 2, and 3, respectively. Solid cyan curve: spectrum of the non-detected ^{13}CO(4–3) line at the core.

better tracer of H_2 as they can probe higher column densities than ^{12}CO (Papadopoulos et al. 2004). Recent studies have shown that cosmic rays can destroy CO in molecular clouds but leaving H_2 intact in typical star-forming galaxies in the Universe (Bisbas et al. 2015, 2017). This would change the abundance of CO in H_2 clouds and may suggest that [C I] is a more reliable tracer of molecular gas mass in the environments where cosmic rays are anticipated to play an important role in induced destruction of CO molecules. Furthermore, it has also been suggested that cosmic rays can lead to molecular gas that is CO-poor/CI-rich in outflows in star-forming galaxies, AGNs, near synchrotron radio jets and in radio-loud cores of radio galaxies (Papadopoulos et al. 2018). We therefore determine the molecular gas mass (M_{H_2}) from the [C I](1–0) detection at the host galaxy, following Papadopoulos & Greve (2004); Wagg et al. (2006); Alaghband-Zadeh et al. (2013); Gullberg et al. (2016b)

$$M_{H_2} = 1375.8 \frac{D_L^2}{(1+z)} \left[\frac{X_{[CI]}}{10^{-5}}\right]^{-1} \left[\frac{A_{10}}{10^{-7} s^{-s}}\right]^{-1} Q_{10}^{-1} \left[\frac{S_{[CI]} dV}{\mathrm{Jy\,km\,s^{-1}}}\right], \tag{4.1}$$

in units of $M_\odot$, where $X_{[C\,I]}$ is the [C I]-to-H_2 abundance ratio, we assume $X_{[C\,I]}=3\times10^{-5}$ (Weiß et al. 2003). The Q_{10} is the excitation factor and depends on the temperature, density and radiation field of the gas (Papadopoulos et al. 2004). Without having any other lines (e.g., CO or [C I](2–1)) we cannot constrain this and we assume the median value of Q_{10}=0.48 (Papadopoulos & Greve 2004). A_{10} is the Einstein A-coefficient $A_{10}=7.93\times10^{-8}$ s^{-1} (Papadopoulos et al. 2004) and D_L is the luminosity distance. At the location of the host galaxy, the integrated [C I] flux density is 1.12±0.41 Jy km s^{-1} which yields a total molecular gas mass $M_{H_2}^{Core}$=3.06±1.11×10^{10} M$_\odot$ at the core and $M_{H_2}^{north}$=1.42±0.95×10^{10} M$_\odot$ at the extended north detection. The error of the M_{H_2} is calculated from the one sigma error of $S_{[CI]}$, without additional error arising from from uncertainties in $X_{[C\,I]}$, Q_{10} and A_{10}. To check if your estimated value of $M_{H_2}^{Core}$ is reasonable we compare with the molecular gas mass estimated from the observed continuum flux density with ALMA band 3 (via Eq. 16, Scoville et al. 2016). For ν_{obs} = 103 GHz, S_{103GHz} = 0.07 mJy (Falkendal et al. 2018) and T_{dust}=40 K, we find a molecular gas mass of $M_{mol} = 6 \times 10^{10}$ M$_\odot$, which is close to the $M_{H_2}^{Core} \sim 3\times10^{10}$ M$_\odot$ estimated using the [C I] line. Considering that there are uncertainties in the [C I]-to-H_2 and CO-to-H_2 abundance depending on environment, it seems reasonable to have a factor of two between different molecular gas mass estimates.

The ionized gas mass can be estimated from the Lyα emission. We do this following the relation given in (De Breuck et al. 2003),

$$M_{HII} = 10^9 \left[f_{-5}\, L_{44}\, V_{70}\right]^{1/2}, \tag{4.2}$$

in units of M$_\odot$, where f_{-5} is the filling factor in units of 10^{-5}, L_{44} is the Lyα luminosity in units of 10^{44} ergs s^{-1}, and V_{70} is the total volume in units of 10^{70} cm^3. We assume a filling factor of 10^{-5} (McCarthy et al. 1990) and a volume of 2"×2"×2" and we find M_{HII}^{Core}>1.65×10^7 M$_\odot$ at the core (region B), M_{HII}^{north}>0.59×10^7 M$_\odot$ in the north (region A) and M_{HII}^{south}>1.28×10^7 M$_\odot$ in the south (region C). We have estimated the Lyα line flux for the three regions by integrating over the bins which contain signal, and it is not the integrated flux from line profile fitting. Since the Lyα is affected by sky lines (and at least one absorber at the core), we can only estimate a lower limit to the luminosity and thus also only a lower limit of the ionized gas mass, since we know that most of the line emission is missing.

We estimate the star formation efficiency as SFE = SFR/M_{H_2}, using the molecular gas mass estimated from the [C I] at the core as the total gas mass and the SFR (Table 4.1), SFE=$2.74^{+5.57}_{-0.99}$ Gyr^{-1}. The corresponding depletion time scale is defined as t_{depl} =SFR^{-1}=$0.36^{+1.08}_{-0.18}$ Gyr and is the time it takes a galaxy to consume its molecular gas reservoir. The large uncertainty in these derived quantities arises mainly from the SFR estimate (Falkendal et al. 2018). The SFR is estimated from the total far-IR luminosity of the star-forming component (integrated over λ_{rest}=8–1000 μm) disentangled from the AGN contribution. The star-formation component is only constrained by two detections which is why there is a large uncertainty associated to the SFR.

4.3.4 Foreground objects

In the field around 4C19.71 four foreground galaxies are detected (blue markers G1, G2, G3 and G4 in Fig. 4.1). Galaxy 1 is located south of the southern radio lobe at z=0.483 and detected in both X-ray, K-band and IRAC 1. Galaxy 2 at z=3.31 is also located in the southern part of the field, but is not seen in any continuum and was detected in line emission while searching thorough the MUSE cube. Galaxy 3 is located close to the hotspot of the southern radio lobe and is at z=0.693, detected in MUSE but not seen in any continuum emission. Galaxy 4 is detected in the K-band and IRAC 1 image and is at z=1.03, and not at the redshift of 4C19.71 as previously reported from long-slit spectroscopy of Lyα (Maxfield et al. 2002). In the aperture of galaxy 4, Lyα is detected at the same redshift as 4C19.71 in the extracted MUSE spectra, but this is just weak extended emission from 4C19.71 itself and not Lyα emission originating from Galaxy 4. For details about the redshift confirmation of the four foreground galaxies we refer the reader to appendix A.4.

4.4 Discussion

4.4.1 A normal star-forming galaxy?

4C19.71 is a massive high-z radio galaxy with relative low star formation rate (SFR$\sim$90 $M_\odot$,yr^{-1}) and falls slightly below the main sequence of star forming galaxies (Falkendal et al. 2018). The star formation efficiency (SFE=2.74 Gyr^{-1}) or gas depletion time (τ_{dep}=0.36 Gyr) etimated in Section 4.3.3 are consistent with star-forming galaxies at high-z (Daddi et al. 2010a; Tacconi et al. 2013; Elbaz et al. 2017). From the estimated total gas mass, we estimate a gas fraction, $f_{gas} = M_{H_2}/(M_{H_2}+M_\star)$, of f_{gas}=0.19$\pm$0.07, which is low in comparison to star-forming galaxies at $z\sim$1-3 which have an average $f_{gas}\sim$0.5 (Daddi et al. 2010a; Tacconi et al. 2013; Elbaz et al. 2017). Santini et al. (2014) find that the gas fraction increases with SFR and decreases with stellar mass for main sequence galaxies out to $z\sim$2.5. For galaxies with a constant log ($M_\star/M_\odot$)$\approx$11.5 at $z\sim$2.5, they find a gas fraction of $f_{gas}\sim$0.2 or for the same $M_\star$ but at a fixed log SFR$\sim$2, they find $f_{gas}\sim$0.5. This is consistent with our estimated gas fraction, since 4C19.71 has a high stellar mass log($M_\star/M_\odot$)=11.13 $M_\odot$ (De Breuck et al. 2010) and low SFR. It should be emphasized that the work by Santini et al. (2014) only includes normal star-forming galaxies, not AGNs, and does not cover the redshift of 4C19.71. To characterize 4C19.71 further, we estimate the star-formation surface density, Σ_{SFR}, and the gas surface density, Σ_{gas}, by assuming the size of an ALMA beam (1.9"$\times$1.8") as the size of both the gas and stellar component (which have been shown to be the case for other radio galaxies: Miley et al. 1992; Pentericci et al. 2001; Emonts et al. 2015a). We estimate logΣ_{SFR}=-0.87 $M_\odot$ kpc^{-2} and log Σ_{gas}=1.69 $M_\odot$ pc^{-2}, both of which are consistent with 4C19.71 lying along the Schmidt-Kennicutt relation within the large uncertainty in our estimated SFR and the scatter of the relationship itself (Daddi et al. 2010b; Kennicutt 1998a; Genzel et al. 2010). Thus 4C19.71 appears to be a normal star-forming galaxy with a low SFR.

4.4.2 Galaxy disk miss-aligned with nuclear launching region?

The kinematics of the (sub)-mm [C I] and the rest-frame UV line Lyα line emission from the the nucleus of 4C19.71 are vastly different, with a FWHM of $\sim$90 km s^{-1} and $\gtrsim$1000 km s^{-1}, respectively. The width of the Lyα emission is only a crude estimate, and we do not know if the broadening is due to resonance scattering, scattered broad line emission, or due to the intrinsic kinematics of the warm ionized gas around the AGN and circum-nuclear region. Still, it is clear that the Lyα is much broader than the [C I] over this region. The [C I] line is very narrow and dynamically cold. The gas traced by [C I] cannot be within the gravitational influence of the AGN. The gas is not part of an outflow. It must be outside the ionization cone of the AGN, because, unlike other emission lines from the nuclear regions, it is much more dynamically quiescent. The core of the radio source is not detected (Fig. 4.1) and the source is lobe dominated. The core to lobe fraction can serve as an orientation indicator (Kapahi & Saikia 1982; Drouart et al. 2012). We are likely observing the radio jets propagating more or less in the plane of the sky.

If the [C I] gas is confined within the disk of the host galaxy, we would expect the [C I] line width to be larger, unless we are observing the disk almost face on. To confirm this, we estimate the dynamical mass (following, Feng & Gallo 2014), taking the radius of the galaxy as half a beam size, assume the [C I] line probes the total stellar plus gas mass and that it is equal to the dynamical mass. This results in an inclination $i\sim3^\circ$ and that we viewing a rotating disk traced by [C I] emission almost face-on. This means that the galaxy is rotating in the plane of the sky and the radio structure is also propagating in the plane of the sky. Since it is thought that the radio jets are propagating perpendicular to the accretion disk, this means that the orientation of the nuclear launch region is not aligned with the host galaxy. This is not impossible and have been observed in the nearby universe (e.g., Morganti et al. 1998). This is also not the first HzRG that have been observed showing narrow molecular line emission at the nucleus of a radio galaxy.

Gullberg et al. (2016a) found molecular gas traced by CO(8–7) with FWHM=43±13 km s^{-1} at the nucleus for the high-*z* radio galaxy MRC 0943-242. The galaxy has extended Lyα emission with FWHM=1592±44 km s^{-1} within the circum-nuclear region. This galaxy show similar properties to what we observe and could also be explained with being viewed face-on and having a misalignment between the central nuclear launch region and the galaxy disk.

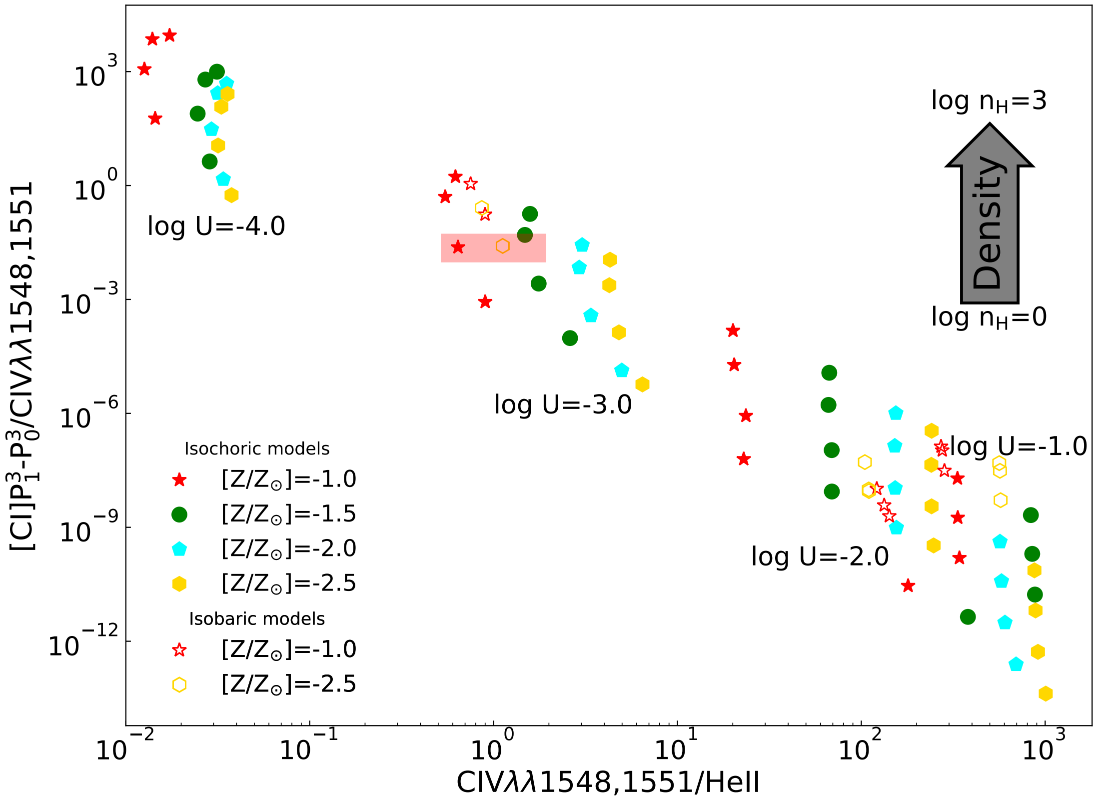

FIGURE 4.5: The line ratios of [C I]/C IV as a function of C IV/He II. The colored points represent the models as indicated in the legend. The ionization parameter of each of the group of points in the figure are indicated in the appropriate regions (decreasing from -1 to -4 from left to right). For each of the isochoric models, the density of the gas increases upwards from log n$_H$=0 to 3. We also show a set of isobaric models for 3 pressures, P/k=2, 3 and 4. The red box show the estimated location from our observations. We note that the box shown greatly exaggerates that uncertainty in [C I]/C IV and show the range of plausible values for C IV/He II and not the uncertainties in the estimate.

4.4.3 The nature of the CGM

We observe a region ∼75 kpc from the nucleus (∼40 kpc from the northern radio lobe, region A) of diffuse gas, detected in C IV and [C I](1–0). To ensure that the [C I] detection is not from a galaxy in the halo, we confirm that the [C I] is not detected in any continuum emission with ALMA, in the K-band, in any of the 4 IRAC bands or with MIPS 24 μm. The MUSE spectrum at this location only shows weak C IV (at the redshift of the radio galaxy) and does not show any additional lines, suggesting that there is no additional galaxy coinciding with the northern [C I] detection. Four other foreground galaxies are on the other hand detected in the MUSE cube (see § 4.3.4 and § A.4). The C IV and [C I] gas has a low velocity shift with respect to the systemic redshift of the host galaxy, $\Delta v=5\pm23\,\mathrm{km\,s^{-1}}$ for [C I](1–0) and $\Delta v = -133\pm14\,\mathrm{km\,s^{-1}}$ for C IV. Both lines are also very narrow $108\pm54\,\mathrm{km\,s^{-1}}$ and $179\pm27\,\mathrm{km\,s^{-1}}$ for [C I](1–0) and C IV, respectively. The dynamics of the gas is quiescent compared to the gas in between the radio lobes. While the kinematics are such that it is not completely clear if the ionized gas and the molecular gas are physically related they do overlap spatially.

In order to investigate the physical state of the multi-phase gas detected in the CGM, we modeled the ionization front with Cloudy 17.01, last described by Ferland et al. (2013). Grids of models were made assuming the standard ISM abundance ratios scaled to a range of metallicities. The ionizing spectrum of the AGN was implemented as a simple hard power-law with a slope of -1 over the energy range of 0.01 to 12 Ryd. The density, for the isochoric models, varied from log n_H=0 to 3 in steps of 1 dex and the log of the ionization parameters ranged from -4 to -1 in 1 dex increments. For the isobaric models, we kept all the parameters the same as for the isochoric models, now allowing the pressure, P/k, to vary from 2 to 4 in steps of 1 dex. The initial densities, log n_H of the isobaric models was 1.0. The modeling was not intended to be exhaustive but illustrative of the fact whether or not we could fit the line ratios with a reasonable set of assumptions.

In the extended CGM cloud, we measure the [C I] flux and C IV fluxes and can only roughly estimate the He II flux due to skyline residuals. This yields [C I]/C IV=0.017 ± 0.011 and C IV/He II$\sim$0.5-2. We show the results of the Cloudy modeling in Fig. 4.5. The line ratio between [C I]/C IV and C IV/He II (Fig. 4.5), suggests that this could be an ionization front in a molecular cloud (a photon-dominated region or PDR) in the CGM perhaps ionized by the AGN. The characteristics of the cloud are not well constrained as a range of models provide acceptable matches with the data given both the uncertainties in the data and also the simplicity of the modeling. We can only conclude from this that the cloud is not solar metallicity with a normal dust to gas mass ratio for the ISM of our Milky Way (not shown because they fall very low in the [C I]/C IV ratios) and that the gas is low metallicity for the isochoric models, about 0.1 to 0.03 solar, and low ionization. The gas is likely low density, $n_{\mathrm{H}}\sim1$ to 10 or low pressure for the isobaric models, P/k$\sim$1000–10000. We note the isobaric models favor a low metallicity gas, $\approx$1/300 solar. However, we caution that given the simplicity of the modeling, we can only make the broadest of statements that the cloud is likely not solar metallicity and has a diffuse ionization and low intensity PDR. More observations are certainly needed but we can say that it might be possible to construct models for CGM clouds linking the warm ionized gas with the diffuse molecular gas in photo-ionization/PDR models.

As a consistency check, we estimate the total ionizing energy rate of the AGN in the radio galaxy to ensure that it has sufficient energy to actually ionize the cloud. To do this, we use the definition of the ionization parameter, which the Cloudy modeling suggests is approximately 1/1000. For a cloud that is 75 kpc from the ionizing source we find an ionizing intensity of 2.1×10^{55} $(d_{\mathrm{cloud}}/75\ \mathrm{kpc})^2$ n_{H} photons $\mathrm{s^{-1}}$. If we assume that all of the ionizing photons have an energy of 13.6 eV for simplicity, we find that the total ionizing energy of the AGN in the radio galaxy is 4.6×10^{44} $(d_{\mathrm{cloud}}/75\ \mathrm{kpc})^2$ n_{H} erg $\mathrm{s^{-1}}$. In Falkendal et al. (2018), we fit the SED of 4C 19.71 estimating the IR luminosity of the AGN to be 4.2×10^{46} erg $\mathrm{s^{-1}}$. This estimate puts a rough upper limit on the likely ionizing luminosity of the AGN and thus there are sufficient photons for only low density gas with $n_{\mathrm{H}}\lesssim100\ \mathrm{cm^{-3}}$. Thus, for the model to be applicable, either the gas is low density or the cloud is seeing a particularly clear line-of-sight since we assumed isotropic QSO emission in our crude calculation.

The dynamics of this emission region perhaps suggest that the warm ionized gas and the diffuse molecular gas are not related in contrast to the photon ionization/PDR modeling. The explanation however may lie in the differences in the nature of the ionization fronts. We do not have enough detailed observations to know for sure but perhaps the best analogy for this situation is a cloud of gas being photo-evaporated such as the "Pillars of Creation" in M16 (McLeod et al. 2015) or in the pillars of dense gas near NGC 3603 (Westmoquette et al. 2013). In these photo-evaporation flows, the highly ionized gas is accelerated at the edge of the denser molecular pillar by the intense radiation field responsible for ionizing the gas. Over time, the cloud will

Mass	Host galaxy $M_\odot$	North extension $M_\odot$
$M_\star$	1.3×10^{11}	...
M_{HII}	$>1.7 \times 10^7$	$>0.6 \times 10^7$
M_{H_2}	3.1×10^{10}	1.4×10^{10}

TABLE 4.3: Stellar mass, ionised- and molecular gas mass for the host galaxy and the diffuse extended north component detected in C IV and [C I](1–0).

be completely dispersed by the intense radiation field. While perhaps not a perfect analogy, it does provide the sense that the warm ionized gas gets accelerated as well as ionized and reach both a high thermal and ram pressure than the quiescent dense diffuse molecular gas. Such a picture may explain the differences in the kinematics while as being consistent with a very simplistic photo-ionization/photon-dominated model of a cloud of gas.

4.4.4 Importance of multi-phase observations

Tracing the CGM gas in ionized emission from rest frame UV lines has revealed large extended haloes around high-z galaxies. The Lyα emission is seen to be distributed as a more or less uniform sphere around the galaxies (Wisotzki et al. 2016; Leclercq et al. 2017) or to show more complex structures (e.g. Cantalupo et al. 2014; Vernet et al. 2017). Observing the CGM in emission such as Lyα is thus a powerful tool to probe the extent and structure of the CGM. On the other hand, the ionized gas only traces very diffuse gas, which is not where most of the mass is. Emonts et al. (2016) showed that the cold gas phase in the CGM around the HzRGs known as the Spiderweb, contains a large reservoir of molecular gas, $M_{H_2}\sim 1.5 \pm 0.4 \times 10^{11}$ $M_\odot$. We find that the northern extension (region A) of quiescent CGM gas contains a large amount of molecular gas mass, M_{H_2}=1.4×10^{10} $M_\odot$, compared to the ionized gas mass, M_{HII}>1.7×10^7 $M_\odot$. The molecular mass is 3 orders of magnitude higher than the ionized gas mass. This large difference would still remain of we could trace the total ionized gas mass with Lyα. Tracing the CGM in molecular gas probes where the main mass of the CGM resides. Most of the work on high-z galaxies has so far studied either ionized gas, or molecular gas, but not both. Complementing ionized emission studies with molecular line tracers provides a novel way to probe the complex multi-phase nature of the CGM. It also probes a larger fraction of the mass of the CGM and the morphology of the mass distribution.

4.5 Conclusions

We have observed the HzRG 4C19.71 in rest-frame UV emission lines with MUSE and in [C I](1–0) with ALMA. This is one of the first studies combining measurements from both facilities. The combination allowed us to probe the ionized gas and the molecular gas of the host galaxy, as well as of the surrounding CGM.

- We detect narrow, dynamically quiescent [C I](1–0) at the core of the host galaxy. In order to explain the very narrow line width we need to be viewing the galaxy face-on, rotating in the place of the sky. This would mean that the galaxy is not aligned with the nuclear launching region, as we are viewing the AGN edge-on and the radio jets are propagating in the plane of the sky.

- We detect [C I](1–0) emission ∼75 kpc away from the host galaxy. This detection is co-spatial with weak extended C IV emission. The two carbon lines do not have exactly the same

FWHM and velocity offset compared to the systemic redshift, but they are both very narrow and must originate from very quiescent gas.

- We perform modeling using Cloudy, to investigate the possible nature of the extended quiescent gas detected in C IV and [C I]. We are able to explain the observed [C I]/C IV and C IV/He II flux ratios with simple assumptions and they are consistent with a PDR in the CGM. We stress that this is meant as a proof of concept and not intended to be an exhaustive analysis.

- The modeling suggests that the observed multi-phase region has a low metallicity, low ionization and low density. We show that the luminosity of the AGN is sufficient to ionize the gas out to 75 kpc if the gas is diffuse enough, $n_H \lesssim 100\,cm^{-3}$.

We show observational evidence that suggests that the CGM contains a multi-phase region of ionized and molecular gas. This gas cloud can be explained as being ionized by the AGN. We are limited to low signal-to-noise and the source is at an unfortunate redshift, which makes the Lyα and He II unusable for kinematic studies. We therefore rely only on the weak C IV emission. The [C I] has been shown to probe a larger amount of gas mass than what ionization lines can trace. This work shows the possibilities and power of observing galaxies using both ionized and molecular gas. We would need to observe 4C19.71 in more lines to get a deeper understanding of the physical condition of the CGM. HzRGs provide unique opportunities to study the CGM, since they are luminous enough to excite the gas out to large distances. The radio jets and ionization cones act as flashlights, illuminating the surrounding diffuse CGM.

Chapter 5

Conclusion and outlook

Conclusions

I have studied the effects of AGN feedback in a sample of 25 HzRGs, by constraining the star formation rate (SFR) in them. The SFR is estimated through SED fitting of FIR to radio wavelengths. The SFRs of the parent sample of 70 HzRGs were estimated by Drouart et al. (2014). My analysis adds to this by using new ALMA continuum data, which has a four times better spatial resolution and an order-of-magnitude lower noise level than single-dish 850 μm observations. The ALMA data reveals a more complex picture of the continuum emission at $\sim$ 1 mm wavelengths than previously expected. From previous SFRs, it was expected that each host galaxy contains a single source. Instead, we detected multiple morphologies. Firstly, a large fraction of the sources are below the detection limit of ALMA, which means their SFRs were overestimated. Of the detected sources, some have exactly one detection coinciding with the host galaxy, consistent with the classical picture. However, other detected sources exhibit several continuum detections. In the wavelength regime of ALMA data, synchrotron and thermal dust emission can be of the same order-of-magnitude. By comparing the position of the ALMA detections with radio measurements, it became clear that synchrotron radiation may contaminate the thermal dust emission at $\sim$ 1 mm. This and the finding of multiple ALMA detections in some sources were the main motivations for developing a computer code capable of simultaneously fitting multiple components of galaxies detected in multiple photometric bands.

During my doctoral research, I developed the SED fitting routine Mr-Moose from scratch. Mr-Moose is capable of simultaneously fitting several spatially resolved components in high resolution photometric bands, as well as the total combined emission without resolved structures in low resolution photometric bands. The code is flexible regarding the number of models to be used during the fit. It can be used for galaxies with both simple and complex morphologies. Mr-Moose was applied to the sample of 25 HzRGs and could successfully disentangle the FIR emission into AGN and star formation heated dust emission as well as synchrotron radiation. This together with the large fraction of sources with no ALMA detections lead to much lower SFRs then previously estimated from *Herschel* and *Spitzer* data alone.

The new estimates for the SFRs are 7 time lower than before. The sample now falls both on and below the main sequence of star-forming galaxies. The population of HzRGs is no longer on starburst levels of star formation, but consistent with normal star-forming galaxies. Since a large fraction of the sources also fall below the main sequence (but are not deviating as much as 1 dex) they are interpreted as being on their way of becoming quenched. This would mean that we are observing negative AGN feedback, where the AGN is partly responsible for shutting down the star-formation.

The galaxies are observed at an epoch during which their SMBHs are over-massive, meaning they do not fall on the $M_{\bullet}$-σ relationship. In order for the galaxies to evolve into the local empirical relationship, the host galaxies need to "catch up" with the mass of the black hole. Growth has to happen through a process which increases the stellar mass of the host galaxy, but does not fuel the

SMBH. One such way would be through dissipationless merging with low mass, likely gas-poor galaxies.

As a second approach to probe in situ AGN feedback, I studied tracers of the molecular and ionized gas of 4C19.71, one of the 25 HzRGs, by combining ALMA and MUSE data cubes. The gas of the host galaxy, the AGN and the CGM gas were investigated. 4C19.71 has a confirmed extended Lyα halo extending $\sim$100 kpc in the direction of the radio lobes. In my data I also find an even more extended C IV structure of $\sim$150 kpc, extending well beyond the north radio lobe. The diffuse north extension of quiescent C IV coincides with a weak [C I] detection. Modeling with Cloudy shows that the line ratios can be explained by simple assumptions about the gas and ionizing sources. This is more a proof of concept rather than putting real constraints on the observed gas. Our detections suggest there might be a PDR in the halo, $\sim$75 kpc away form the host galaxy. ALMA and MUSE together are powerful tools to probe high-z galaxies. However, this work illustrates the limitations if only few lines are detected and what happens if the source is at an unfortunate redshift.

High-z radio galaxies provide unique opportunities to study the important ingredients for galaxy evolution. New facilities and instruments have revealed that these objects can have in-situ star formation in the CGM (Emonts et al. 2016), show signatures of accretion flows from the cosmic web (Vernet et al. 2017), undergo mergers and experience starbursts (Emonts et al. 2015b) and have star-forming companions $\sim$ 90 kpc from the AGN (Gullberg et al. 2016a). The more information we obtain, the more complicated and unique each object seems to get, and sometimes these observations raise more questions than answers. Nevertheless, by looking at both the average and individual properties, it is possible to provide constrains on AGN feedback and CGM gas physics. But our current findings need to be complemented with further observations to improve our understanding of how these objects contribute to shaping the evolution of galaxies.

Outlook

The energy output of AGN has become a critical ingredient in modern galaxy formation theories, but the relationship between the SMBH and its host galaxy is still not well understood. It seems to be clear that the SMBH releases enough energy to affect the host galaxy; the important question is instead what the driving mechanisms for energy transfer/coupling are. HzRGs provide a unique observational opportunity to study the connection between the SMBH and the host galaxy, because both components can be studied while they are active at the same time. However, these studies are often limited by observational constraints. Many of their results only provide indirect measures of the connection between the SMBH and its host galaxy.

Future studies of HzRGs should investigate if these objects are indeed on their way of being quenched. This could be tested, for example, by using X-Shooter data to observe the stellar population through photospheric lines. This could reveal whether there is a continuous sequence of O- and B-stars, or if the O-stars are missing. If the spectra lack the most short lived stars, this would indicate that the galaxy has ceased forming stars recently. This would provide additional support for negative AGN feedback, quenching the host galaxy.

The CGM around HzRGs promises to reveal both the current gas supply and the accretion of new gas through streams. It might hold clues about the possible regulation of this through AGN feedback heating the halo gas. New instruments and telescopes have made it possible to study the CGM at high-z. Especially IFU instruments like MUSE, PCWI and KCWI have proven to be powerful tools tracing the ionized gas in and around high-z galaxies. However, current observations are often limited to rest-frame UV emission lines and it can be difficult to determine the mechanism for ionization. This is where multi-wavelength observations become even more important. Additional ALMA data for example, provides the possibility of probing the same gas in several other lines, which also helps in determining the physical properties of the gas.

For the work I have presented in this thesis, a next step would be to obtain additional ALMA data for the HzRG 4C19.71. Currently we do not know what the real ionization source for the very extended gas detected in C IV and [C I](1–0) is. Given the data available, we showed that it is consistent with being the AGN of the host galaxy. But our data is limited by a very low signal-to-noise. By observing additional lines, we would be able to address these issues. Observing the brighter [C I](2–1) would trace the diffuse molecular gas much better and confirm our low signal-to-noise detection of extended molecular gas. ALMA observations would make it possible to also observe CO(7–6) in one of the side bands, which adds a tracer of dense gas and could provide a way to determine the systemic redshift of the host galaxy. The singly ionized carbon [C II] line is much brighter than both the [C I] lines, and traces extended gas originating mainly from PDR, but also from HII regions. The brightness of the [C II] line might enable line kinematics studies with reasonable on source integration times. The [N II] line would provide supporting data for the origin of the ionizing source. This is because the from the [N II]/[C II] ratio, the PDR/HII fraction can be calculated (e.g. Decarli et al. 2014). This will reveal whether the region is ionized by the AGN or if some other source is creating an HII region. If the galaxy is not detected in several lines, it is not possible to properly constrain the gas physics. These are essential in determining the effects of AGN feedback on the CGM.

Few HzRGs have been studied in greater detail so far, either in molecular and/or ionized gas. In them, we see a wide variety in morphologies. There is currently not a combined picture of the impact of the AGN, how the environment looks like and how these relate to the growth of the host galaxy. It would therefore be useful to study a larger sample of galaxies to discover recurring features. By combining both MUSE and ALMA we could start to understand the interaction between the host galaxy, the AGN and the halo gas in a more general sense. This can provide answers to questions like; How common are accretion streams? How much gas is residing in the halo? Does the CGM contain many clouds of denser gas? Will the gas eventually accrete onto the galaxy? Is the AGN stopping/delaying the gas accretion?

Another natural step following the work presented in this thesis is to further develop Mr-Moose. This will make the code applicable to more scientific questions and more useful for the community. A current limitation is that the emission is calculated using an analytic model. Ideally, Mr-Moose should include the capability of fitting discrete models, i.e. templates of AGN models or galaxy evolution models, increasing its versatility.

We are fortunate to be in an era in which new facilities allow us to do more detailed studies of high-z galaxies than ever before. Numerical simulations are finally reaching sufficiently high resolutions for calculating the observed properties of galaxies. Combining both observations and simulations can provide a powerful tool to shed light on the evolution of galaxies during the cosmic history. New facilities are on the horizon, such as the James Webb Space Telescope (JWST), the European Extremely Large Telescope (E-ELT) and the Square Kilometer Array (SKA). They will open new windows for the study of the high-z Universe. This will lead to a better understanding of the evolution of our Universe. It will also reveal unexpected results, leading to new and unforeseeable questions.

Appendix A

Appendix of chapter

A.1 List of packages used in Mr-Moose and references

The list of packages, their version and their respective reference.

- astropy v2.0rc1, http://www.astropy.org, Astropy Collaboration et al. (2013)
- corner v2.0.1, https://pypi.python.org/pypi/corner
- emcee v2.2.1, http://dan.iel.fm/emcee/current/#, Foreman-Mackey et al. (2013)
- guppy v0.1.10, https://pypi.python.org/pypi/guppy/
- matplotlib v1.5.1, http://matplotlib.org/
- numpy v1.9.1, http://www.numpy.org/
- pathos v0.2.0, https://pypi.python.org/pypi/pathos/0.2.0
- pycallgraph v1.0.1, http://pycallgraph.slowchop.com/en/master/#,
- PyYAML v3.12, http://pyyaml.org/
- tqdm v4.8.4, https://github.com/tqdm/tqdm
- scipy v0.14.0, https://www.scipy.org/

A.2 Input files for both examples. used in Mr-Moose

LISTING A.1: Example #1 of model file. Note the latex notation of the parameter (used in the generation of the plots)

```
sync_law   2
$N$        -25   -15
$\alpha$   -2.0   0.0
```

LISTING A.2: Example #1 of the fit file.

```
source_file: data/fake_source_ex1.dat
model_file: models/fake_source_ex1.mod
all_same_redshift: True
redshift: [0.0,]
nwalkers: 200
nsteps: 200
nsteps_cut: 180
```

```
percentiles: [10., 25., 50., 75., 90.]
skip_imaging: False
skip_fit: False
skip_MCChains: False
skip_triangle: False
skip_SED: False
unit_obs: 'Hz'
unit_flux: 'Jy'
```

LISTING A.3: Example #2 of model file. Note the latex notation of the parameter (used in the generation of the plots)

```
AGN_law 2
$N_{AGN}$ -38 -28
$\alpha_{AGN}$ -4.0 0.0
BB_law 2
$N_{BB1}$ -28 -18
$T_1$ 10 80
BB_law 2
$N_{BB2}$ -28 -18
$T_2$ 10 80
sync_law 2
$N_{s1}$ -28 -18
$\alpha_{s1}$ -2.0 0.0
sync_law 2
$N_{s2}$ -28 -18
$\alpha_{s2}$ -2.0 0.0
```

LISTING A.4: Example #2 of the fit file.

```
source_file: data/fake_source_ex6.dat
model_file: models/fake_source_ex6.mod
all_same_redshift: True
redshift: [2.0, 2.0, 2.0, 2.0, 2.0]
nwalkers: 400
nsteps: 3500
nsteps_cut: 3450
percentiles: [10., 25., 50., 75., 90.]
skip_imaging: False
skip_fit: False
skip_MCChains: False
skip_triangle: False
skip_SED: False
unit_obs: 'Hz'
unit_flux: 'Jy'
```

LISTING A.5: Example #3 of model file. Note the latex notation of the parameter (used in the generation of the plots)

```
MBB_law 2
$N$ -28 -9
$T$ 20 100
```

LISTING A.6: Example #3 of the fit file.

```
source_file: data/Gilli2014a.dat
model_file: models/MBB.mod
all_same_redshift: True
redshift: [4.75,]
nwalkers: 200
nsteps: 400
nsteps_cut: 350
percentiles: [10., 25., 50., 75., 90.]
skip_imaging: False
skip_fit: False
skip_MCChains: False
skip_triangle: False
skip_SED: False
unit_obs: 'Hz'
unit_flux: 'Jy'
```

LISTING A.7: Example #1 of data file. The wavelength references are reported in Hz and the flux are reported in Jy (10^{-23} erg s^{-1} cm^{-2} Hz^{-1}).

```
# filter          RA              Dec            resolution   lambda0    det_type   flux       flux_error    arrangement
component   component_number
74MHz(VLA)        12h00m00s       -40d00m00s           12.0  7.377042e+07  d        1.188135e-07  9.036851e-09  1
sync          0
408MHz            12h00m00s       -40d00m00s           12.0  4.078365e+08  d        2.526585e-08  1.634557e-09  1
sync          0
1.4GHz            12h00m00s       -40d00m00s           12.0  1.399439e+09  d        7.190462e-09  4.763989e-10  1
sync          0
4.85GHz           12h00m00s       -40d00m00s           12.0  4.848056e+09  d        2.188714e-09  1.375087e-10  1
sync          0
8.4GHz            12h00m00s       -40d00m00s           12.0  8.396633e+09  d        1.161870e-09  7.939377e-11  1
sync          0,
```

LISTING A.8: Example #2 of data file. The wavelength references are reported in Hz and the flux are reported in Jy (10^{-23} erg s^{-1} cm^{-2} Hz^{-1}).

```
# filter      RA             Dec             resolution  lambda0      det_type  flux          flux_error    arrangement
component   component_number
VLA_L         12h00m00s      -40d00m00s      20.0  1.400000e+09  d   6.642489e-08  1.310263e-08  4
'total sync'  3,4
VLA_C         12h00m00.1s    -39d59m59s       1.0  4.710000e+09  d   1.726653e-08  3.875161e-09  6
'E sync'    4
VLA_C         11h59m59.95s   -40d00m01s       1.0  4.710000e+09  d   1.994406e-08  3.875161e-09  5
'W sync'    3
VLA_X         12h00m00.1s    -39d59m59s       0.5  8.210000e+09  d   1.115211e-08  2.226486e-09  6
'E sync'    4
VLA_X         11h59m59.95s   -40d00m01s       0.5  8.210000e+09  d   9.245703e-09  2.226486e-09  5
'W sync'    3
ATCA_47       12h00m00s      -40d00m00s      10.0  4.799800e+10  d   2.015150e-09  4.231155e-10  4
'total sync'  3,4
ALMA_3        12h00m00s      -40d00m00s       3.0  1.022500e+11  d   1.701354e-09  3.677694e-10  7
'all sources'  0,1,2,3,4
ALMA_6        12h00m00.1s    -39d59m59s       0.3  2.452500e+11  d   5.485048e-09  9.451120e-10  3
'E sync/host'  2,4
ALMA_6_nr1    11h59m59.95s   -40d00m00.5s     0.3  2.291500e+11  d   4.714464e-09  8.537784e-10  2
'W sync/comp'  1,3
laboca_870    12h00m00s      -40d00m00s      15.0  3.440046e+11  u   9.107478e-09  9.107478e-09  1
'Dust/AGN'  0,1,2
spire_500     12h00m00s      -40d00m00s      35.0  6.048278e+11  u   1.595681e-08  1.595681e-08  1
'Dust/AGN'  0,1,2
spire_350     12h00m00s      -40d00m00s      25.0  8.498941e+11  u   1.553297e-08  1.553297e-08  1
'Dust/AGN'  0,1,2
spire_250     12h00m00s      -40d00m00s      17.0  1.221085e+12  d   1.666475e-08  3.975734e-09  1
'Dust/AGN'  0,1,2
pacs_160      12h00m00s      -40d00m00s       5.0  1.909476e+12  d   1.166623e-08  2.640865e-09  1
'Dust/AGN'  0,1,2
pacs_70       12h00m00s      -40d00m00s       4.0  4.304211e+12  d   1.416861e-09  3.018548e-10  1
'Dust/AGN'  0,1,2
mips_24       12h00m00s      -40d00m00s       7.0  1.283529e+13  d   2.471502e-10  4.419324e-11  1
'Dust/AGN'  0,1,2
irs_16        12h00m00s      -40d00m00s       5.0  1.946903e+13  d   1.054598e-10  2.169550e-11  1
'Dust/AGN'  0,1,2
irac_4        12h00m00s      -40d00m00s       5.0  3.909498e+13  d   3.153092e-11  6.182625e-12  1
'Dust/AGN'  0,1,2
```

LISTING A.9: Example #3 of data file. The wavelength references are reported in Hz and the flux are reported in Jy (10^{-23} erg s^{-1} cm^{-2} Hz^{-1}). Note that in configuration *a*, only the detection are used (see § 2.3.3).

```
# filter          RA              Dec            resolution  lambda0        det_type  flux       flux_error  arrangement
component    component_number
pacs_70           03h32m29.35s    -27d56m19.6s   4.0   4.304211e+12  u    0.3e-3     0.3e-3     1
'Dust'       0
pacs_100          03h32m29.35s    -27d56m19.6s   4.0   3.000000e+12  u    0.2e-3     0.2e-3     1
'Dust'       0
pacs_160          03h32m29.35s    -27d56m19.6s   5.0   1.909476e+12  u    0.43e-3    0.43e-3    1
'Dust'       0
spire_250         03h32m29.35s    -27d56m19.6s   17.0  1.221085e+12  d    4.1e-3     1.9e-3     1
'Dust'       0
spire_350         03h32m29.35s    -27d56m19.6s   25.0  8.498941e+11  u    4.0e-3     4.0e-3     1
'Dust'       0
spire_500         03h32m29.35s    -27d56m19.6s   35.0  6.048278e+11  u    5.0e-3     5.0e-3     1
'Dust'       0
ALMA_B7_344       03h32m29.35s    -27d56m19.6s   1.5   3.440000e+11  d    6.1e-3     0.5e-3     1
'Dust'       0
ALMA_B6_254       03h32m29.35s    -27d56m19.6s   1.5   2.540000e+11  d    3.5e-3     0.1e-3     1
'Dust'       0
ALMA_B6_230       03h32m29.35s    -27d56m19.6s   0.8   2.299000e+11  d    2.47e-3    0.07e-3    1
'Dust'       0
ATCA_40GHz        03h32m29.35s    -27d56m19.6s   10.0  4.000000e+10  u    0.013e-3   0.013e-3   1
'Dust'       0,
```

A.3 SED fits and continuum images

MRC 0037-258

MRC 0037-258 is detected with a single continuum component which coincides with the position of the radio core (Fig. A.2). SED fitting with Mr-Moose is done with three components, a synchrotron power law for the radio core (the lobes are excluded), a modified BB and an AGN component. The VLA data are assigned to only the synchrotron component while the ALMA flux density is assigned to both the synchrotron and modified BB. The PACS, SPIRE, MIPS and IRS data are fitted to the modified BB and AGN components. In the best fit model, the ALMA flux is dominated by synchrotron emission (Fig. A.1). This is because the 3σ upper limits in the FIR are not given a high weight and there is a solution where the synchrotron power law can account for all of the observed flux. The PDF of the free parameters is shown in Fig. A.3 where it is clear that the two free parameters N_{BB} and T are completely unconstrained.

TABLE A.1: Data for MRC 0037-258 (z=1.10)

Photometric band	Flux[mJy]	Ref.
IRS (16 μm)	0.877 ± 0.1	A
MIPS (24 μm)	1.740 ± 0.039	A
PACS (70 μm)	<7.5	B
PACS (160 μm)	<28.0	B
SPIRE (250 μm)	<14.6	B
SPIRE (350 μm)	<6.6	B
SPIRE (500 μm)	<18.9	B
LABOCA (870 μm)	<12.9	B
ALMA 6	0.4± 0.08	this paper
VLA X[c]	1.20 ± 0.12[a]	A
VLA C[c]	1.73 ± 0.17[a]	A

Notes (*c*) Radio core, (*a*) Flux estimated using AIPS from original radio map, convolved to the resolution of the VLA C band.
References. (A) De Breuck et al. (2010), (B) Drouart et al. (2014)

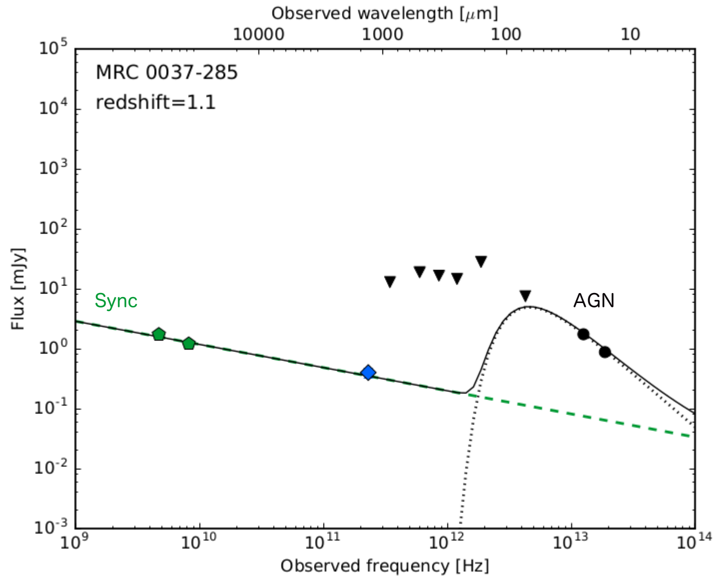

FIGURE A.1: SED of **MRC 0037-258**. Black solid line represents the best fit total model, green dashed line is synchrotron power-law of the radio core, dotted line indicates the AGN contribution. The colored data points indicate the data which have sub-arcsec resolution and black points indicate data of low spatial resolution. Green pentagons represent the fluxes from the radio core and the blue diamond indicates ALMA band 6 detection. Filled black circles indicate detections (>3σ) and downward pointing triangles indicate the 3σ upper limits (Table A.1).

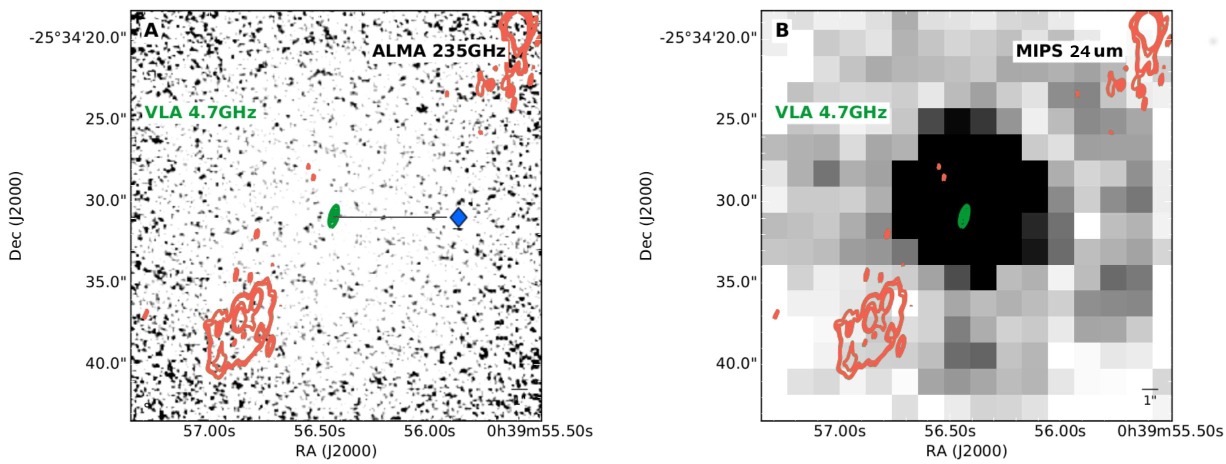

FIGURE A.2: *Panel A:* continuum map of ALMA band 6 in grayscale with overplotted VLA C contours (the levels are 3σ, $\sqrt{2} \times 3\sigma$, $3\sqrt{2} \times 3\sigma$ and $5\sqrt{2} \times 3\sigma$ ($\sigma = 46\,\mu$Jy)). The blue diamond indicates the ALMA detection and is the same marker used in Fig. A.1. The green contours show the portion of the VLA data that is used in the SED fit, the red contours are excluded in the fit. *Panel B:* MIPS 24 μm continuum map with the same VLA C contours overplotted.

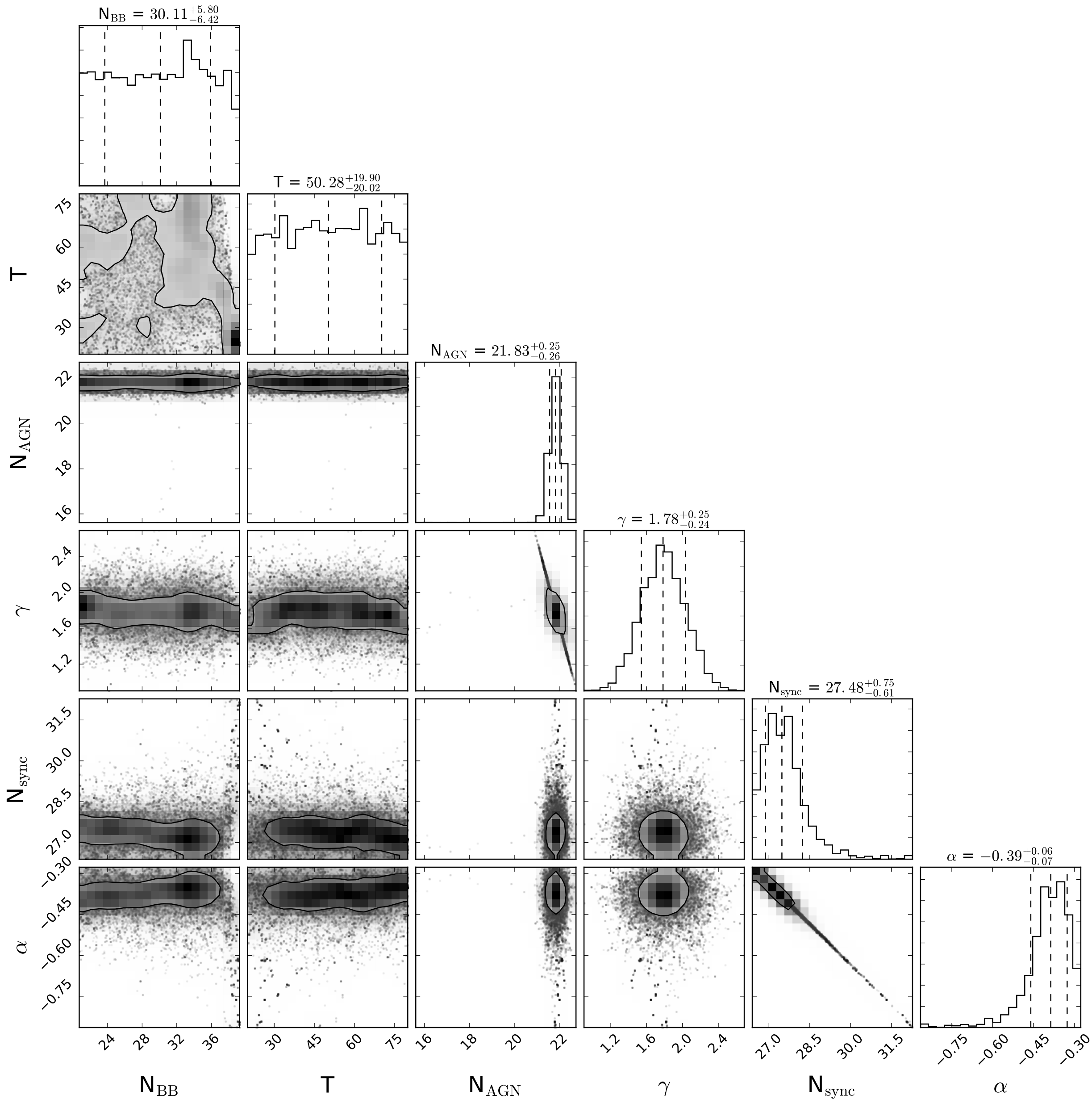

FIGURE A.3: **MRC 0037-258** Corner plot of the free parameters.

MRC 0114-211

MRC 0114-211 has two detected continuum components in ALMA band 6. Both detections coincide with the two lower-frequency radio components (Fig. A.5). The SED fitting is done with five components, two synchrotron components (eastern and western radio components), two modified BB (one for each ALMA detection) and one AGN component. The western radio component (detected in VLA bands C and X) is assigned to the western ALMA detection and the same setup is also applied to the eastern radio and ALMA components. The VLA band X, ATCA 7 mm, and ALMA band 3 detections do not resolve the individual components and are only considered for fitting the total radio flux (the combination of the western and eastern synchrotron power-law components). The two ALMA band 6 points are both fitted with a combination of a synchrotron power-law and a modified BB. The PACS. SPIRE, MIPS and IRS data points are fitted to the combination of the two modified black bodies and a AGN component. The best fit model is where the brighter western component in ALMA band 6 is pure synchrotron and the eastern component is dominated by thermal emission (Fig. A.4). The PDF of the free parameters is shown in Fig. A.6, where it is clear that the free parameters, $N_{BB,1}$ and T_1 of the first BB associated with the western ALMA detection are completely unconstrained.

TABLE A.2: Data for MRC 0114-211 (z=1.41)

Photometric band	Flux[mJy]	Ref.
IRS (16 μm)	1.690 $\pm$ 0.1	A
MIPS (24 μm)	2.09$\pm$ 0.04	A
PACS (70 μm)	5.5 $\pm$ 2.7	B
PACS (160 μm)	32.2$\pm$ 9.4	B
SPIRE (250 μm)	24.3 $\pm$ 7.5	B
SPIRE (350 μm)	<36.2	B
SPIRE (500 μm)	<30.8	B
LABOCA (870 μm)	<16.8	B
ALMA 6^e	2.21 $\pm$ 0.31	this paper
ALMA 6^w	9.82 $\pm$ 0.9	this paper
ALMA 3	32.6 $\pm$ 3.2	this paper
ATCA (7mm)	82.5 $\pm$ 24.7	this paper
VLA X^w	599.9 $\pm$ 59^a	A
VLA X^e	9.99 $\pm$ 0.99^a	A
VLA C^w	1084.5 $\pm$ 108^a	A
VLA C^e	63.7 $\pm$ 6.37^a	A
VLA L	4091.6 $\pm$ 409	C

Notes (*e*) East component, (*w*) west component, (*a*) flux estimated using AIPS from original radio map, convolved to the resolution of the VLA C band.

References. (A) De Breuck et al. (2010), (B) Drouart et al. (2014), (C) Condon et al. (1998).

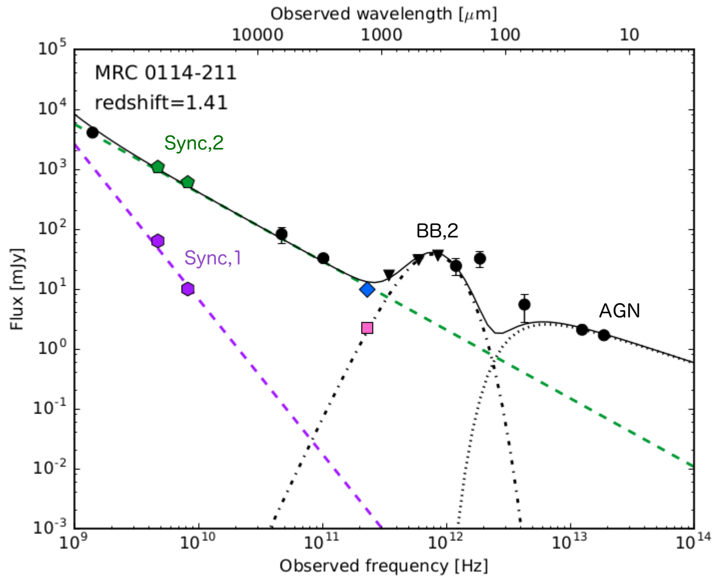

FIGURE A.4: SED of **MRC 0114-211**. Black solid line shows best fit total model, green and purple dashed lines are the western and eastern synchrotron lobes, respectively. The black dash-dotted line is one black body component associated to one of the ALMA band 6 detections. Black dotted line indicates the AGN component. The colored points indicate data with sub-arcsec resolution and black ones indicate the data with low spatial resolution. Green pentagons indicate the western radio lobe, purple hexagons indicate the eastern radio lobe, the blue diamond indicates one of the ALMA band 6 detection, and the magenta square is the second ALMA detection. Filled black circles indicate detections (>3σ) and downward pointing triangles the 3σ upper limits (Table A.2).

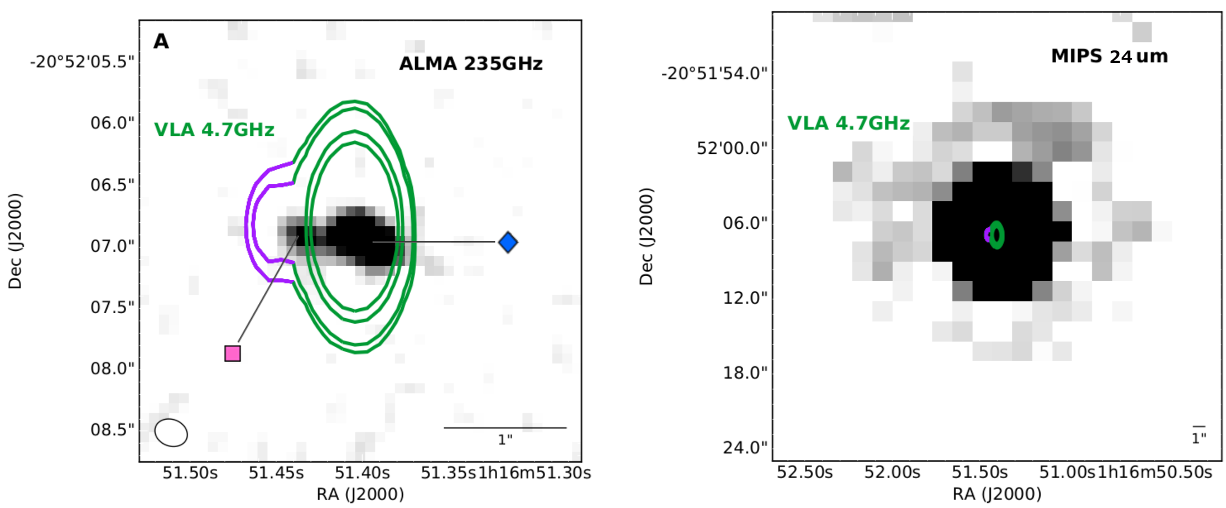

FIGURE A.5: *Panel A:* continuum map of ALMA band 6 with VLA C contours overlaid (levels are as Fig. A.2; σ = 71 μJy). The blue and pink markers indicate the two different components detected with ALMA and correspond to the same data points as Fig. A.4. The purple and green contours show the two components of the VLA data and correspond to the markers of the same colors as in the SED fit. *Panel B:* MIPS 24 μm continuum map with VLA 4.7 GHz contours overlaid.
Note that the scale of the MIPS image is 5 times larger than the image displayed in panel A.

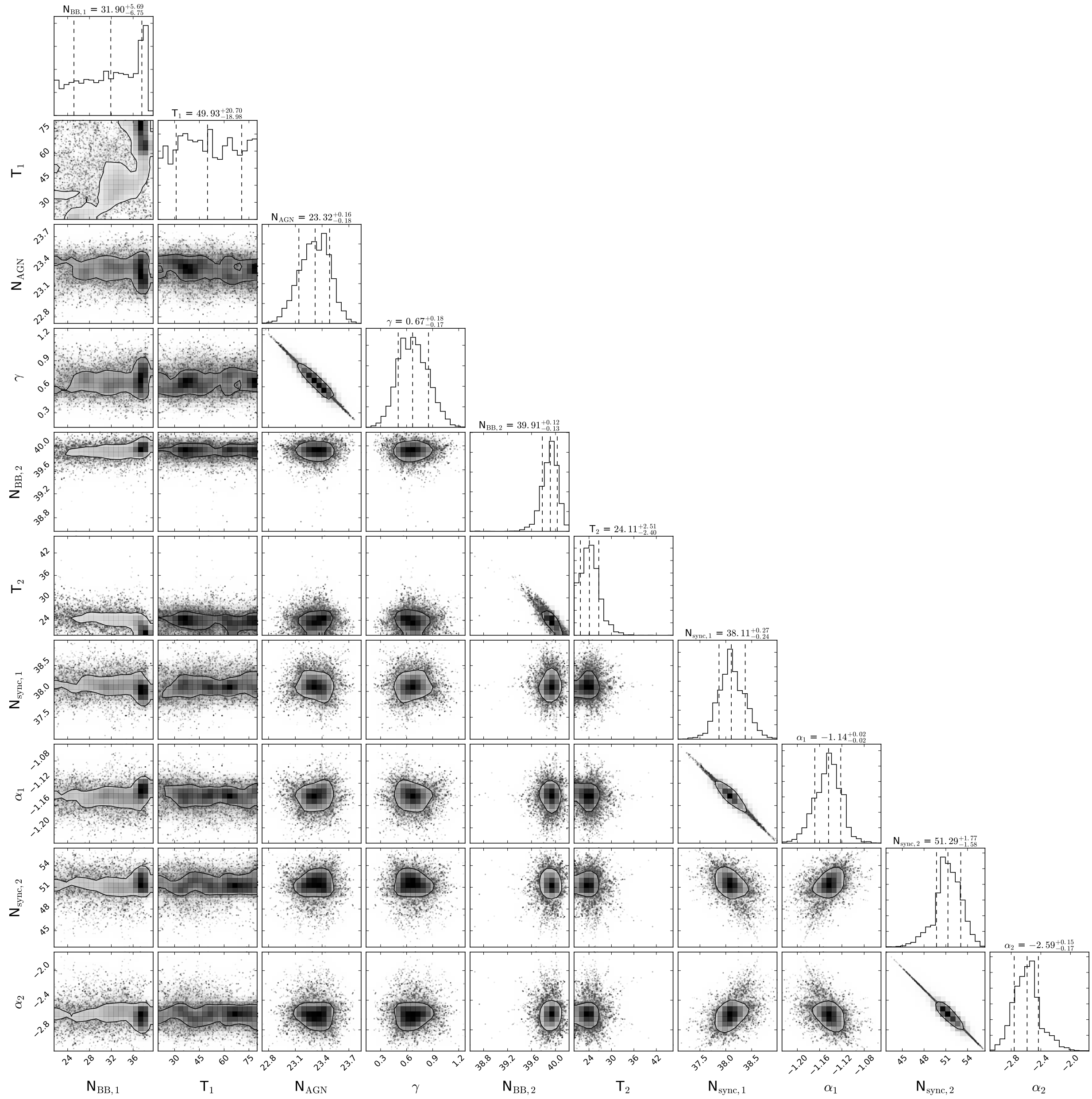

FIGURE A.6: **MRC 0114-211** Corner plot of the free parameters.

TN J0121+1320

TN J0121+1320 has one continuum detection in the ALMA band 3 observations which coincides marginally with the compact radio component (Fig. A.8). SED fitting is done with three components, a single synchrotron power law, a modified BB, and an AGN component. The single component in radio VLA C and X bands is assigned to a synchrotron power-law, the ALMA detection is assigned to both a synchrotron and a modified BB model. The PACS, SPIRE, MIPS and IRS data points are fitted with a combination of the modified BB component and an AGN component. The best fit solution implies that the ALMA emission is due to thermal dust emssion but the AGN component is unconstrained as there are only upper limits in the mid-infrared. The PDF of the free parameters as shown in Fig. A.9, where it is clear that the AGN model is completely unconstrained.

TABLE A.3: Data for TN J0121+1320 (z=3.516)

Photometric band	Flux[mJy]	Ref.
IRS (16 μm)	<0.204	A
MIPS (24 μm)	<0.131	A
PACS (100 μm)	<7.9	B
PACS (160 μm)	<24.2	B
SPIRE (250 μm)	15.9 $\pm$ 5.7	B
SPIRE (350 μm)	18.0$\pm$ 6.6	B
SPIRE (500 μm)	<18.4	B
SCUBA (850 μm)	4.7 $\pm$ 1.0	B
ALMA 3	0.19 $\pm$ 0.012[a]	this paper
VLA C	8.4 $\pm$ 0.5[a]	C
VLA L	57.3 $\pm$ 2.7	D

Notes(*a*) flux estimated using AIPS from original radio map, convolved to the resolution of the VLA C band.

References. (A) De Breuck et al. (2010), (B) Drouart et al. (2014), (C) De Breuck et al. (2000) (D) Condon et al. (1998).

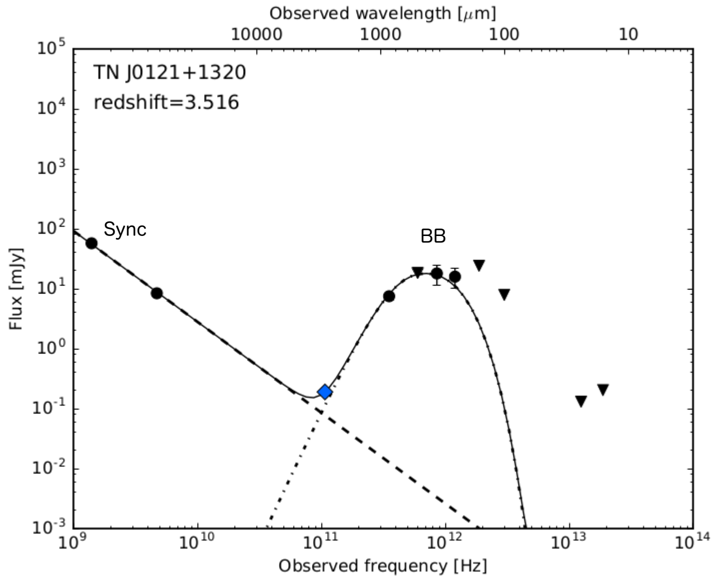

FIGURE A.7: SED of **TN J0121+1320**. Black solid line shows the best fit total emission model, black dashed line represents the synchrotron emission and the black dash-dotted lines represents the black body emission. The colored data point indicate the data with sub-arcsec resolution and black ones indicated data of low spatial resolution. The blue diamond indicates the ALMA band 3 detection. Filled black circles indicate detections (>3σ) and downward pointing triangles the 3σ upper limits (Table A.3).

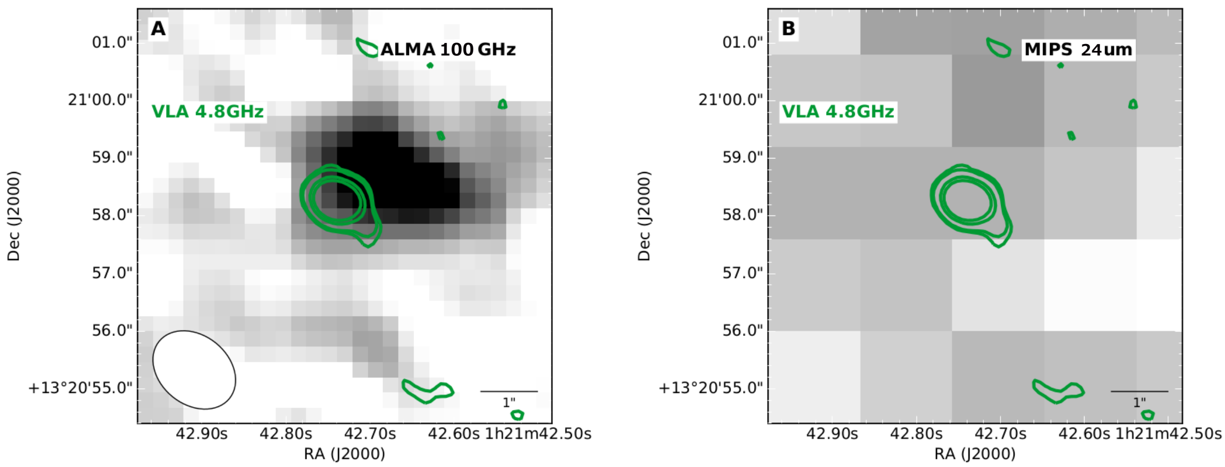

FIGURE A.8: *Panel A:* continuum map of ALMA band 3 with overlaid VLA C contours (levels are as Fig. A.2, σ = 70 μJy) *Panel B:* MIPS 16 μm continuum map.

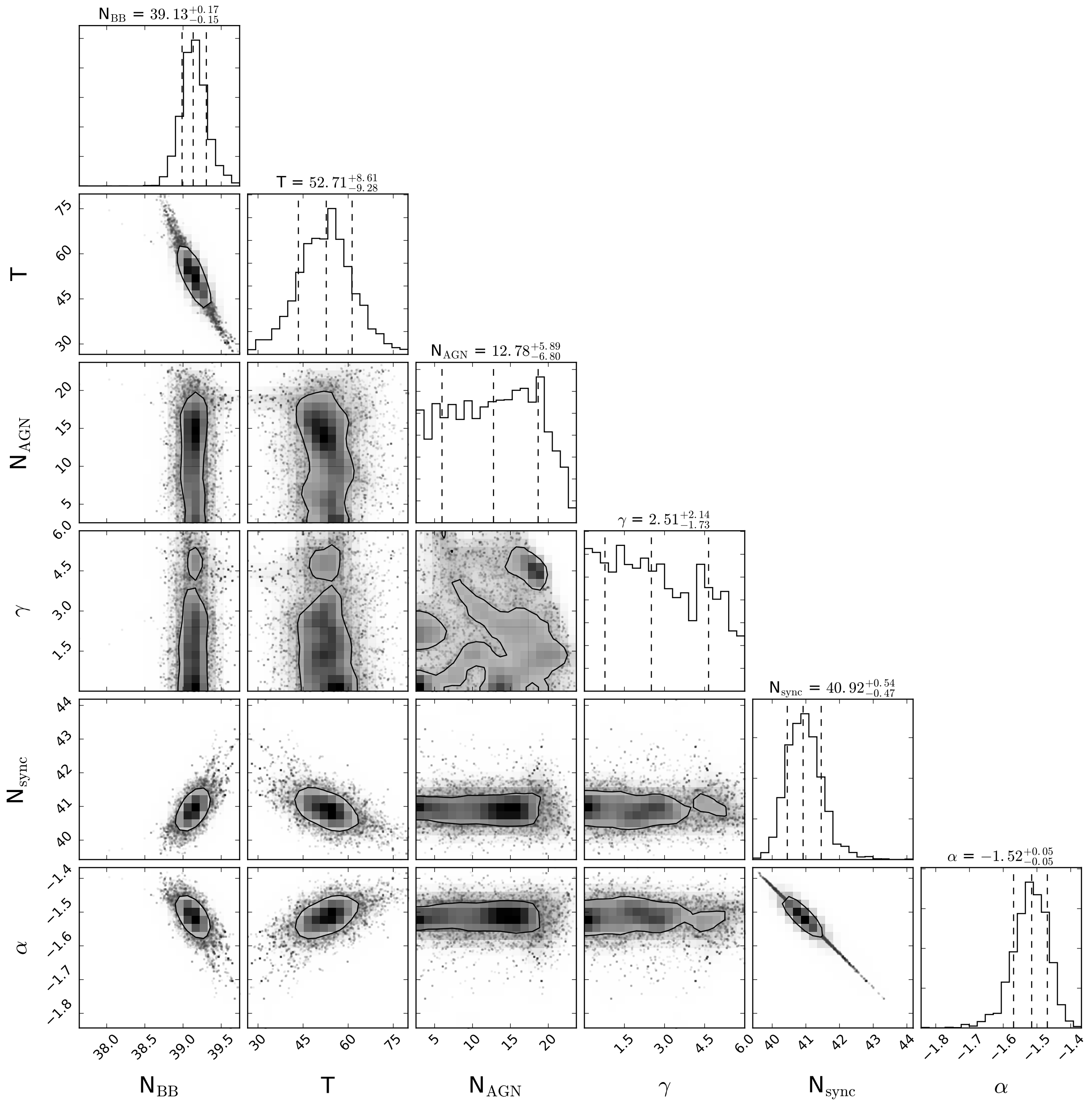

FIGURE A.9: **TN J0121+1320** Corner plot of the free parameters.

MRC 0152-209

MRC 0152-209 has two detected continuum components in the ALMA observations and both of which coincide with lower frequency radio detections (Fig. A.11). SED fitting is done with four components, one total synchrotron, two modified BB and one AGN component. The VLA data is fitted to one synchrotron power-law since it is not possible to resolve individual components in any of the observed bands. The two ALMA band 6 detections are fitted to the same total synchrotron power-law and two individual modified BB for each ALMA detection. The LABOCA, PACS, SPIRE, MIPS and IRS data points are all fitted with a combination of the two individual modified BB and an AGN component. The best fit model is one where both of the ALMA detections are dominated by dust emission. The radio slope is too steep to be able to account for the observed ALMA continuum. It is unclear wherever the northern or southern dust component corresponds to the host galaxy, but since the southern component (indicated by the blue BB line in Fig. A.10) is brighter, this component is more likely to be the host galaxy and the northern emission, is an interacting companion. Though this is not enough to determine which of the component host the radio-loud AGN. In Emonts et al. (2015b) they argue that the NW component is the host, which might be more correct. If this is the case, then the SFR would be one order of magnitude lower and the galaxy would be on the MS, instead of lying above the MS relation. Though the morphology of the source strongly suggest it is a merger, a SFR$\sim$1000 $M_{\odot}yr^{-1}$ is reasonable for a merging system. The PDF of the free parameters can be found in Fig. A.12.

TABLE A.4: Data for MRC 0152-209 (z=1.92)

Photometric band	Flux[mJy]	Ref.
IRS (16 μm)	1.580 $\pm$ 0.1	A
MIPS (24 μm)	3.32 $\pm$ 0.133	A
PACS (70 μm)	22.6 $\pm$ 3.5	B
PACS (160 μm)	110.2 $\pm$ 9.8	B
SPIRE (250 μm)	105.0 $\pm$ 8.6	B
SPIRE (350 μm)	81.3 $\pm$ 7.3	B
SPIRE (500 μm)	64.4 $\pm$ 6.8	B
LABOCA (870 μm)	14.5 $\pm$ 3.3	B
ALMA 6^s	2.30 $\pm$ 0.23	this paper, C
ALMA 6^n	1.75 $\pm$ 0.175	this paper, C
ATCA (7 mm)	5.1 $\pm$1.5	D
VLA X	42.75 $\pm$ 0.03^a	E
VLA C	101.44 $\pm$ 0.08	E
VLA L	453.10 $\pm$ 45.30	F

Notes (*s*) South companion, (*n*) north companion, likely to be the host as discussed in Emonts et al. (2015b), (*a*) flux estimated using AIPS from original radio map.

References. (A) De Breuck et al. (2010), (B) Drouart et al. (2014), (C) (Emonts et al. 2015b) , (D) Emonts et al. (2011a) (E) Carilli et al. (1997), (F) Condon et al. (1998).

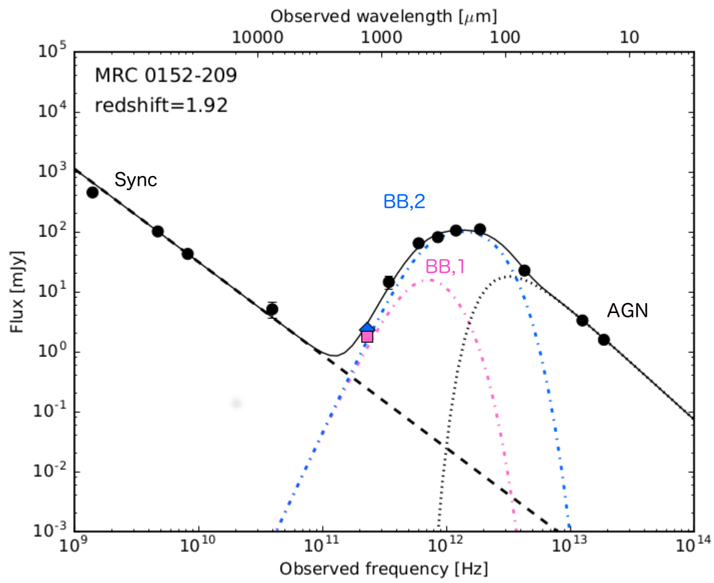

FIGURE A.10: SED of **MRC 0152-209**. Black solid line shows best fit total model, black dashed line represents the total synchrotron emission. The magenta and blue dashed-dotted line represent the two black bodies of the northern and southern ALMA 6 detections, respectively. Black dotted line indicates the AGN component. The colored data points indicate data with sub-arcsec resolution and black ones indicate data of lower spatial resolution. The magenta square and blue diamond indicates the ALMA band 6 detection of the northern and southern components, respectively. Filled black circles indicate detections (>3σ) and downward pointing triangles the 3σ upper limits (Table A.4).

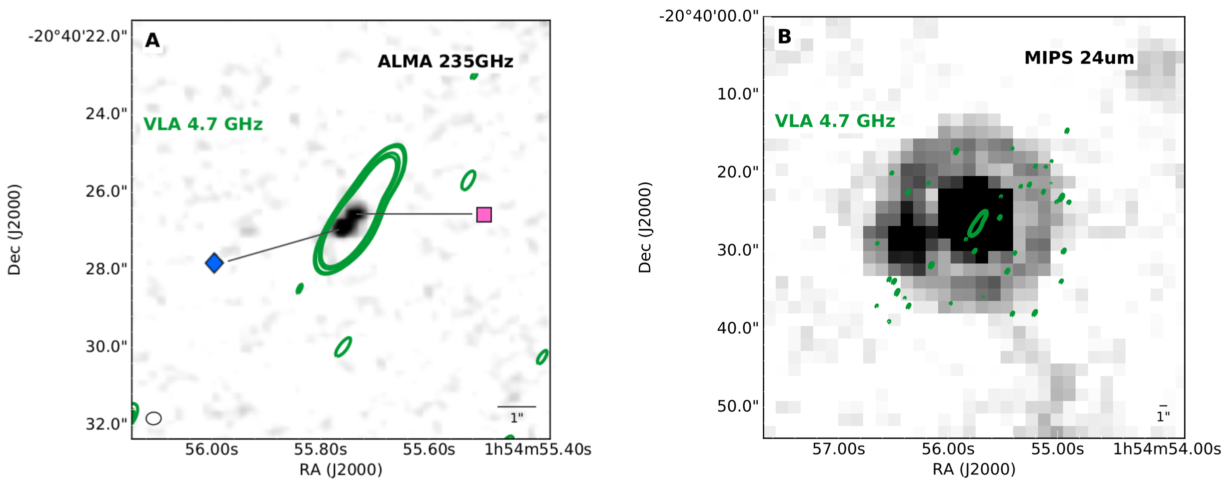

FIGURE A.11: *Panel A:* continuum map of ALMA band 6 with overlaid VLA C contours (levels are as Fig. A.2, $\sigma = 56\,\mu$Jy). The blue and pink markers show the two ALMA detections and correspond the same markers used in Fig. A.10. *Panel B:* MIPS 24 μm continuum map and please note that the scale of the MIPS image is 5 times larger.

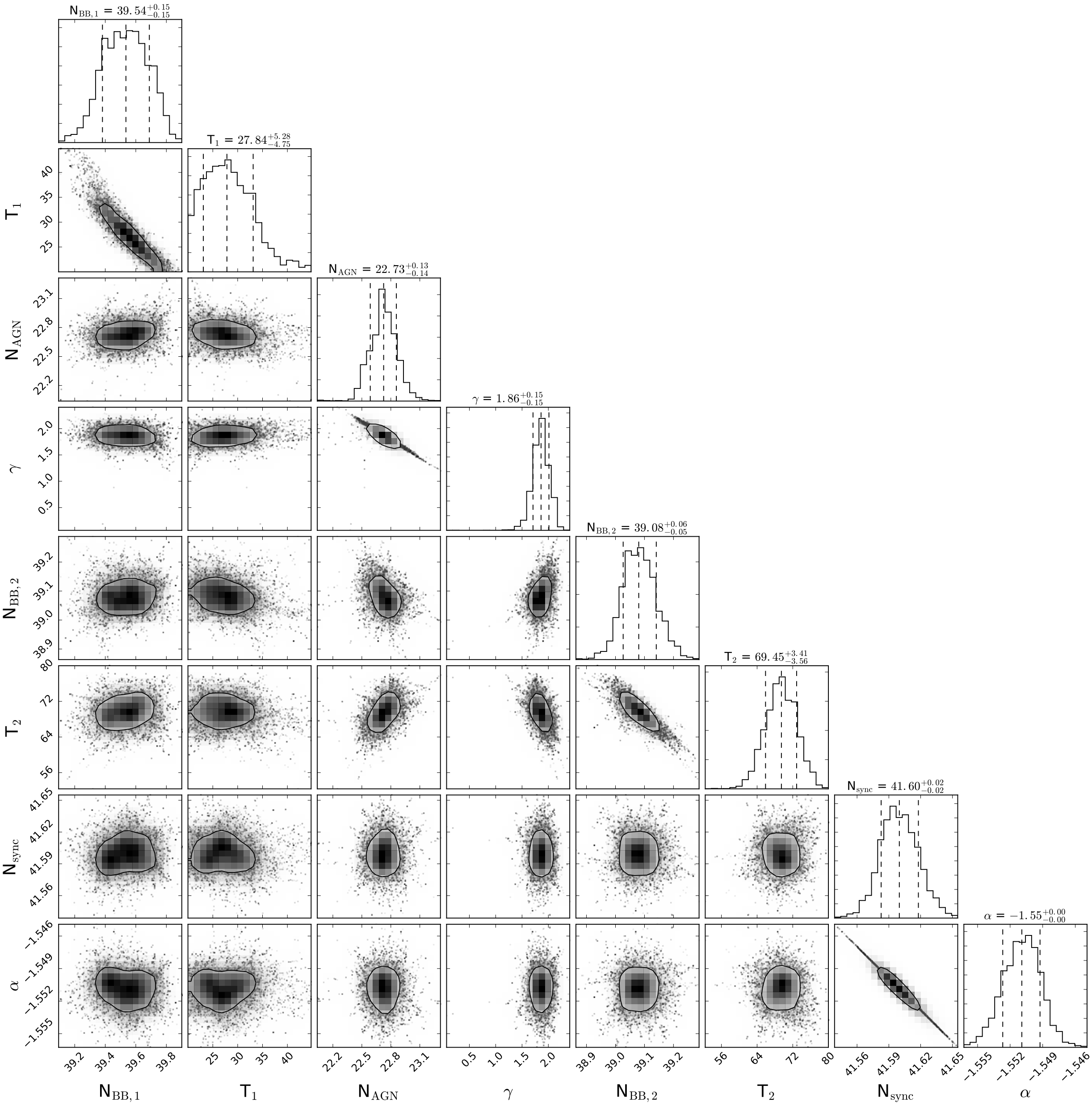

FIGURE A.12: **MRC 0152-209** Corner plot of the free parameters.

MRC 0156-252

MRC 0156-252 has two detected continuum detections, where one detection coincides with the radio core and the other with the northern radio lobe (Fig. A.13). SED fitting is done with five components, two synchrotron power-laws (one for the core, one for the northern lobe, the southern lobe is excluded from the fit), two modified BB for the two ALMA detections, and one AGN component. The VLA L and ATCA 7 mm bands are fitted to the total synchrotron emission since these data do not resolve the individual radio components, while the VLA C and X band fluxes are fitted with two individual synchrotron power-laws. The two ALMA band 6 flux points are fitted to a combination of the individual synchrotron power-law and modified black bodies. The LABOCA, PACS, SPIRE, MIPS and IRS data points are fitted by a combination of a modified BB and an AGN component. The best fit model is one where both the ALMA detections are dominated by synchrotron emission. This is because there are only upper limits in the FIR and they do not require the modified BB to be very bright (Fig. A.13). The PDF of the free parameters is shown in Fig. A.15, which clearly demonstrates that both BB models are completely unconstrained as expected given the upper limits in the FIR.

TABLE A.5: Data for MRC 0156-252 (z=2.02)

Photometric band	Flux[mJy]	Ref.
IRS (16 μm)	1.980 ± 0.1	A
PACS (70 μm)	13.8 ± 3.7	A
PACS (160 μm)	<23.3	B
SPIRE (250 μm)	<15.0	B
SPIRE (350 μm)	<18.0	B
SPIRE (500 μm)	<20.9	B
LABOCA (870 μm)	<21.0	C
ALMA 6^h	0.63 ± 0.39	this paper
ALMA 6^n	0.97 ± 0.58	this paper
ATCA (7 mm)	12.23 ± 1.2	this paper
VLA X^c	6.8 ± 1.64 [a]	D
VLA X^n	42.84 ± 4.2[a]	D
VLA C^c	10.19 ± 2.32 [a]	D
VLA C^n	81.48 ± 8.1 [a]	D
VLA L	415.9 ± 41.59	E

Notes (*h*) ALMA detection at host location, (*c*) Synchrotron core, (*n*) North synchrotron lobe, (*a*) flux estimated using AIPS from original radio map, convolved to the resolution of the VLA C band.

References. (A) De Breuck et al. (2010), (B) Drouart et al. (2014), (C) Archibald et al. (2001), (D) Kapahi et al. (1998), (E) Condon et al. (1998).

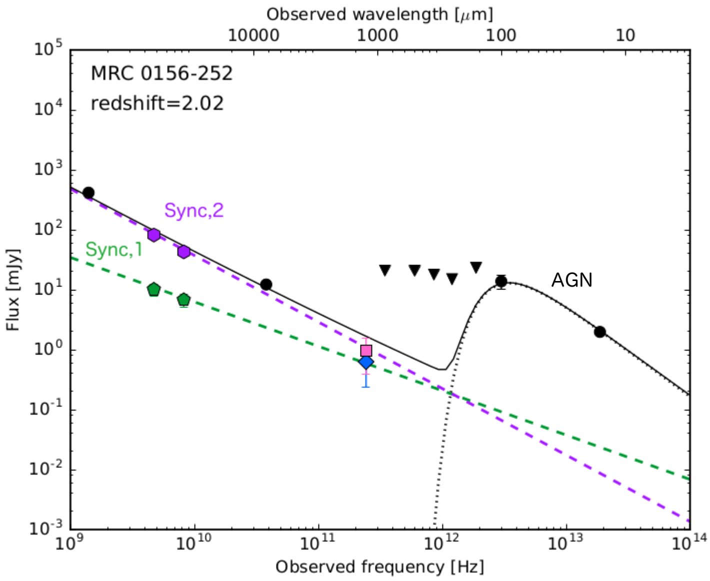

FIGURE A.13: The SED of **MRC 0156-252**. Black solid line shows the best fit total model, green and purple dashed line represents the northern lobe and synchrotron emission from the core, respectively. Black dotted line indicates the AGN component. The colored points are data which have sub-arcsec resolution and black ones indicate data of lower resolution. Green pentagons represent the fluxes of the radio core, purple hexagons are the fluxes of the northern radio lobe, the blue diamond indicates the ALMA band 6 detection which coincides with the radio core and the magenta square is the second ALMA detection of the northern radio lobe. Filled black circles indicate detections (>3σ) and downward pointing triangles 3σ upper limits (Table A.5).

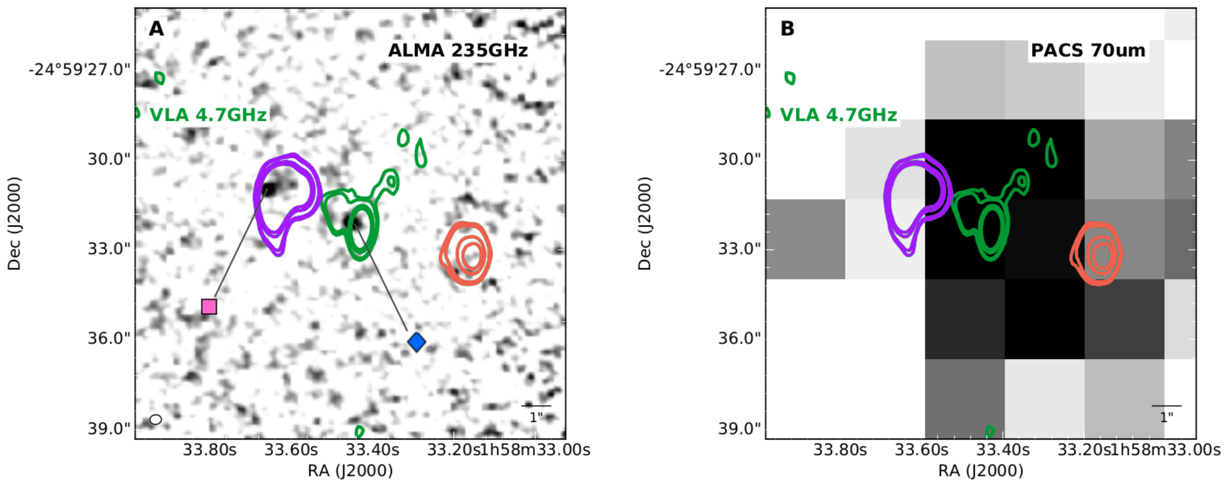

FIGURE A.14: *Panel A:* continuum map of ALMA band 6 with overlaid VLA C contours (levels are as Fig. A.2, $\sigma = 96\,\mu$Jy). The blue and pink markers show the two ALMA detections and correspond to the same markers used for the SED in Fig A.13. The core and northern radio lobes are color coded in the same colors as the flux markers in Fig. A.10, the flux of the southern lobe (red radio contours) was not used in the SED fit. *Panel B:* PACS 70 μm continuum map with radio contours overlaid.

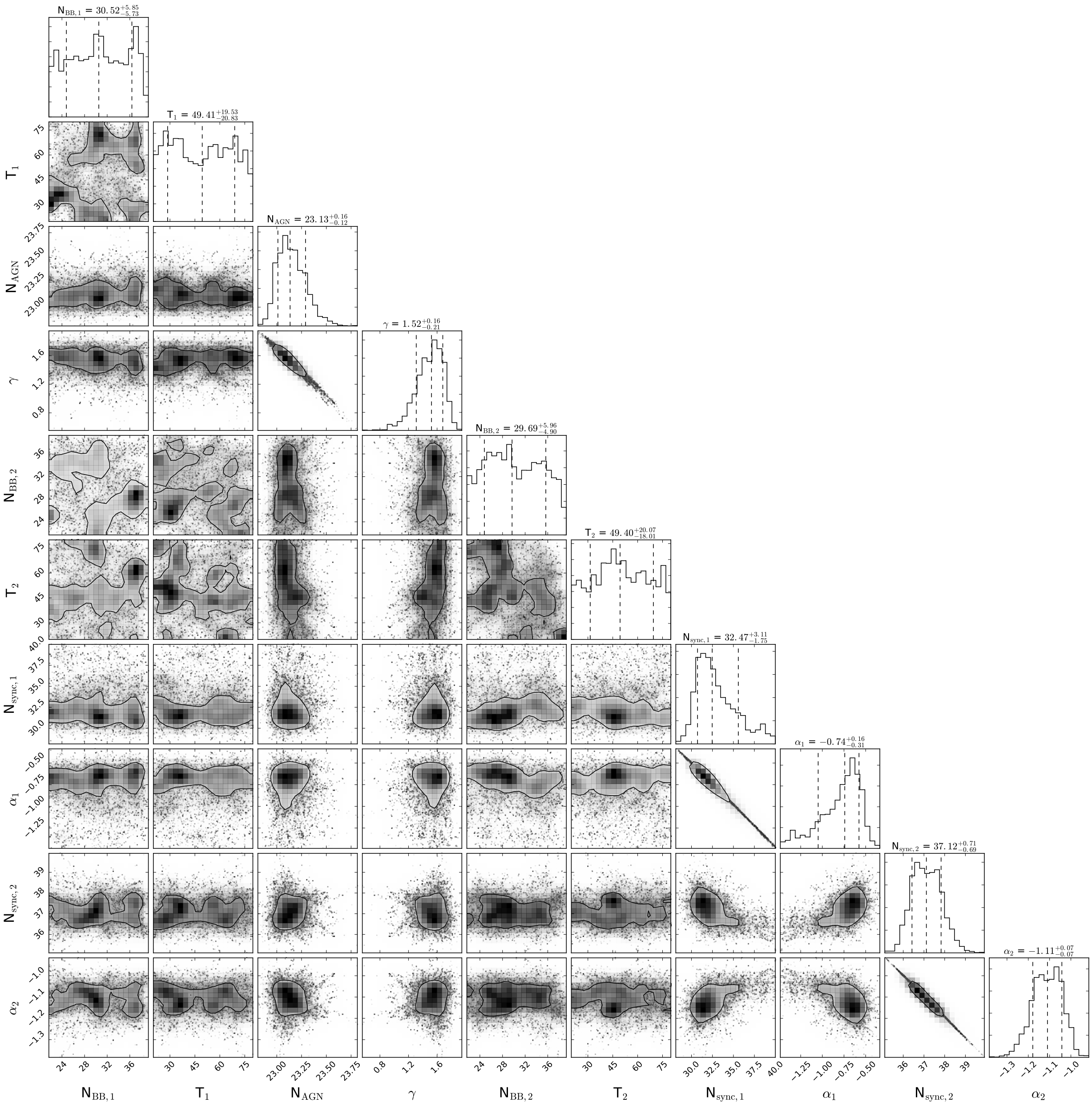

FIGURE A.15: **MRC 0156-252** Corner plot of the free parameters.

TN J0205+2242

TN J0205+2242 has no continuum detection (Fig. A.17). SED fitting with MrMoose is done with five models, two synchrotron power-laws (northern and southern radio component), two modified BB and one AGN component. The northern radio component (detected in VLA bands C and X) is assigned to the northern ALMA upper limit and the same setup is also applied to the southern radio and ALMA upper limit. The VLA band X detection does not resolve the individual components and are only considered for fitting the total radio flux (the combination of the northern and southern synchrotron power-law components). The two ALMA band 3 upper limits are both fitted with a combination of a synchrotron power-law and a modified BB. The SCUBA, PACS, SPIRE and IRS data points are fitted to the combination of the two modified black bodies and a AGN component. The best fit only constrain the two synchrotron models, both the SF and AGN dust components are unconstrained, due to the fact that all FIR and MIR data points are upper limits (Fig. A.16). The PDF of the free parameters can be found in Fig. A.18, where it is clear that only the two synchrotron components are constrained.

TABLE A.6: Data for TN J0205+2242 (z=3.506)

Photometric band	Flux[mJy]	Ref.
IRS (16 μm)	<0.211	A
PACS (70 μm)	<0.116	A
PACS (160 μm)	<7.3	B
SPIRE (250 μm)	<30.2	B
SPIRE (350 μm)	<14.6	B
SPIRE (500 μm)	<14.7	B
SCUBA (850 μm)	<5.2	C
ALMA 3^n	<0.051	this paper
ALMA 3^s	<0.045	this paper
VLA C^n	5.78 ± 0.59 [a]	D
VLA C^s	2.87 ± 0.28 [a]	D
VLA L	60.4 ± 2.8	E

Notes (*n*) North synchrotron component, (*s*) South synchrotron component, (*a*) flux estimated using AIPS from original radio map, convolved to the resolution of the VLA C band.

References. (A) De Breuck et al. (2010), (B) Drouart et al. (2014), (C) Reuland et al. (2003a), (D) De Breuck et al. (2000), (E) Condon et al. (1998).

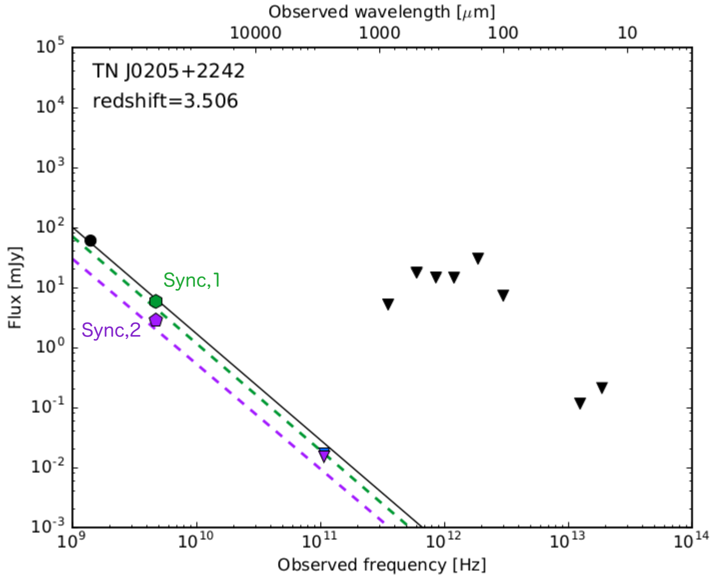

FIGURE A.16: SED of **TN J0205+2242**. Black solid line shows best fit total model, green and purple dashed line is the north and south synchrotron, respectively. The colored data points are sub-arcsec resolution data and black ones indicated data of low resolution. The blue and purple downward pointing triangles indicates the ALMA band 3 upper limits at the location of the two radio lobes, where the blue triangle is the upper limit of the host galaxy and the north synchrotron component. Filled black circles indicate detections (>3σ) and downward pointing triangles the 3σ upper limits (Table A.6).

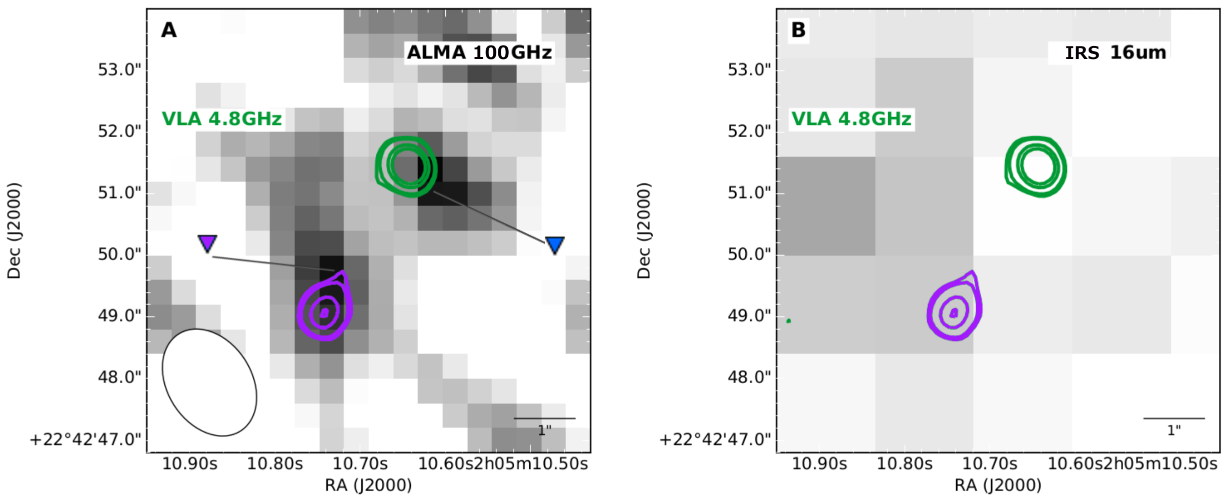

FIGURE A.17: *Panel A:* continuum map of ALMA band 3, overlaid VLA C contours (levels are as Fig. A.2, $\sigma = 85\,\mu$Jy). Blue and purple markers indicate the two different upper limits with ALMA and correspond to the same data points as Fig. A.16. The green and purple show the two components of the VLA data and correspond to the markers of the same colors as in the SED fit. *Panel B:* IRS 16 μm continuum map.

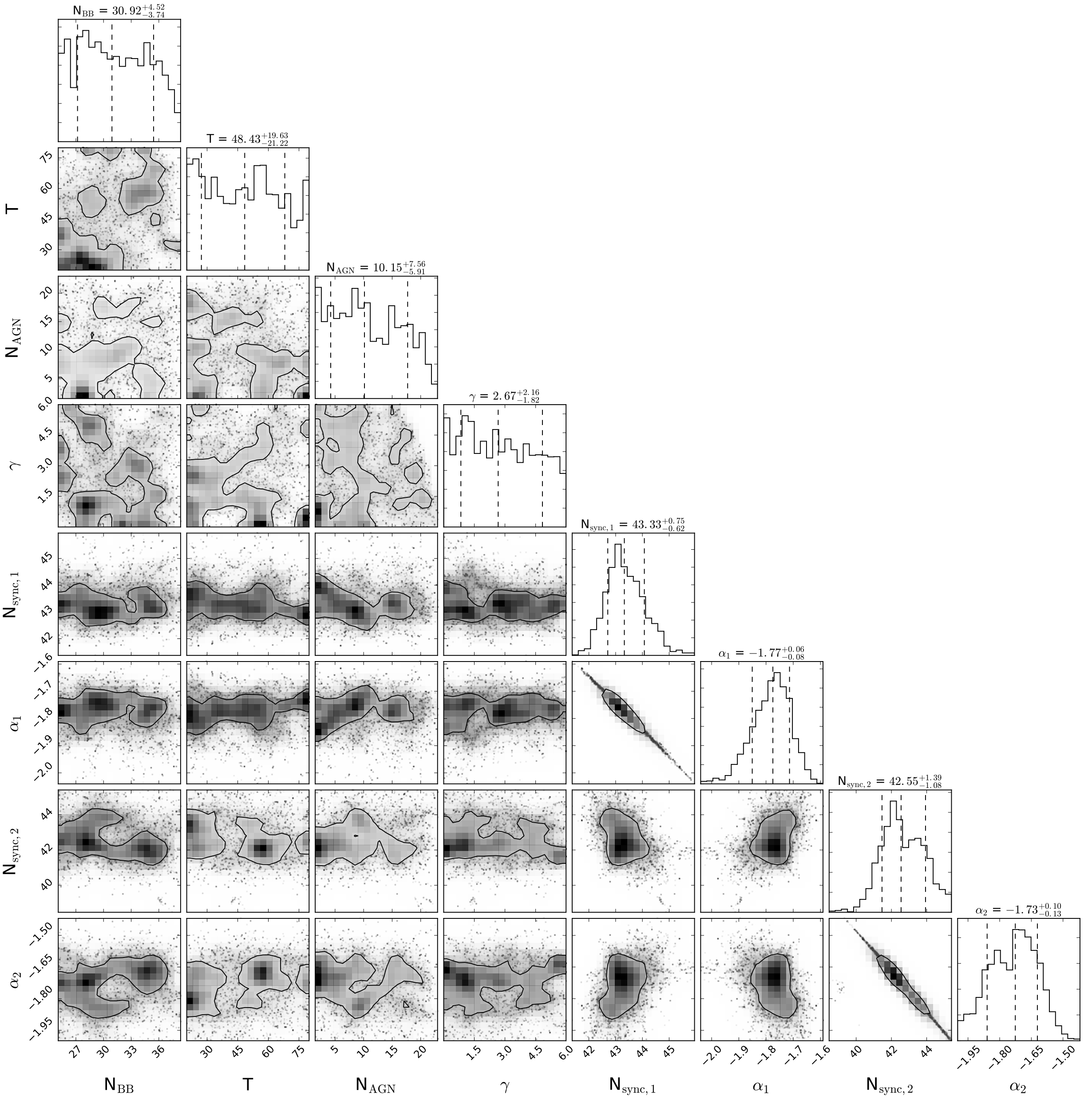

FIGURE A.18: **TN J0205+2242** Corner plot of the free parameters.

MRC 0211-256

MRC 0211-256 has one single continuum detection, which does not coincide with the radio emission (Fig. A.20). SED fitting with MrMosse is done with three components, one synchrotron power-law, one modified BB and one AGN component. VLA L, X, and C bands are only considered for fitting the total radio flux since only the total integrated flux for band L and X, C are reported in Condon et al. (1998) and Kapahi et al. (1998). The ALMA detection is assigned to both the synchrotron power-law and a modified BB component. The LABOCA, SPIRE, PACS, MIPS and IRS data points are fitted to the combination of the modified BB and a AGN component. The best fit model gives a solution where the ALMA band 6 flux is dominated by thermal dust emission (Fig. A.19). The PDF of the free parameters can be found in Fig. A.21.

TABLE A.7: Data for MRC 0211-256 (z=1.3)

Photometric band	Flux[mJy]	Ref.
IRS (16 μm)	0.378 ± 0.08	A
MIPS (24 μm)	0.710 ± 0.03	A
PACS (70 μm)	<9.5	B
PACS (160 μm)	17.4 ± 6.6	B
SPIRE (250 μm)	25.0 ± 3.8	B
SPIRE (350 μm)	25.9 ± 5.8	B
SPIRE (500 μm)	15.7 ± 5.9	B
LABOCA (870 μm)	<26.1	B
ALMA 6	0.67 ± 0.09	this paper
VLA X	19.04 ± 2.03 [a]	C
VLA C	79 ± 7.9	C
VLA L	337 ± 33.7	D

Notes (*a*) Flux estimated using AIPS from original radio map.

References. (A) De Breuck et al. (2010), (B) Drouart et al. (2014), (C) Carilli et al. (1997), (D) Condon et al. (1998).

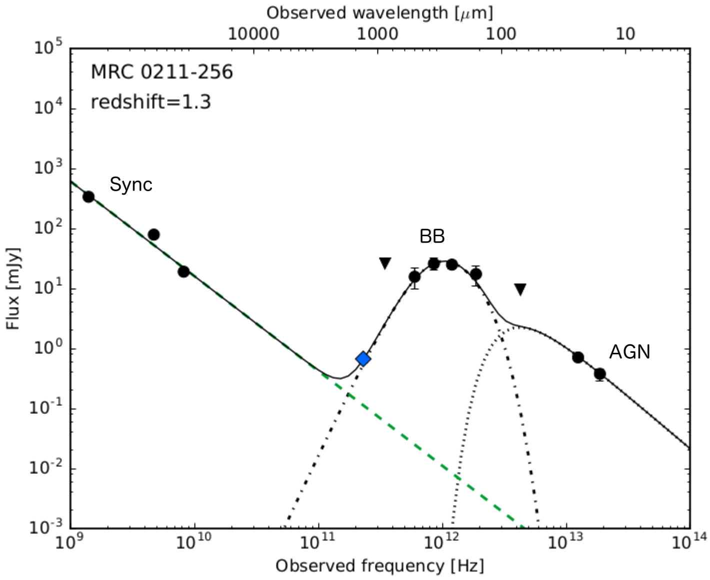

FIGURE A.19: SED of MRC 0211-256. Black solid line shows best fit total model, dashed line is total synchrotron, dash-dotted line is the black body component and the dotted line indicates the AGN component. The colored data point is sub-arcsec resolution data and black ones indicated data of low resolution. Blue diamond indicates ALMA band 6 detection. Filled black circles indicate detections (>3σ) and downward pointing triangles the 3σ upper limits (Table A.7).

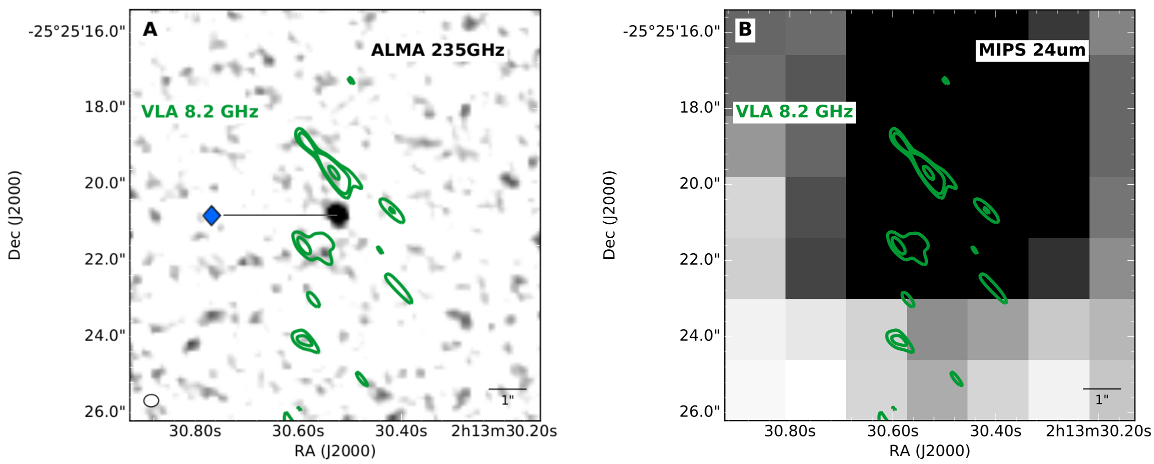

FIGURE A.20: *Panel A:* continuum map of ALMA band 6 with overlaid VLA C contours (levels are as Fig. A.2, $\sigma = 86\,\mu$Jy). The blue diamond indicates the ALMA detection and is the same marker used in Fig. A.19. The green contours show the portion of the VLA data that is used in the SED fit. *Panel B:* MIPS 24 μm continuum map.

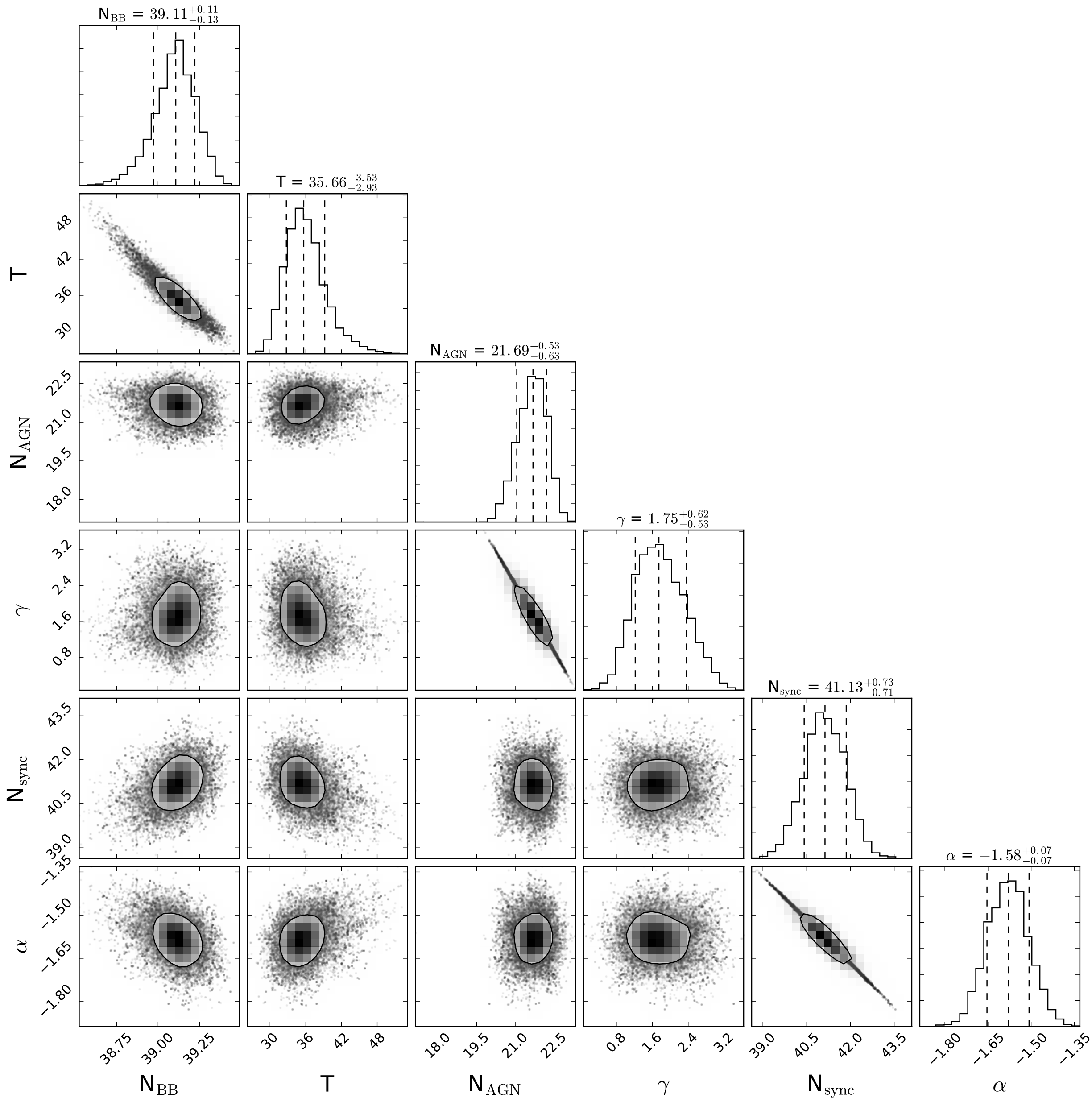

FIGURE A.21: **MRC 0211-256** Corner plot of the free parameters.

TXS 0211-122

TXS 0211-122 have one single continuum detection, which coincide with the radio core (Fig. A.23). SED fitting with Mr-Moose is done with three components, one synchrotron power-law (for the radio core, the two lobes are excluded in the fit), one modified BB and one AGN component. The VLA data is fitted to the synchrotron component, the ALMA data point is assigned to both the synchrotron power-law and a modified BB. The LABOCA, PACS, SPIRE, MIPS and IRS are fitted to the combination of the modified BB and a AGN component. The best fit model gives a solution where the ALMA band 6 flux is dominated by emission from heated dust (Fig. A.22). The reason why the PACS 160 μm data point is not well fitted is due to the fact that the AGN power-law have a fixed exponential cut off at 33 μm rest frame and the ALMA point puts hard constraints on the normalization parameter of the modified BB. The PDF of the free parameters can be found in Fig. A.24.

TABLE A.8: Data for TXS 0211-122 (z=2.34)

Photometric band	Flux[mJy]	Ref.
IRS (16 μm)	1.590 $\pm$ 0.22	A
MIPS (24 μm)	2.75 $\pm$ 0.04	A
PACS (100 μm)	7.4 $\pm$ 3.4	B
PACS (160 μm)	11.7 $\pm$ 5.9	B
SPIRE (250 μm)	<15.9	B
SPIRE (350 μm)	<19.2	B
SPIRE (500 μm)	<24.5	B
LABOCA (870 μm)	<24.6	B
ALMA 6	0.30$\pm$ 0.08	this paper
VLA X^c	1.31 $\pm$ 0.13^a	C
VLA C^c	2.66 $\pm$ 0.26 ^{a}	C
ATCA (7mm)*	4.25$\pm$1.5 3	this paper

Notes (*c*) Radio core (*a*) Flux estimated using AIPS from original radio map, convolved to the resolution of the VLA C band (*) data not used in SED fitting.

References. (A) De Breuck et al. (2010), (B) Drouart et al. (2014), (C) Carilli et al. (1997).

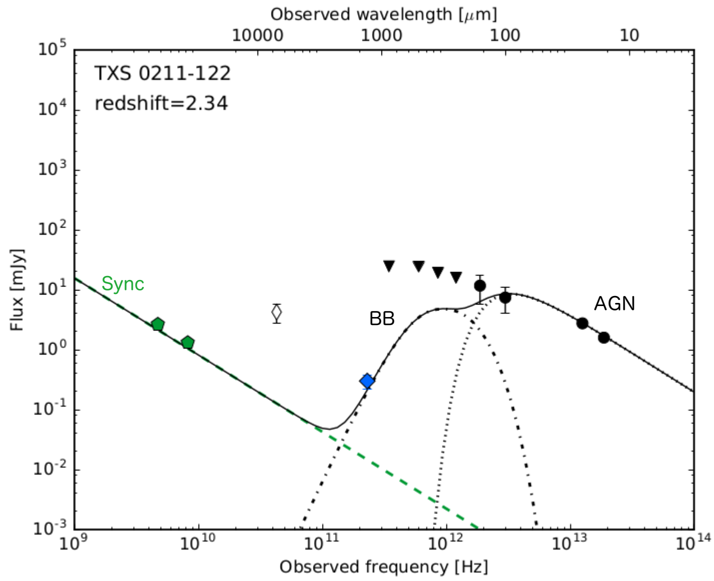

FIGURE A.22: SED of **TXS 0211-122**. Black solid line shows best fit total model, green dashed line is total synchrotron, black dash-dotted line is the black body component, black dotted line indicates the AGN component. The colored data points are sub-arcsec resolution data and black ones indicate data of low resolution. Green pentagons are the radio core and the blue diamond indicates ALMA band 6 detection. Filled black circles indicate detections (>3σ) and downward pointing triangles the 3σ upper limits (Table A.8). The open diamond shows available ATCA data but only plotted as a reference and was not used in the SED fit.

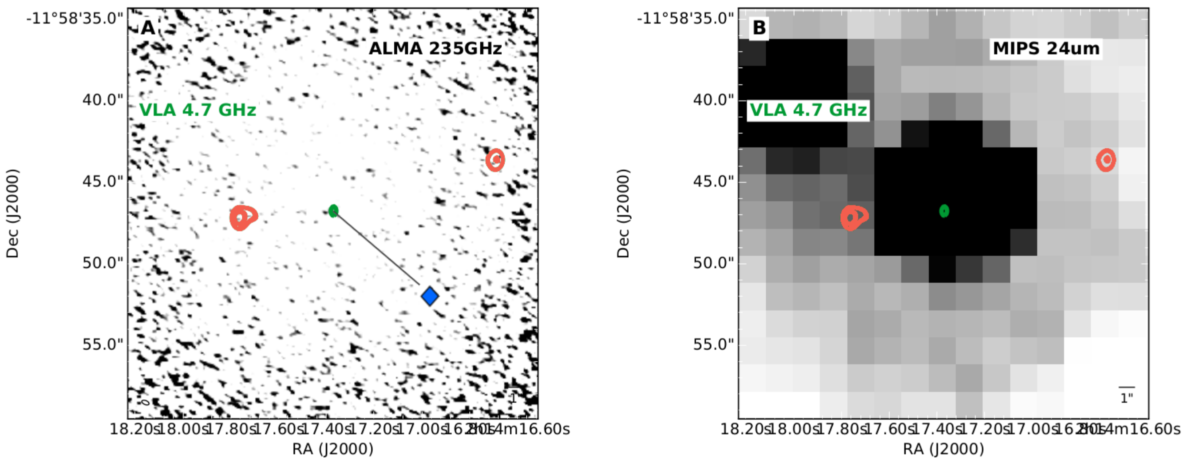

FIGURE A.23: *Panel A:* continuum map of ALMA band 6 with overlaid VLA C contours (levels are as Fig. A.2, $\sigma = 53\,\mu$Jy). The blue diamond indicates the ALMA detection and is the same marker used in Fig. A.22. The green contours show the portion of the VLA data that is used in the SED fit, the red contours are excluded in the fit. *Panel B:* MIPS 24 μm continuum map.

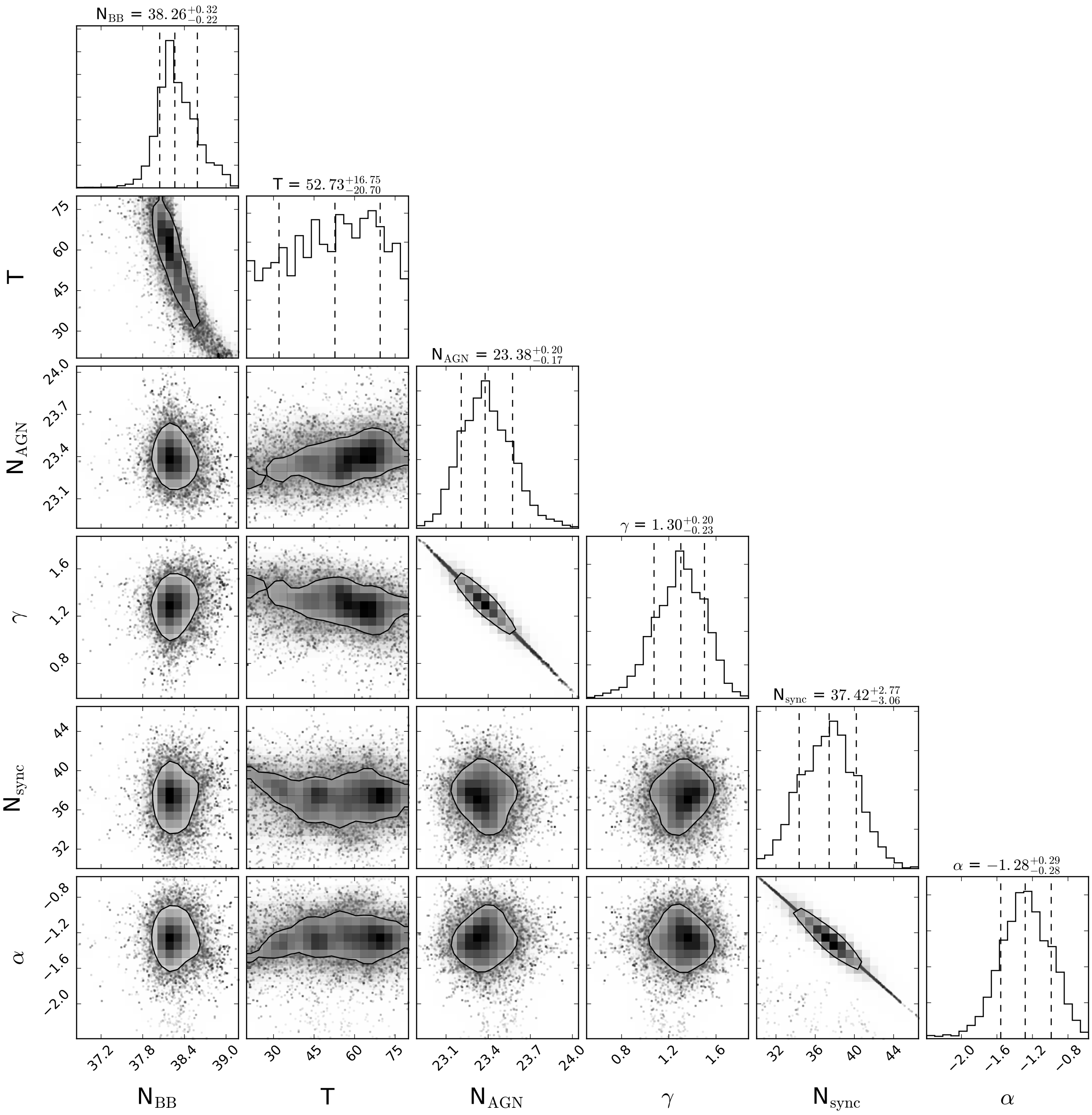

FIGURE A.24: **TXS 0211-122** Corner plot of the free parameters.

MRC 0251-273

MRC 0251-273 has one continuum detection which coincides with one of the two radio components (Fig. A.26). SED fitting with MrMoose is done with four components, two synchrotron (northern and southern radio component), one modified BB and one AGN component. The northern radio component (detected in VLA bands C and X) is assigned to the ALMA detection and fitted with with an individual power-law. The southern radio component is only assigned to the VLA bands C and X. The ALMA detection is associated to the northern synchrotron power-law and a modified BB. The SCUBA, SPIRE, PACS, MIPS and IRS data are fitted to the combination of the modified BB and a AGN component. The best fit model gives that the ALMA detection is dominated by dust emission (Fig. A.25). The slope of the northern synchrotron component is very steep and this can be due to not properly extracted photometry because of blending between the two components. The PDF of the free parameters can be found in Fig. A.27.

TABLE A.9: Data for MRC 0251-273 (z=3.16)

Photometric band	Flux[mJy]	Ref.
IRS (16 μm)	0.102 ± 0.033	A
MIPS (24 μm)	0.476 ± 0.033	A
PACS (100 μm)	<10.0	B
PACS (70 μm)	<18.7	B
SPIRE (250 μm)	<15.7	B
SPIRE (350 μm)	<14.1	B
SPIRE (500 μm)	<19.3	B
SCUBA (850 μm)	<8.9	C
ALMA 6	0.35 ± 0.07	this paper
VLA X^n	1.35 ± 0.14 [a]	A
VLA X^s	34.86 ± 0.35 [a]	A
VLA C^n	12.22 ± 0.12 [a]	A
VLA C^s	72.36 ± 0.72 [a]	A

Notes (*n*) North radio component, (*s*) south radio component, (*a*) flux estimated using AIPS from original radio map, convolved to the resolution of the VLA C band.

References. (A) De Breuck et al. (2010), (B) Drouart et al. (2014), (C) Carilli et al. (1997).

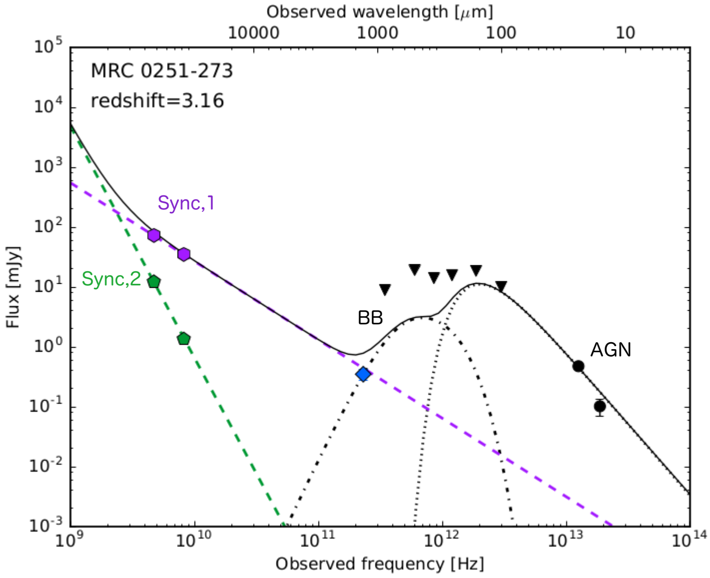

FIGURE A.25: SED of **MRC 0251-273**. Black solid line shows best fit total model, green and purple dashed line is north and south synchrotron lobes, respectively. Black dashed-dotted line shows the black body and the black dotted line indicates the AGN component. The coloured data points are sub-arcsec resolution data and black ones indicate data of low resolution. Green pentagons are north synchrotron, purple hexagons are the south radio component and the blue diamond indicates the ALMA band 6 detection. Filled black circles indicate detections (>3σ) and downward pointing triangles the 3σ upper limits (Table A.9).

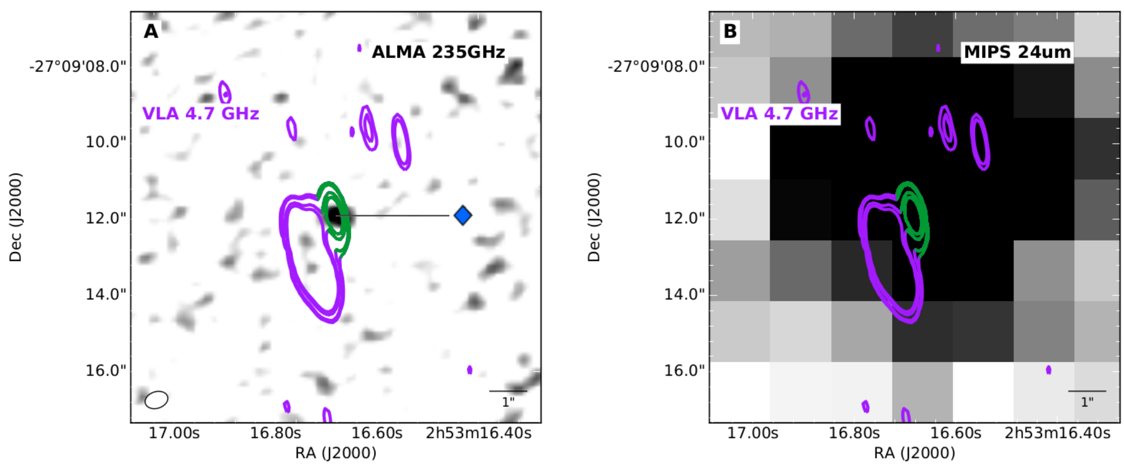

FIGURE A.26: *Panel A:* continuum map of ALMA band 6 with overlaid VLA C contours (levels are as Fig. A.2, $\sigma = 48\,\mu$Jy). The blue diamond indicates the ALMA detection and is the same marker style used in Fig. A.25. Green contours show the two components of the VLA data and correspond to the markers of the same colors as in the SED fit. Panel B: MIPS. *Panel B:* MIPS 24 μm continuum map

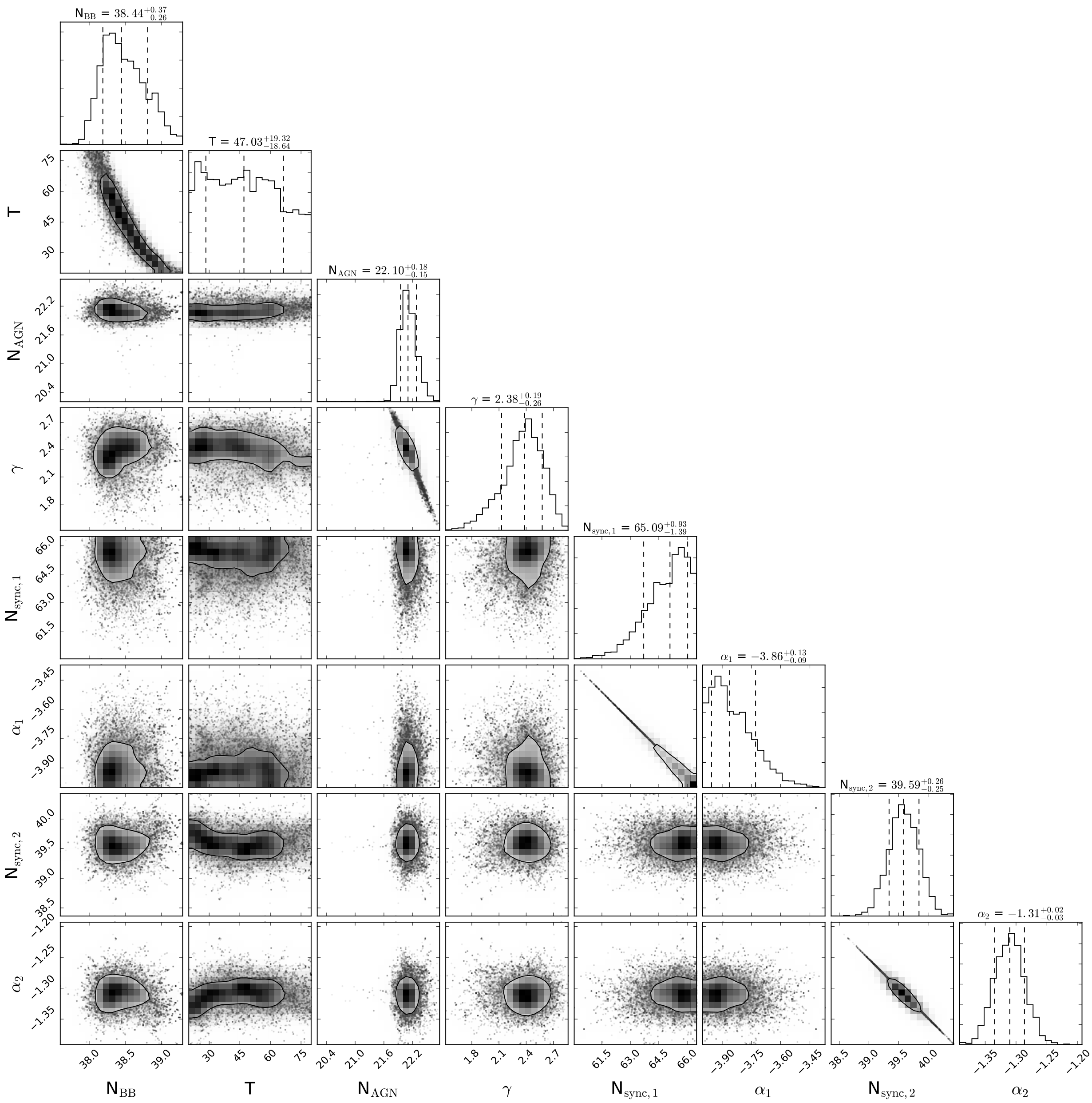

FIGURE A.27: **MRC 0251-273** Corner plot of the free parameters.

MRC 0324-228

MRC 0324-228 has no continuum detection with ALMA (Fig. A.29). SED fitting with MrMoose is done with four components, two synchrotron power-law (northern and southern radio component), one modified BB and one AGN component. The northern radio component (detected in VLA bands C and X) is assigned to an individual synchrotron power-law and the same setup is also applied for the southern radio component. The VLA band L and ATCA 7 mm data do not resolve the individual components and are only considered for fitting the total radio flux (the combination of the northern and southern synchrotron power-law components). The ALMA band 6 detection is also assigned to the total radio flux and to a modified BB. The LABOCA, SIPRE, PACS, MIPS and IRS data are fitted to the combination of the modified BB and a AGN component. The best fit model does not constrain the modified BB due to only upper limits in the FIR. Without an intermediate data point between ALMA and ATCA 7 mm it is not possible to determine where the steepening occurs, but the upper limit in ALMA is consistent with a continued synchrotron slope. The PDF of the free parameters can be found in Fig. A.30.

TABLE A.10: Data for MRC 0324-228 (z=1.89)

Photometric band	Flux[mJy]	Ref.
IRS (16 μm)	0.530 ± 0.054	A
MIPS (24 μm)	1.880 ± 0.035	A
PACS (70 μm)	<9.1	B
PACS (160 μm)	27.9 ± 5.4	B
SPIRE (250 μm)	61.8 ± 6.7	B
SPIRE (350 μm)	35.5 ± 5.9	B
SPIRE (500 μm)	17.5 ± 7.4	B
LABOCA (870 μm)	<9.0	B
ALMA 6	<0.21	this paper
ATCA (7 mm)	5.9 ± 1.77	this paper
VLA X^n	24.54 ± 0.24^a	A
VLA X^s	12.22 ± 0.12^a	A
VLA C^n	77.86 ± 0.77^a	A
VLA C^s	28.70 ± 0.28^a	A
VLA L	518.7 ± 51	C

Notes (n) North radio component, (s) south radio component, (a) flux estimated using AIPS from original radio map, convolved to the resolution of the VLA C band.

References. (A) De Breuck et al. (2010), (B) Drouart et al. (2014), (C) Condon et al. (1998).

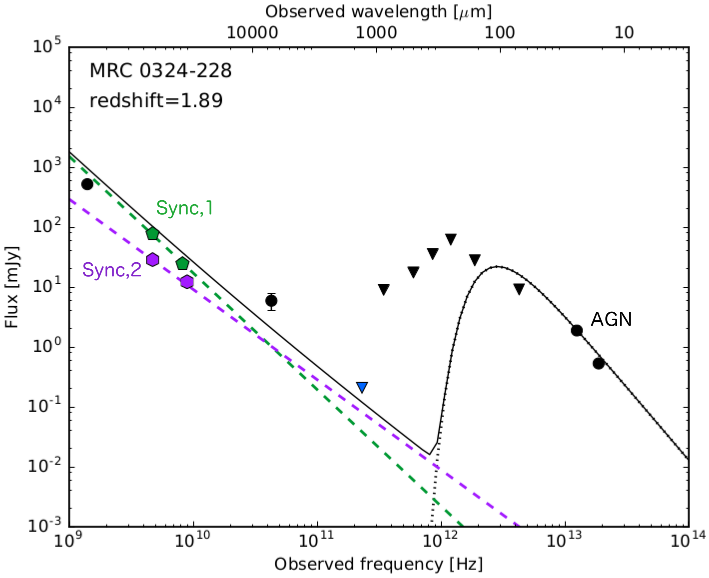

FIGURE A.28: SED of **MRC 0324-228**. Black solid line shows best fit total model, green and purple dashed line is north and south synchrotron lobes, respectively. Black dotted line indicates the AGN component. The coloured data points are sub-arcsec resolution data and black ones indicate data of low resolution. Green pentagons are north synchrotron, purple hexagons are the south radio component and the blue triangle indicates the ALMA band 6 3σ upper limit. Filled black circles indicate detections (>3σ) and downward pointing triangles the 3σ upper limits (Table A.10).

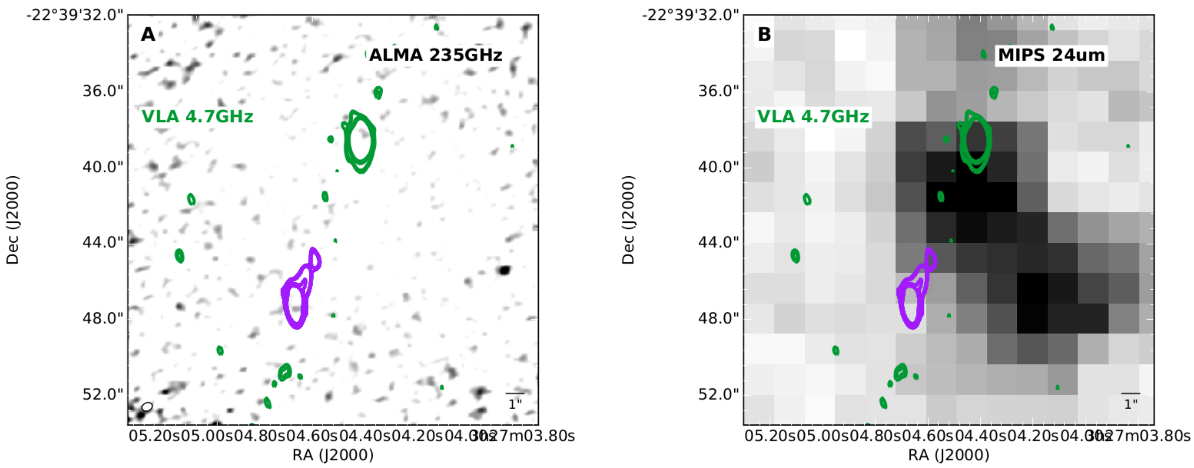

FIGURE A.29: *Panel A:* continuum map of ALMA band 6 with overlaid VLA C (levels are as Fig. A.2, σ = 53 μJy). The green and purple contours show the two components of the VLA data and correspond to the markers of the same colors as in the SED fit (Fig. A.28). *Panel B:* MIPS 24 μm continuum map.

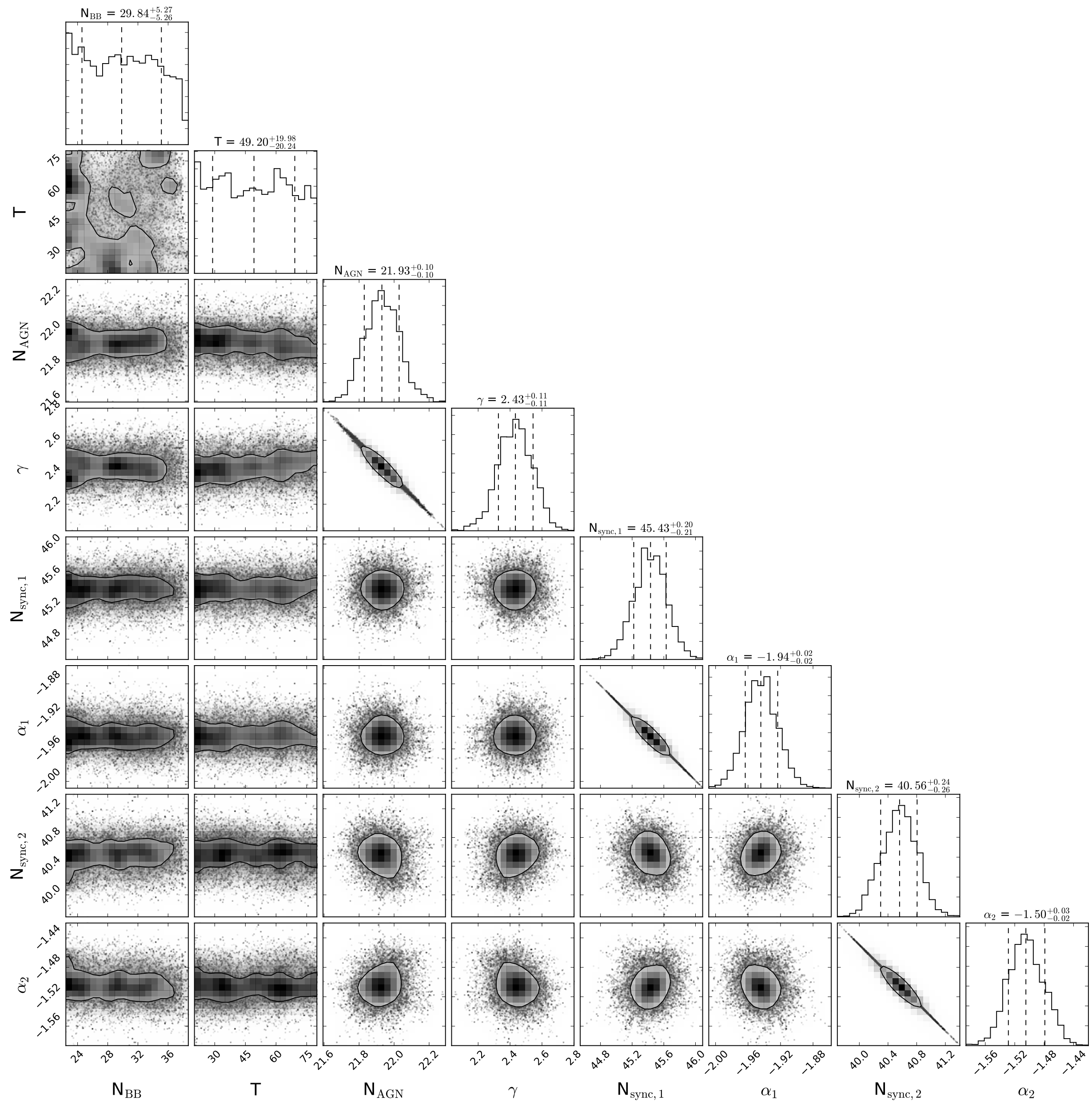

FIGURE A.30: **MRC 0324-228** Corner plot of the free parameters.

MRC 0350-279

MRC 0350-279 has no continuum detection with ALMA (Fig. A.32). SED fitting with MrMoose is done with four components two synchrotron power-law (northern and southern radio component), one modified BB and one AGN component. The northern radio component (detected in VLA bands C and X) is assigned to an individual synchrotron power-law and the same setup is also applied for the southern radio component. The VLA band L and ATCA 7 mm data do not resolve the individual components and are only considered for fitting the total radio flux (the combination of the northern and southern synchrotron power-law components) The ALMA band 6 upper limit is assigned to the total radio flux and a modified BB. The LABOCA, SIPRE, PACS, MIPS and IRS data are fitted to the combination of the modified BB and a AGN component. The best fit model gives a solution where the ALMA detection is dominated by synchrotron, but the combined models is slightly over predict the 3σ upper limit at 235 GHz (Fig. A.31). The PDF of the free parameters can be found in Fig. A.33.

TABLE A.11: Data for MRC 0350-279 (z=1.90)

Photometric band	Flux[mJy]	Ref.
IRS (16 μm)	0.208 ± 0.04	A
MIPS (24 μm)	0.306 ± 0.044	A
PACS (70 μm)	<11.3	B
PACS (160 μm)	<25.5	B
SPIRE (250 μm)	<14.2	B
SPIRE (350 μm)	<14.0	B
SPIRE (500 μm)	<15.9	B
LABOCA (870 μm)	<23.1	B
ALMA 6	<0.19	this paper
ATCA (7 mm)	4.9 ± 1.47	this paper
VLA X^n	17.48 ± 0.17 [a]	A
VLA X^s	15.61 ± 0.15 [a]	A
VLA C^n	41.05 ± 0.41 [a]	A
VLA C^s	32.67 ± 0.32 [a]	A
VLA L	350.3 ± 35	C

Notes (*n*) North radio component, (*a*) south radio component, (*a*) flux estimated using AIPS from original radio map, convolved to the resolution of the VLA C band.

References. (A) De Breuck et al. (2010), (B) Drouart et al. (2014), (C) Condon et al. (1998).

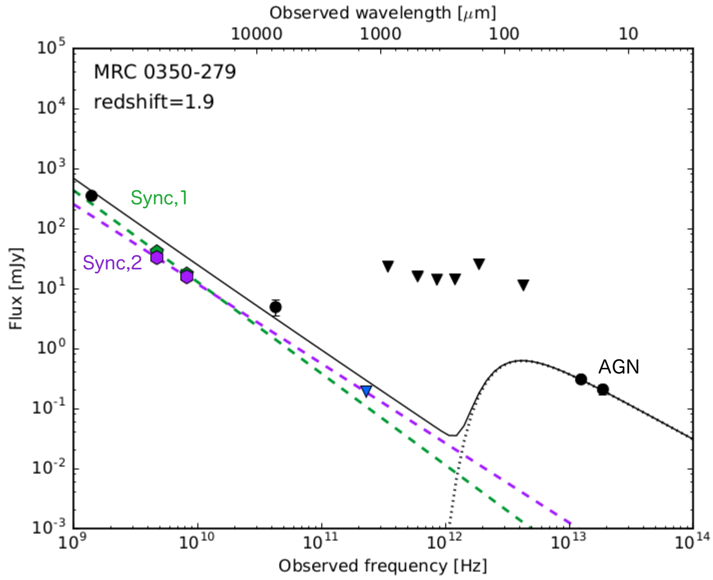

FIGURE A.31: SED of **MRC 0350-279**. Black solid line shows best fit total model, green and purple dashed line are the north and south synchrotron lobes, respectively. Black dotted line indicates the AGN component. The coloured data points are sub-arcsec resolution data and black ones indicate data of low resolution. Green pentagons and purple hexagons are the north and south radio component, respectively and the blue triangle indicates the ALMA band 6 3σ upper limit. Filled black circles indicate detections (>3σ) and downward pointing triangles the 3σ upper limits (Table A.11).

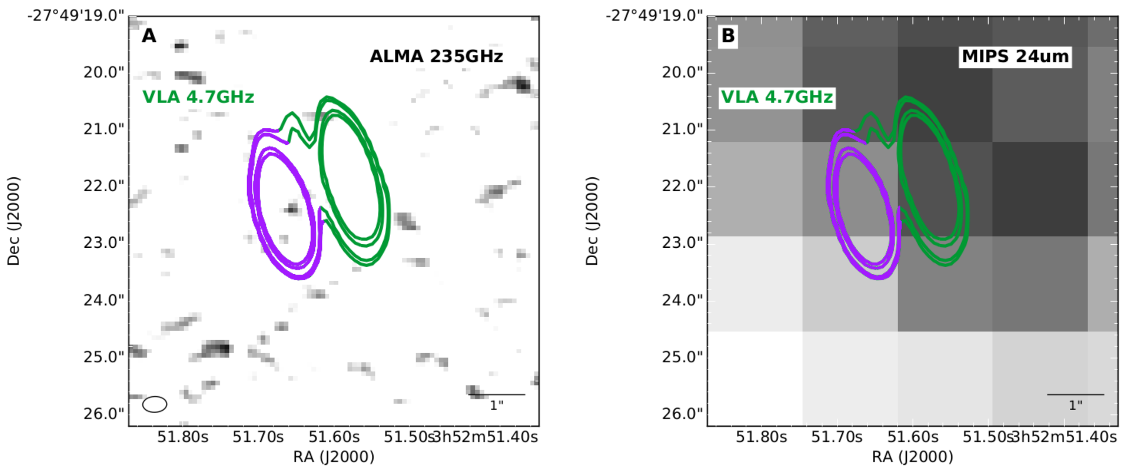

FIGURE A.32: *Panel A:* continuum map of ALMA band 6 with overlaid VLA C contours (levels are as Fig. A.2,σ = 58 μJy). The purple and green contours show the two components of the VLA data and correspond to the markers of the same colors as in the SED fit. *Panel B:* MIPS 24 μm continuum map.

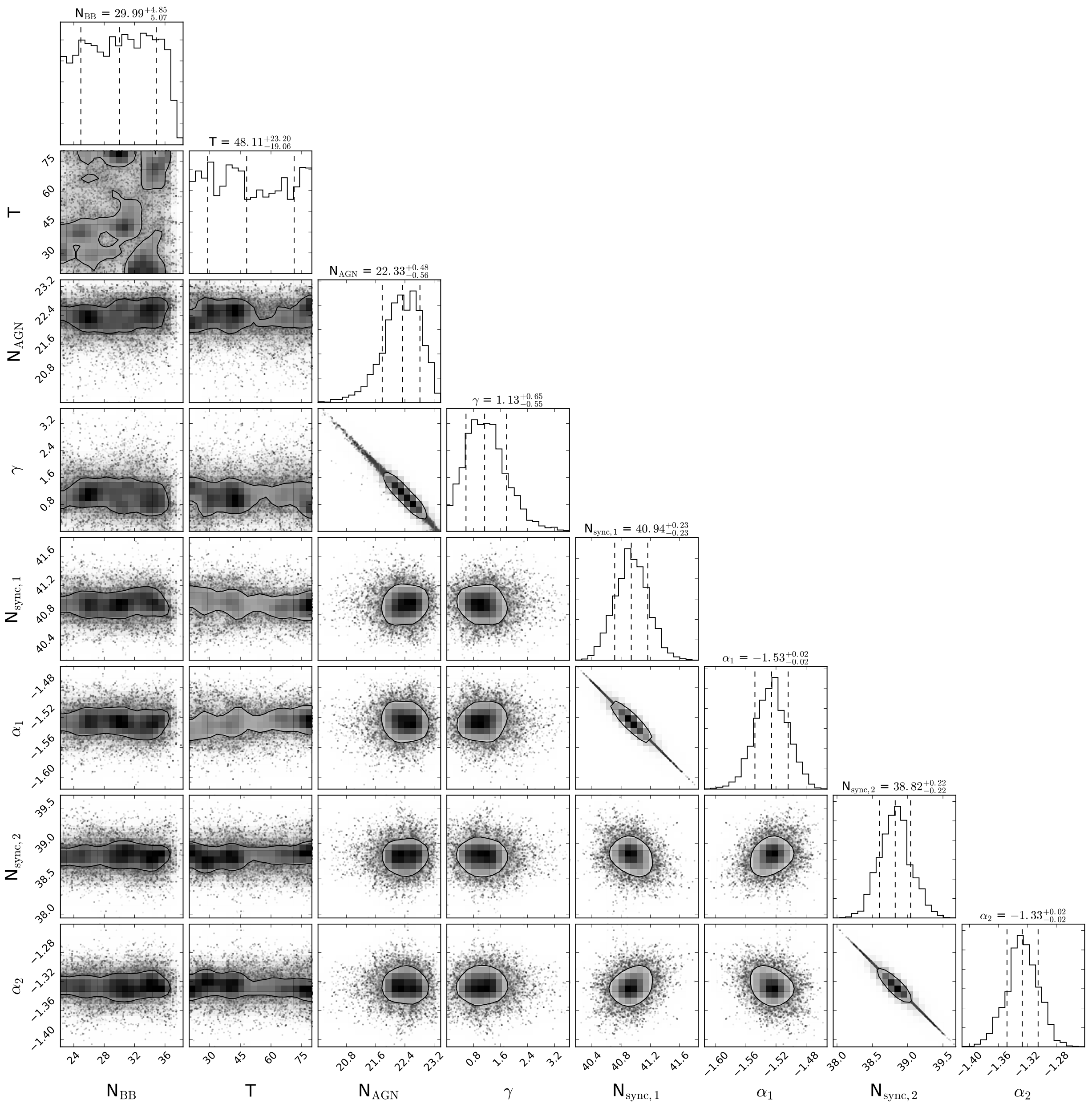

FIGURE A.33: **MRC 0350-279** Corner plot of the free parameters.

MRC 0406-244

MRC 0406-244 has one single continuum detection which coincides with the radio core (Fig. A.35). SED fitting with MrMoose is done with three components, one synchrotron (of the radio core, the two lobes are excluded in the fit), one modified BB and one AGN component. The VLA data is fitted to the synchrotron power-law, the ALMA detection is assigned to both the synchrotron component and a modified BB. The LABOCA, SPIRE, PACS, MIPS and IRS is fitted to combination of the modified BB and a AGN component. The best SED fits favors a solution where the ALMA detection is dominated by synchrotron emission, due to the many upper limits in FIR and that there is no intermediate data point which could conclude whether the synchrotron is steepening at higher frequencies. The modified BB is completely unconstrained (Fig. A.34). The PDF of the free parameters can be found in Fig. A.36.

TABLE A.12: Data for MRC 0406-244 (z=2.43)

Photometric band	Flux[mJy]	Ref.
IRS (16 μm)	0.637 ± 0.086	A
MIPS (24 μm)	1.540 ± 0.04	A
PACS (100 μm)	<12.3	B
PACS (160 μm)	21.5 ± 7.9	B
SPIRE (250 μm)	47.6 ± 5.6	B
SPIRE (350 μm)	38.7 ± 5.3	B
SPIRE (500 μm)	22.8 ± 5.9	B
LABOCA (870 μm)	<17.8	B
ALMA 6	0.5 ± 0.1	this paper
VLA X[c]	1.84 ± 0.18[a]	A
VLA C[c]	2.70 ± 0.21[a]	A
ATCA (7mm)*	6.82±2.43	this paper

Notes(*c*) Radio core, (*a*) Flux estimated using AIPS from original radio map, convolved to the resolution of the VLA C band (*) data not used in fitting.
References. (A) De Breuck et al. (2010), (B) Drouart et al. (2014).

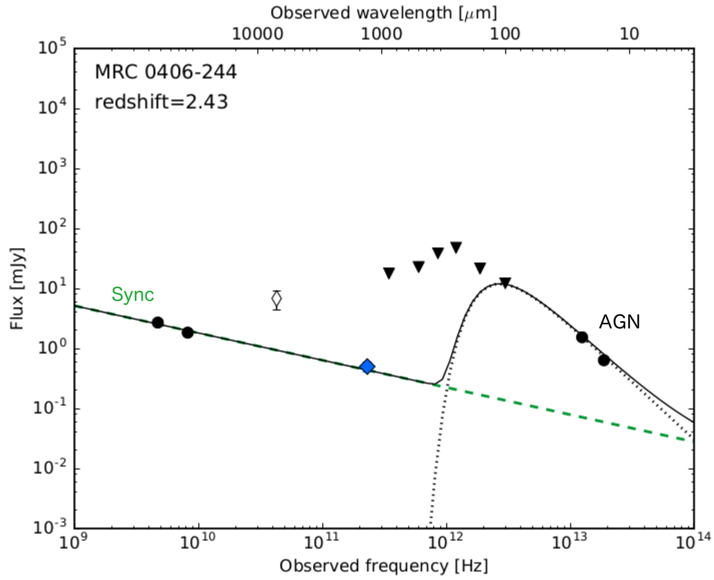

FIGURE A.34: SED of **MRC 0406-244**. Black solid line shows best fit total model, green dashed line is the synchrotron core and the black dotted line indicates the AGN component. The coloured data points are sub-arcsec resolution data and black ones indicate data of low resolution. Green pentagons are the radio core and the blue diamond indicates the ALMA band 6 detection. Filled black circles indicate detections (>3σ) and downward pointing triangles the 3σ upper limits (Table A.12). The open diamond indicate available ATCA data but only plotted as a reference and was not used in the SED fit.

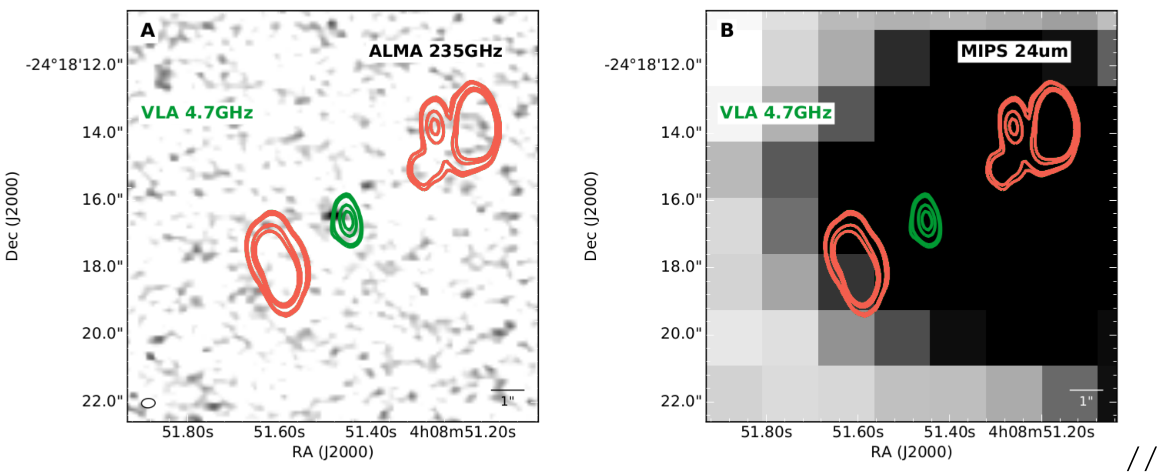

FIGURE A.35: *Panel A:* continuum map of ALMA band 6 with overlaid VLA C contours (levels are as Fig. A.2, $\sigma = 92\,\mu$Jy). The green contours show the portion of the VLA data that is used in the SED fit, the red contours are excluded in the fit. *Panel B:* MIPS 24 μm continuum map.

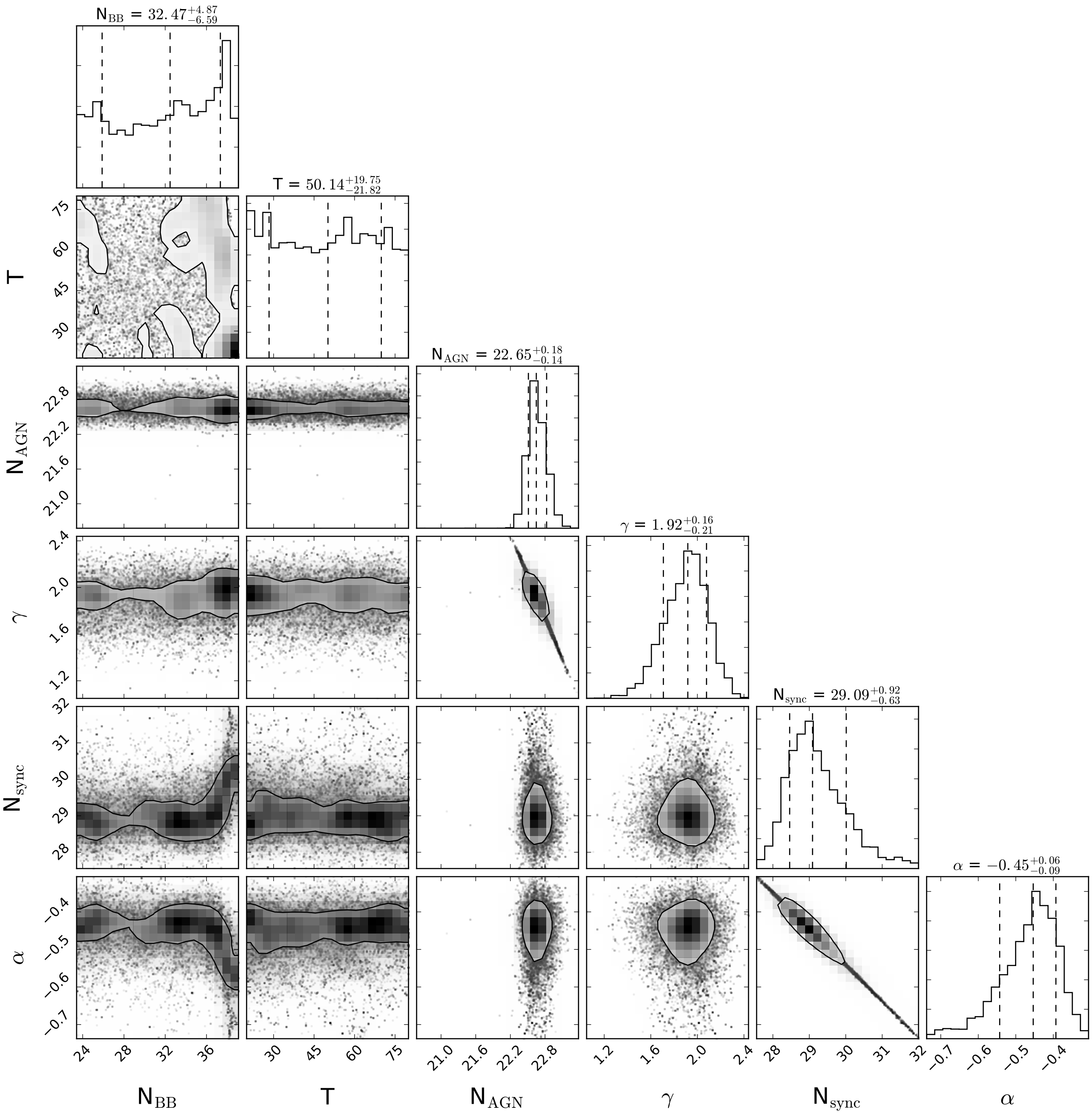

FIGURE A.36: **MRC 0406-244** Corner plot of the free parameters.

PKS 0529-549

PKS 0529-549 has two continuum detections, both coinciding with the two radio components (Fig. A.38). The SED fit is done with five components, two synchrotron power-laws (eastern and western radio components), two modified BB and one AGN component. The western radio component (detected in ATCA 8640-18496 MHz) is assigned to the western ALMA detection and fitted with an individual synchrotron power-law and the same setup is also applied to the eastern radio and ALMA components. The ATCA 7 mm data do not resolve the individual components and are only considered for fitting the total radio flux (the combination of the western and eastern synchrotron power-law components). The eastern ALMA detection is assigned to the first synchrotron component and to a modified BB component, while the western ALMA detection is similarly assigned to the second synchrotron component and another modified BB component. The SPIRE, PACS, MIPS and IRS data are fitted to the combination of the two modified black bodies and an AGN component. The best solution finds that the western ALMA detection is dominated by thermal dust emission and the eastern component is pure synchrotron emission (Fig. A.37). The PDF of the parameters shows that the second BB is completely unconstrained (Fig. A.39).

TABLE A.13: Data for PKS 0529-549 (z=2.58)

Photometric band	Flux[mJy]	Ref.
IRS (16 μm)	0.248 ± 0.089	A
MIPS (24 μm)	0.966 ± 0.040	A
MIPS (70 μm)	<4.11	A
MIPS (160 μm)	<74.1	A
PACS (100 μm)	8.3 ± 4.0	B
PACS (160 μm)	31.9 ± 9.0	B
SPIRE (250 μm)	35.1 ± 7.3	B
SPIRE (350 μm)	43.8 ± 8.3	B
SPIRE (500 μm)	40.0 ± 8.9	B
ALMA 6^w	1.33 ± 0.16	this paper
ALMA 6^e	0.37 ± 0.074	this paper
ATCA (18496 MHz)^w	23.4 ± 1.5	C
ATCA (18496 MHz)^e	6.3 ± 0.63	C
ATCA (16448 MHz)^w	26.3 ± 1.3	C
ATCA (16448 MHz)^e	7.3 ± 0.73	C
ATCA (8640 MHz)^w	55.2 ± 5.52	C
ATCA (8640 MHz)^e	20.7 ± 2.07	C
ATCA (7 mm)	158 ± 15.8	this paper

Notes (w) West component, (e) East component.
References. (A) De Breuck et al. (2010), (B) Drouart et al. (2014), (C) Broderick et al. (2007)

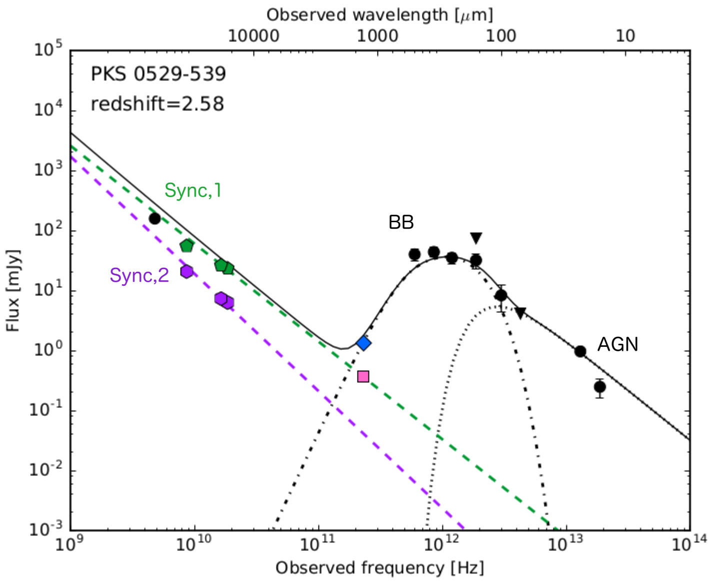

FIGURE A.37: SED of **PKS 0529-549**. The black solid line shows best fit summed model, green and purple dashed lines are eastern and western synchrotron lobes, respectively. Blue dashed-dotted line shows the scaled BB assigned to the west ALMA detection. The coloured data points indicate data with sub-arcsec resolution and black ones indicate data with lower resolution. Green pentagons indicate the location of the eastern synchrotron emission, purple hexagons represent the western radio component, the blue diamond and pink square represents the west and east ALMA detection, respectively. Filled black circles indicate detections (>3σ) and downward pointing triangles the 3σ upper limits (Table A.13).

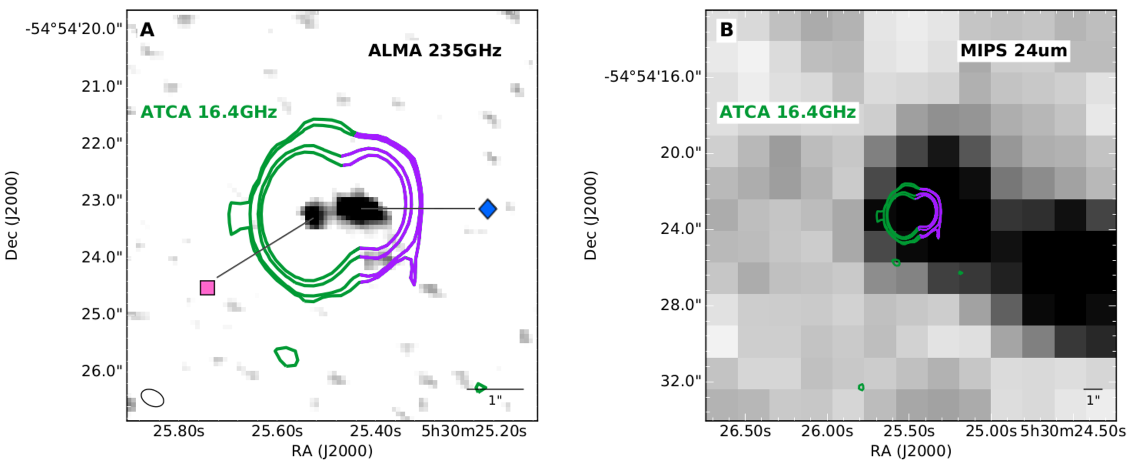

FIGURE A.38: *Panel A:* continuum map of ALMA band 6 with overlaid ATCA 16.4 GHz contours (levels are as Fig. A.2, σ = 55 μJy). The blue and pink markers indicate the two ALMA detections and correspond to the same marker used in the SED (Fig. A.37). The green and purple contours show the two components of the VLA data and correspond to the markers of the same colour as in the SED fit. *Panel B:* MIPS 24 μm continuum map, observe that the scale of the MIPS image is 5 times larger than panel A.

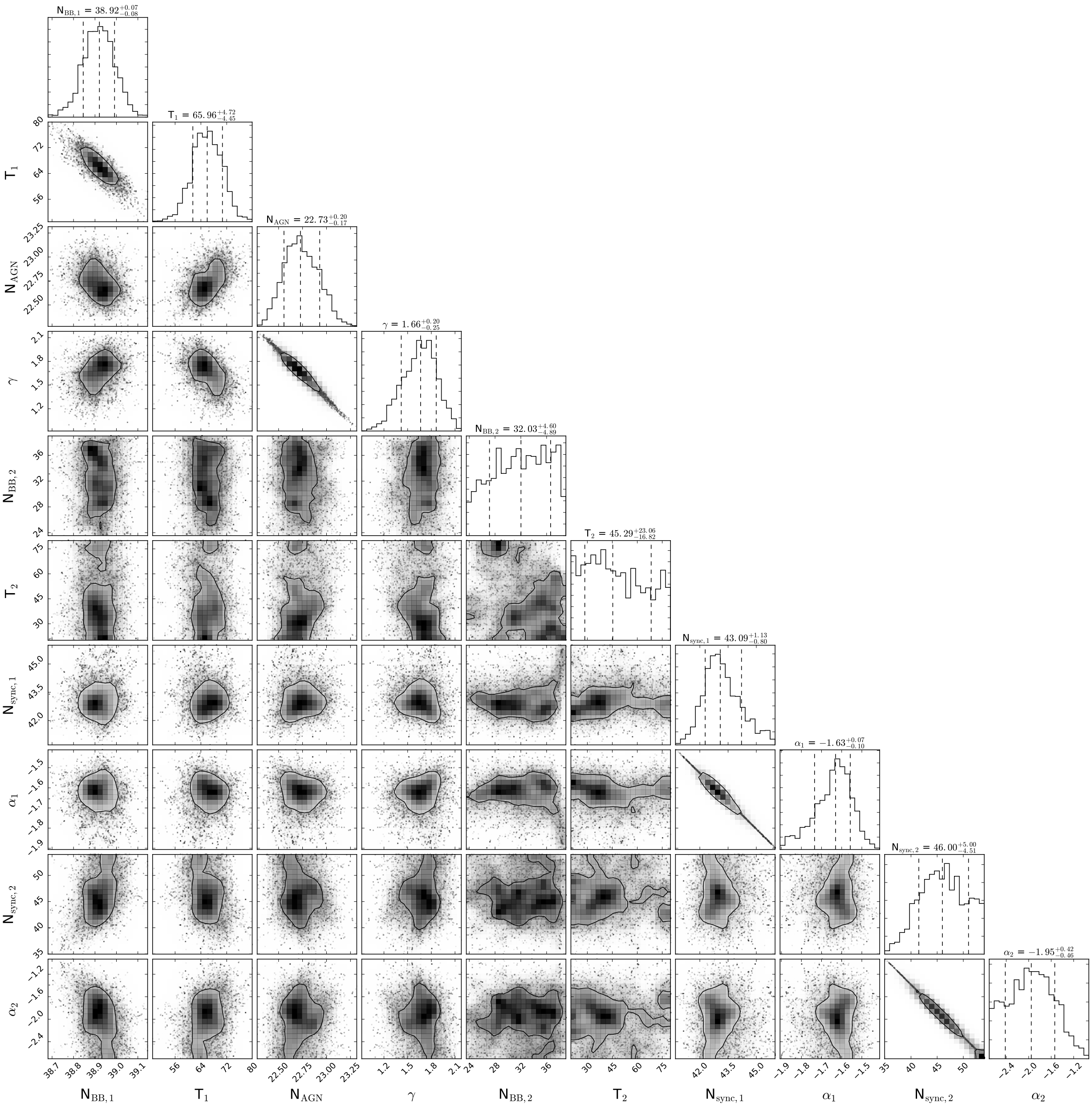

FIGURE A.39: **PKS 0529-549** Corner plot of the free parameters.

TN J0924-2201

TN J0924-2201 has one single continuum detection which coincides with the eastern radio component (Fig. A.41). SED fitting with MrMoose is done with four components, two synchrotron power laws (eastern and western radio component), one modified BB and one AGN component.

The western radio component (detected in VLA bands U and K) is assigned to the ALMA detection and fitted with an individual synchrotron power-law. The eastern radio component (detected in VLA bands U and K) is only fitted with a synchrotron power-law Sync, 2). The VLA bands C and L do not resolve the individual components and are only considered for fitting the total radio flux (the combination of the western and eastern synchrotron power-law components). The western ALMA detection is assigned to the western synchrotron component (Sync, 1), and to a modified BB component. The SCUBA, SPIRE, PACS, MIPS and IRS data is fitted to the combination of the modified BB and a AGN component. The SED fit only constrain the synchrotron models and the modified BB and AGN are unconstrained. This is due to the fact that there is only one detection in the FIR and it is not possible to constrain the modified BB with two free parameters to only one data point. The solution for the two radio lobes shows that the ALMA detection is likely completely dominated by thermal dust emission. The plotted modified BB in Fig. A.40 is scaled to the ALMA detection with slope and temperature fixed to $\beta = 2.5$ and T= 50, like in the case where the upper-limit of the L^{IR}_{SF}, is calculated for the sources with ALMA non-detections. The PDF of the free parameters can be found in Fig. A.42, which shows that both the BB and AGN is unconstrained.

TABLE A.14: Data for TN J0924-2201 (z=5.195)

Photometric band	Flux[mJy]	Ref.
IRS (16 μm)	<0.168	A
MIPS (24 μm)	<0.125	A
PACS (70 μm)	<4.6	B
PACS (160 μm)	<16.3	B
SPIRE (250 μm)	<11.4	B
SPIRE (350 μm)	<16.1	B
SPIRE (500 μm)	<14.3	B
SCUBA (850 μm)	<3.2	C
ALMA 6^e	<0.25	this paper
ALMA 6^w	0.88±0.7	this paper
VLA U^w	0.65±0.2[1]	this paper
VLA K^w	0.42±0.1[1]	this paper
VLA U^e	0.78±0.22[1]	this paper
VLA K^e	0.32±0.17[1]	this paper
VLA C	8.79±1.44[1]	this paper
VLA L	71.5±2.2	F

(*a*) Integrated flux extracted using AIPS with imfit 1 Gaussian component (e) eastern component, (w) western component.

References. (A) De Breuck et al. (2010), (B) Drouart et al. (2014), (C) Reuland et al. (2003a) (F) Pentericci et al. (2000).

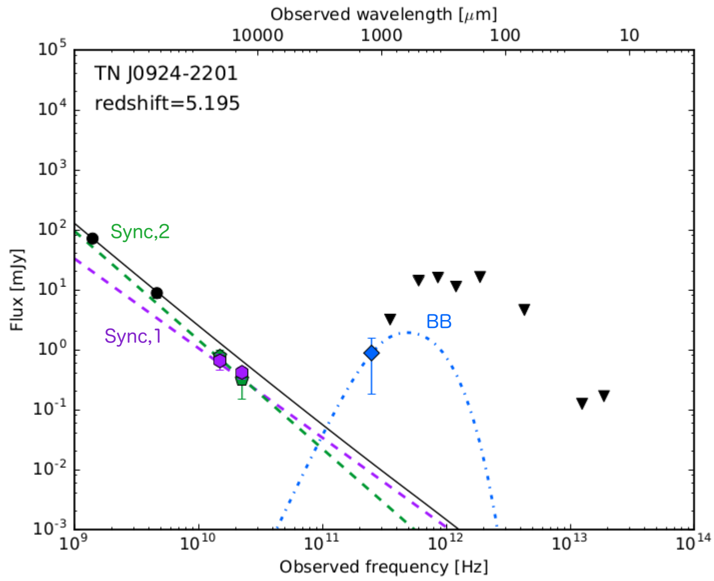

FIGURE A.40: SED of **TN J0924-2201**. Black solid line shows best fit total model, black dashed line is the total synchrotron, the black dash-dotted lines is the black body and the black dotted line indicates the AGN component. The coloured data points are sub-arcsec resolution data and black ones indicate data of low resolution. The blue diamond indicates the ALMA band 3 detection. Filled black circles indicate detections (>3σ) and downward pointing triangles the 3σ upper limits (Table A.14).

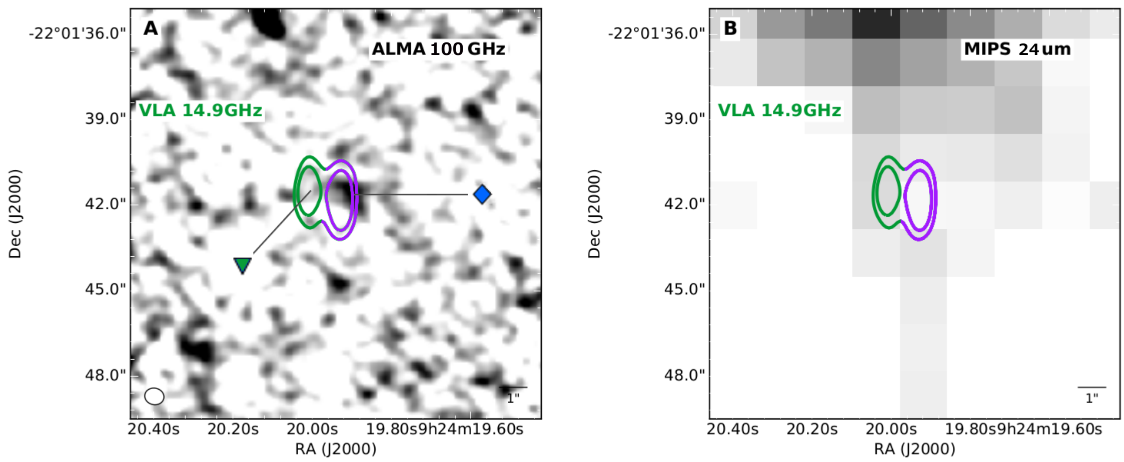

FIGURE A.41: *Panel A:* continuum map of ALMA band 3 with overlaid VLA U contours (levels are as Fig. A.2, $\sigma = 85\,\mu$Jy). The blue marker indicates the ALMA detection and correspond to the same marker in the SED (Fig. A.40). The green and purple contours show the two components of the VLA data and corresponds to the markers if the same color as in the SED. *Panel B:* MIPS 24 μm continuum map.

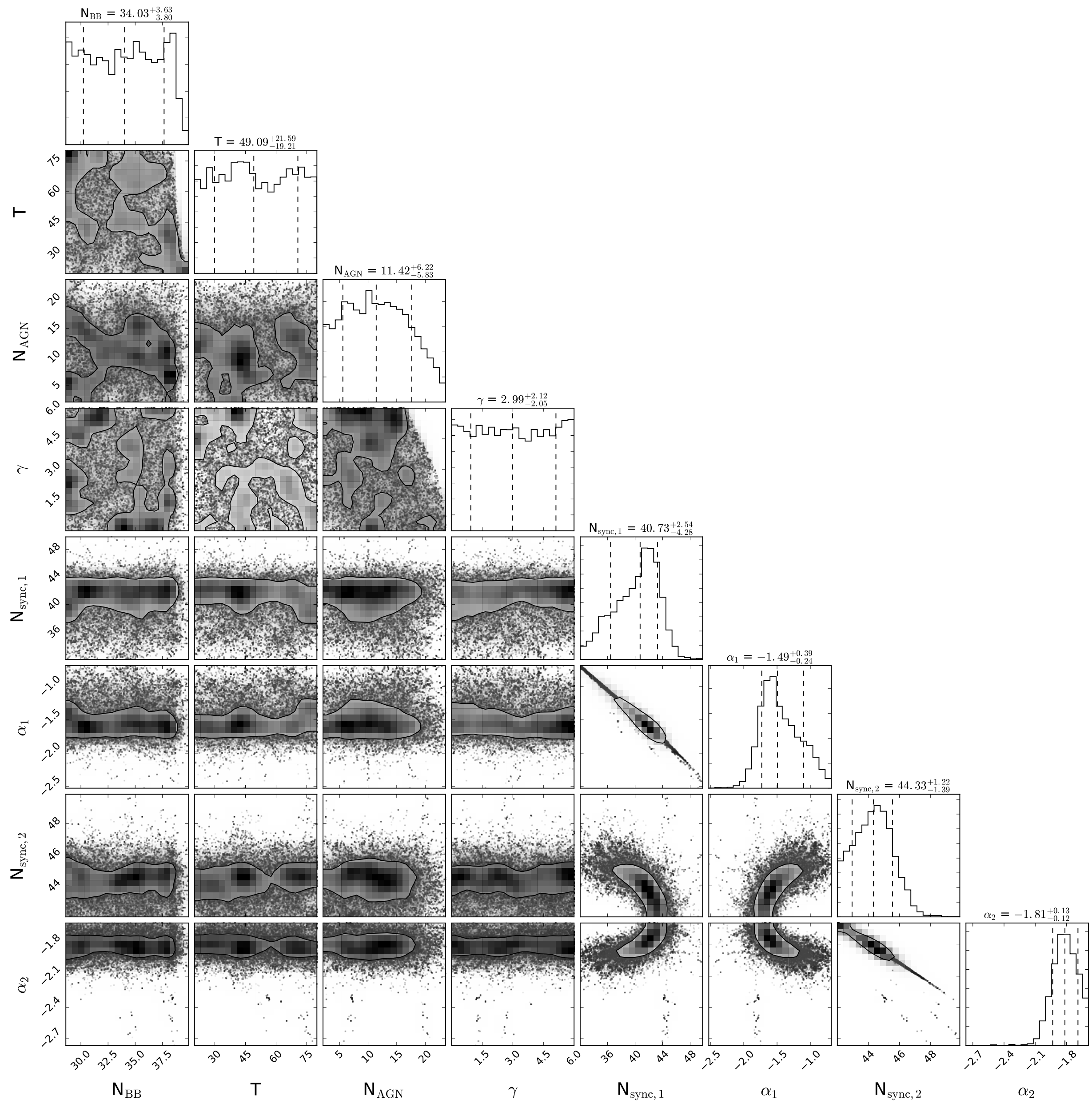

FIGURE A.42: **TN J0924-2201** Corner plot of the free parameters.

MRC 0943-242

MRC 0943-242 has several continuum detections with ALMA band 6, one at the host galaxy and three resolved companions (Fig. A.44). With ALMA band 4 the three companions are also detected, as well as two additional continuum components which coincide with the two radio components seen with VLA. SED fitting with MrMoose is done with five models, two synchrotron power-laws (north and south component), two modified BB (one for the host and one for the three companions grouped together) and one AGN component. The VLA X, C and ALMA band 4 resolve the synchrotron components and the two radio lobes are fitted with two individual power-laws. The VLA L, ATCA 3 mm and 7 mm do not resolve any individual components and are assigned to the combination of both synchrotron models. The LABOCA, SPIRE, PACS, MIPS and IRS data are assigned to both the modified BB of the host and companions as well as the AGN component. The best fit model, shows that ALMA detection at the host galaxy is dominated by thermal dust emission, and the three companions are also consistent with emission from heated dust. The two synchrotron components are consistent with a power-law from radio to ALMA band 4 (Figure A.43). One reason why the PACS 100 μm, is not well fitted is because either the temperature of the modified BB must be higher which is outside the parameter space or because the fixed ν_{cut} does not allow the AGN component to account fully for the observed flux. The PDF of the free parameters can be found in Fig. A.45.

TABLE A.15: Data for MRC 0943-242 (z=2.933)

Photometric band	Flux[mJy]	Ref.
IRS (16 μm)	0.170± 0.048	A
MIPS (24 μm)	0.518 ±0.040	A
MIPS (70 μm)	<3.390	A
MIPS (160 μm)	<50.900	A
PACS (100 μm)	<27.6	B
PACS (160 μm)	23.6 ±7.7	B
SPIRE (250 μm)	25.7 ±5.2	B
SPIRE (350 μm)	<31.7^a	B
SPIRE (500 μm)	<35.2^a	B
LABOCA (870 μm)	<24	B
ALMA 6^h	0.84 ± 0.4	this paper
ALMA 6^c	40.72± 0.47	this paper
ALMA 4^c	0.41 ± 0.04	this paper
ALMA 4^n	0.21 ±0.15	this paper
ALMA 4^s	0.14 ±0.07	this paper
ATCA (3mm)	<1	this paper
ATCA (7mm)	3.6 ±1.08	C
VLA X ^{n}	15.86 ±1.5^b	D
VLA X ^{s}	3.42 ±0.3 ^{b}	D
VLA C ^{n}	44 ±4.3	D
VLA C ^{s}	11 ±1.1	D
VLA L	272.1 ±27.2	E

Notes (*h*) AGN host, (*c*) companions, (*n*) north synchrotron lobe, (*n*) south synchrotron lobe, (*a*) changed to upper limits because of contamination sources seen in MIPS image, (*b*) flux obtained from Carilli et al. (1997) using the listed $I_{4.7}$ and $\alpha_{4.7}^{8.2}$ values of the north and south hot spot.

References. (A) De Breuck et al. (2010), (B) Drouart et al. (2014), (C) Emonts et al. (2011b) (D) Carilli et al. (1997), (E) Condon et al. (1998).

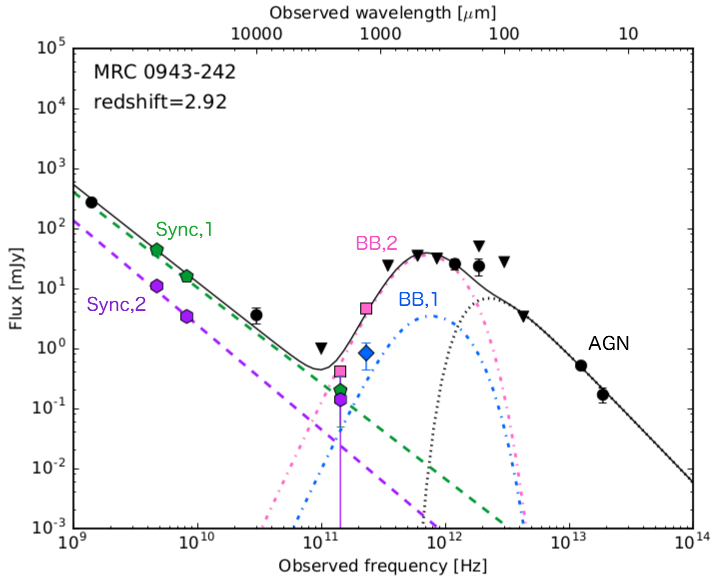

FIGURE A.43: SED of **MRC 0943-242**. Black solid line shows best fit total model, green and purple dashed line is north and south synchrotron lobes, respectively. Black dashed-dotted line shows the black body fitted associated to one of the ALMA detections and the black dotted line indicates the AGN component. The coloured data points are sub-arcsec resolution data and black ones indicate data of low resolution. Green pentagons are north synchrotron, purple hexagons are the south radio component, the blue diamond shows the ALMA 6 host detection and magenta squares indicates the total ALMA 4 and 6 flux of the 3 companions. Filled black circles indicate detections (>3σ) and downward pointing triangles the 3σ upper limits (Table A.15).

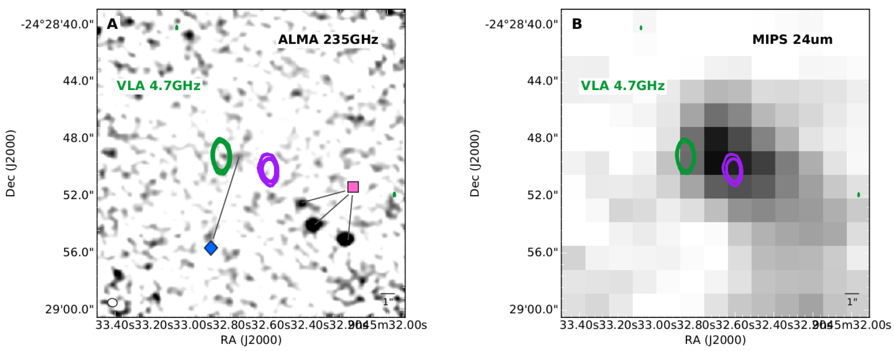

FIGURE A.44: *Panel A:* continuum map of ALMA band 6 (cycle 1 and 2) with overlaid VLA C contours (levels are as Fig. A.2, σ = 75 μJy). Blue and pink markers indicate the two different components detected with ALMA detections and corresponds to the same data points in the SED fit. The green and purple contours show the two components if the VLA data and corresponds to the markers of the same colors as in the SED fit. *Panel B:* MIPS 24 μm continuum map.

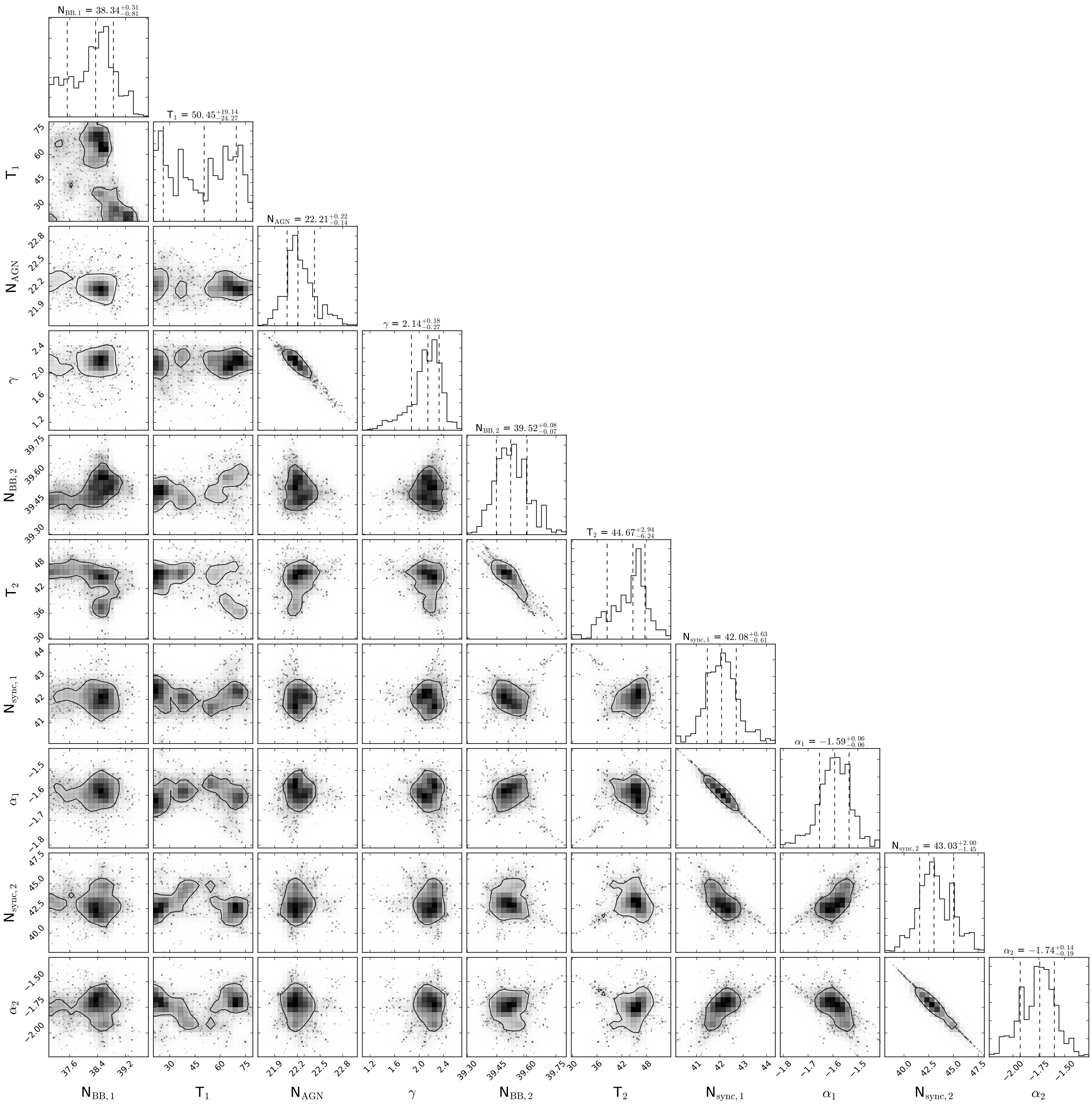

FIGURE A.45: **MRC 0943-242** Corner plot of the free parameters.

MRC 1017-220

MRC 1017-220 has one single continuum detection with ALMA, which coincides with the unresolved synchrotron component (Fig. A.47). SED fitting with MrMoose is done with three components, one synchrotron, one modified BB and one AGN component. The VLA L, C, X and ATCA 7 mm bands are assigned to the synchrotron component and the ALMA detection is assigned to both the synchrotron power-law and a modified BB. The LABOCA SPIRE, PACS, MIPS and IRS points are assigned to the combination of the modified BB and an AGN component. The best fit solution gives a dominating synchrotron contribution to the ALMA detection (Fig. A.46), due to the many upper limit in the FIR. But studying the SED it seems likely that the synchrotron is turning over at high frequencies but without a data point at an intermediate frequency between the radio and ALMA data, it is not possible to make a final conclusion whether the ALMA detection is synchrotron dominated or not. The PDF of the free parameters can be found in Fig. A.48, which shows that the modified BB is unconstrained.

TABLE A.16: Data for MRC 1017-220 (z=1.77)

Photometric band	Flux[mJy]	Ref.
IRS (16 μm)	0.740±0.120	A
MIPS (24 μm)	1.140±0.030	A
PACS (70 μm)	<7.7	B
PACS (160 μm)	<25.1	B
SPIRE (250 μm)	<17.4	B
SPIRE (350 μm)	<23.6	B
SPIRE (500 μm)	<22.4	B
LABOCA (870 μm)	<18.6	B
ALMA 6	0.52±0.11	this paper
ATCA (7 mm)	21.1±6.33	this paper
VLA X	148±14.8	C
VLA C	257±25.7	C
VLA L	673.2±67.3	D

References. (A) De Breuck et al. (2010), (B) Drouart et al. (2014), (C) Pentericci et al. (2000), (D) Condon et al. (1998).

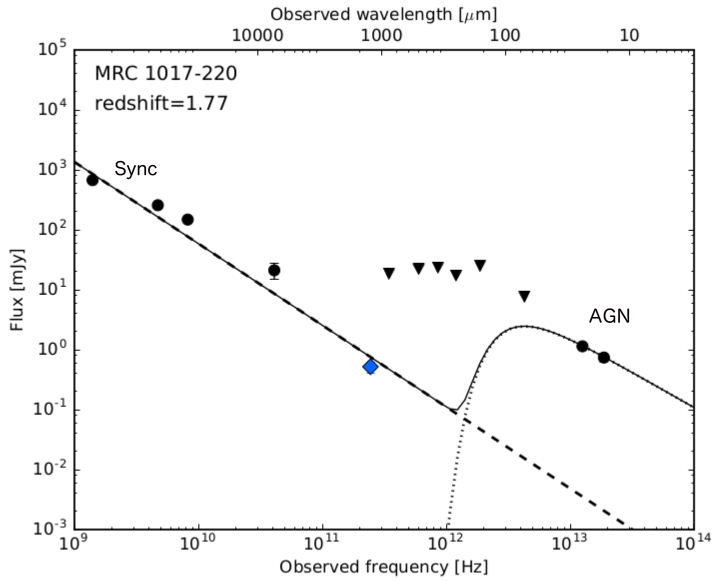

FIGURE A.46: SED of **MRC 1017-220**. Black solid line shows best fit total model, black dashed line is the total synchrotron and the black dotted line indicates the AGN component. The coloured data point is sub-arcsec resolution data and black ones indicate data of low resolution. The blue diamond indicates the ALMA band 6 detection. Filled black circles indicate detections (>3σ) and downward pointing triangles the 3σ upper limits (Table A.16).

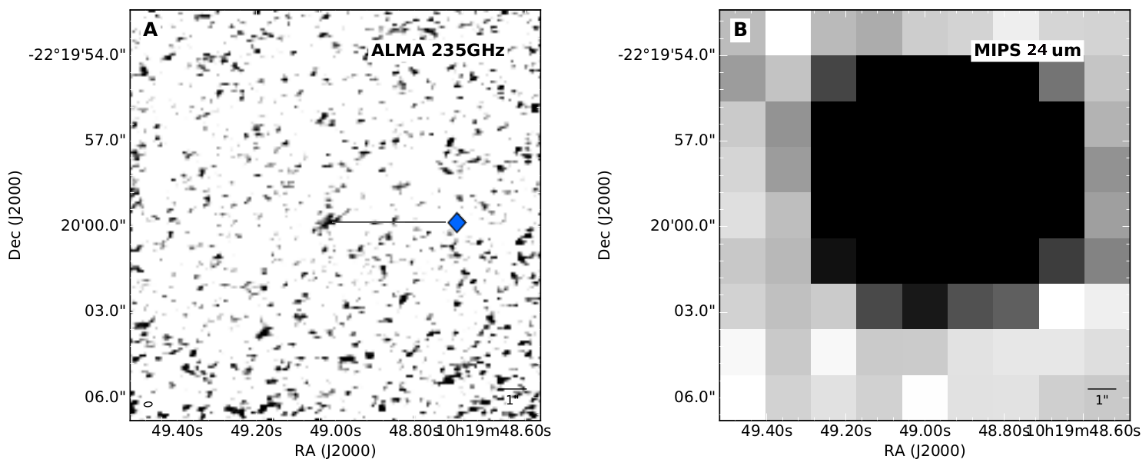

FIGURE A.47: *Panel A:* continuum map of ALMA band 6, VLA maps not accessible, but the source is unresolved as shown in Pentericci et al. (2000). The blue diamond indicate the ALMA component and correspond to the same data point as Fig. A.46. *Panel B:* MIPS 24 μm continuum map

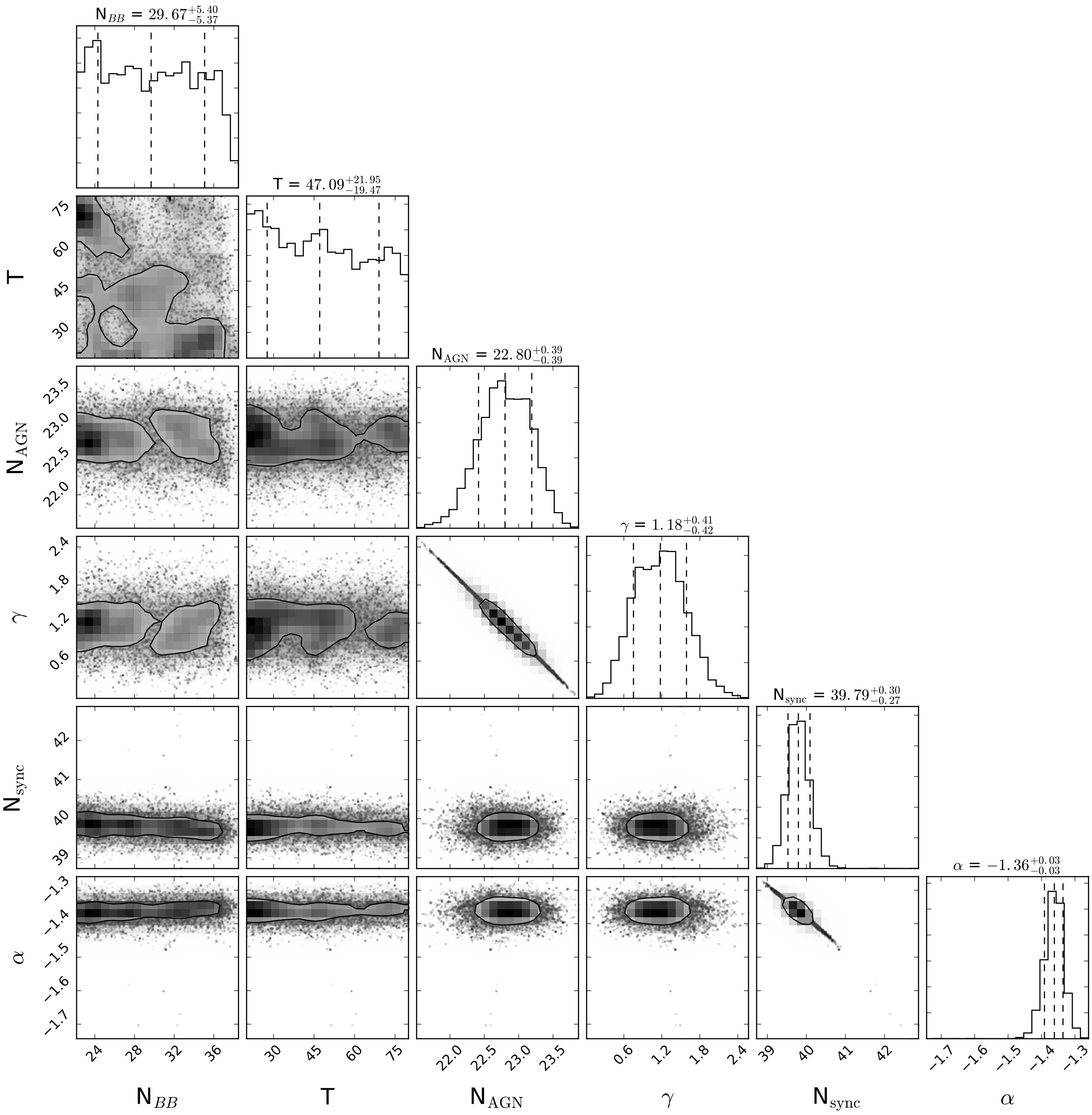

FIGURE A.48: **MRC 1017-220** Corner plot of the free parameters.

4C 03.24

4C 03.24 two continuum detections in ALMA band 3, one that coincides with the north synchrotron lobe and one that covers both the radio core and hot spot of the south lobe (Fig. A.50). The SED fitting with MrMoose is done with six components, three synchrotron (core, northern and southern radio component), two modified BB (northern and southern) and one AGN component. The VLA L detection does not resolve the individual components and are only considered for fitting the total radio flux (the combination of the western, eastern and core synchrotron power-law components). The C and X bands resolves the three components are there assigned to individual synchrotron models. The northern ALMA detection is assigned to the northern synchrotron power-law and one modified BB and the southern ALMA detection is assigned to a combination of the southern and core synchrotron components, as well as a modified BB. The SCUBA, SPIRE, PACS, MIPS and IRS are fitted to the combination of the two modified BB and a AGN component. The best fit model finds that the north ALMA detection is dominated by thermal dust emission and the southern ALMA detection is dominated by synchrotron emission from the south radio lobe. The PDF of the free parameters can be found in Fig. A.51.

TABLE A.17: Data for 4C 03.24 (z=3.57)

Photometric band	Flux[mJy]	Ref.
IRS (16 μm)	<0.260	A
MIPS (24 μm)	0.511±0.043	A
PACS (100 μm)	8.3±3.1	B
PACS (160 μm)	14.1±6.3	B
SPIRE (250 μm)	16.6±5.6	B
SPIRE (350 μm)	<19.6	B
SPIRE (500 μm)	<22.2	B
SCUBA (850 μm)	2.3±1.1	C
ALMA 3^h	0.08±0.07	this paper
ALMA 3^s	0.71±0.14	this paper
VLA X^n	5.2 ±0.52	D
VLA C^n	20.3 ±2.03	D
VLA X^c	0.7±0.07	D
VLA C^c	1.4±0.14	D
VLA X^s	14.6±1.5	D
VLA C^s	33.8±3.4	D
VLA L	368.2±11.1	E

References. (A) De Breuck et al. (2010), (B) Drouart et al. (2014), (C) , Archibald et al. (2001), (D) van Ojik et al. (1996), (E) Condon et al. (1998).

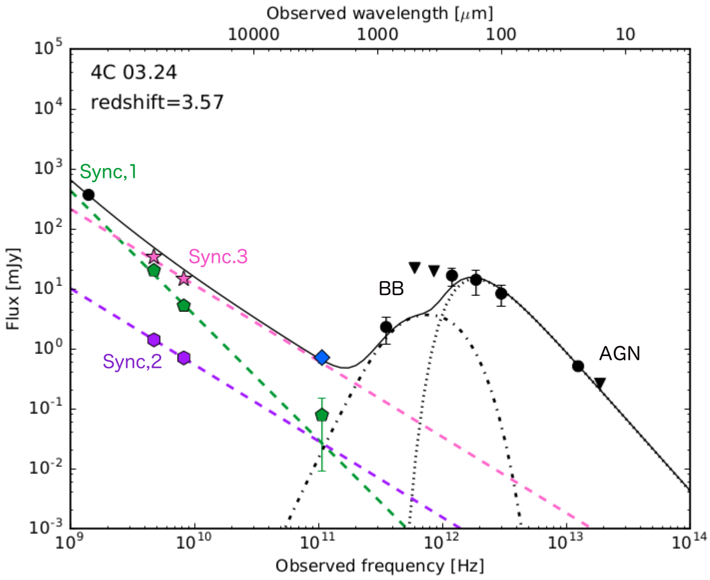

FIGURE A.49: SED of **4C 03.24**. Black solid line shows best fit total model, pink, green and purple dashed line is the north, core and south synchrotron component, respectively, the black dash-dotted lines is the black body and the black dotted line indicates the AGN component. The coloured data points are sub-arcsec resolution data and black ones indicate data of low resolution. Green pentagons are the north synchrotron lobe, purple hexagrams are the radio core and the pink stars corresponds to the southern lobe. The blue diamond indicates the ALMA band 3 detection spatially coincident with the host galaxy, radio core and southern hotspot. Filled black circles indicate detections (>3σ) and downward pointing triangles the 3σ upper limits (Table A.17).

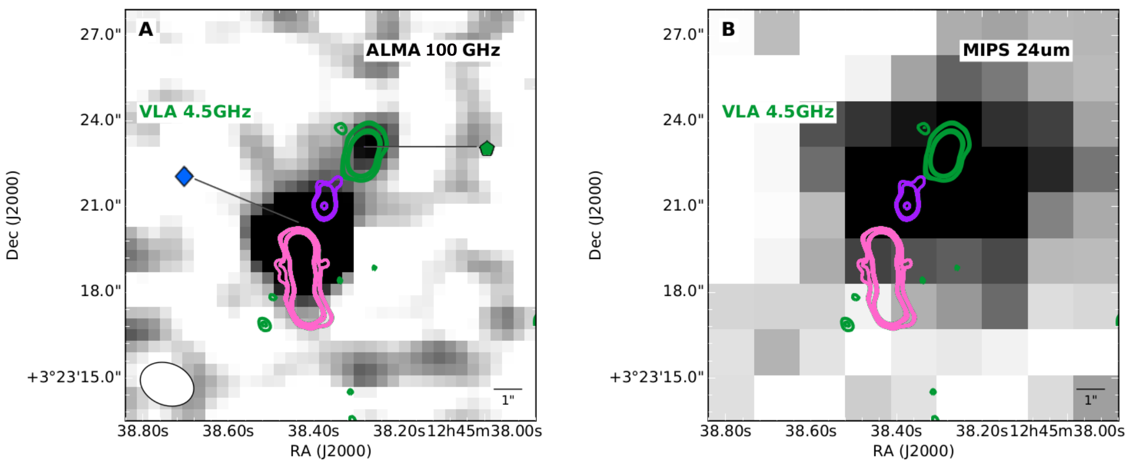

FIGURE A.50: *Panel A:* continuum map of ALMA band 3 with overlaid VLA C contours (levels as Fig. A.2, σ = 50 μJy). The blue and green markers indicate the two different ALMA detections and correspond to the same data points as Fig. A.49. The green, purple and pink contours show the three components of the VLA data and correspond to the markers of the same colors as in the SED fit. *Panel B:* MIPS 24 μm continuum map.

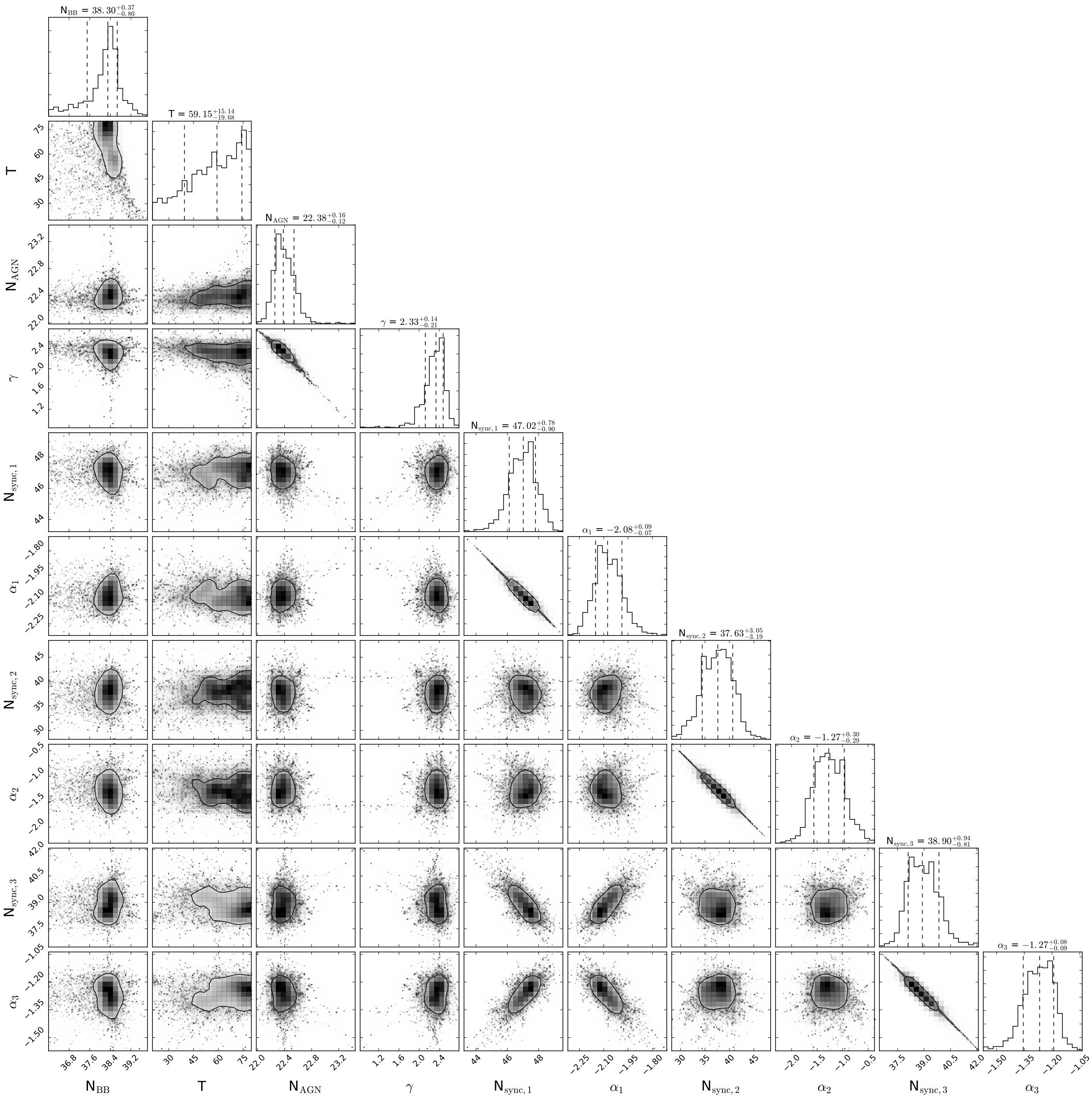

FIGURE A.51: **4C 03.24** Corner plot of the free parameters.

TN J1338-1942

TN J1338-1942 has one coninuum detection with ALMA, which coincides with the northern radio component (Fig. A.53). SED fitting with MrMoose is done with four components, two synchrotron (northern and southern radio component), one modified BB and one AGN component. The northern radio component (detected in VLA bands C and X) is assigned to the northern ALMA detection and fitted with an individual synchrotron power-law. The southern radio component (detected in VLA bands C and X) is also fitted with an individual power-law and assigned to the southern ALMA upper limit. The VLA L data do not resolve the individual components and are only considered for fitting the total radio flux (the combination of the northern and southern synchrotron power-law components). The northern ALMA detection is assigned to the norther synchrotron component and to a modified BB component. The MAMBO SCUBA, SPIRE, PACS, MIPS and IRS are fitted to the combination of the modified BB and a AGN component. The best fit is where the ALMA flux is a combination of the northern synchrotron lobe and dust emission. The PDF of the free parameters can be found in Fig. A.54.

TABLE A.18: Data for TN J1338-1942 (z=4.110)

Photometric band	Flux[mJy]	Ref.
IRS (16 μm)	<0.226	A
MIPS (24 μm)	0.384±0.178	B
PACS (100 μm)	<5.9	C
PACS (160 μm)	<27.1	C
SPIRE (250 μm)	<16.6	C
SPIRE (350 μm)	<17.6	C
SPIRE (500 μm)	<18.0	C
SCUBA (850 μm)	10.1±1.3	D
SCUBA (450 μm)	21.4±6.4	D
MAMBO	6.2±1.2	D
ALMA 3	0.18±0.09	this paper
ALMA 3	<0.036	this paper
VLA X^s	1.6 ±0.16	E
VLA C^s	4.7 ±0.47	E
VLA X^n	7.9±0.79	E
VLA C^n	20.6±2.06	E
VLA L	121.4±4.3	F

References. (A) De Breuck et al. (2010),(B) Capak et al. (2013) (C) Drouart et al. (2014), (D) De Breuck et al. (2004), (E) Pentericci et al. (2000), (F) Condon et al. (1998).

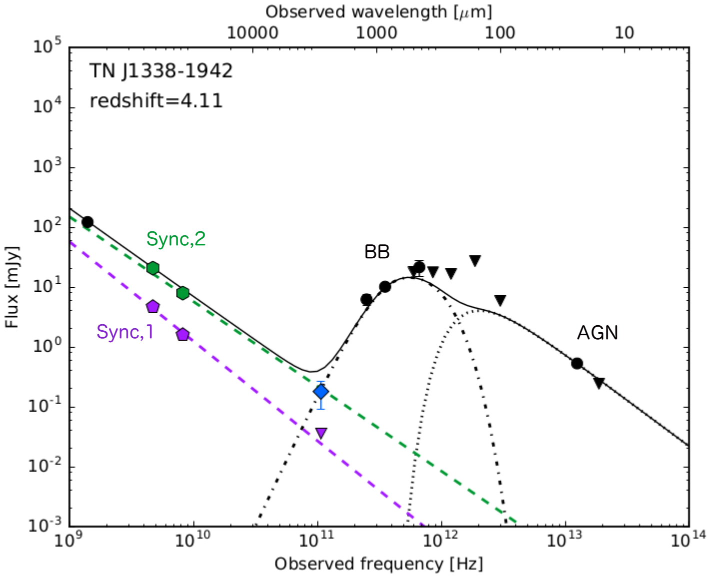

FIGURE A.52: SED of **TN J1338-1942**. Black solid line shows best fit total model, green and purple dashed line is the north and south synchrotron component, respectively. The black dash-dotted lines represents the black body and the black dotted line indicates the AGN component. The coloured data points are sub-arcsec resolution data and black ones indicate data with low spatial resolution. The green hexagons and purple pentagons are radio data of the northern and southern synchrotron component, respectively. The blue diamond indicates the ALMA band 3 detection. Filled black circles indicate detections (>3σ) and downward pointing triangles the 3σ upper limits (Table A.18).

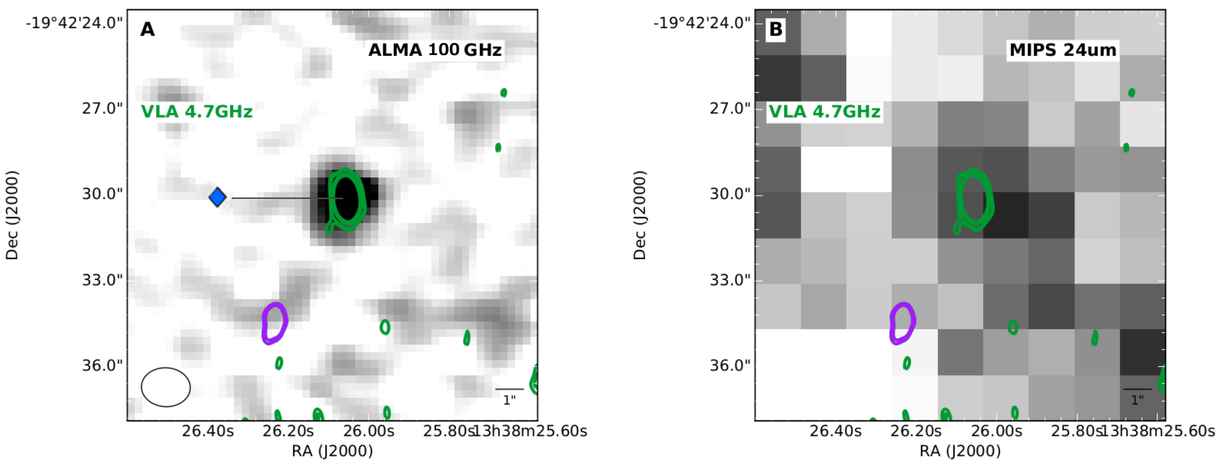

FIGURE A.53: *Panel A:* continuum map of ALMA band 3 with plotted VLA C contours (levels are as Fig. A.2, σ = 55 μJy) The blue diamond indicates the ALMA detection and is the same marker used in Fig. A.52. The green and purple contours show the north and south radio component with the same color coding as in the SED plot. *Panel B:* MIPS 24 μm continuum map.

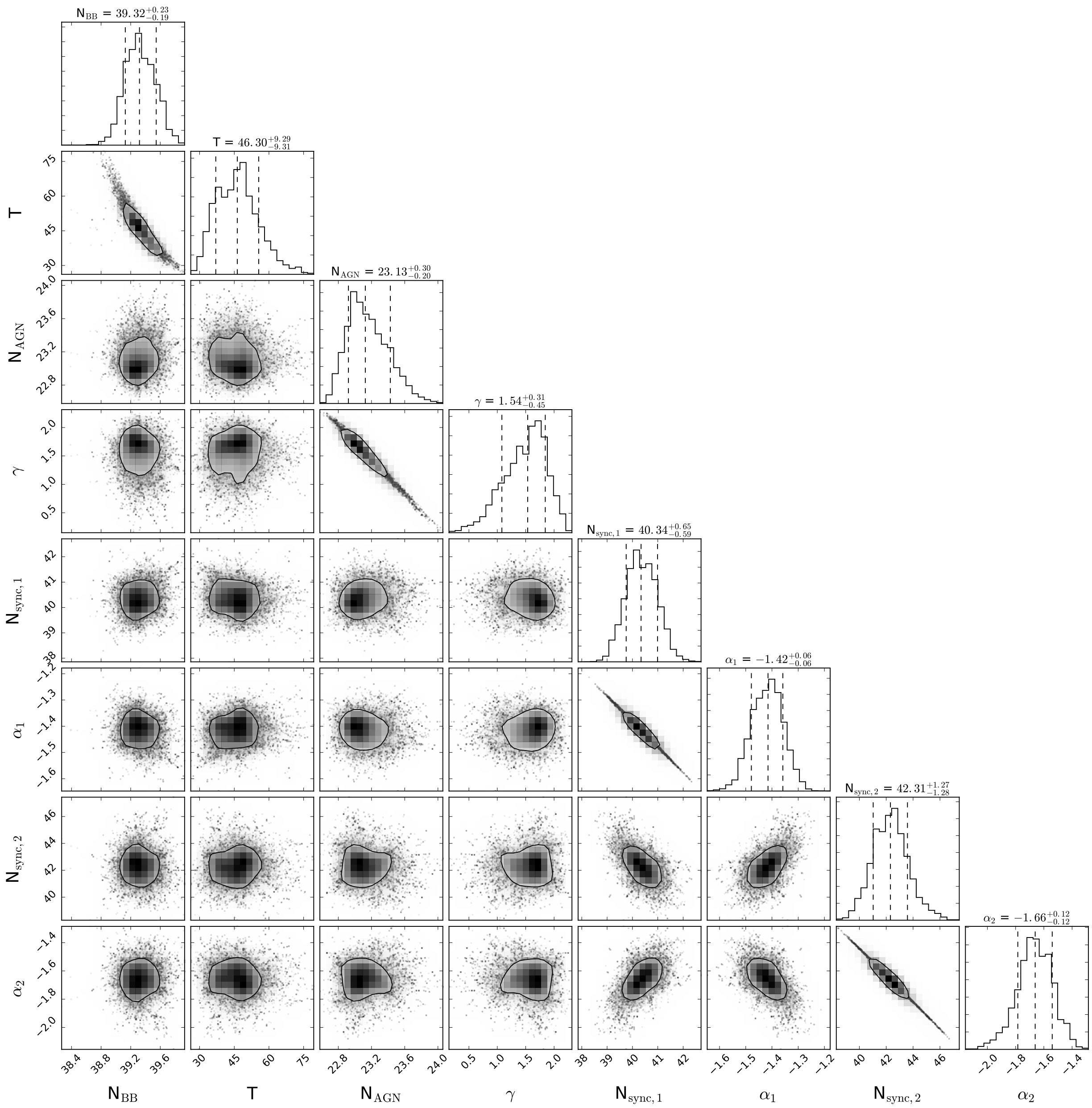

FIGURE A.54: **TN J1338-1942** Corner plot of the free parameters.

TN J2007-1316

TN J2007-1316 has no ALMA continuum detection (Fig. A.56). SED fitting with MrMoose is done with four components, two synchrotron (northern and southern radio component), one modified BB and one AGN component. The northern and southern radio components (detected in VLA bands C and X) are each assigned to an individual synchrotron power-law. The VLA L band do not resolve individual components and is only considered for fitting the total radio flux (the combination of the north and south synchrotron power-law). The ALMA upper limit at the AGN host location is assigned to both synchrotron components and the modified BB. The SPIRE, PACS, MIPS and IRS data a fitted to the combination of the modified BB and a AGN component. The best fit model only constrains the synchrotron and AGN components, while the modified BB remains unconstrained because there are only upper limits in the FIR (Fig. A.55). The PDF of the free parameters can be found in Fig. A.57, which shows that the BB is completely unconstrained.

TABLE A.19: Data for TN J2007-1316 (z=3.840)

Photometric band	Flux[mJy]	Ref.
IRS (16 μm)	0.378±0.113	A
MIPS (24 μm)	0.385±0.040	A
PACS (100 μm)	<7.7	B
PACS (160 μm)	<20.8	B
SPIRE (250 μm)	<16.7	B
SPIRE (350 μm)	<16.8^a	B
SPIRE (500 μm)	<18.9^a	B
ALMA 4	<0.25	this paper
VLA X^s	4.71±0.3^b	A
VLA X^n	2.46±0.38^b	A
VLA C^s	10.30±1.03^b	A
VLA C^n	7.49±0.7^b	A
VLA L	113.2±13.	C

Notes (*s*) South synchrotron lobe, (*n*) north synchrotron lobe, (*a*) changed to upper limits because of foreground object contamination (*b*) flux estimated using AIPS from original radio map, convolved to the resolution of the VLA C band.

References. (A) De Breuck et al. (2010), (B) Drouart et al. (2014), (C) Condon et al. (1998).

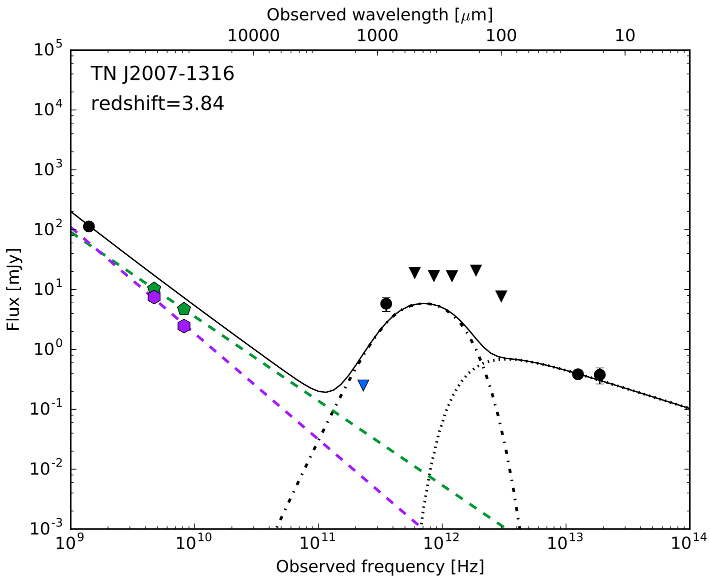

FIGURE A.55: SED of **TN J2007-1316**. Black solid line shows best fit total model, green and purple dashed line are northern and southern synchrotron lobes, respectively. The black dotted line represents the AGN component. The coloured data points indicate sub-arcsec resolution data and black ones indicate data with low spatial resolution. Green pentagons are northern synchrotron emission, purple hexagons are from the southern radio component and the blue triangle indicates the ALMA 4 3σ upper limit. Filled black circles indicate detections (>3σ) and downward pointing triangles the 3σ upper limits (Table A.19).

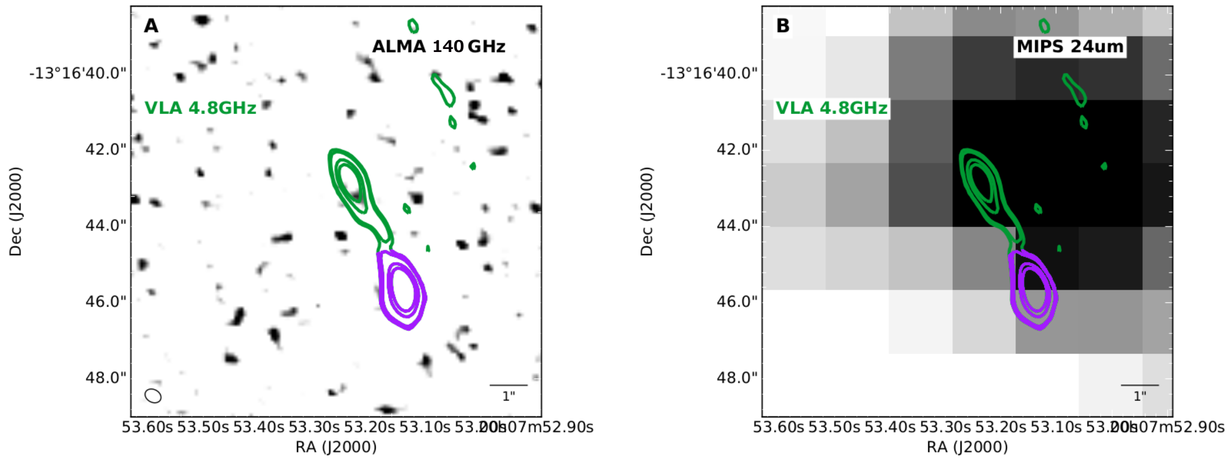

FIGURE A.56: *Panel A:* continuum map of ALMA band 4 with overlaid VLA C contours (levels are as Fig. A.2, $\sigma = 12\,\mu$Jy). The green and purple contours show the two components of the VLA data and corresponds to the markers of the same colors as in the SED fit. *Panel B:* MIPS 24 μm continuum map.

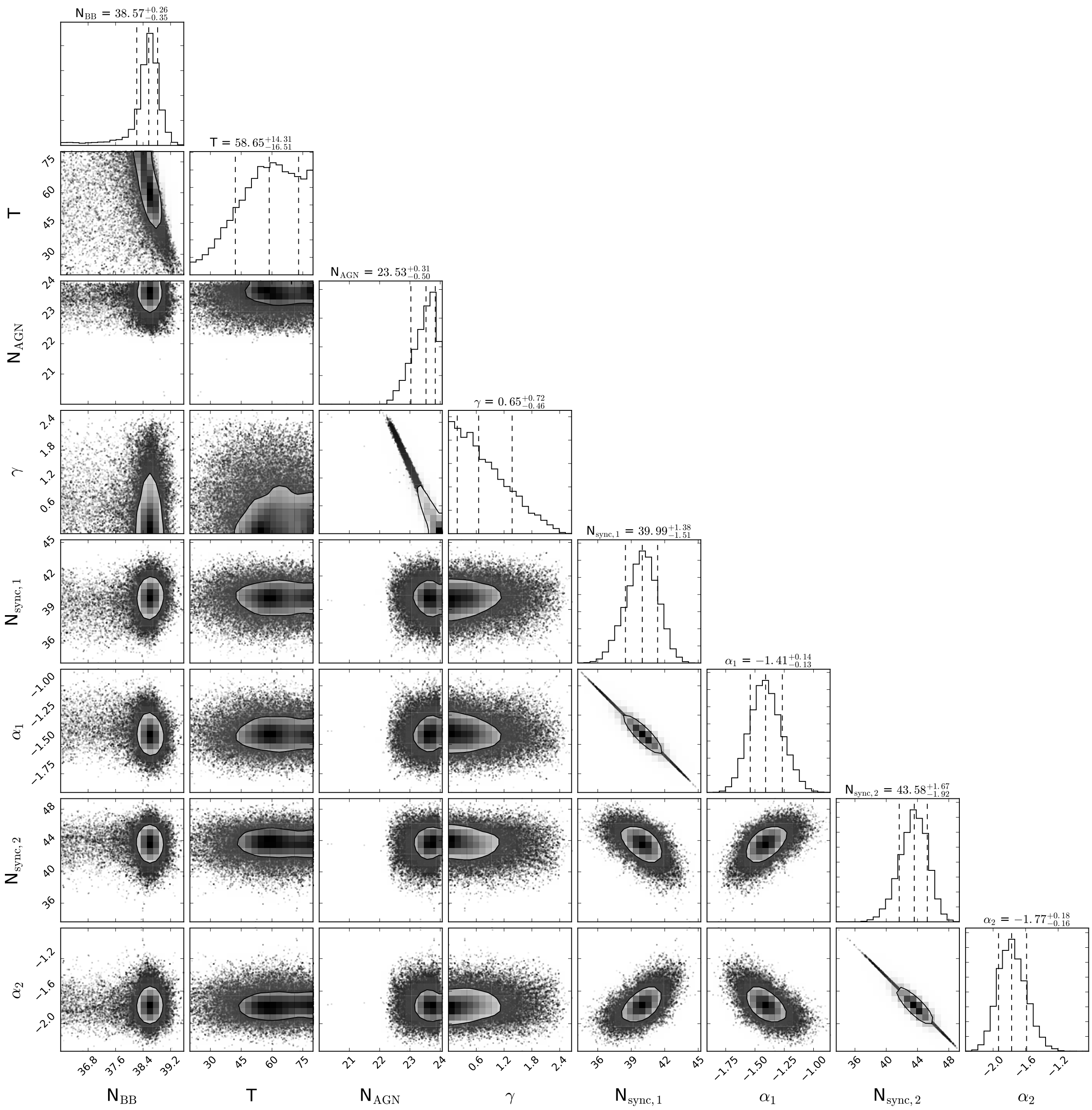

FIGURE A.57: **TN J2007-1316** Corner plot of the free parameters.

MRC 2025-218

MRC 2025-218 has no detection continuum detection (Fig. A.59, neither the host nor the synchrotron are detected. SED fitting with MrMoose is done with four components, two synchrotron (north and south radio component), one modified BB and one AGN component. The north radio component (detected in VLA bands C and X) is assigned to an individual synchrotron power-law, the same set up is used for the southern radio component. The VLA L and ATCA 7 mm to does not resolve any individual components and are only considered for fitting the total synchrotron power-law (the combination of the north and south power-laws). The ALMA upper limit at the AGN host location is associated to both synchrotron components and the modified BB. The LABOCA, SPIRE, PACS, MIPS and IRS data are fitted to combination of the modified BB and a AGN component. The best fit model only constrains the synchrotron and AGN parts, the modified BB are unconstrained because there are only upper limits in the FIR, see Fig. A.58. The PDF of the free parameters can be found in Fig. A.60, which shows that the BB is unconstrained.

TABLE A.20: Data for MRC 2025-218 (z=2.630)

Photometric band	Flux[mJy]	Ref.
IRS (16 μm)	0.2±0.062	A
MIPS (24 μm)	0.216±0.043	A
PACS (100 μm)	<11.1	B
PACS (160 μm)	<30.7	B
SPIRE (250 μm)	<18.5	B
SPIRE (350 μm)	<28.4	B
SPIRE (500 μm)	<19.5	B
LABOCA (870 μm)	<10.5	B
ALMA 6	<0.12	this paper
ATCA (7mm)	8.6±2.58	this paper
VLA X^n	17.35 ± 1.7^a	C
VLA X^s	29.59 ± 2.9^a	C
VLA C^n	35.46 ± 3.5^a	C
VLA C^s	50.36 ± 5.0^a	C
VLA L	343.2±34	D

Notes (1) North synchrotron lobe, (*s*) south synchrotron lobe, (*a*) flux estimated using AIPS from original radio map, convolved to the resolution of the VLA C band.

References. (A) De Breuck et al. (2010), (B) Drouart et al. (2014), (C) Carilli et al. (1997), (D)Condon et al. (1998).

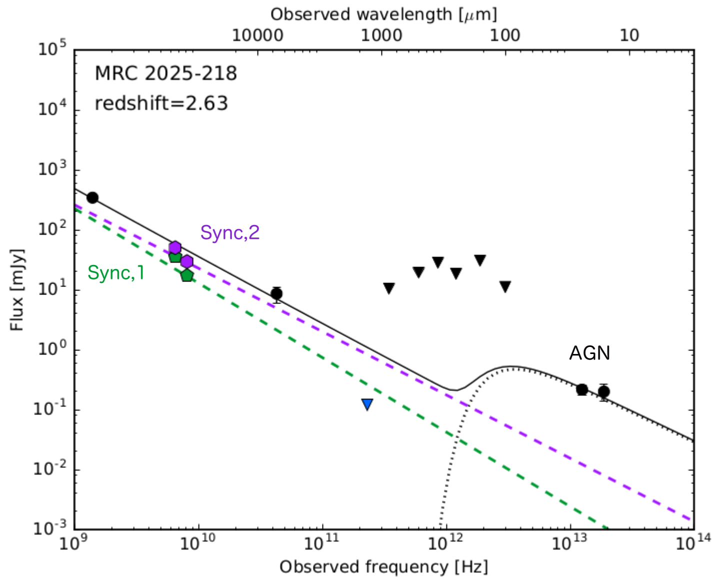

FIGURE A.58: SED of **MRC 2025-218**. Black solid line shows best fit total model, green and purple dashed lines are northern and southern synchrotron lobes, respectively and the black dotted line indicates the AGN component. The coloured data points are sub-arcsec resolution data and black ones indicate data with low spatial resolution. Green pentagons are for the northern radio component, purple hexagons are for the southern radio component, and the blue triangle indicates the ALMA 6 3σ upper limit. Filled black circles indicate detections (>3σ) and downward pointing triangles the 3σ upper limits (Table A.20).

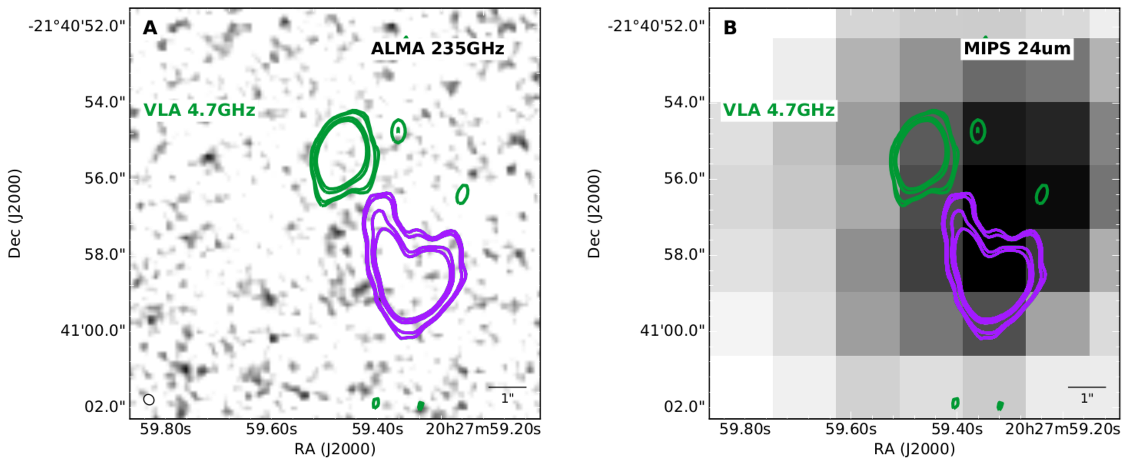

FIGURE A.59: *Panel A:* continuum map of ALMA band 6, plotted VLA C contours (levels are as Fig. A.2, σ = 57 μJy). The green and purple contours show the two components of the VLA data and correspond to the makers of the same colors as in the SED fit. *Panel B:* MIPS 24 μm continuum map.

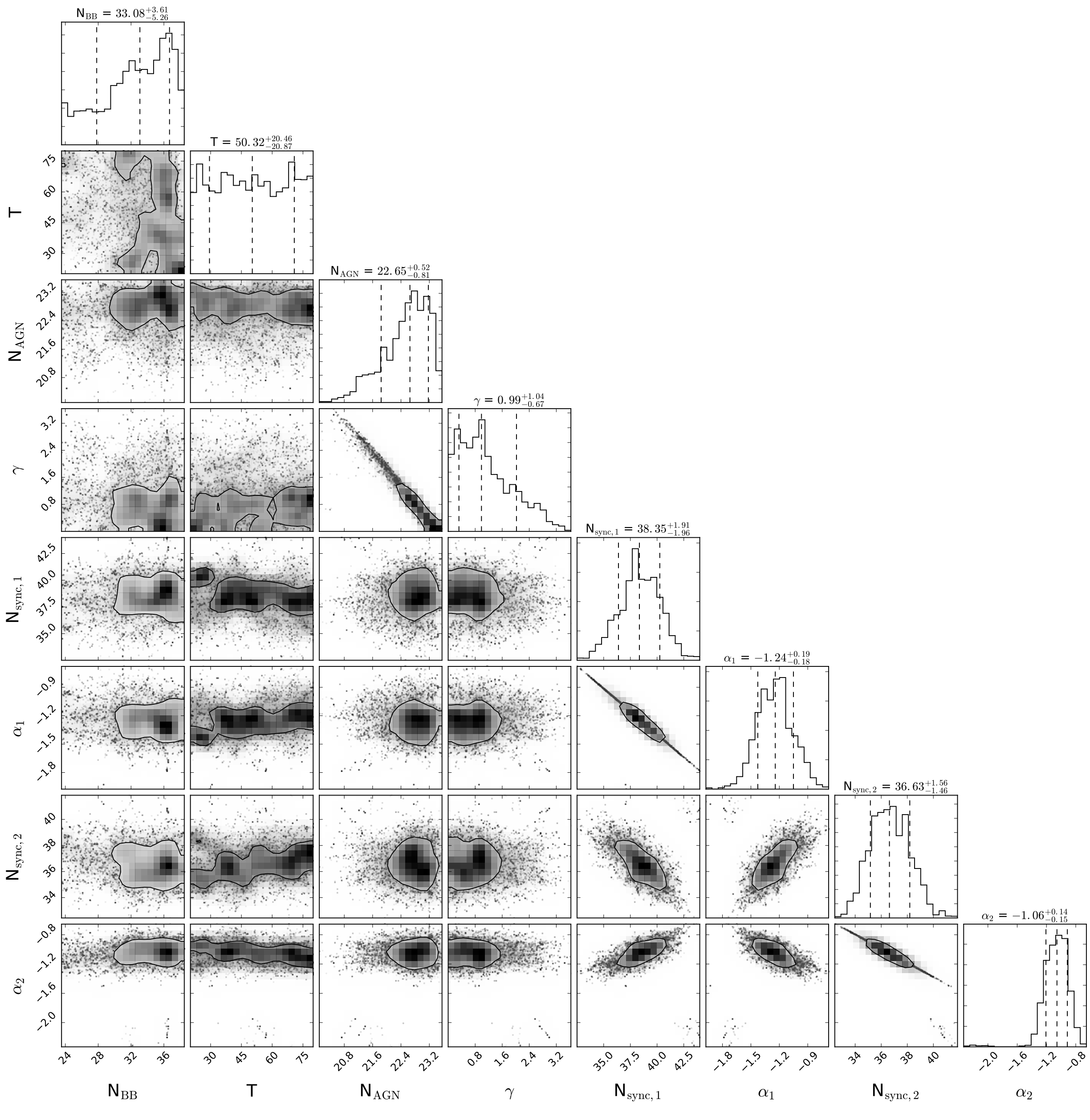

FIGURE A.60: **MRC 2025-218** Corner plot of the free parameters.

MRC 2048-272

MRC 2048-272 has no continuum detection with ALMA (Fig. A.62). SED fitting with MrMoose is done with four components, two synchrotron (north and south radio component), one modified BB and one AGN component. The northern and southern radio component (detected in VLA bands C and X) are each assigned to an individual synchrotron power-law. The VLA L and ATCA 7 mm bands do not resolve any individual components and are only considered for fitting the total radio flux (the combination of the northern and southern synchrotron power-law components). The ALMA upper limit at the AGN host location is associated to both synchrotron components and the modified BB. The LABOCA, SPIRE, PACS, MIPS and IRS data are fitted to the combination of the modified BB and AGN component. The best fit model only constrains the synchrotron, and both the AGN the modified BB models are unconstrained because the FIR through mid-infrared data are only upper limits. The PDF of the free parameters can be found in Fig. A.63, which shows that both the BB and AGN is unconstrained.

TABLE A.21: Data for MRC 2048-272 (z=2.060)

Photometric band	Flux[mJy]	Ref.
IRS (16 μm)	<0.22	A
PACS (100 μm)	<8.5	B
PACS (160 μm)	<25.3	B
SPIRE (250 μm)	<15.3	B
SPIRE (350 μm)	<16.0	B
SPIRE (500 μm)	<18.6	B
LABOCA (870 μm)	<21.0	B
ALMA 6	<0.17	this paper
ATCA (7 mm)	3.22 ± 0.96^a	this paper
VLA X^n	25.81 ± 0.04^a	C
VLA X^s	0.71 ± 0.07^a	C
VLA C^n	77.06 ± 0.10^a	C
VLA C^s	4.90 ± 0.15	C
VLA L	498.1 ± 49	D

Notes (*n*) North lobe, (*s*) South lobe, (*a*) flux estimated using AIPS from original radio map, convolved to the resolution of the VLA C band.

References. (A) De Breuck et al. (2010), (B) Drouart et al. (2014), (C) Carilli et al. (1997), (D)Condon et al. (1998).

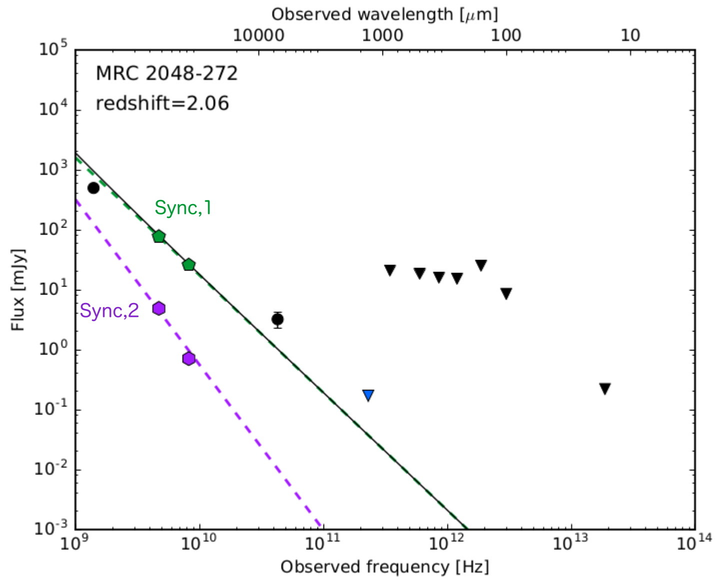

FIGURE A.61: SED of **MRC 2048-272**. The black solid line shows the best fit total model, green and purple dashed lines are the northern and southern synchrotron lobes. Neither the black body nor the AGN component are fitted to the upper limits. The coloured data points are sub-arcsec resolution data and black ones indicate data of low spatial resolution. Green pentagons are northern synchrotron, purple hexagons are the southern synchrotron component and the blue triangle shows the ALMA 6 3σ upper limit. Filled black circles indicate detections (>3σ) and downward pointing triangles the 3σ upper limits (Table A.21).

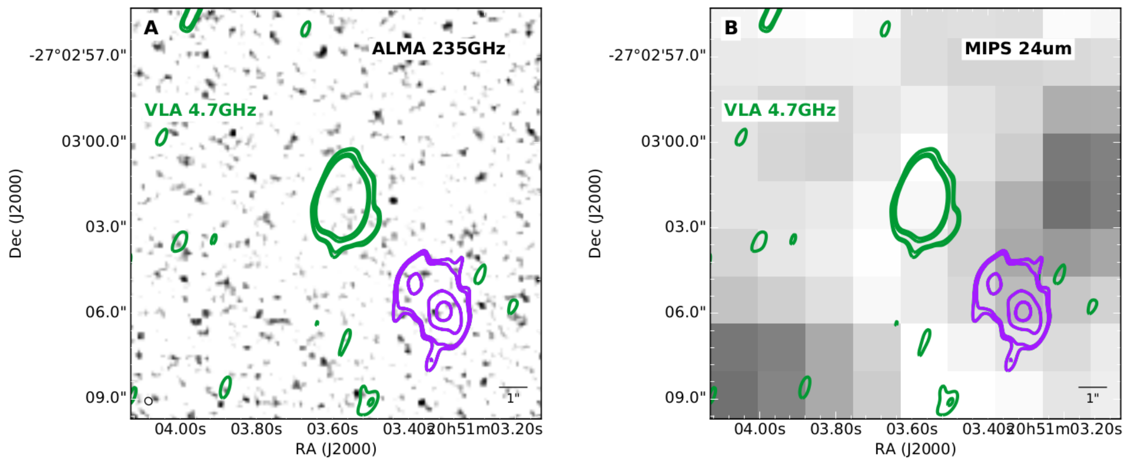

FIGURE A.62: *Panel A:* continuum map of ALMA band 6 with overlaid VLA C contours (levels as Fig. A.2,σ = 53 μJy). The green and purple contours show the two components of the VLA data and corresponds to the markers of the same colors as in the SED fit. *Panel B:* MIPS 24 μm continuum map.

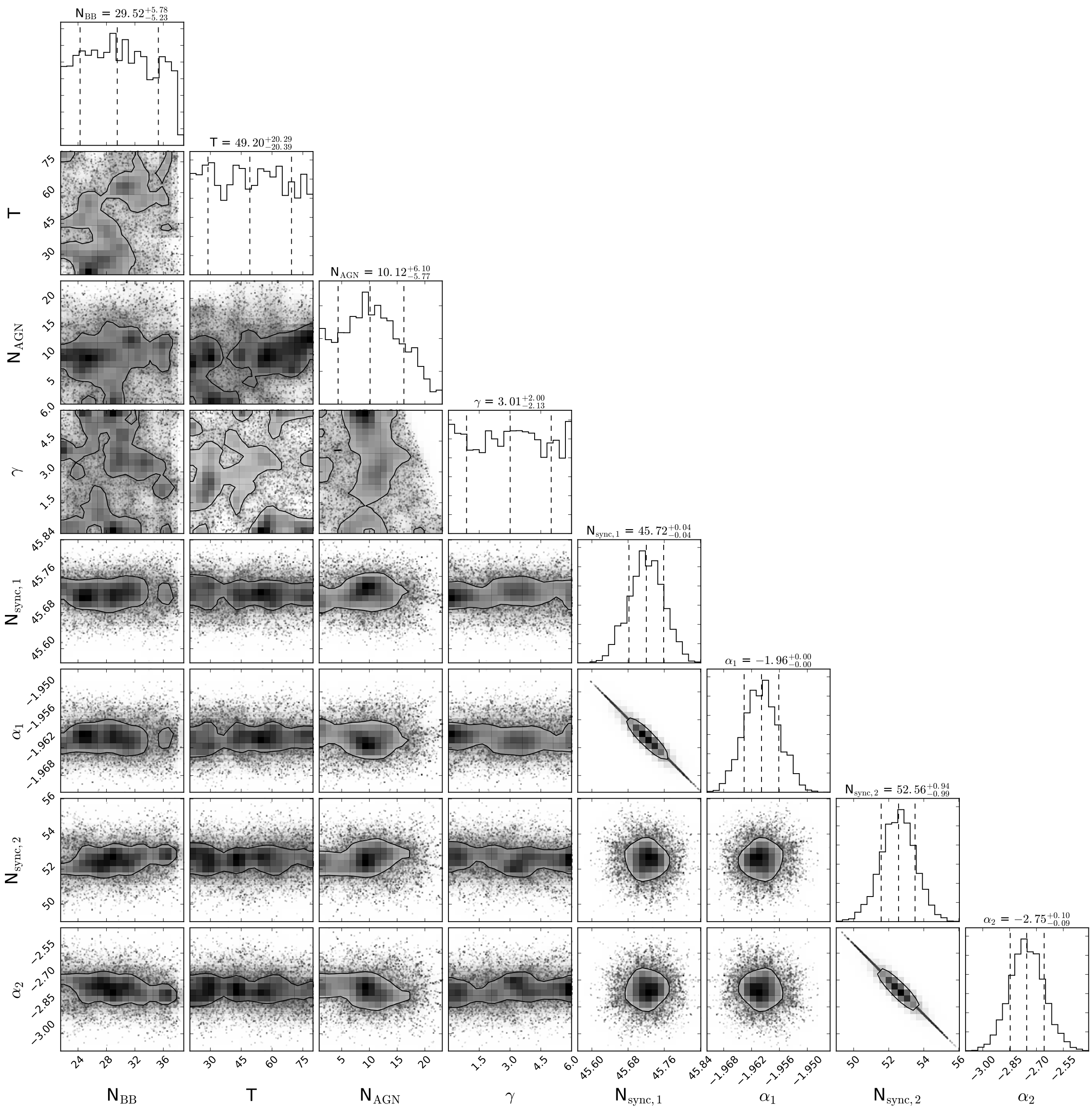

FIGURE A.63: **MRC 2048-272** Corner plot of the free parameters.

MRC 2104-242

MRC 2104-242 has no continuum detection with ALMA (Fig. A.65). SED fitting with MrMoose is done with three components, one synchrotron (only the core, the northern and southern radio components are excluded in the fit), one modified BB and one AGN component. The VLA C and X band data are assigned to the sychrotron power law of the radio core. The ALMA upper limit at the AGN host location is associated to both synchrotron components and the modified BB. The SPIRE, PACS, MIPS and IRS data are fitted to the combination of the modified BB and a AGN component. The best fit model only constrains the synchrotron and AGN component, the modified BB models are unconstrained due to the FIR data consisting only of upper limits (Fig. A.64). The PDF of the free parameters can be found in Fig. A.66, which shows that the BB is unconstrained.

TABLE A.22: Data for MRC 2104-242 (z=2.491)

Photometric band	Flux[mJy]	Ref.
IRS (16 μm)	<0.217	A
MIPS (24 μm)	0.709±0.048	A
PACS (100 μm)	14.4±3.5	B
PACS (160 μm)	22.0±8.4	B
SPIRE (250 μm)	<14.2^a	B
SPIRE (350 μm)	21.1±6.6	B
SPIRE (500 μm)	<15.8	B
ALMA 6	<0.12	this paper
VLA X^c	0.63±0.03^b	C
VLA C^c	1.53±0.14^b	C
ATCA (7mm)*	0.64 ±0.44	this paper

Notes (*c*) Radio core, (*a*) changed to upper limit because of contaminating forground object (*b*) flux estimated using AIPS from original radio map, convolved to the resolution of the VLA C band (*) data not used in fitting.

References. (A) De Breuck et al. (2010), (B) Drouart et al. (2014), (C) Pentericci et al. (2000).

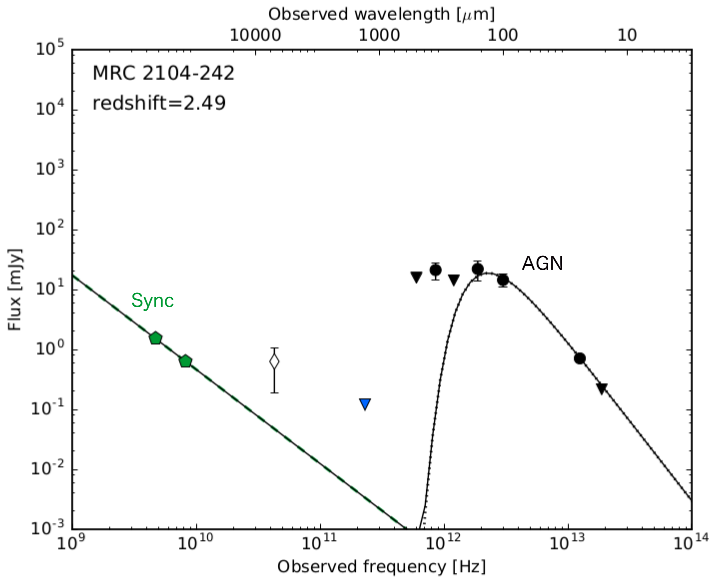

FIGURE A.64: SED of **MRC 2104-242**. Black solid line shows best fit total model, green dashed line is the radio core and the black dotted line is the AGN component. The coloured data points are sub-arcsec resolution data and black ones indicate data of low resolution. Green pentagons represent the synchrotron core and the blue triangle indicates the ALMA 6 3σ upper limit. Filled black circles indicate detections ($>3\sigma$) and downward pointing triangles the 3σ upper limits (Table A.22). The open diamond indicates available ATCA data but is only plotted as a reference and not used in the SED fit.

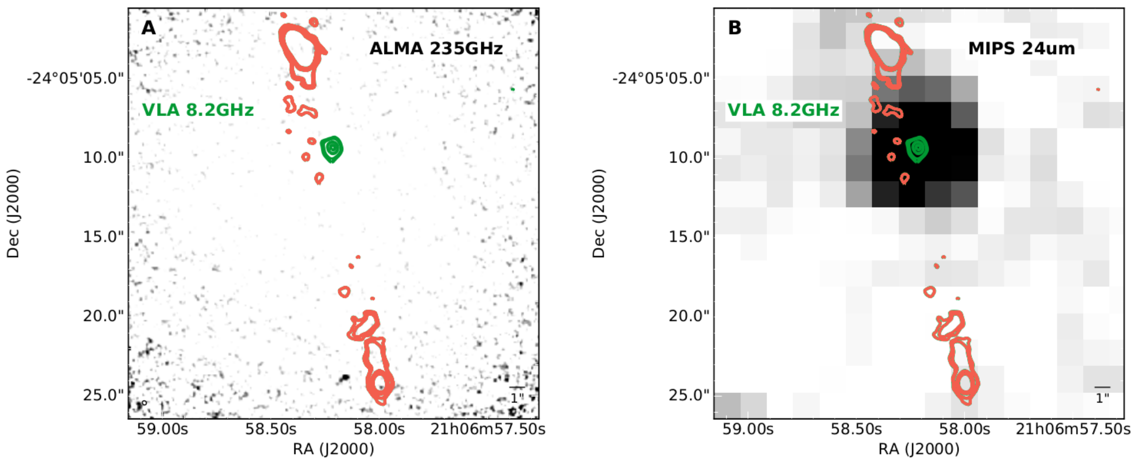

FIGURE A.65: *Panel A:* continuum map of ALMA band 6 with overlaid VLA C contours (levels are as Fig. A.2, $\sigma = 22\,\mu$Jy). The green contours show the two components of the VLA data and correspond to the markers of the same colors as in the SED fit (Fig. A.64). The red contours are excluded in the fit. *Panel B:* MIPS 24 μm continuum map.

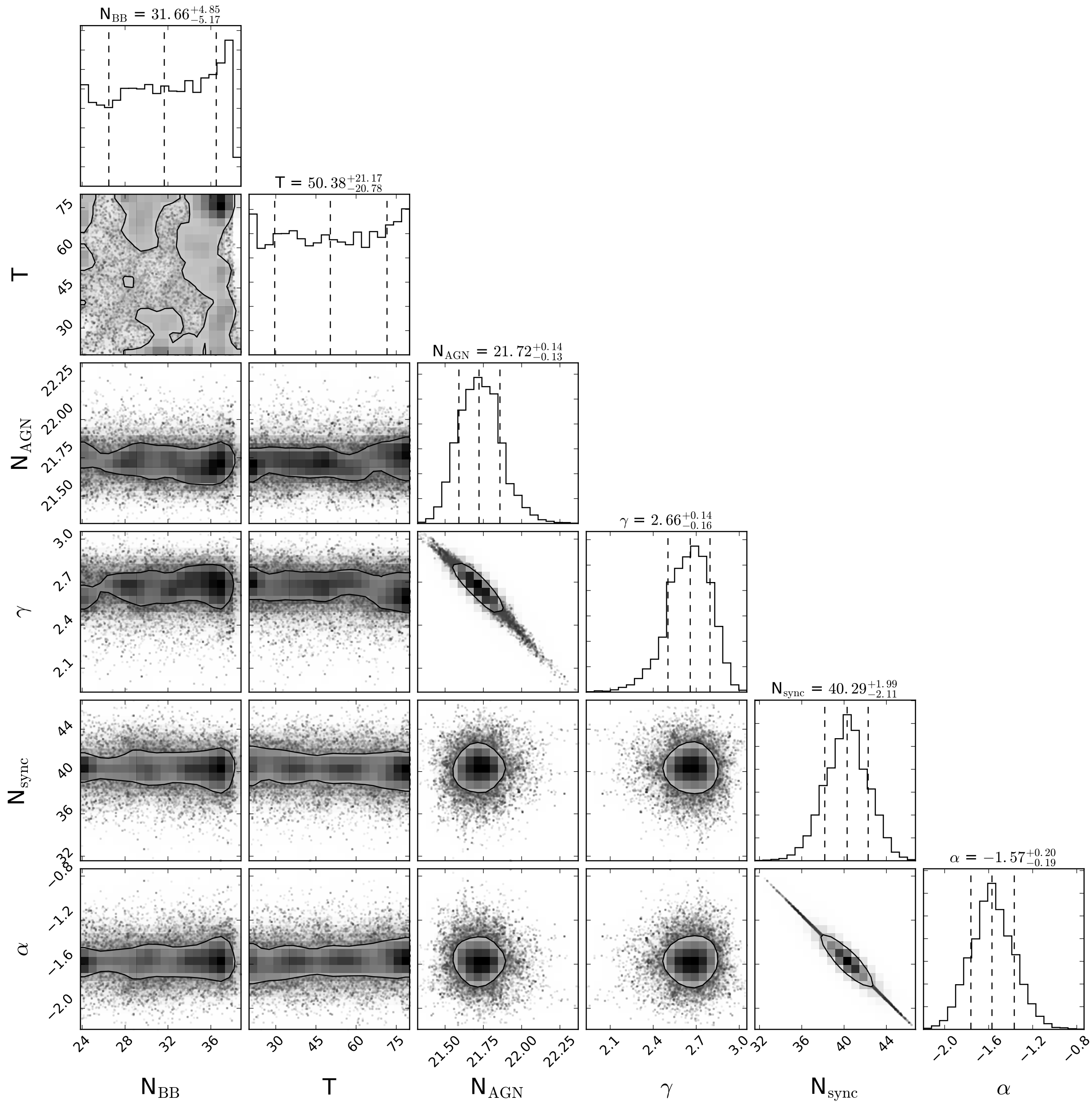

FIGURE A.66: **MRC 2104-242** Corner plot of the free parameters.

4C 23.56

4C 23.56 has no continuum detection in ALMA band 6, but is detected in band 3. The detection coincides with the radio core (Fig. A.68). SED fitting with MrMoose is done with three components, one synchrotron power-law (of the core, the north and south lobe are excluded for the fit), one modified BB and one AGN component. The VLA C and X band fluxes are assigned to the synchrotron power-law. The ALMA band 3 detection is assigned to both the synchrotron model and modified BB and the same set up is used for the ALMA band 6 upper limit. The LABOCA, SPIRE, PACS, MIPS and IRS are assigned to the combination of the modified BB and a AGN component. The best fit model constrains the synchrotron and gives that the ALMA band 3 detection is dominated by synchrotron emission. The modified BB is unconstrained (Fig. A.67) due to the fact that all the FIR data points are upper limits. This source has a low SFR and the IR emission is dominated by the AGN. We note that this galaxy was use to fix the ν_{cut}=33 μm for the model describing the AGN heated dust, because the SF contribution in the FIR is very weak. The PDF of the free parameters can be found in Fig. A.69, which shows that the BB is unconstrained.

TABLE A.23: Data for 4C 23.56 (z=2.483)

Photometric band	Flux[mJy]	Ref.
IRS (16 μm)	2.40 ± 0.090	A
MIPS (24 μm)	4.630 ± 0.040	A
PACS (70 μm)	29.2 ± 3.2	B
PACS (160 μm)	17.2 ± 6.8	B
SPIRE (250 μm)	<18.5	B
SPIRE (350 μm)	< 24.2	B
SPIRE (500 μm)	<25.9	B
LABOCA (870 μm)	<12.9	C
ALMA 6	$<0.4^{a}$	D
ALMA 3	0.23 ± 0.05^{a}	this paper
VLA X^{c}	5.11 ± 0.51^{b}	E
VLA C^{c}	8.77 ± 0.87^{b}	E

Notes (*c*) Radio core, (*a*) Flux estimated using AIPS for primary beam corrected images. (*b*) flux estimated using AIPS from original radio map, convolved to the resolution of the VLA C band.

References. (A) De Breuck et al. (2010), (B) Drouart et al. (2014), (C) Archibald et al. (2001), (D) Lee et al. (2017), (E) Carilli et al. (1997)

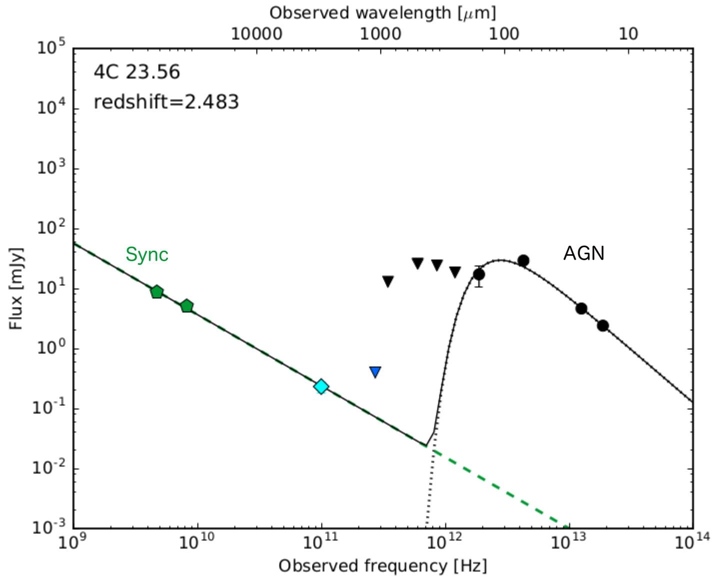

FIGURE A.67: SED of **4C 23.56**. Black solid line shows best fit total model, green dashed line is synchrotron power law for the radio core, dotted line indicates the AGN component. The coloured data points are sub-arcsec resolution data and black ones indicate data with low spatial resolution. Green pentagons are emission from the radio core, cyan diamond from ALMA band 3, blue triangle indicates the ALMA band 3 3σ upper limit. Filled black circles indicate detections (>3σ), downward pointing triangles the 3σ upper limits (Table A.1).

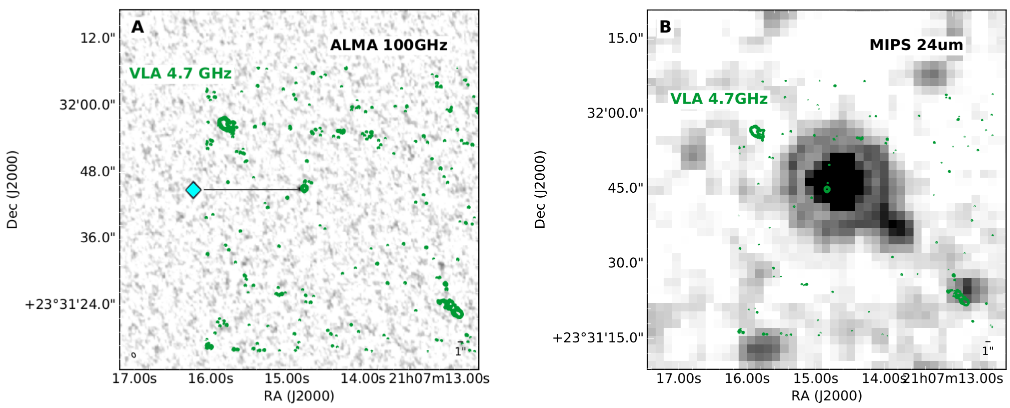

FIGURE A.68: *Panel A:* continuum map of ALMA band 3 with overlaid VLA C contours (levels are as Fig. A.2, σ = 67 μJy). The cyan marker indicate the ALMA detection and corresponds to the marker use in the SED fit (Fig. A.67). The green contours show the portion of the VLA data that is used in the SED fit, the red contours are excluded in the fit. *Panel B:* MIPS 24 μm continuum map.

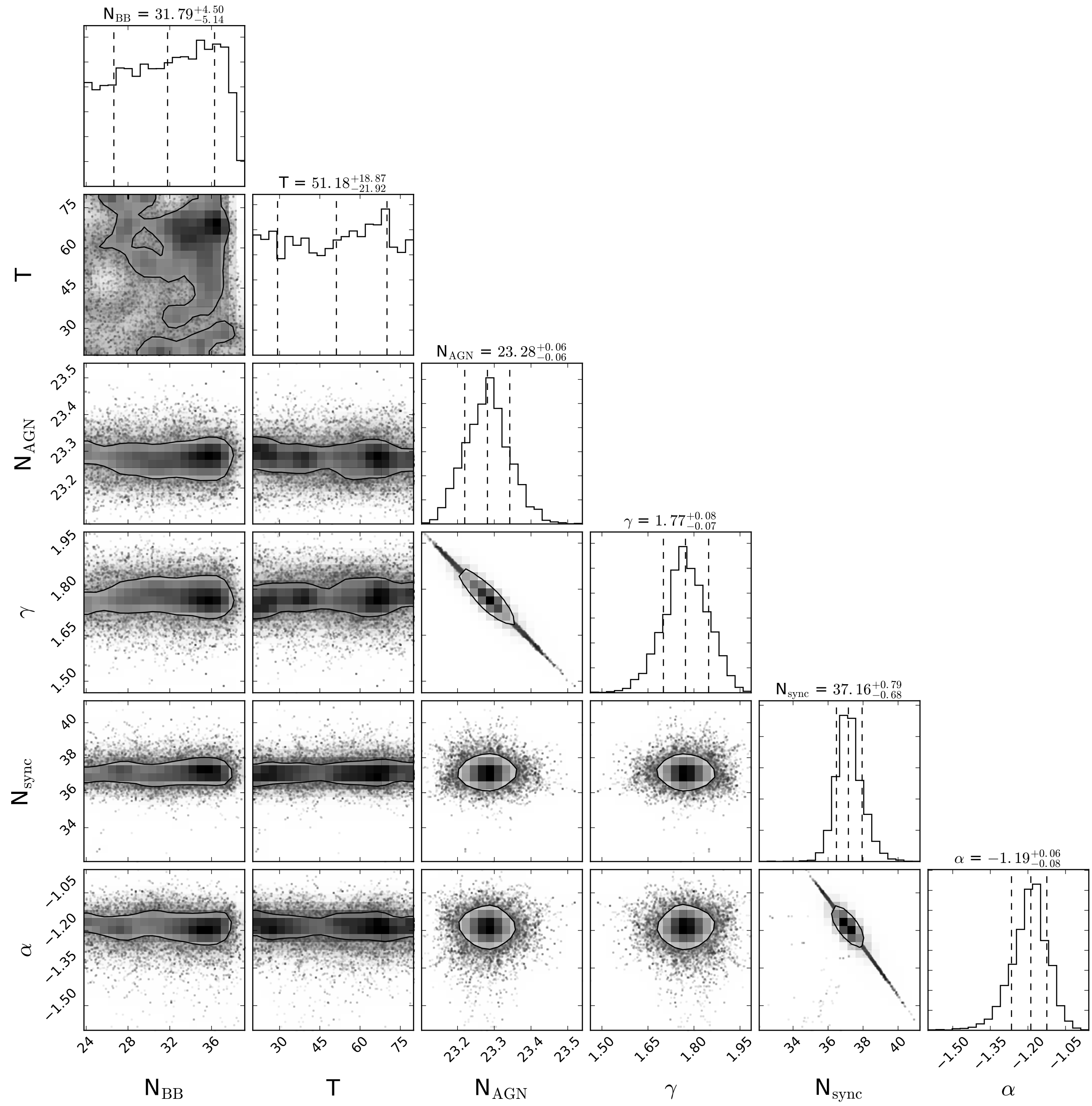

FIGURE A.69: **4C 23.56** Corner plot of the free parameters.

4C 19.71

4C 19.71 has three detected continuum components in ALMA band 3, one coincides with the AGN host galaxy and two coincide with the northern and southern synchrotron lobes (Fig. A.71). SED fitting with MrMoose is done with four components, two synchrotron (northern and southern radio components), one modified BB and one AGN component. The northern radio component (detected in VLA bands C and X) is assigned to the northern ALMA detection and fitted to a individual synchrtoron component, the same setup is also applied to the southern radio and ALMA components. The VLA L detection does not resolve any individual components and are only considered for fitting the the total radio flux (the combination of the northern and southern synchrtorn power-laws). The ALMA detection at the host location is assigned to only the modified BB and the SCUBA, SPIRE, PACS, MIPS and IRS are fitted to the combination of the modified BB and a AGN component. The best fit model constrains the two synchrotron components and they are fitted out to ALMA band 3. The ALMA detection at the host is dominated by thermal dust emission. The PDF of the free parameters can be found in Fig. A.72.

TABLE A.24: Data for 4C 19.71 (z=3.592)

Photometric band	Flux[mJy]	Ref.
IRS (16 μm)	<0.244	A
MIPS (24 μm)	0.529±0.033	A
PACS (100 μm)	<46.1	B
PACS (160 μm)	<40.4	B
SPIRE (250 μm)	<14.8	B
SPIRE (350 μm)	<18.1	B
SPIRE (500 μm)	<17.5	B
SCUBA (450 μm)	12±13	C
SCUBA (850 μm)	2.3±0.9	C
ALMA 3^c	0.07±0.05[1]	this paper
ALMA 3^n	0.29±0.53[1]	this paper
ALMA 3^s	0.11±0.05[1]	this paper
VLA X^n	14.36	D
VLA C^n	34.99±3.5	D
VLA X^s	9.02±0.9	D
VLA C^s	21.98±2.2	D
VLA L	343.2±10.3	E

(1) Integrated flux extracted using AIPS with imfit 1 Gaussian component

References. (A) De Breuck et al. (2010), (B) Drouart et al. (2014), (C) (Reuland et al. 2004) (D) Reuland et al. (2003a) (E) Pentericci et al. (2000).

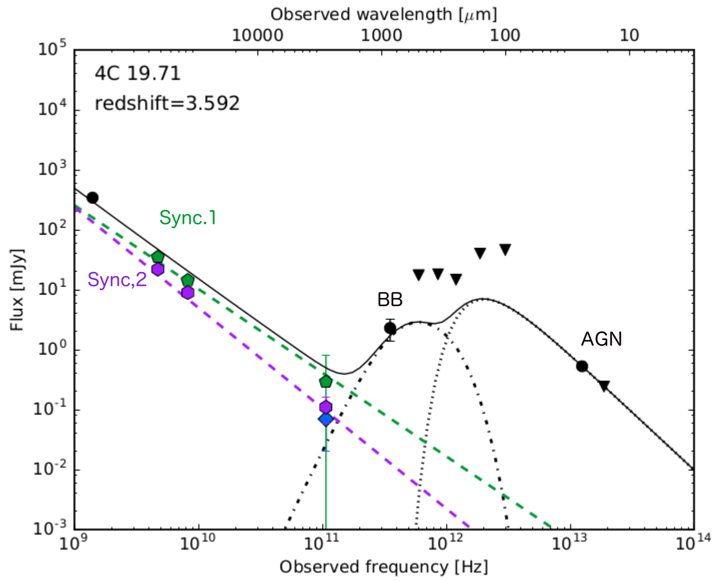

FIGURE A.70: SED of **4C 19.71**. Black solid line shows best fit total model, black dashed line is the total synchrotron, the black dash-dotted lines is the black body and the black dotted line indicates the AGN component. The coloured data points are sub-arcsec resolution data and black ones indicate data of low resolution. The blue diamond indicates the ALMA band 3 detection. Filled black circles indicate detections (>3σ) and downward pointing triangles the 3σ upper limits (Table A.24).

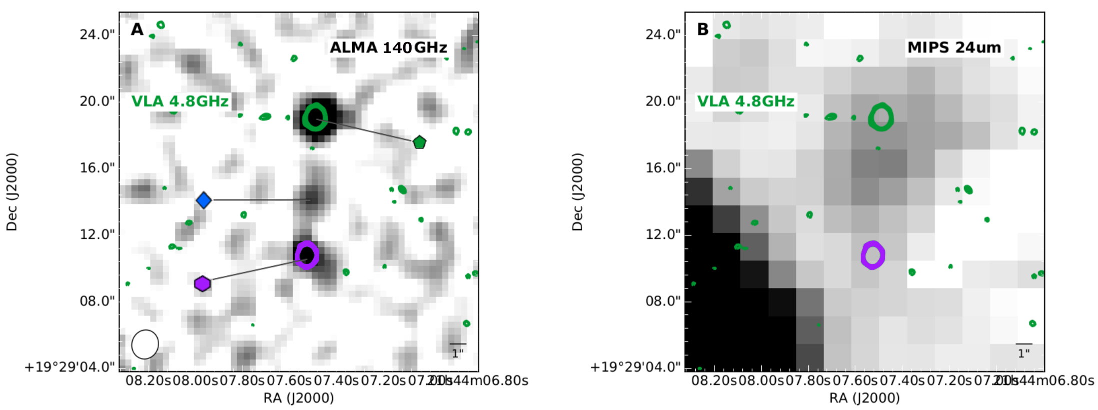

FIGURE A.71: *Panel A:* continuum map of ALMA band 3 with overlaid VLA C contours (levels are as Fig. A.2, $\sigma = 45\,\mu$Jy). The blue, green and purple markers indicate the three different components detected with ALMA and correspond to the same data point as Fig. A.70. The green and purple contours show the two components of the VLA data and correspond to the markers of the same colors as in the SED fit. *Panel B:* MIPS 24 μm continuum map.

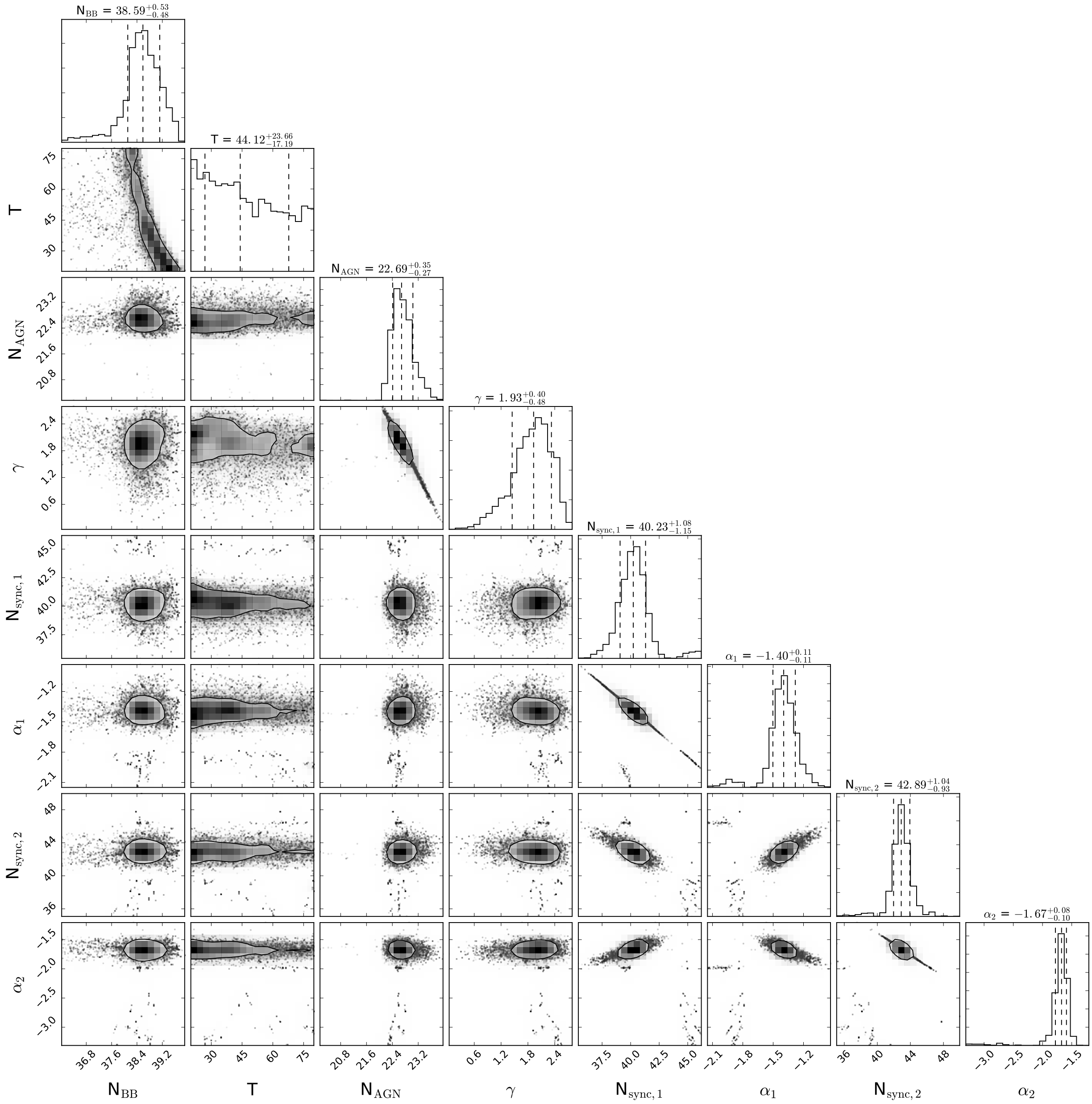

FIGURE A.72: **4C 19.71** Corner plot of the free parameters.

MRC 2224-273

MRC 2224-273 has a single continuum detection which coincides with the compact synchrotron emission (Fig. A.74). SED fitting with MrMoose is done with three components, one synchrotron power-law, one modified BB and one AGN component. The VLA X, C and L data are assigned to the synchrotron power-law, the ALMA detection is assigned to both synchrotron component and a modified BB. The LABOCA, SPIRE, PACS, MIPS and IRS are fitted to the combination of the modified BB and a AGN component. The best fit model gives that the ALMA detection is dominated by thermal dust emission. Without a flux at intermediate radio frequencies between the VLA and ALMA data, it is not possible to constrain whether or not the synchrotron is steeping. In any case, the synchroton emission does not significantly contribute to the emission detected by ALMA. The PDF of the free parameters can be found in Fig. A.75.

TABLE A.25: Data for MRC 2224-273 (z=1.68)

Photometric band	Flux[mJy]	Ref.
IRS (16 μm)	0.625±0.117	A
MIPS (24 μm)	1.06±0.04	A
PACS (70 μm)	<10.5	B
PACS (160 μm)	<28.9	B
SPIRE (250 μm)	14.6±4.8	B
SPIRE (350 μm)	<17.6	B
SPIRE (500 μm)	<18.3	B
LABOCA (870 μm)	<12.3	B
ALMA 6	0.22±0.06	this paper
VLA X	19±0.022	C
VLA C	48±0.56	C
VLA L	269.9±26	D

References. (A) De Breuck et al. (2010), (B) Drouart et al. (2014), (C) Pentericci et al. (2000), (D)Condon et al. (1998).

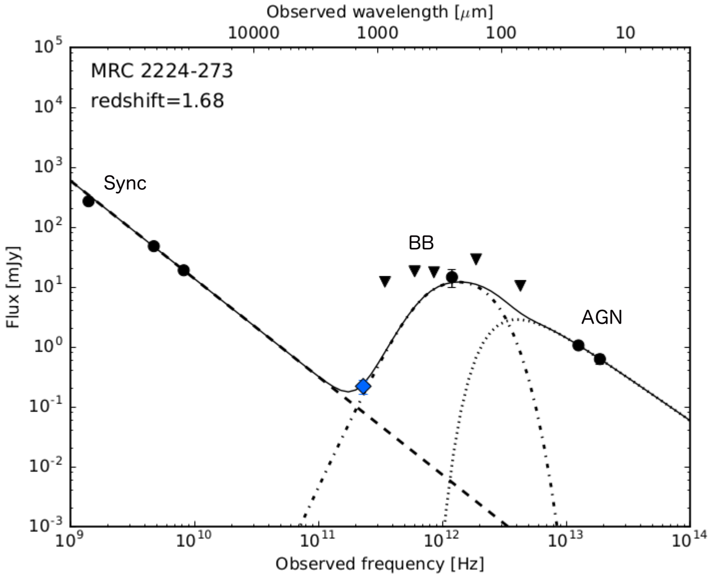

FIGURE A.73: SED of **MRC 2224-273**. Black solid line shows best fit total model, black dashed line is the total synchrotron, the black dash-dotted lines is the black body and the black dotted line indicates the AGN component. The coloured data points are sub-arcsec resolution data and black ones indicate data of low resolution. The blue diamond indicates the ALMA band 6 detection. Filled black circles indicate detections (>3σ) and downward pointing triangles the 3σ upper limits (Table A.25).

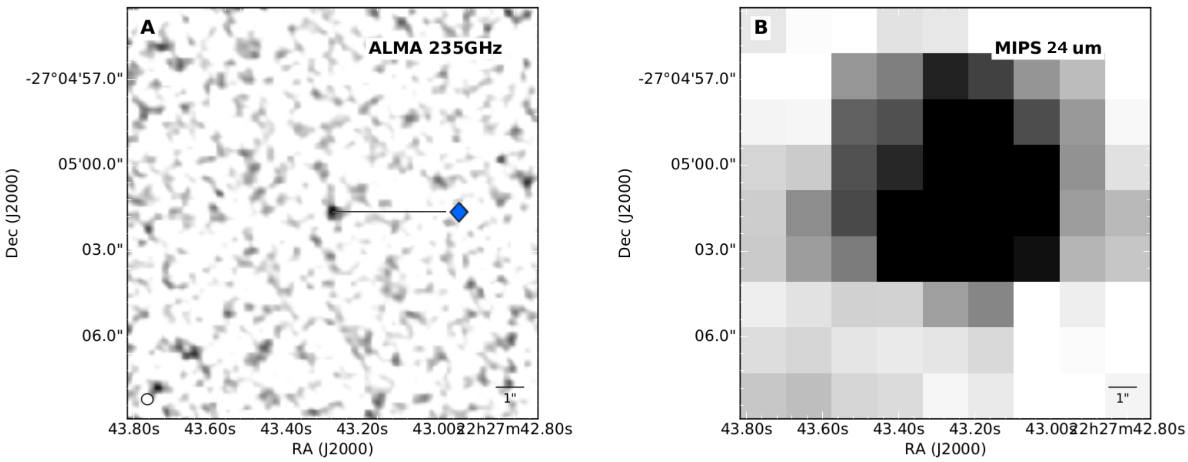

FIGURE A.74: *Panel A:* continuum map of ALMA band 6. The blue marker indicates the ALMA dectection and corresponds to same data point in Fig. A.73. VLA maps not accessible, but the source is unresolved, as shown in Pentericci et al. (2000). *Panel B:* MIPS 24 μm continuum map.

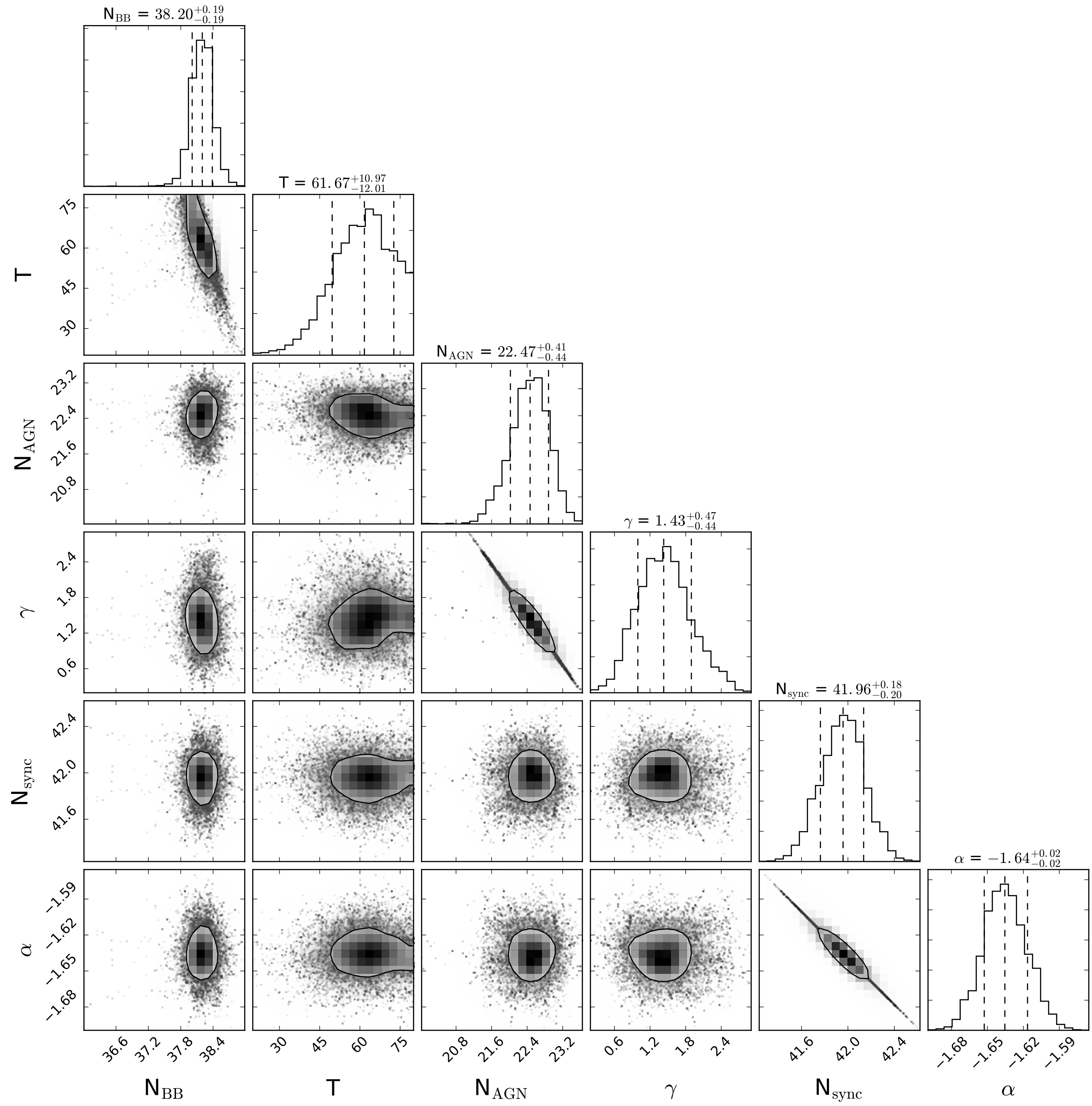

FIGURE A.75: **MRC 2224-273** Corner plot of the free parameters.

A.4 Redshift of foreground sources around 4C19.71

In the view around 4C19.71 there are four foreground galaxies, two of which have previously been reported in literature (to the knowledge of the authors) with counterparts in other wavelengths and two of which are new and detected in the MUSE cube published in this paper. Table A.26 summaries the detected lines, redshift and also lists the coordinates for the sources and objects shown in figure 4.1.

Galaxy 1 is detected in X-ray, K-band and IRAC 1 and now with MUSE also in the line emission from Hβ, [O III]λ4959, [O III]λ5007 (Fig. A.76). From the three lines the redshift is found to be z=0.483. Galaxy 2 is only detected in Lyα (Fig. A.77) which would result in a redshift of z=3.31. Unfortunately there are no other strong line in the spectra so the redshift is not completely reliable, but it is likely a high-z source since it is not seen in any of the previous observations. Galaxy 3 is not observed in any of the photomteric bands, but is detected in O II] λ3727, [O III]λ4959, [O III]λ5007 (Fig. A.78) and has a redshift of z=0.639. The fourth foreground source, Galaxy 4 is detected in K-band and IRAC 1 and the MUSE spectra show only one strong line. We interpret this as O II] λ3727 since the line coincide with a continuum break, likely to be the 4000 Å having $D_{4000} = 1.6$ between the average flux density of 4100–4400 Å and 3600–3900 Å.

Source	α(J2000)	δ(J2000)	redshift	line of which z is determined
4C19.71*	21:44:07.52	19:29:14.2	3.5895	[C I]
North radio hot spot	21:44:07.49	19:29:19.1	...	...
South radio hot spot	21:44:07.53	19:29:10.8	...	...
Galaxy 1	21:44:07.67	19:29:07.7	0.483	Hβ, [O III]λ4959, [O III]λ5007
Galaxy 2	21:44:07.47	19:29:05.7	3.31^u	Lyα λ1215.7
Galaxy 3	21:44:07.56	19:29:11.1	0.639	O II] λ3727, [O III]λ4959, [O III] λ5007
Galaxy 4	21:44:07.36	19:29:19.3	1.03	O II] λ3727

TABLE A.26: Coordinates of sources in the field and redshift of the foreground objects. ($*$) center of the host galaxy determined from the peak of the thermal dust emission of the ALMA band 3 continuum image. (u) redshift only estimated from one line

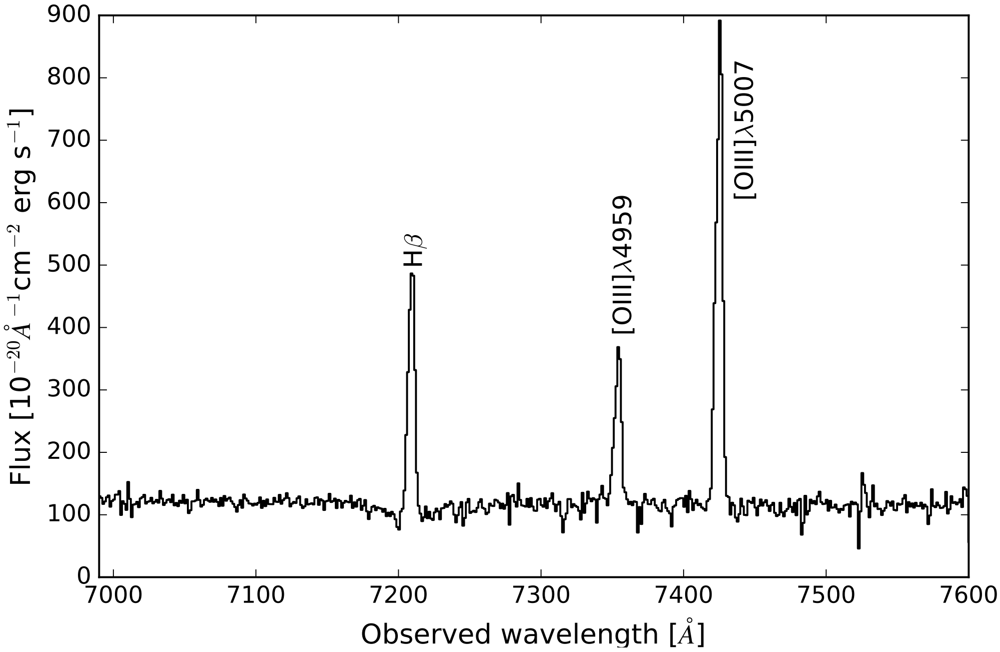

FIGURE A.76: Foreground Galaxy 1 at z=0.483, extracted spectrum is with a circular aperture of 3 pixel radius. The [O III] λ5007, λ4959 doublet and Hβ are detected.

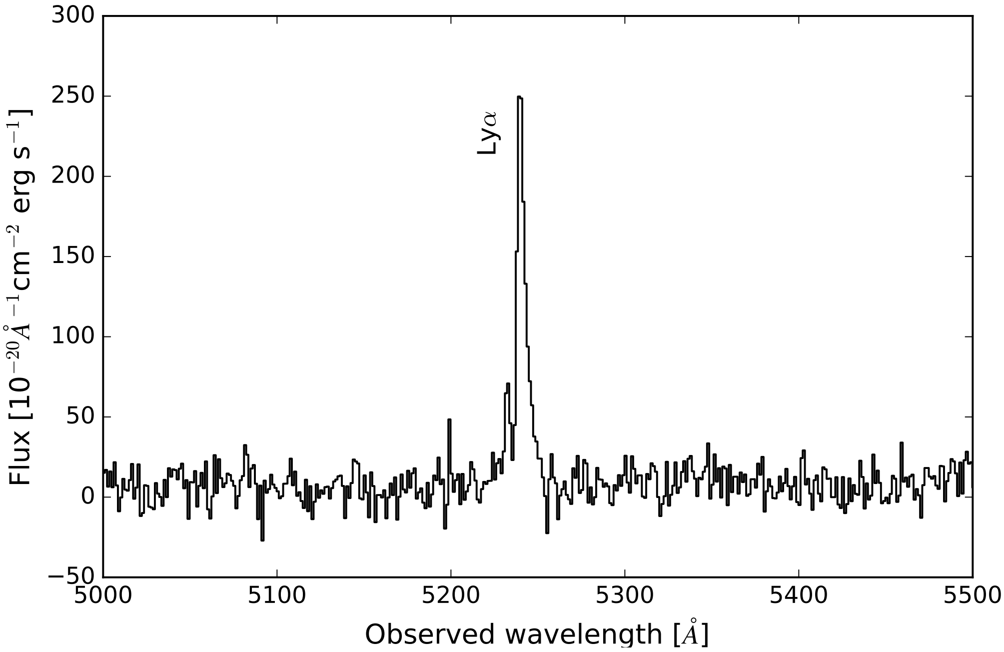

FIGURE A.77: Foreground Galaxy 2 at z=3.31, extracted spectrum is with a circular aperture of 3 pixel radius. The Lyα lines is used for the redshift estimate, but without other strong lines it is not possible to determine to confirm a solid redshift.

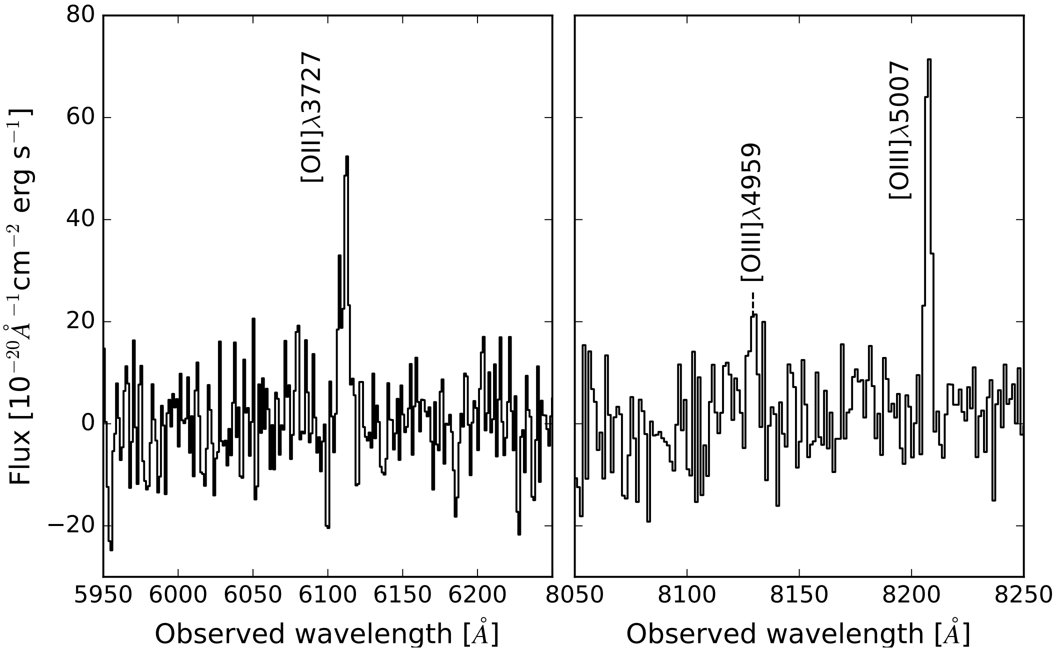

FIGURE A.78: Foreground Galaxy 3 at z=0.639, the extracted spectrum is with a circular aperture of 3 pixel radius. The O II] λ3727, [O III]λ4959, [O III]λ5007 are detected.

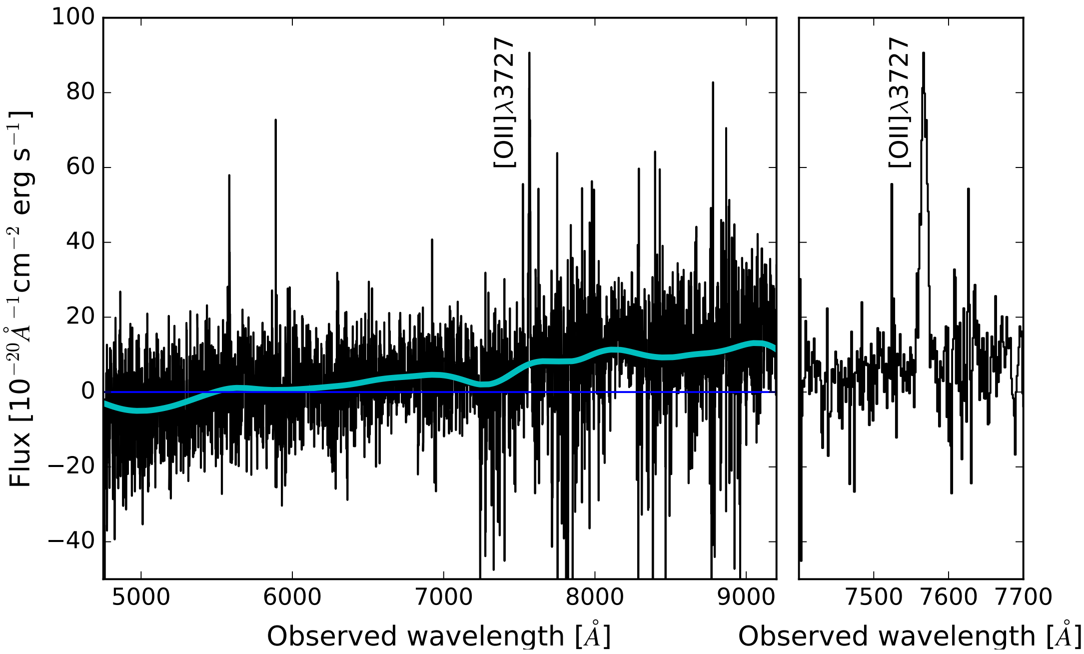

FIGURE A.79: Foreground Galaxy 4 at z=1.03, the extracted spectrum is with a circular aperture of 3 pixel radius. *Left panel:* the full spectrum of the extracted region which has contaminating Lyα from 4C19.71 at $\lambda_{\rm obs}$ ~5580 Å. The cyan line shows the Hanning smooth spectrum and the blue line highlights the zero line; *right panel:* zoom in of the line at $\lambda_{\rm obs}$=7567.95 Å originating from Galaxy 4. The redshift it determined only from the O II] line, but the continuum break seen in association with the line is likely the 4000 Åbreak, which strengthens the assumption that we are really looking at the O II]λ3727 line.

Appendix B

Co-author papers

B.1 Are we seeing accretion flows in a 250 kpc Lyα halo at z = 3?

B.1.1 The paper

For the paper I proofread the draft version and commented on the discussion.

A&A 602, L6 (2017)
DOI: 10.1051/0004-6361/201730865

Astronomy & Astrophysics

Letter to the Editor

Are we seeing accretion flows in a 250 kpc Lyα halo at $z = 3$?[⋆]

J. Vernet[1], M. D. Lehnert[2], C. De Breuck[1], M. Villar-Martín[3], D. Wylezalek[4], T. Falkendal[1,2], G. Drouart[5], S. Kolwa[1], A. Humphrey[6], B. P. Venemans[7], and F. Boulanger[8,⋆⋆]

[1] European Southern Observatory, Karl-Schwarzschild-Str. 2, 85748 Garching, Germany
e-mail: jvernet@eso.org
[2] Sorbonne Universités, UPMC, Paris VI, CNRS UMR 7095, Institut d'Astrophysique de Paris, 98bis Bd Arago, 75014 Paris, France
[3] Centro de Astrobiologìa (INTA-CSIC), Carretera de Ajalvir, km 4, 28850 Torrejòn de Ardoz, Madrid, Spain
[4] Department of Physics and Astronomy, Johns Hopkins University, 3400 N. Charles St, Baltimore, MD 21218, USA
[5] International Centre for Radio Astronomy Research, Curtin University, Perth WA 6845, Australia
[6] Instituto de Astrofísica e Ciências do Espaço, Universidade do Porto, CAUP, Rua das Estrelas, 4150-762 Porto, Portugal
[7] Max-Planck Institute for Astronomy, Königstuhl 17, 69117 Heidelberg, Germany
[8] Institut d'Astrophysique Spatiale, 91405 Orsay, Université Paris Sud et CNRS, France

Received 24 March 2017 / Accepted 18 May 2017

ABSTRACT

Using MUSE on the ESO-VLT, we obtained a four-hour exposure of the $z = 3.12$ radio galaxy MRC 0316-257. We detect features down to $\sim 10^{-19}$ erg s^{-1} cm^{-2} arcsec^{-2}, with the highest surface brightness regions reaching more than a factor of 100 higher. We find Lyα emission out to ∼250 kpc in projection from the active galactic nucleus (AGN). The emission shows arc-like morphologies arising at 150−250 kpc from the nucleus in projection, with the connected filamentary structures reaching down into the circumnuclear region. The most distant arc is offset by ∼700 km s^{-1} relative to circumnuclear HeIIλ1640 emission, which we assume to be at the systemic velocity. As we probe emission closer to the nucleus, the filamentary emission narrows in projection on the sky, the relative velocity decreases to ∼250 km s^{-1}, and the line full-width at half maximum ranges from ∼300−700 km s^{-1}. From UV line ratios, the emission on scales of 10s of kpc from the nucleus along a wide angle in the direction of the radio jets is clearly excited by the radio jets and ionizing radiation of the AGN. Assuming ionization equilibrium, the more extended emission outside of the axis of the jet direction would require 100% or more illumination to explain the observed surface brightness. High-speed ($\gtrsim$300 km s^{-1}) shocks into rare gas would provide sufficiently high surface brightness. We discuss the possibility that the arcs of Lyα emission represent accretion shocks and the filamentary emission represents gas flows into the halo, and compare our results with gas accretion simulations.

Key words. galaxies: evolution – galaxies: high-redshift – galaxies: active – galaxies: ISM – galaxies: halos

1. Introduction

High-redshift radio galaxies, quasars (Heckman et al. 1991a,b), QSOs (Christensen et al. 2006), and "Lyα blobs" (Steidel et al. 2000) exhibit strong, extended Lyα emission. High-redshift radio galaxies play a central role in our evolving understanding of the association between massive galaxies, their clustered environments, and halo gas. The first galaxies at high redshift, $z > 2$, where halo gas was detected in Lyα emission over scales of 10−100s kpc, were radio galaxies (Chambers et al. 1990). These Lyα halos are generally aligned with the radio jets but extend well beyond the radio lobes (Villar-Martín et al. 2003). The association between the active galactic nuclei (AGN) and the extended Lyα emission is unclear. In the circumgalactic environment within the radius subtended by the radio lobes, the Lyα kinematics are complex, while outside the radio emission, the gas is relatively quiescent (Villar-Martín et al. 2003).

The energy sources of Lyα nebulae are poorly constrained (Cantalupo 2017). All processes that excite the Lyα emission depend on the distribution of the emission line gas, the type of objects within the nebula, and on how far away the emission is located from sources of ionizing photons. While ionizing photons from galaxies embedded within the Lyα emission are a plausible explanation (Overzier et al. 2013), other sources powering the Lyα emission include ionization by the meta-galactic flux, mechanical heating, dissipation of potential energy as the gas falls into the halo, and resonance scattering of Lyα and UV continuum photons. The mechanisms powering the emission are inextricably linked with the origin of the gas. If the emission is related to outflows, the excitation of the gas might be due to shocks and ionization by stars or AGN (Swinbank et al. 2015). If the gas extends >100 kpc, it may be accreting from the cosmic web or gas instabilities in the halo (Maller & Bullock 2004). In this case, we expect the emission to be due to mechanical heating associated with accretion shocks (Birnboim & Dekel 2003) or from the dissipation of potential energy that the flows gain as they fall into the potential.

While these general arguments motivated us to obtain deep integral-field spectroscopy of radio galaxies using MUSE on the ESO-VLT, in the specific case of MRC 0316-257, we are motivated by its striking Lyα morphology. MRC 0316-257 is a well-studied massive $\approx 2 \times 10^{11}\,M_{\odot}$ radio galaxy (De Breuck et al. 2010) that lies in a galaxy overdensity

[⋆] Based on observations made with ESO Telescopes at the La Silla Paranal Observatory under program ID 094.B-0699(A).
[⋆⋆] Research associate at Institut d'Astrophysique de Paris.

Table 1. Characteristics of spectra of particular regions.

Id	SB × 10^{-19} erg s^{-1} cm^{-2} $arcsec^{-2}$	ΔV km s^{-1}	*FWHM* km s^{-1}	Area $arcsec^2$
1	1.3 ± 0.2	142 ± 13	250 ± 32	14.3
2	1.6 ± 0.1	220 ± 9	430 ± 21	46.5
3	1.4 ± 0.1	211 ± 12	550 ± 29	40.5
4	5.5 ± 0.2	224 ± 5	410 ± 13	9.3
5	2.8 ± 0.1	225 ± 11	550 ± 26	11.4
6	2.1 ± 0.1	230 ± 6	395 ± 16	43.4
7	0.8 ± 0.1	227 ± 25	525 ± 62	35.0
8	0.9 ± 0.1	226 ± 28	670 ± 70	17.2
9	2.6 ± 0.2	250 ± 14	510 ± 32	8.5
10	0.8 ± 0.1	290 ± 13	510 ± 32	74.0
11	1.9 ± 0.1	610 ± 11	720 ± 27	36.6

Notes. The identification numbers correspond to the regions in Fig. 2. The measured ΔV of regions 2−9 are statistically the same.

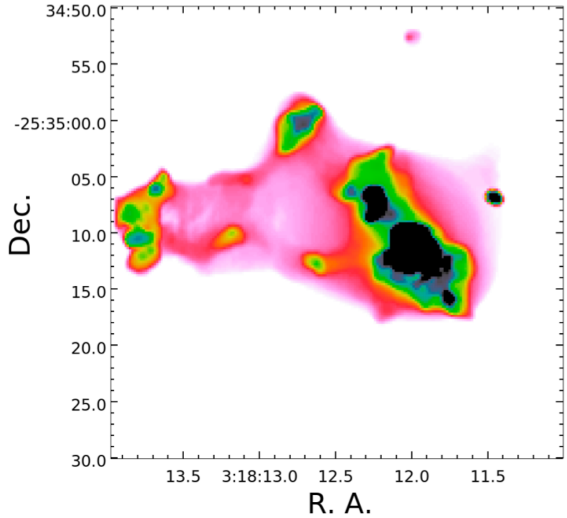

Fig. 1. Narrow-band image 25 Å wide centered on Lyα extracted from an adaptively smoothed datacube with the algorithm described in Martin et al. (2014). We used a maximum spatial smoothing scale of 14″ and a signal-to-noise ratio threshold of 2.5 in making this image. This plot is intended to be illustrative and was not used in the analysis.

(Kuiper et al. 2012). The Lyα emission around MRC 0316-257 is filamentary on scales of ~250 kpc and has a morphology and surface brightness distribution similar to those seen in galaxy simulations. Simulations of gas accretion imply that streams will be visible via their Lyα emission if we detect down to a surface brightness of $\approx 10^{-19}$ erg s^{-1} cm^{-2} $arcsec^{-2}$ at $z \sim 3$ (Rosdahl & Blaizot 2012). It is not clear whether these simulations capture all the physics necessary to model the emission and evolution of the accreting gas (e.g., Cornuault et al. 2016). Observational constraints are needed. Of course, one must worry about expectation bias (Jeng 2006). Do we call what we observe a "stream" because its morphology agrees with the results of simulations? While we are concerned about this bias, it is still instructive to compare our results with those of simulations.

2. Observations, analysis, and results

Multi Unit Spectroscopic Explorer (MUSE; Bacon et al. 2010) observations of MRC 0316-257 were obtained in service mode between UT January 2015 14 and 17. We used the Wide Field Mode (1′ × 1′ field of view) with the second-order blocking filter, resulting in a wavelength coverage of 480−935 nm. Our eight 900 s exposures were taken at position angles of 0, 90, 180, and 270° with a small pointing offset to mitigate systematic artifacts. We processed the data using MUSE pipeline version 1 (Weilbacher et al. 2012) to produce a fully calibrated (wavelength, flux, and astrometry) sky-subtracted data cube. The measured image quality of the reconstructed white-light image is ~1″. To preserve any possible extended low surface-brightness features, we did not use sky-residual cleaning algorithms.

To remove remaining artifacts, we subtracted all continuum sources from the datacube using a linear interpolation between two bins 50 Å wide on both sides of the emission line. The very extended Lyα emission is only marginally detected. To make the Lyα morphology more evident, we implemented our own version of the algorithm of Martin et al. (2014, Fig. 1). To provide the characteristics of the Lyα emission, we extracted and fit the Lyα line from several regions (Table 1, Fig. 2). The line ratios of Lyα, CIV$\lambda\lambda$1548, 1551, HeIIλ1640, and CIII]$\lambda\lambda$1907, 1909 of the highest surface brightness regions (3−5) imply they are ionized by the AGN. Beyond the circumnuclear emission, ≳10″ from the AGN, the Lyα emitting regions are too faint to determine line ratios necessary to constrain the ionization source.

We find Lyα emission down to $\approx 10^{-19}$ erg s^{-1} cm^{-2} $arcsec^{-2}$ and up to ~35″ from the radio galaxy (~250 kpc in projection). The morphology of the emission, outside of the emission that is likely to be excited by the AGN, is arc- and stream-like, with the higher surface brightness arcs appearing at ~150−250 kpc (regions 1, 2, and 11) from the nucleus, with the connected filamentary structures reaching into the circumnuclear regions (regions 6−8). The most distant arc (region 11) has an offset velocity relative to the arcsecond-scale HeIIλ1640 emission from the AGN of ~700 km s^{-1}. We assumed that the velocity of the HeII line represents the systemic velocity of the system. This assumption is supported by the low relative offset velocity (≲50 km s^{-1}) between circumnuclear dense gas (from CO(8−7)) and HeII in another radio galaxy (Gullberg et al. 2016). Closer to the nucleus, the filaments of Lyα emission narrow on the sky, the redshifted offset velocity decreases to ~250 km s^{-1}, the line full-width at half maximum (FWHM) remains very high, reaching up to 700 km s^{-1} and ~50−100 kpc from the nucleus. Throughout the emission, the lines are broad, ~300−700 km s^{-1}.

Projected onto region 11, we find a $z = 3.1245$ galaxy, which we have dubbed the "Arrow" because of its arrow-like morphology in HST/ACS F814W imaging (Fig. 2).

3. Which mechanisms power the Lyα emission?

Photoionization by the AGN or star formation. While the rest-frame UV emission line ratios indicate that the AGN is likely ionizing the gas within several 10s kpc along the direction of the radio jets (regions 3−6), it is not clear whether the AGN could plausibly provide sufficient ionizing photons to explain the surface brightness of the most extended gas. We can estimate the intensity of the radiation field that is necessary to power the Lyα emission observed at distances larger than ~100 kpc. The surface brightness ranges from ~1−4 × 10^{-19} erg s^{-1} cm^{-2} $arcsec^{-2}$ at such large distances (3−10 × 10^{-17} erg s^{-1} cm^{-2} $arcsec^{-2}$ after correcting for surface brightness dimming). Assuming case B recombination, the recombination rate per unit area that is necessary to sustain this surface brightness is $R_{\rm rec} = 4\pi I_{\rm Ly\alpha}/\gamma_{\rm Ly\alpha}$, where $I_{\rm Ly\alpha}$ is the intensity of the Lyα emission

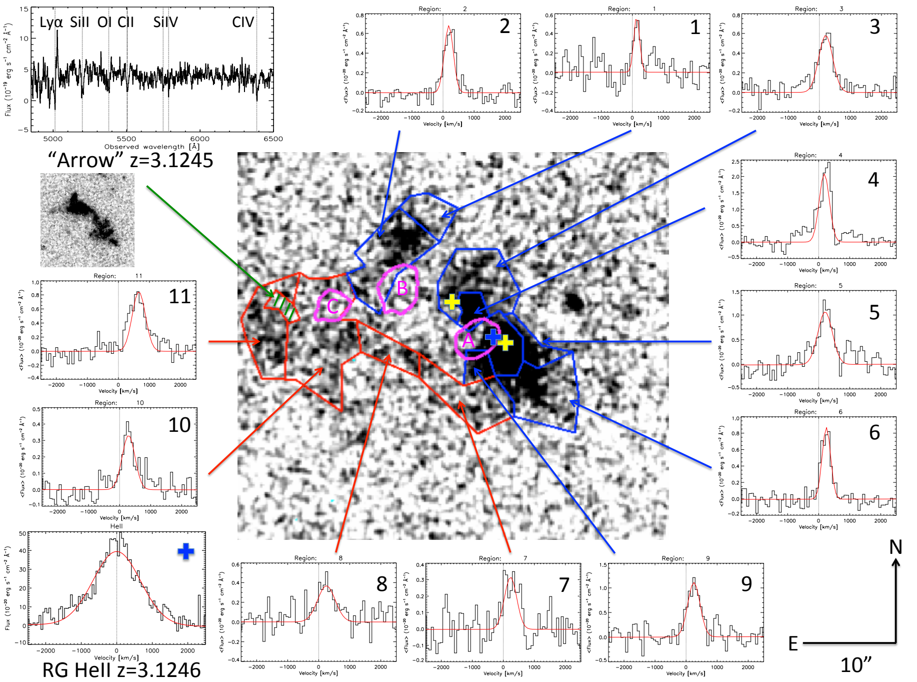

Fig. 2. Grayscale image of the Lyα emission in MRC 0316-257 (scale and orientation at the bottom right). The red and blue lines demarcate 11 regions with their mean Lyα spectra shown in the surrounding plots. The regions bounded by blue lines are probably directly excited by the AGN, while the regions bounded by red lines indicate regions that are perhaps associated with a stream. In each of the spectral plots, we approximate the Lyα profile with the best-fit Gaussian (red). The velocity is relative to systemic (in km s^{-1}; indicated by the black vertical line) measured from the HeII profile (*bottom left*). The purple contours show the region of [OII] emission for three foreground galaxies, labeled A, B, and C, whose redshifts are 0.874, 0.851, and 0.667, respectively. We indicate the positions of the radio lobes (yellow crosses) and AGN (blue cross). The *top two left panels* show the spectrum and HST F814W image of the "Arrow" (green hatched region in the grayscale image).

in photons cm^{-2} s^{-1} sr^{-1} and $\gamma_{\mathrm{Ly}\alpha}$ is the number of Lyα photons produced per recombination (0.61). Assuming that every ionizing photon has an energy of 13.6 eV[1] and unity or greater covering fraction, we find that the energy flux necessary to sustain the range of surface brightness we observe is $\approx 0.7{-}2\times10^{-3}$ erg cm^{-2} s^{-1} sr^{-1}.

We used Hβ emission line luminosity as an indicator of the photoionization rate from the AGN and massive stars. The luminosity of Hβ (Nesvadba et al. 2008) implies an ionizing luminosity, $L_{\mathrm{ion}} = 4.8\times10^{45}$ erg s^{-1}. The ionizing intensity of the AGN at a radius of 100 kpc is $\approx10^{-3}$ erg s^{-1} cm^{-2} sr^{-1}. The AGN provides sufficient photons to explain the extended Lyα nebula within ~100 kpc, but generally falls short for gas at larger distances. This estimate only applies along lines of sight that are free of intervening absorption and scattering, which may be true within the ionization cone, which is assumed to lie along the radio axes with an opening angle ~45°(blue regions in Fig. 2; Drouart et al. 2012). It is therefore plausible for the gas along the radio jet, even the most extended gas along this direction (regions 1 and 2), to have its surface brightness regulated by the AGN. Away from the ionization cone (red regions 6–11 in Fig. 2), it is unlikely that the AGN provides sufficient photons; young stars embedded in these regions would be an alternative. However, the remarkable uniformity of regions 6–10 suggests that there is no significant local ionization by stars as observed in MRC 0943-242 (Gullberg et al. 2016), for example, and it also argues against a central source such as an AGN ionizing the gas.

Ionization by the meta-galactic flux. At $z \sim 3$, the intensity of ionizing photons due to the meta-galactic flux is $\approx 2\times10^{5}$ photons cm^{-2} s^{-1} (Haardt & Madau 1996). When we assume ionization equilibrium and that the clouds are optically thick, this implies that the meta-galactic ionization rate is about two orders of magnitude lower than the rate necessary to maintain the ionization of the extended gas. This means that while the meta-galactic flux contributes to the ionization of the diffuse gas, it does not maintain it.

Resonance scattering. If the extended gas has a sufficiently high column of neutral HI to be optically thick at the wavelength of Lyα, then resonance scattering of the Lyα and UV continuum from the AGN can contribute to its surface brightness. The line profiles of the extended Lyα emission do not mirror those of the nuclear gas – they are narrower and have significant velocity offsets relative to the nuclear emission (Table 1). The approximately constant surface brightness of the extended emission argues against a central source exciting the emission. In addition, spectropolarimetry of MRC 0316-257 (Reuland et al. 2003) finds unpolarized (<4%) Lyα emission, arguing against any significant contribution of scattered light to the circumnuclear emission.

Shock heating in the outer halo. Another possibility for exciting the Lyα emission in the halo of MRC 0316-257 is an accretion shock from inflowing gas at the halo boundary and/or shocks from cloud-cloud collisions in a multiphase stream (Cornuault et al. 2016). The morphology of the most extended emission to the west-southwest (region 11) is shell-like and certainly suggestive of compression (a "splash"). We observe a velocity shear between region 11 and that of the inner halo accross regions 6–10 of ~400–500 km s^{-1}. In addition, over regions 6–11, the gas appears to be highly disturbed with FWHM ranging from 300 to 700 km s^{-1}. These violent motions and shears make shock heating a plausible mechanism for exciting the gas.

To test this possibility, we compared our measured surface brightness with those predicted for high-velocity shocks. The models of Allen et al. (2008) imply that even in relatively low-density low-metallicity gas (>few$\times10^{-3}$ cm^{-3}), the surface brightness produced by shocks is sufficient to explain our observations for the relative velocities we observe in the data, 300–700 km s^{-1}. Simulations indicate filament densities on the order of 10^{-3} to 10^{-1} cm^{-3} (Rosdahl & Blaizot 2012), in agreement with what is required. The surface brightness is related to the mass flow rate. These densities and velocities imply a mass flow rate, $\rho_{\mathrm{pre-shock}}\, v_{\mathrm{shock}}\, A_{\mathrm{shock}} \approx 250\, M_{\odot}\,\mathrm{yr}^{-1}$, for pre-shock density, $\rho_{\mathrm{pre-shock}} = 0.01$ cm^{-2}, shock velocity,

[1] The photoionization cross-section of hydrogen peaks at 13.6 eV, and this estimate is the maximum number of photons expected. It is therefore an upper limit to the number of photons.

$v_{\rm shock} = 500\,{\rm km\,s^{-1}}$, and area, $A_{\rm shock}$, and for simplicity, of a circle with a radius of 25 kpc.

While we have used the observed high relative velocities and large line widths as a justification to explore the possibility of shock heating, caution is warranted. The relative velocities and large line widths may both be partially due to radiative transfer effects (Cantalupo et al. 2005). The size of the effect depends on whether the medium is multiphasic and on the cause of the ionization. However, none of the Lyα lines in the most extended regions (1, 2, and 6–11) appear split, as might be expected if radiative transfer effects are important.

4. Lyα structures as accretion streams

Comparing the relative velocities of galaxies surrounding MRC 0316-257 with those from cosmological simulations, Kuiper et al. (2012) suggested that it is a result of the ongoing merger of two massive protoclusters of $\sim 10^{14}\,M_\odot$. The combinded findings of the surface brightness of the gas in the outer halo, which is is consistent with being shocked heated, its arc- or shell-like and filamentary morphology, large line widths, redshifted velocities, and relatively smooth change in velocity as a function of distance from the AGN suggest that this may be gas accreting from the cosmic web (Rosdahl & Blaizot 2012; Goerdt et al. 2015). If we make this assumption, then what do our results tell us about gas accretion into massive halos, and do they agree with results from cosmological simulations?

For this comparison, we focus exclusively on the filamentary structure to the west-southwest of the AGN (regions 6–11). We limit ourselves to these regions because none of the low surface brightness emission shows obvious evidence for being ionized by the AGN, they do not lie along the direction of the radio jets (which trace the direction of the ionization cone, and the ionization cones have opening angles $\sim 45°$, suggesting these regions lie outside; Drouart et al. 2012), and they extend rather continuously in emission from the outer halo into the circumnuclear region. As we noted in the introduction, these regions have surface brightnesses consistent with estimates from simulations (Rosdahl & Blaizot 2012). The Arrow lies in this structure, which is seen in simulated filaments (Gheller et al. 2016, Fig. 2). These observations form the basis for our assumption that these regions are part of an accretion stream.

The surface brightness of the distant arc can be explained by shock heating. When we assume that such a shock occurs at the virial radius, simple scaling relations imply radii of ~ 150 and 330 kpc for 10^{13} and $10^{14}\,M_\odot$ halos, respectively. Similarly, the virial velocities for halos with these masses are 500 and $1100\,{\rm km\,s^{-1}}$. We do not necessarily expect the velocities of the streams to be equal to the virial velocity, but they can be as low as half velocity (Goerdt & Ceverino 2015). The distance of the outermost shell from the nucleus and the velocities we observe are both consistent with virial expectations. We observe projected distances and velocities (and the projection of the velocity could change with position), not true positions and velocities, therefore, by necessity, this is only an order-of-magnitude comparison. Simulations do show broad lines in Lyα, on the same order ($100{\rm s\,km\,s^{-1}}$) as we observe (Goerdt et al. 2010).

Gas accretion through a stream, while able to make up most of the total accretion rate, can also vary substantially within a filament. Goerdt et al. (2015) found accretion rates of ~ 50–$5000\,M_\odot\,{\rm yr^{-1}\,sr^{-1}}$ through filaments for a halo mass of $\approx 10^{12}\,M_\odot$. Scaling these rates per sr upwards by the virial mass as is appropriate for total mass accretion rates ($\dot{M} \propto M_{\rm vir}^{1.25}$, Goerdt et al. 2015), we estimate rates 15 to 300× higher for 10 to 100× higher halo masses. A rough estimate suggests that the shock subtends $\sim 1\%$ of the spherical surface area at 250 kpc, and when we use the mass flow rate (Sect. 3), this implies an accretion rate per unit solid angle $\sim 2\times 10^4\,M_\odot\,{\rm yr^{-1}\,sr^{-1}}$ – a value consistent with simulations.

Many properties of the Lyα emission we observed in the circumgalactic medium of MRC 0316-257 are broadly consistent with the results of simulations of gas accretion streams. However, we view aspects of this agreement as fortuitous. Simulations generally lack the spatial and temporal resolution necessary to capture thermal and dynamical instabilities, resolve high Mach shock fronts, fragmentation of the post-shock gas, and turbulence, which naturally occur in astrophysical gas flows (Kritsuk & Norman 2002; Cornuault et al. 2016). It is not clear if simulations show conspicuously large shock fronts and strong post-shock cooling at approximately the halo boundary, as we have suggested. Such fronts, if real, are important for establishing many properties of the gas on its inward journey deeper into the potential well (fragmenting the gas and inducing turbulence). Until simulations reach the necessary resolutions and input physics to resolve shock fronts and fragmentation, it is fair to say that our theoretical understanding of these flows is limited. Observational constraints, such as those provided here, are crucial for obtaining a deeper understanding of how galaxies obtain their gas through gas accretion flows.

Acknowledgements. M.D.L. thanks the ESO visitor program for support.

References

Allen, M., Groves, B., Dopita, M., Sutherland, R., & Kewley, L. 2008, ApJS, 178, 20
Bacon, R., Accardo, M., Adjali, L., et al. 2010, in Ground-based and Airborne Instrumentation for Astronomy III, Proc. SPIE, 7735, 773508
Birnboim, Y., & Dekel, A. 2003, MNRAS, 345, 349
Cantalupo, S. 2017, in Gas Accretion onto Galaxies, Astrophys. Space Sci. Lib., 430, 195
Cantalupo, S., Porciani, C., Lilly, S. J., & Miniati, F. 2005, ApJ, 628, 61
Chambers, K. C., Miley, G. K., & van Breugel, W. J. M. 1990, ApJ, 363, 21
Christensen, L., Jahnke, K., Wisotzki, L., & Sánchez, S. F. 2006, A&A, 459, 717
Cornuault, N., Lehnert, M. D., Boulanger, F., & Guillard, P. 2016, A&A, submitted [arXiv:1609.04405]
De Breuck, C., Seymour, N., Stern, D., et al. 2010, ApJ, 725, 36
Drouart, G., De Breuck, C., Vernet, J., et al. 2012, A&A, 548, A45
Gheller, C., Vazza, F., Brüggen, M., et al. 2016, MNRAS, 462, 448
Goerdt, T., & Ceverino, D. 2015, MNRAS, 450, 3359
Goerdt, T., Dekel, A., Sternberg, A., et al. 2010, MNRAS, 407, 613
Goerdt, T., Ceverino, D., Dekel, A., & Teyssier, R. 2015, MNRAS, 454, 637
Gullberg, B., De Breuck, C., Lehnert, M. D., et al. 2016, A&A, 586, A124
Haardt, F., & Madau, P. 1996, ApJ, 461, 20
Heckman, T., Lehnert, M., Miley, G., & van Breugel, W. 1991a, ApJ, 381, 373
Heckman, T., Miley, G., Lehnert, M., & van Breugel, W. 1991b, ApJ, 370, 78
Jeng, M. 2006, Am. J. Phys., 74, 578
Kritsuk, A. G., & Norman, M. L. 2002, ApJ, 569, L127
Kuiper, E., Venemans, B. P., Hatch, N. A., Miley, G. K., & Röttgering, H. J. A. 2012, MNRAS, 425, 801
Maller, A. H., & Bullock, J. S. 2004, MNRAS, 355, 694
Martin, D. C., Chang, D., Matuszewski, M., et al. 2014, ApJ, 786, 107
Nesvadba, N., Lehnert, M., De Breuck, C., Gilbert, A., & van Breugel, W. 2008, A&A, 491, 407
Overzier, R. A., Nesvadba, N., Dijkstra, M., et al. 2013, ApJ, 771, 89
Reuland, M., van Breugel, W., Röttgering, H., et al. 2003, ApJ, 592, 755
Rosdahl, J., & Blaizot, J. 2012, MNRAS, 423, 344
Steidel, C. C., Adelberger, K. L., Shapley, A. E., et al. 2000, ApJ, 532, 170
Swinbank, A. M., Vernet, J. D. R., Smail, I., et al. 2015, MNRAS, 449, 1298
Villar-Martín, M., Vernet, J., di Serego Alighieri, S., et al. 2003, MNRAS, 346, 273
Weilbacher, P. M., Streicher, O., Urrutia, T., et al. 2012, in Software and Cyberinfrastructure for Astronomy II, Proc. SPIE, 8451, 84510B

B.2 Neutral versus ionized gas kinematics at z≈2.6: the AGN-host starburst galaxy PKS 0529-549

B.2.1 The paper

I reduced the ALMA data and proofread the paper.

Monthly Notices of the ROYAL ASTRONOMICAL SOCIETY

MNRAS **479,** 5440–5447 (2018) doi:10.1093/mnras/sty1795
Advance Access publication 2018 July 6

Neutral versus ionized gas kinematics at $z \simeq 2.6$: the AGN-host starburst galaxy PKS 0529-549

Federico Lelli,[1]†,⋆ Carlos De Breuck,[1] Theresa Falkendal,[1,2] Filippo Fraternali,[3] Allison W. S. Man,[1] Nicole P. H. Nesvadba[4] and Matthew D. Lehnert[2]

[1]*European Southern Observatory, Karl-Schwarzschild-Strasse 2, D-85748 Garching bei München, Germany*
[2]*Sorbonne Université, CNRS UMR 7095, Institut d'Astrophysique de Paris, 98 bis bd Arago, F-75014 Paris, France*
[3]*Kapteyn Astronomical Institute, University of Groningen, Postbus 800, NL-9700 AV, Groningen, the Netherlands*
[4]*Institut d'Astrophysique Spatiale, UMR 8617, Université Paris-Sud, Bât. 121, F-91405, Orsay, France*

Accepted 2018 June 28. in original form 2018 June 4

ABSTRACT

We present a multiwavelength study of the AGN-host starburst galaxy PKS 0529-549 at $z \simeq 2.6$. We use (1) new ALMA observations of the dust continuum and of the [CI] 370 μm line, tracing molecular gas, (2) SINFONI spectroscopy of the [O III] 5007 Å line, tracing ionized gas, and (3) ATCA radio continuum images, tracing synchrotron emission. Both [CI] and [O III] show regular velocity gradients, but their systemic velocities and position angles differ by $\sim$300 km s^{-1} and $\sim 30^{\circ}$, respectively. The [C I] is consistent with a rotating disc, aligned with the dust and stellar continuum, while the [O III] likely traces an outflow, aligned with two AGN-driven radio lobes. We model the [C I] cube using 3D disc models, which give best-fitting rotation velocities $V_{\rm rot} \simeq 310$ km s^{-1}and velocity dispersions $\sigma_V \lesssim 30$ km s^{-1}. Hence, the [C I] disc has $V_{\rm rot}/\sigma_V \gtrsim$10 and is not particularly turbulent, similar to local galaxy discs. The dynamical mass ($\sim 10^{11}$ M$_{\odot}$) is comparable to the baryonic mass within the errors. This suggests that baryons dominate the inner galaxy dynamics, similar to massive galaxies at $z \simeq 0$. Remarkably, PKS 0529-549 lies on the local baryonic Tully–Fisher relation, indicating that at least some massive galaxies are already in place and kinematically relaxed at $z \simeq 2.6$. This work highlights the potential of the [C I] line to trace galaxy dynamics at high z, as well as the importance of multiwavelength data to interpret gas kinematics.

Key words: galaxies: active – galaxies: evolution – galaxies: individual: PKS 0529-549 – galaxies: kinematics and dynamics – galaxies: starburst – *(cosmology:)* dark matter.

1 INTRODUCTION

Over the past decade much progress has been made in the study of gas dynamics at high redshifts. Integral field spectroscopy (IFS) in the near-infrared (NIR) has been widely used to trace the ionized gas kinematics in star-forming galaxies at $z \simeq 1$–3 (e.g. Förster Schreiber et al. 2009; Gnerucci et al. 2011; Wisnioski et al. 2015; Stott et al. 2016; Nesvadba et al. 2017). Radio and submillimetre observations with the Jansky Very Large Array and the Plateau de Bure Interferometer have proved to be powerful in tracing CO kinematics up to $z \simeq 4$ (e.g. Hodge et al. 2012; Ivison et al. 2012; Tacconi et al. 2013). Moreover, the Atacama Large Millimeter Array (ALMA) has opened a new window to study galaxy dynamics at even higher redshifts ($z \simeq 4$–7) using the [C II] emission line (e.g. De Breuck et al. 2014; Jones et al. 2017; Shao et al. 2017; Smit et al. 2018).

These different studies probe different gas phases. NIR spectroscopy probes emission lines like Hα and [O III], tracing warm ionized gas ($\sim 10^4$ K). Radio and submillimetre observations, instead, probe CO, [C I], and [C II] transitions, tracing cold neutral gas (<100 K) like molecular hydrogen (H_2).

In nearby galaxies, H_2 and H I generally display regular disc rotation, whereas Hα and [O III] kinematics may be more complex. For example, in galaxies hosting starbursts and/or active galactic nuclei (AGNs), Hα and [OIII] are often associated with galactic winds (e.g. Harrison et al. 2014; Arribas et al. 2014). In high-z galaxies, it is unclear how these different gas phases relate to each other and whether they share the same kinematics, since only a few galaxies have been studied using multiple gas tracers (Chen et al. 2017; Übler et al. 2018). In this context, the redshift window $z \simeq 2$–3 is very interesting because (1) both ionized and neutral gas can be observed and spatially resolved with existing facilities, and (2) it

⋆ ESO fellow.
† E-mail: flelli@eso.org

corresponds to the peak of the cosmic star formation history (SFH; Madau & Dickinson 2014), a key epoch to understand the formation of massive galaxies.

Here, we compare neutral and ionized gas kinematics in the starburst galaxy PKS 0529-549 at $z \simeq 2.6$, combining new [C I] (2–1) data from ALMA with IFS data from SINFONI (Nesvadba et al. 2017). PKS 0529-549 is a well-studied radio galaxy with an exquisite set of ancillary data: optical spectroscopy, ground-based NIR imaging, and radio polarimetry (Broderick et al. 2007), *Spitzer*/IRAC imaging (De Breuck et al. 2010), and 1.1 mm data from AzTEC (Humphrey et al. 2011). PKS 0529-549 hosts a Type-II AGN and shows two radio lobes. The eastern lobe holds the record for the highest Faraday rotation measure to date, implying a strong magnetic field and/or a dense circumgalactic medium (Broderick et al. 2007). With only 5 min of ALMA on-source integration time, we spatially resolve the [C I] emission of PKS 0529-549. We show that [C I] and [O III] display different kinematics and discuss possible interpretations with the aid of 3D kinematic models.

Throughout this paper, we assume a flat Λ cold dark matter (ΛCDM) cosmology with $H_0 = 67.8\,\mathrm{km\,s^{-1}\,Mpc^{-1}}$, $\Omega_\mathrm{m} = 0.308$, and $\Omega_\Lambda = 0.692$ (Planck Collaboration XIII 2016). In this cosmology, 1 arcsec = 8.2 kpc at $z = 2.6$.

2 DATA ANALYSIS

2.1 ALMA data

PKS 0529-549 was observed on 2014 September 2 during ALMA Cycle 2 with 34 working antennas, giving maximum and minimum baselines of 1090 and 33 m, respectively. The on-source integration time was 5 min. The flux and bandpass calibrator was J0519-4546, while the phase calibrator was J0550-5732. We used four 1.875 GHz-wide spectral windows centred at 224.99, 226.87, 239.99, and 241.87 GHz. The second spectral window contains the redshifted [C I] (2–1) line, which corresponds to the $^3P_2 \rightarrow {}^3P_1$ transition and has a rest-frame frequency of 809.3435 GHz.

The data reduction was performed using the Common Astronomy Software Applications (CASA) package (McMullin et al. 2007). The *uv* data were flagged and calibrated using the standard CASA pipeline. The imaging was performed using the task *clean* with *Robust* = 2, which corresponds to natural weighting of the visibilities. This provides the highest sensitivity but the lowest spatial resolution. The resulting synthesized beam is 0.43 arcsec × 0.28 arcsec with a position angle (PA) of 64.5°. A continuum image was obtained combining all four spectral windows, reaching a sensitivity of 0.055 mJy beam^{-1}. The [C I] cube was imaged using a channel width of 50 km s^{-1}, giving a sensitivity of 0.55 mJy beam^{-1} per channel. The continuum was subtracted from the [C I] cube in the image plane, after fitting a first-order polynomial to line-free channels. We also attempted continuum subtraction in the *uv* plane (before the Fourier transform), but sanity checks revealed that the continuum was oversubtracted in this way. In any case, the continuum subtraction does not strongly affect our kinematic analysis. The [C I] flux is 2.1 ± 0.4 Jy km s^{-1}, as estimated from fitting the global [C I] profile (presented in Man et al. in preparation).

After imaging, the [C I] cube was analysed using the Groningen Imaging Processing System (GIPSY, Vogelaar & Terlouw 2001). To build the total [C I] map (moment zero), we sum the signal within a Boolean mask, which follows the kinematic structure of the [C I] emission. Given the low signal-to-noise ratio (S/N), the mask is constructed interactively on a channel-by-channel basis by defining regions in which contiguous pixels have S/N $\gtrsim 2$. When using a mask, the noise in the total map is not uniform because a different number of channels is summed at each spatial pixel. It is however possible to construct S/N maps and define a pseudo-3σ contour by considering spatial pixels with S/N between 2.75 and 3.25 (see the appendix in Lelli, Verheijen & Fraternali 2014). We measure pseudo-3$\sigma \simeq 150$ mJy beam^{-1} km s^{-1}.

To build the velocity map (moment one), we estimate an intensity-weighted mean velocity for the pixels inside the Boolean mask. We stress that the velocity map is very uncertain due to beam smearing effects and the low S/N. This map merely provides a rough overview of the gas kinematics. We do not consider the dispersion map (moment two) because it is even more strongly affected by beam smearing: moment-two values are not indicative of the intrinsic gas velocity dispersion because the [C I] line is largely broadened by the low spatial and spectral resolutions. Our kinematic analysis uses the full 3D information and takes resolution effects into account: we build model cubes and compare them with the observed one using position–velocity (*PV*) diagrams and channel maps (Section 3.2).

2.2 SINFONI and ATCA data

Nesvadba et al. (2017) present IFS data of PKS 0529-549 using SINFONI at the ESO Very Large Telescope (VLT). Two different datacubes were obtained: one at low spatial resolution (1.2 arcsec × 1.2 arcsec), where the stellar continuum and several emission lines are detected, and one at high spatial resolution (0.7 arcsec × 0.6 arcsec), where only the strongest emission lines ([O III] λ4958, [O III] λ5007, and Hα) are recovered. The Hα line is blended with the [N II] doublet, creating a broad ($\gtrsim$100 Å) and asymmetric line. We refer to Nesvadba et al. (2017) for further details.

We use the GIPSY package to analyse the high-resolution cube. To increase the S/N of the emission lines, the cube was box-averaged over 3 × 3 pixels. We constructed emission-line maps by summing the signal within narrow wavelength ranges, which were determined by visual inspection excluding channels contaminated by sky lines. No continuum subtraction was attempted, but we used the low-resolution datacube to estimate that the net continuum contribution on the emission-line maps is negligible. We constructed velocity fields by fitting a Gaussian function at each spatial pixel. This is preferable to intensity-weighted mean velocities given the relatively high S/N. Each emission line was fitted independently considering a narrow wavelength range and rejecting fit results with unphysically small amplitudes ($\lesssim$5 counts) and/or dispersions ($\lesssim$5 Å). Given the overall data quality, it would be untrustworthy to fit multiple Gaussians to try de-blending the Hα and [N II] lines. Hereafter, we consider only the [O III] λ5007 velocity field because the Hα+[N II] and [O III] λ4958 ones have lower quality due to the lower S/N. These emission lines, however, display similar kinematics.

The absolute positional accuracy of the SINFONI data relative to the World Coordinate System is ∼1 arcsec (see Nesvadba et al. 2017 for details). Since the ALMA positional accuracy is much higher than 1 arcsec, we improve the SINFONI astrometry using the following approach. It is sensible to assume that the SINFONI stellar continuum and the ALMA dust continuum are physically related: the two maps indeed display a similar elongated morphology with a PA ≃ 75° (Fig. 2.2). Thus, we overlay the emission peak of the SINFONI stellar continuum with that of the ALMA dust continuum. The resulting spatial shift is smaller than 1 arcsec.

We also consider radio continuum images from the Australia Telescope Compact Array (ATCA), which were provided by

Broderick et al. (2007). These authors published natural-weighted images at various frequencies and resolutions. Here, we show the uniform-weighted image at 18.5 GHz because it has the highest spatial resolution (0.55 arcsec × 0.37 arcsec). This image is published here for the first time.

3 RESULTS

3.1 Multiwavelength overview

Fig. 2.2 provides a multiwavelength view of PKS 0529-549. The top panels present the ALMA data. The ALMA continuum (left-hand panel) is studied in detail in Falkendal et al. (in preparation) by modelling its spectral energy distribution (SED). It consists of two components: a central one due to dust emission and a secondary one to the east due to synchrotron emission. The secondary component, indeed, nicely overlaps with the eastern radio lobe from ATCA observations. The [C I] emission (middle panel) coincides with the dust emission and displays a similar elongated morphology with PA $\simeq 75^{\circ}$. Both dust and [C I] emissions are spatially resolved with $\sim$2 beams along the major axis, so their morphology is not strongly driven by the elongated beam shape, which has a similar PA of $\sim$64.5°. No [C I] emission is associated with the synchrotron lobes. The [C I] velocity field (right-hand panel) shows a velocity gradient along the major axis: this is consistent with a rotating disc as we show in Section 3.2.

The bottom panels of Fig. 2.2 present the SINFONI data. The stellar continuum (left-hand panel) is barely resolved but it seems to display roughly the same PA as the dust and [C I] emissions. The ionized gas (middle panel) appears more extended than any other galaxy component. The SINFONI point spread function (PSF) is significantly larger than the ALMA beam, but if we smooth the ALMA maps to the same spatial resolution (0.7 arcsec × 0.6 arcsec), they remain less extended than the ionized gas. The [O III] λ5007 velocity field (right-hand panel) displays a velocity gradient with PA$\sim$105°, so it is tilted by $\sim$30° with respect to the [C I] distribution and kinematics. The [O III] velocity gradient, instead, aligns well with the orientation of the two synchrotron lobes. Strikingly, the [O III] velocities are systematically higher than the [C I] velocities by $\sim$300 km s^{-1}.

The Hα displays similar kinematics as the [O III], but its velocity field (not shown) is very uncertain due to the low S/N and contamination from the [N II] lines. In Man et al. (in preparation), we present an X-Shooter spectrum of PKS 0529-549 revealing that the [O III] and Hα velocities are consistent with other emission lines from ionized gas like [OII] and CII], while the [C I] velocities are consistent with photospheric absorption lines from young stars.

Given the evidence above, we interpret the [C I] emission as a rotating gas disc, having a similar PA as both the dust component and the stellar continuum. The [O III] and the Hα emission, instead, could trace a gas outflow, being aligned with the synchrotron lobes. Nesvadba et al. (2017) provide additional arguments for the outflow interpretation. For example, the [O III] λ5007 profiles are very broad, ranging from $\sim$300 to $\sim$900 km s^{-1} (see their fig. A.5): this is likely due to the contribution of different velocity components along the line of sight as expected in a gas outflow. The velocity difference between [C I] and ionized gas may indicate that the outflow does not propagate exactly from the centre of the [C I] disc, but from its north-eastern, redshifted side. Alternatively, we may be seeing only the redshifted side of the flow (further away from the observer) because the ionized bi-cone may have asymmetric density distribution, as observed in some local starburst galaxies (e.g. NGC 253, Boomsma et al. 2005) and high-z ones (e.g. TN J1338-1942, Zirm et al. 2005). Interestingly, if only SINFONI data were available, it would be much more difficult to distinguish the [O III] velocity field of an outflow from that of a rotating disc. This highlights the importance of having multiwavelength observations to interpret ionized gas data. This point is further discussed in Section 4.1.

3.2 Disc modelling

To test the hypothesis of a rotating [C I] disc, we use two different codes:GALMOD in GIPSY (Sicking 1997) and ^{3D}BAROLO (Di Teodoro & Fraternali 2015). Both codes build 3D kinematic models of rotating discs, taking projection and resolution effects into account. The main difference between the two is that GALMOD needs to be used iteratively by trial and error, while ^{3D}BAROLO explores the full parameter space to find a best-fitting solution by χ^2 minimization. In practice, we use GALMOD to set the initial estimates of ^{3D}BAROLO and to fix several geometric parameters that are otherwise degenerated.

The disc is built using a set of circular rings. Each ring is characterized by four projection parameters (centre, PA, inclination i, and systemic velocity $V_{\rm sys}$) and four physical ones (surface density Σ, vertical scale height h, rotation velocity $V_{\rm rot}$, and velocity dispersion $\sigma_{\rm V}$). The disc is then projected onto the sky to generate model cubes that are smoothed to the same spatial and spectral resolutions of the observations. Since the [C I] distribution is resolved with only $\sim$2 beams, we assume that the disc parameters are constant with radius (R). This is equivalent to using a single, large ring. Effectively, the physical parameters are intensity-weighted average values over the semimajor axis of the [C I] disc.

We explored two basic models: a disc with uniform surface density (the ring extends from $R = 0$ to $R \simeq 0.45$ arcsec) and a disc with a central hole (the ring extends from $R \simeq 0.20$ arcsec to $R \simeq 0.45$ arcsec). Both models give comparable results because the ALMA beam (0.43 arcsec × 0.28 arcsec) smooth out any intrinsic structure in the gas density. This degeneracy only affects the determination of Σ, which cannot be robustly estimated and is not used in our analysis. For similar reasons, the model is insensitive to the vertical density distribution: we assume an exponential vertical profile with fixed $h = 0.04$ arcsec $\simeq 300$ pc.

We use GALMOD following Lelli et al. (2015): we inspect channel maps and *PV* diagrams to obtain initial estimates of the disc parameters, which are then refined until we find a good match between model and observations. The centre, PA, and $V_{\rm sys}$ are easy to estimate and kept fixed during subsequent iterations. The remaining parameters (i, $V_{\rm rot}$, and σ_V) are more challenging to determine due to degeneracies. The inclination is estimated by comparing model [C I] maps (after beam convolution) to the observed one. Fig. 2 (top panels) shows that the observed [C I] map is well reproduced by our model map: the residuals are smaller than $\sim 3\sigma$ and less extended than the beam. These residuals are probably due to deviations from a pure axisymmetric gas distribution in the central regions. Clearly, the [C I] disc is not face-on ($i > 30^{\circ}$), so the net correction on $V_{\rm rot}$ is relatively small going as 1/sin (i).

Finally, $V_{\rm rot}$ and σ_V are estimated by comparing *PV* diagrams extracted from both the model and observed cubes (Fig. 2 , bottom panels). The major axis *PV* diagram is well reproduced by our axisymmetric kinematic model: the residuals are smaller than $\sim 2\sigma$. The width of the [C I] line profiles is largely driven by resolution effects, but it can be used to constrain the intrinsic gas velocity dispersion. Near the [CI] centre, the observed *PV* diagram shows asymmetric [C I] profiles with a tail of emission towards the systemic

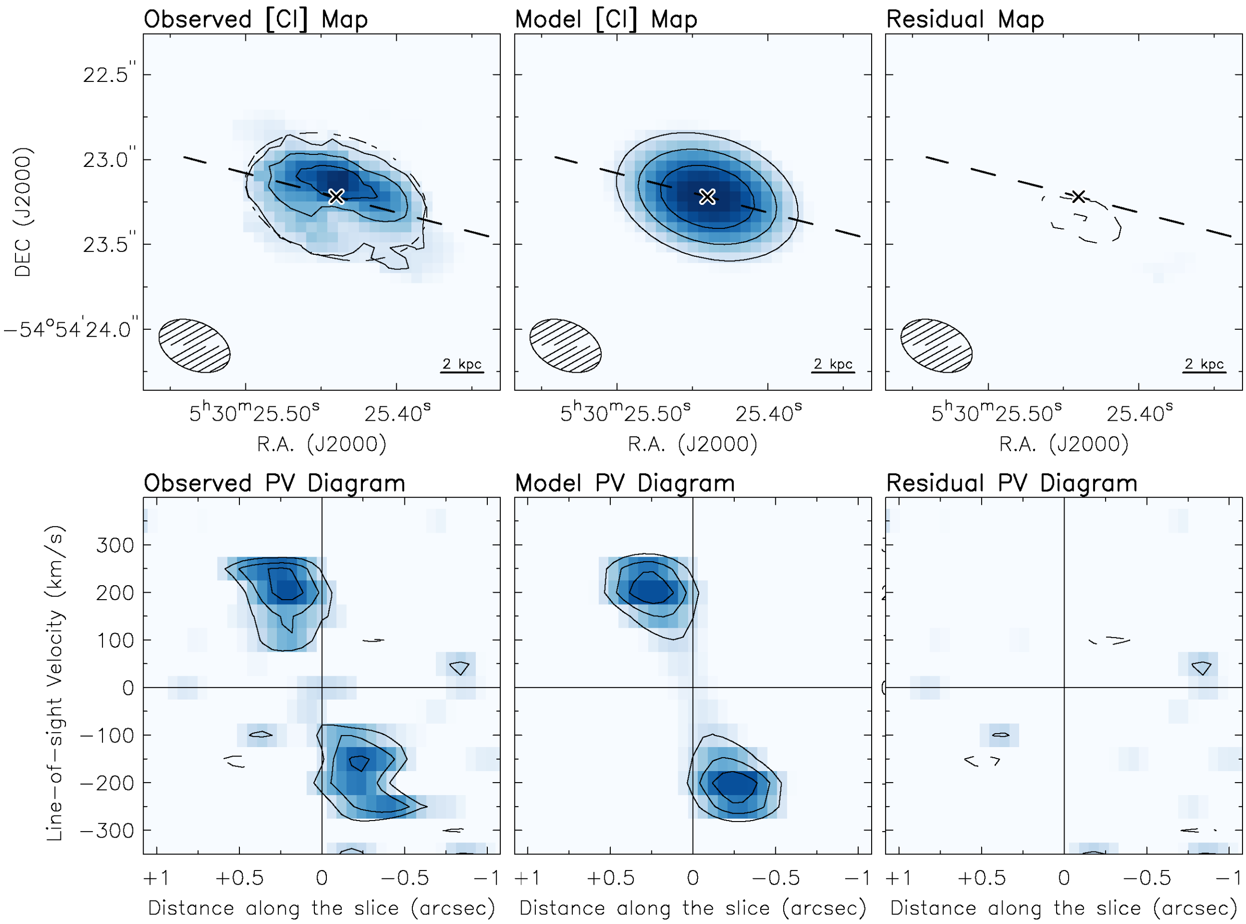

Figure 2. *Top panels*: observed [C I] map (*left*), model [C I] map (*middle*), and residual map (*right*). Contours are at 150, 300, and 450 mJy beam^{-1} km s^{-1}. In the left-hand panel, the dashed line shows the 3σ contour from the model map. In all panels, the cross, the dashed line, and the ellipse show the disc centre, the major axis, and the ALMA beam, respectively. *Bottom panels*: Major axis *PV* diagrams obtained from the observed (*left*), model (*middle*), and residual (*right*) cubes. Contours are at -2σ (dashed), 2σ (solid), 3σ, and 4σ where $\sigma = 0.55$ mJy beam^{-1}. The vertical and horizontal lines correspond to the dynamical centre and systemic velocity, respectively.

velocity. These asymmetric profiles are well reproduced by our disc model, indicating that they are probably due to unresolved rotation. This is the typical effect of beam smearing in poorly resolved galaxy discs (e.g. Lelli, Fraternali & Sancisi 2010). Channel maps are also individually inspected (Fig. 3): the [C I] emission progresses along the major axis of the dust component, which is natural if both dust and [C I] lie in a rotating disc. In particular, the estimated values of centre, PA, and i are consistent with the dust continuum, providing an independent constraint to the model.

Given the relatively low-resolution and S/N, ^{3D}BAROLO cannot be run blindly leaving all the parameters free. We use $V_{\rm rot}$ and σ_V as free parameters, but keep the others fixed to the values estimated with GALMOD. The fit is performed within the Boolean mask described in Section 2.1. The best-fitting values do not strongly depend on the mask definition, but they do depend on the initial estimates. The best-fitting values of $V_{\rm rot}$ show a weak dependence and cluster around 310 km s^{-1}. The best-fitting values of σ_V show a stronger dependence on the initial estimates, but they are always smaller than $\sim$30 km s^{-1}. Considering that the [C I] cube has low S/N and independent channels with a width of 50 km s^{-1}, the minimum detectable velocity dispersion is $\sim$50/2.35 $\simeq$ 21 km s^{-1}, so we consider $\sigma_V \lesssim 30$ km s^{-1}as an hard upper limit. These values of $V_{\rm rot}$ and $\sigma_{\rm V}$ are in agreement with the previous visual estimates from GALMOD. To estimate errors on each variable, we re-run ^{3D}BAROLO leaving such variable free and keeping all the others fixed to their best-fitting values. The final parameters are given in Table 1.

One may wonder whether the [C I] velocity gradient may be explained by a gas outflow or a galaxy merger. The outflow scenario implies that (1) the gas is ejected along the major axis of the dust/stellar component rather than the minor axis (see Fig. 2.2), and (2) the PA of the outflow is tilted with respect to the synchrotron lobes, which are generally tracing the AGN ionization cone (e.g. Drouart et al. 2012). Both facts seem unlikely.

The merger origin for the [C I] velocity gradient cannot be definitively ruled out, but we disfavour this scenario, given the high symmetry of the observed *PV* diagram. A kinematic merger model would have twice as many free parameters compared to a disc model and would need to be fine tuned: (1) two merging [C I] components should have roughly the same mass, size, and velocity dispersion, (2) they should be aligned along the major axis of the dust continuum and have the same projected distance from its centroid (see Fig. 3), and (3) they should be well separated in velocity by $\sim$500 km s^{-1} and lie very close on the sky ($\lesssim$0.5 arcsec), but they should not overlap at any spatial position after beam convolution, otherwise we should observe double-peaked [CI] profiles (contrary to what is

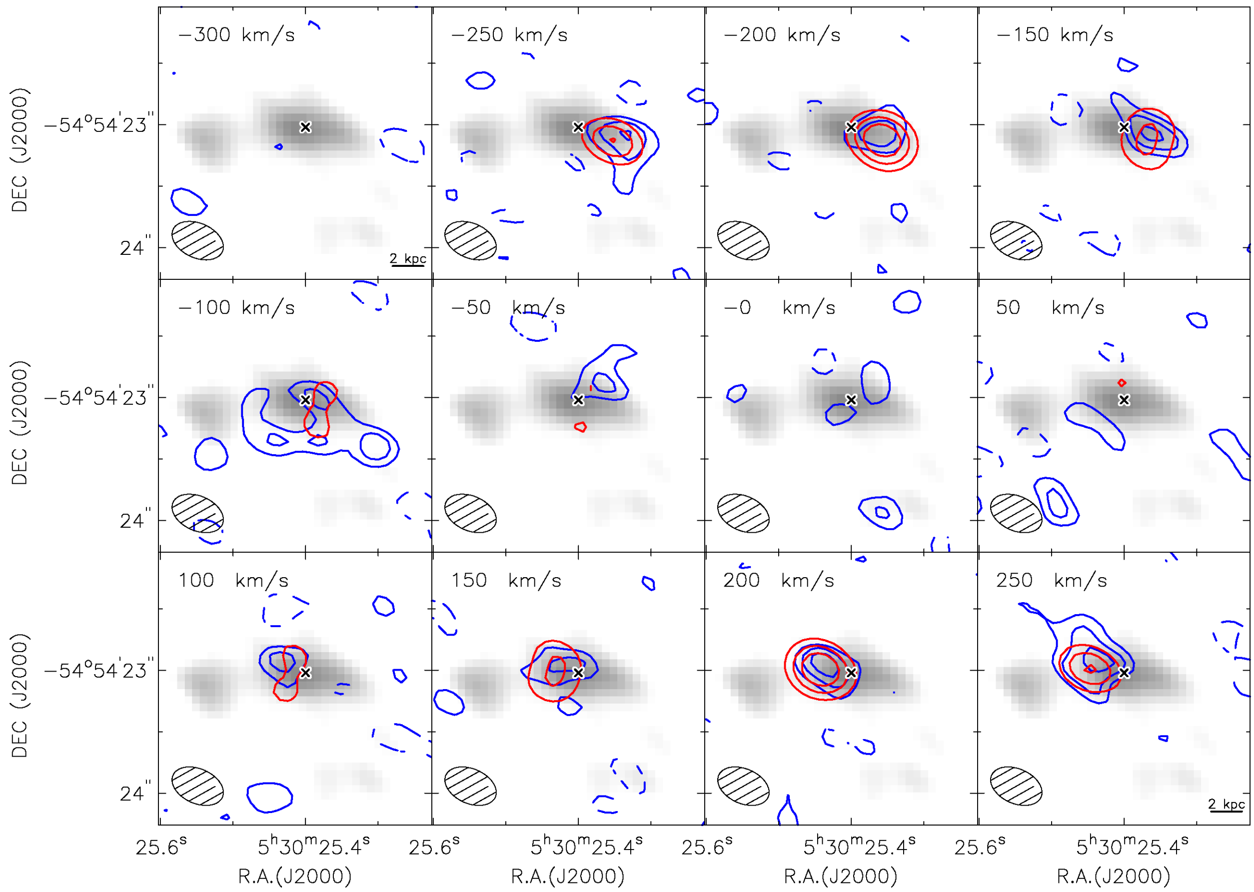

Figure 3. [CI] channel maps from the observed (blue) and model (red) datacubes overlaid on the ALMA continuum (grey scale). Contours are at -2σ (dashed), 2σ (solid), 3σ, and 4σ where $\sigma = 0.55$ mJy beam^{-1}. In the top-left corner, we provide the line-of-sight velocity with respect to $V_{\rm sys}$. The ALMA beam is shown in the bottom-left corner. The cross corresponds to the dynamical centre.

Table 1. Results of the 3D dynamical analysis.

Parameter	Value
x_0 (J2000)	$05^{\rm h}30^{\rm m}25.44^{\rm s} \pm 0.01^{\rm s}$
y_0 (J2000)	$-54°54'23''.2 \pm 0.1''$
z (from $V_{\rm sys}$)	2.570 ± 0.001
PA (°)	75 ± 12
i (°)	50 ± 4
$V_{\rm rot}$(km s^{-1})	310 ± 50
σ_V(km s^{-1})	$\lesssim$30
$M_\star$ (10^{11} M$_\odot$)	3.0yy $\pm$ 2.0[a]
$M_{\rm mol}$ (10^{11} M$_\odot$)	0.4 ± 0.2[b]
$M_{\rm WIM}$ (10^{11} M$_\odot$)	0.02 ± 0.02[c]
$M_{\rm bar}$ (10^{11} M$_\odot$)	3.4 ± 2.0
$M_{\rm 4\,kpc}$ (10^{11} M$_\odot$)	0.9 ± 0.3
$M_{\rm 8\,kpc}$ (10^{11} M$_\odot$)	1.8 ± 0.6

[a] De Breuck et al. (2010), [b]Man et al. (in preparation), [c]Nesvadba et al. (2017).

seen in Fig. 2). Naturally, PKS 0529-549 may still be a late-stage merger with an inner rotating disc, as observed in some starburst galaxies at $z \simeq 0$ (e.g. Kregel & Sancisi 2001; Weaver et al. 2018). Here, we simply point out that the observed [C I] velocity gradient is probably due to rotation, allowing the following dynamical analysis.

3.3 Mass budget

De Breuck et al. (2010) measured the rest-frame *H*-band luminosity ($L_{\rm H}$) and stellar mass ($M_\star$) of 70 radio galaxies. For PKS 0529-549, they give $L_{\rm H} \simeq 4 \times 10^{11}$ L$_\odot$ and $M_\star \simeq 3 \times 10^{11}$ M$_\odot$. The stellar mass is derived by fitting the *Spitzer* SED and assuming (i) a formation redshift of 10, (ii) an exponentially declining SFH, and (iii) a Kroupa (2001) initial mass function (IMF). These assumptions are sensible for radio galaxies in a statistical sense (Rocca-Volmerange et al. 2004). For individual galaxies, however, the SFH remains uncertain. PKS 0529-549 is indeed bursting at $z \simeq 2.6$ since the estimated star formation rate (SFR) is ~1000 M$_\odot$ yr^{-1} (Falkendal et al. in preparation). For reference, galaxies with $M_\star \gtrsim 10^{11}$ M$_\odot$ at $z \simeq 2$–3 have SFRs of the order of ~100 M$_\odot$ yr^{-1} (e.g. Bisigello et al. 2018): PKS 0529-549 lies well above the mean SFR–$M_\star$ relation (the so-called star-forming main sequence).

The effect of starbursts in high-z radio galaxies has been studied by Drouart et al. (2016) in 11 objects by modelling their full SED, from ultraviolet to NIR wavelengths. Unfortunately, their sample does not include PKS 0529-549, but it does include 4C 41.17, which is analogous to PKS 0529-549 in several aspects. In particular, the rest-frame optical spectrum of 4C 41.17 is strikingly similar to the one of PKS 0529-549 (Man et al. in preparation). Drouart et al. (2016) finds that 4C 41.17 is experiencing a recent starburst (~30 Myr) that makes up ~92 per cent of the bolometric luminosity and forms ~44 per cent of the total stellar mass. Using this analogy and considering the large uncertainties, we adopt a conservative errorbar on the stellar mass of PKS 0529-549: $M_\star = (3.0 \pm 2.0) \times 10^{11}$ M$_\odot$. This errorbar does not include systematic uncertainty due to the IMF: a Salpeter IMF would increase the stellar mass by ∼60 per cent.

The gas mass is given by three main mass components: atomic hydrogen ($M_{\rm H\,I}$), molecules ($M_{\rm mol}$), and the warm ionized medium ($M_{\rm WIM}$). Unfortunately, H I emission is currently not accessible at high z. However, it is likely that the central parts of massive starburst galaxies are dominated by H_2 rather than H I, as observed in nearby interacting galaxies (Kaneko et al. 2017). Considering the observed [C I](2–1) flux of 2.1 Jy km s^{-1} and the theoretical relations from Papadopoulos, Thi & Viti (2004), we estimate $M_{\rm mol} \simeq 4 \times 10^{10}$ M$_\odot$. This [C I]−to−H_2 conversion assumes the [C/H_2] abundance of the local starburst galaxy M82 and is uncertain by about a factor of 2 (see also Man et al. in preparation). Finally, the mass of the WIM is clearly negligible: Nesvadba et al. (2017) estimate 2.4×10^9 M$_\odot$ for a fiducial electron density of 500 cm^{-3}. Hence, the total baryonic mass of PKS 0529-549 is $M_{\rm bar} = (3.4 \pm 2.0) \times 10^{11}$ M$_\odot$.

The dynamical mass within a radius R is given by

$$M_{\rm R} = \varepsilon \frac{R\, V_{\rm rot}^2}{G}, \qquad (1)$$

where G is the gravitational constant and ϵ is a parameter of the order of unity that depends on the 3D geometry of the *total* mass distribution. For simplicity, we adopt $\epsilon = 1$ (spherical geometry). For local disc galaxies, McGaugh (2005) estimates $\epsilon \simeq 0.8$, so one would infer a slightly smaller dynamical mass. For PKS 0529-549, we measure $V_{\rm rot} = 310 \pm 50$ km s^{-1} within the deconvolved radius of the [C I] disc ($R \simeq 0.45$ arcsec $\simeq 4$ kpc), thus $M_{4\,{\rm kpc}} = (0.9 \pm 0.3) \times 10^{11}$ M$_\odot$.

The value of $M_{4\,{\rm kpc}}$ is consistent with $M_{\rm bar}$ within the errors albeit it appears somewhat smaller. It is likely, however, that the stellar component is more extended than the [C I] disc. Unfortunately, the available NIR images have poor spatial resolution, but they tentatively indicate that the stellar component may be twice as extended as the [C I] disc (cf. with fig. 5 of Broderick et al. 2007). If we extrapolate the measured rotation velocity out to 8 kpc, we get $M_{8\,{\rm kpc}} = (1.8 \pm 0.6) \times 10^{11}$ M$_\odot$ that is closer to $M_{\rm bar}$. Alternatively, one may question the estimated inclination. If the [C I] disc were oriented more face-on ($i \simeq 30°$), the rotation velocity would increase to ∼475 km s^{-1} and give $M_{4\,{\rm kpc}} \simeq 2 \times 10^{11}$ M$_\odot$. These values of i and $V_{\rm rot}$, however, are difficult to reconcile with the observed [C I] map (Fig. 2, top panels).

In conclusion, the baryonic and dynamical masses of PKS 0529-549 are consistent within the uncertainties. This suggests that PKS 0529-549 has little (if any) dark matter in its central parts. This is comparable to other massive galaxies at similar redshifts (Toft et al. 2012; Wuyts et al. 2016) as well as massive late-type galaxies (Noordermeer et al. 2007; Lelli, McGaugh & Schombert 2016a) and early-type galaxies (Cappellari 2016) at $z \simeq 0$. The latter ones are commonly thought to be the descendants of high-z radio galaxies like PKS 0529-549 (e.g. Pentericci et al. 2001).

4 DISCUSSION

4.1 Comparison with other high-z galaxies

The first IFS surveys at $z \simeq 1$–3 suggested that one-third of star-forming galaxies were rotation-dominated systems, whereas the remaining two-thirds were either merging systems or dispersion-dominated objects (Förster Schreiber et al. 2009; Gnerucci et al. 2011). Subsequently, it was acknowledged that beam-smearing effects can play a major role in assessing the intrinsic galaxy dynamics: the most recent IFS surveys now indicate that at least ∼80 per cent of massive star-forming galaxies ($10^9 < M_\star/{\rm M}_\odot < 10^{11}$) host rotating gas discs at $z \simeq 1$–3 (Wisnioski et al. 2015; Stott et al. 2016).

While rotating gas discs are now thought to be ubiquitous at $z \simeq 1$–3, their detailed properties are still debated. The general picture is that high-z discs are more turbulent than their local analogues (Förster Schreiber et al. 2009; Lehnert et al. 2009; Gnerucci et al. 2011): σ_V is thought to increase systematically with z, while $V_{\rm rot}/\sigma_V$ decreases (Wisnioski et al. 2015; Stott et al. 2016). Di Teodoro, Fraternali & Miller (2016), however, point out that high-z discs are poorly resolved and beam-smearing effects can lead to systematic overestimates of σ_V and underestimates of $V_{\rm rot}$, unless they are properly modelled in 3D. For PKS 0529-549, we find $V_{\rm rot}/\sigma_V \gtrsim 10$, which is comparable to CO and H I discs in spiral galaxies at $z = 0$ (Leroy et al. 2008; Mogotsi et al. 2016). Thus, the [C I] disc of PKS 0529-549 is not particularly turbulent. This is remarkable considering that PKS 0529-549 is forming stars at ∼1000 M$_\odot$ yr^{-1} and hosts a powerful radio-loud AGN, so a large amount of energy should be injected into the inter-stellar medium (e.g. Lehnert et al. 2009).

The gas phase may be important in assessing the degree of turbulence of a galaxy disc. In general, ionized gas has higher σ_V than neutral gas due to thermal broadening, but is also more strongly affected by stellar and AGN feedback. Thus, it is possible that some high values of σ_V in 'turbulent' discs are actually due to undetected non-circular motions and/or outflows in the ionized gas component. For example, the [O III] velocity field in Fig. 2.2 could be interpreted as a turbulent disc if radio images and/or [C I] kinematics were not available. It is possible, indeed, to fit the [O III] cube with a rotating disc model, following the same procedures described in Section 3.2 for the [C I] cube. This gives $V_{\rm rot} \simeq 100$ km s^{-1}and $\sigma_V \simeq 300$ km s^{-1}, leading to $V_{\rm rot}/\sigma_V \simeq 0.3$. Large IFS surveys find that 'main-sequence' galaxies at $z \simeq 2$–3 have $V_{\rm rot}/\sigma_V \simeq 1$–4 when using H$\alpha$ or [O III] lines (Wisnioski et al. 2015). The lower value of PKS 0529-549 corroborates the outflow interpretation for the [O III] line. However, it also raises the question of how much gas outflows may affect the mean value of $V_{\rm rot}/\sigma_V$ in large IFS surveys. Clearly, a multiwavelength approach is needed to have a complete picture of the gas dynamics of high-z galaxies.

4.2 The baryonic Tully–Fisher relation

A key constraint for galaxy formation models is represented by the emergence and evolution of the Tully–Fisher (TF) relation (Tully & Fisher 1977). Over the past years, both the stellar-mass TF relation (using $M_\star$) and the baryonic TF relation (using $M_{\rm bar} = M_\star + M_{\rm gas}$) have been investigated up to $z \simeq 3$ with contradicting results. Some studies find significant evolution (Tiley et al. 2016; Übler et al. 2017), while others do not (Miller et al. 2011, 2012; Di Teodoro et al. 2016; Pelliccia et al. 2017). According to Turner et al. (2017), these discrepancies are due to selection effects since different authors use different criteria to define 'disc-dominated' galaxies. Data quality must also play a major role. Different authors use different techniques to derive rotation velocities, velocity dispersions, and stellar masses. The latter ones can be particularly uncertain when comparing objects at different redshifts due to systematic effects. For example, Turner et al. (2017) find that the normalization of the stellar-mass TF relation varies by ∼0.1 dex from $z = 0$ to $z \simeq 3$. This offset is comparable to the uncertainty in the absolute calibration of stellar masses at $z = 0$ from *Spitzer* [3.6] photometry (e.g. Lelli

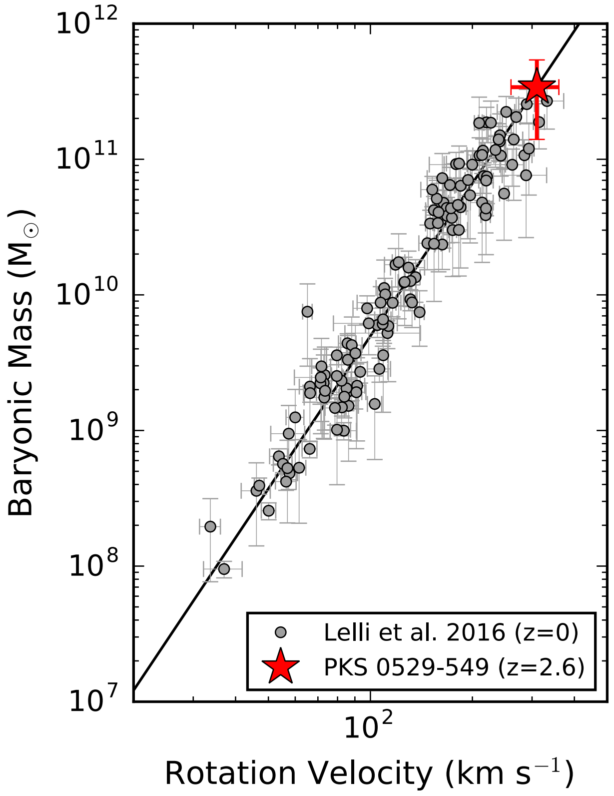

Figure 4. The location of PKS 0529-549 on the local BTFR from the SPARC sample (Lelli et al. 2016a,b).

et al. 2016a), so it is hard to tell whether the stellar-mass TF relation actually evolves. The situation is exacerbated when considering the baryonic TF relation: the gas fraction of galaxies ($M_{\rm gas}/M_\star$) likely evolves with redshift, but direct estimates of gas masses are rarely available.

In this context, PKS 0529-549 is particularly interesting because we have estimates of both $M_\star$ and $M_{\rm mol}$, other than $V_{\rm rot}$ and σ_V. Fig. 4 shows that PKS0529-549 lies on the local baryonic TF relation from the SPARC sample (Lelli et al. 2016a; Lelli, McGaugh & Schombert 2016b). This baryonic TF relation is consistent with previous calibrations (e.g. McGaugh 2005), but has the advantage of using homogeneous photometry at *Spitzer* [3.6], which greatly reduces the uncertainties in $M_\star$. The stellar masses are calculated assuming $M_\star/L_{[3.6]} = 0.5$ M$_\odot$/L$_\odot$ for all galaxies, as expected from stellar population synthesis models with a Kroupa (2001) IMF (same as for PKS 0529-549). The rotation velocities are measured along the flat part of the rotation curve ($V_{\rm flat}$), which is probed by deep H I observations (see Lelli et al. 2016a,b for details). In the case of PKS 0529-549, $V_{\rm rot}$ is an intensity-weighted estimate over the semimajor axis, since the [C I] emission is resolved with ∼2 beams. Thus, one may wonder whether we are probing $V_{\rm flat}$. Local galaxies with similar masses as PKS 0529-549 typically have rotation curves that peak at very small radii ($R \lesssim 1$ kpc) and decline by ∼20–30 per cent before reaching $V_{\rm flat}$ (Noordermeer et al. 2007). If the rotation curve of PKS 0529-549 has a similar shape, then our intensity-weighted value should not differ from $V_{\rm flat}$ by more than ∼20–30 per cent. In general, the adherence of PKS 0529-549 to the baryonic Tully–Fisher relation seems solid against systematic effects. Clearly, a single object cannot be used to infer general conclusions. However, Fig. 4 suggests that some massive galaxies can be in place and kinematically relaxed at $z \simeq 2.6$, when the Universe was only ∼2.5 Gyr old.

5 CONCLUSIONS

We presented ALMA data of the [C I] (2–1) line for the starburst galaxy PKS 0529-549 at $z \simeq 2.6$. With only 5 min of on-source integration time, ALMA spatially resolves the [C I] distribution and kinematics. We also analysed SINFONI data (Nesvadba et al. 2017), probing the ionized gas kinematics, and ATCA radio continuum images (Broderick et al. 2007), probing synchrotron emission from a central AGN. Our results can be summarized as follows:

(i) Both [C I] and [O III] display regular velocity gradients, but their systemic velocities and kinematic PAs differ by ∼300 km s^{-1} and ∼30°, respectively. The [C I] is consistent with a rotating disc, being aligned with both the stellar and dust components, while the [O III] likely traces an outflow, being aligned with two AGN-driven radio lobes.

(ii) The [C I] cube is well reproduced by a 3D disc model with $V_{\rm rot} \simeq 310$ km s^{-1} and $\sigma_V \lesssim 30$ km s^{-1}. This gives $V_{\rm rot}/\sigma_V \gtrsim 10$ similar to local spiral galaxies, indicating that the [C I] disc of PKS 0529-549 is not particularly turbulent.

(iii) The dynamical mass within 8 kpc is $\sim 1.8 \times 10^{11}$ M$_\odot$. This is comparable to the baryonic mass within the errors, implying that baryons dominate over dark matter in the central parts. This is similar to massive galaxies at $z \simeq 0$.

(iv) PKS 0529-549 lies on the local baryonic Tully–Fisher relation, suggesting that some massive galaxies can be already in place and kinematically relaxed at $z \simeq 2.6$.

This study demonstrates the potential of the [C I] line to trace galaxy dynamics at high-z. It also highlights the importance of multiwavelength observations to properly interpret gas kinematics during the early stages of galaxy formation.

ACKNOWLEDGEMENTS

This paper makes use of the following ALMA data: ADS/JAO.ALMA#2013.1.00521.S. ALMA is a partnership of ESO (representing its member states), NSF (USA), and NINS (Japan), together with NRC (Canada), MOST and ASIAA (Taiwan), and KASI (Republic of Korea), in cooperation with the Republic of Chile. The Joint ALMA Observatory is operated by ESO, AUI/NRAO, and NAOJ.

REFERENCES

Arribas S., Colina L., Bellocchi E., Maiolino R., Villar-Martín M., 2014, A&A, 568, A14
Bisigello L., Caputi K. I., Grogin N., Koekemoer A., 2018, A&A, 609, A82
Boomsma R., Oosterloo T. A., Fraternali F., van der Hulst J. M., Sancisi R., 2005, A&A, 431, 65
Broderick J. W., De Breuck C., Hunstead R. W., Seymour N., 2007, MNRAS, 375, 1059
Cappellari M., 2016, ARA&A, 54, 597
Chen C.-C. et al., 2017, ApJ, 846, 108
De Breuck C. et al., 2010, ApJ, 725, 36
De Breuck C. et al., 2014, A&A, 565, A59
Di Teodoro E. M., Fraternali F., 2015, MNRAS, 451, 3021
Di Teodoro E. M., Fraternali F., Miller S. H., 2016, A&A, 594, A77
Drouart G. et al., 2012, A&A, 548, A45
Drouart G., Rocca-Volmerange B., De Breuck C., Fioc M., Lehnert M., Seymour N., Stern D., Vernet J., 2016, A&A, 593, A109

Förster Schreiber N. M. et al., 2009, ApJ, 706, 1364
Gnerucci A. et al., 2011, A&A, 528, A88
Harrison C. M., Alexander D. M., Mullaney J. R., Swinbank A. M., 2014, MNRAS, 441, 3306
Hodge J. A., Carilli C. L., Walter F., de Blok W. J. G., Riechers D., Daddi E., Lentati L., 2012, ApJ, 760, 11
Humphrey A. et al., 2011, MNRAS, 418, 74
Ivison R. J. et al., 2012, MNRAS, 425, 1320
Jones G. C. et al., 2017, ApJ, 850, 180
Kaneko H., Kuno N., Iono D., Tamura Y., Tosaki T., Nakanishi K., Sawada T., 2017, PASJ, 69, 66
Kregel M., Sancisi R., 2001, A&A, 376, 59
Kroupa P., 2001, MNRAS, 322, 231
Lehnert M. D., Nesvadba N. P. H., Le Tiran L., Di Matteo P., van Driel W., Douglas L. S., Chemin L., Bournaud F., 2009, ApJ, 699, 1660
Lelli F. et al., 2015, A&A, 584, A113
Lelli F., Fraternali F., Sancisi R., 2010, A&A, 516, A11
Lelli F., Verheijen M., Fraternali F., 2014, MNRAS, 445, 1694
Lelli F., McGaugh S. S., Schombert J. M., 2016a, AJ, 152, 157
Lelli F., McGaugh S. S., Schombert J. M., 2016b, ApJ, 816, L14
Leroy A. K., Walter F., Brinks E., Bigiel F., de Blok W. J. G., Madore B., Thornley M. D., 2008, AJ, 136, 2782
Madau P., Dickinson M., 2014, ARA&A, 52, 415
McGaugh S. S., 2005, ApJ, 632, 859
McMullin J. P., Waters B., Schiebel D., Young W., Golap K., 2007, in Shaw R. A., Hill F., Bell D. J., eds, ASP Conf. Ser. Vol. 376, Astronomical Data Analysis Software and Systems XVI. Astron. Soc. Pac., San Francisco, p. 127
Miller S. H., Bundy K., Sullivan M., Ellis R. S., Treu T., 2011, ApJ, 741, 115
Miller S. H., Ellis R. S., Sullivan M., Bundy K., Newman A. B., Treu T., 2012, ApJ, 753, 74
Mogotsi K. M., de Blok W. J. G., Caldú-Primo A., Walter F., Ianjamasimanana R., Leroy A. K., 2016, AJ, 151, 15
Nesvadba N. P. H., De Breuck C., Lehnert M. D., Best P. N., Collet C., 2017, A&A, 599, A123
Noordermeer E., van der Hulst J. M., Sancisi R., Swaters R. S., van Albada T. S., 2007, MNRAS, 376, 1513
Papadopoulos P. P., Thi W.-F., Viti S., 2004, MNRAS, 351, 147
Pelliccia D., Tresse L., Epinat B., Ilbert O., Scoville N., Amram P., Lemaux B. C., Zamorani G., 2017, A&A, 599, A25
Pentericci L., McCarthy P. J., Röttgering H. J. A., Miley G. K., van Breugel W. J. M., Fosbury R., 2001, ApJS, 135, 63
Planck Collaboration XIII, 2016, A&A, 594, A13
Rocca-Volmerange B., Le Borgne D., De Breuck C., Fioc M., Moy E., 2004, A&A, 415, 931
Shao Y. et al., 2017, ApJ, 845, 138
Sicking F. J., 1997, PhD thesis, Univ. Groningen
Smit R. et al., 2018, Nature, 553, 178
Stott J. P. et al., 2016, MNRAS, 457, 1888
Tacconi L. J. et al., 2013, ApJ, 768, 74
Tiley A. L. et al., 2016, MNRAS, 460, 103
Toft S., Gallazzi A., Zirm A., Wold M., Zibetti S., Grillo C., Man A., 2012, ApJ, 754, 3
Tully R. B., Fisher J. R., 1977, A&A, 54, 661
Turner O. J., Harrison C. M., Cirasuolo M., McLure R. J., Dunlop J., Swinbank A. M., Tiley A. L., 2017, preprint (arXiv:1711.03604)
Vogelaar M. G. R., Terlouw J. P., 2001, in Harnden F. R., Jr, Primini F. A., Payne H. E., eds, ASP Conf. Ser. Vol. 238, Astronomical Data Analysis Software and Systems X. Astron. Soc. Pac., San Francisco, p. 358
Weaver J. R. et al., 2018, A&A, 614, A32
Wisnioski E. et al., 2015, ApJ, 799, 209
Wuyts S. et al., 2016, ApJ, 831, 149
Zirm A. W. et al., 2005, ApJ, 630, 68
Übler H. et al., 2017, ApJ, 842, 121
Übler H. D. N. et al., 2018, ApJ, 854, L24

This paper has been typeset from a TEX/LATEX file prepared by the author.

Bibliography

Abbott, B. P., Abbott, R., Abbott, T. D., et al. 2016, PHYSICAL REVIEW LETTERS, 116, 061102

Adelberger, K. L., Shapley, A. E., Steidel, C. C., et al. 2005, ApJ, 629, 636

Aird, J., Nandra, K., Laird, E. S., et al. 2010, Monthly Notices of the Royal Astronomical, 401, 2531

Alaghband-Zadeh, S., Chapman, S. C., Swinbank, A. M., et al. 2013, MNRAS, 435, 1493

Alexander, D. M., Swinbank, A. M., Smail, I., McDermid, R., & Nesvadba, N. P. H. 2010, MNRAS, 402, 2211

Alexander, P. & Leahy, J. P. 1987, MNRAS, 225, 1

Anderson, M. E., Churazov, E., & Bregman, J. N. 2016, MNRAS, 455, 227

Antonucci, R. 1993, Annual Review of Astronomy and Astrophysics, 31, 473

Aragon-Salamanca, A., Baugh, C. M., & Kauffmann, G. 1998, MNRAS, 297, 427

Archibald, E. N., Dunlop, J. S., Hughes, D. H., et al. 2001, MNRAS, 323, 417

Arendt, R. G., Odegard, N., Weiland, J. L., et al. 1998, ApJ, 508, 74

Armus, L., Soifer, B. T., Murphy, T. W., J., et al. 1998, ApJ, 495, 276

Arrigoni Battaia, F., Prochaska, J. X., Hennawi, J. F., et al. 2018, MNRAS, 473, 3907

Asensio Ramos, A. & Ramos Almeida, C. 2009, ApJ, 696, 2075

Astropy Collaboration, Robitaille, T. P., Tollerud, E. J., et al. 2013, A&A, 558, A33

Baade, W. & Minkowski, R. 1954, Apj, 119, 206

Balick, B. & Heckman, T. M. 1982, ARA&A, 20, 431

Barbosa, C. E., Arnaboldi, M., Coccato, L., et al. 2016, A&A, 589, A139

Barger, A. J., Cowie, L. L., Chen, C. C., et al. 2014, ApJ, 784, 9

Barnard, E. E. 1907, ApJ, 25, 218

Barnard, E. E. 1910, ApJ, 31, 8

Beckmann, V. & Shrader, C. 2012, 69

Bellstedt, S., Lidman, C., Muzzin, A., et al. 2016, MNRAS, 460, 2862

Benson, A. J., Bower, R. G., Frenk, C. S., et al. 2003, ApJ, 599, 38

Berczik, P., Merritt, D., Spurzem, R., & Bischof, H.-P. 2006, ApJ, 642, L21

Best, P. N., Kauffmann, G., Heckman, T. M., et al. 2005, MNRAS, 362, 25

Biernacki, P. & Teyssier, R. 2018, MNRAS, 475, 5688

Bisbas, T. G., Papadopoulos, P. P., & Viti, S. 2015, ApJ, 803, 37

Bisbas, T. G., van Dishoeck, E. F., Papadopoulos, P. P., et al. 2017, ApJ, 839, 90

Bithell, M. & Rees, M. J. 1990, MNRAS, 242, 570

Blumenthal, G. & Miley, G. 1979, Astronomy and Astrophysics, 80, 13

Blundell, K. M., Fabian, A. C., Crawford, C. S., Erlund, M. C., & Celotti, A. 2006, ApJ, 644, L13

Blundell, K. M., Rawlings, S., Eales, S. A., Taylor, G. B., & Bradley, A. D. 1998, MNRAS, 295, 265

Blundell, K. M., Rawlings, S., & Willott, C. J. 1999, The Astronomical Journal, 117, 677

Bolatto, A. D., Warren, S. R., Leroy, A. K., et al. 2015, ApJ, 809, 175

Boquien, M., Buat, V., & Perret, V. 2014, A&A, 571, A72

Boquien, M., Kennicutt, R., Calzetti, D., et al. 2016, A&A, 591, A6

Bordoloi, R., Lilly, S. J., Knobel, C., et al. 2011, ApJ, 743, 10

Bothwell, M. S., Aguirre, J. E., Aravena, M., et al. 2017, MNRAS, 466, 2825

Bouwens, R. J., Illingworth, G. D., Oesch, P. A., et al. 2012, ApJ, 754, 83

Briggs, D. 1995, PhD thesis, New Mexico Institute of Mining and Technology

Brinchmann, J., Charlot, S., White, S. D. M., et al. 2004, MNRAS, 351, 1151

Broderick, J. W., De Breuck, C., Hunstead, R. W., & Seymour, N. 2007, MNRAS, 375, 1059

Bruzual, G. & Charlot, S. 2003, MNRAS, 344, 1000

Calistro Rivera, G., Lusso, E., Hennawi, J. F., & Hogg, D. W. 2016, Apj, 833, 98

Cantalupo, S., Arrigoni-Battaia, F., Prochaska, J. X., Hennawi, J. F., & Madau, P. 2014, Nature, 506, 63

Capak, P. L., Teplitz, H. I., Brooke, T. Y., Laher, R., & Science Center, S. 2013, in , 340.06

Carilli, C. L., Perley, R. A., Dreher, J. W., & Leahy, J. P. 1991, ApJ, 383, 554

Carilli, C. L., Röttgering, H. J. A., van Ojik, R., et al. 1997, ApJS, 109, 1

Casey, C. M. 2012, MNRAS, 425, 3094

Casey, C. M., Hodge, J., Zavala, J. A., et al. 2018, ArXiv e-prints

Chabrier, G. 2003, Publications of the Astronomical Society of the Pacific, 115, 763

Cicone, C., Maiolino, R., Gallerani, S., et al. 2015, A&A, 574, A14

Cisternas, M., Jahnke, K., Bongiorno, A., et al. 2011, ApJ, 741, L11

Condon, J. J., Cotton, W. D., Greisen, E. W., et al. 1998, AJ, 115, 1693

Conley, A., Cooray, A., Vieira, J. D., et al. 2011, ApJ, 732, L35

Conroy, C. 2013, Annual Review of Astronomy and Astrophysics, 51, 393

Cooke, E. A., Hatch, N. A., Rettura, A., et al. 2015, MNRAS, 452, 2318

Cooke, E. A., Hatch, N. A., Stern, D., et al. 2016, ApJ, 816, 83

Cortese, L., Ciesla, L., Boselli, A., et al. 2012, A&A, 540, A52

Cruz, M. J., Jarvis, M. J., Blundell, K. M., et al. 2006, MNRAS, 373, 1531

da Cunha, E., Charlot, S., & Elbaz, D. 2008, MNRAS, 388, 1595

da Cunha, E., Walter, F., Smail, I. R., et al. 2015, Apj, 806, 110

Daddi, E., Bournaud, F., Walter, F., et al. 2010a, ApJ, 713, 686

Daddi, E., Dickinson, M., Morrison, G., et al. 2007, ApJ, 670, 156

Daddi, E., Elbaz, D., Walter, F., et al. 2010b, ApJ, 714, L118

Daddi, E., Renzini, A., Pirzkal, N., et al. 2005, ApJ, 626, 680

Danielson, A. L. R., Swinbank, A. M., Smail, I., et al. 2013, MNRAS, 436, 2793

Dannerbauer, H., Kurk, J. D., De Breuck, C., et al. 2014, A&A, 570, A55

Dannerbauer, H., Lehnert, M. D., Emonts, B., et al. 2017, A&A, 608, A48

Darvish, B., Martin, C., Gonçalves, T. S., et al. 2018, ApJ, 853, 155

Darvish, B., Mobasher, B., Sobral, D., et al. 2016, ApJ, 825, 113

Davé, R., Oppenheimer, B. D., & Finlator, K. 2011, MNRAS, 415, 11

Davé, R., Thompson, R., & Hopkins, P. F. 2016, MNRAS, 462, 3265

Davidzon, I., Ilbert, O., Faisst, A. L., Sparre, M., & Capak, P. L. 2018, ApJ, 852, 107

De Breuck, C., Bertoldi, F., Carilli, C., et al. 2004, A&A, 424, 1

De Breuck, C., Downes, D., Neri, R., et al. 2005, A&A, 430, L1

De Breuck, C., Neri, R., Morganti, R., et al. 2003, A&A, 401, 911

De Breuck, C., Seymour, N., Stern, D., et al. 2010, ApJ, 725, 36

De Breuck, C., van Breugel, W., Röttgering, H. J. A., & Miley, G. 2000, A&AS, 143, 303

De Breuck, C., van Breugel, W., Stanford, S. A., et al. 2002, AJ, 123, 637

De Cia, A., Ledoux, C., Mattsson, L., et al. 2016, Astronomy and Astrophysics, 596, A97

De Lucia, G. & Blaizot, J. 2007, MNRAS, 375, 2

Decarli, R., Walter, F., Carilli, C., et al. 2014, ApJ, 782, L17

DeGraf, C., Dekel, A., Gabor, J., & Bournaud, F. 2017, MNRAS, 466, 1462

Delaye, L., Huertas-Company, M., Mei, S., et al. 2014, MNRAS, 441, 203

Delvecchio, I., Lutz, D., Berta, S., et al. 2015, MNRAS, 449, 373

Dey, A., van Breugel, W., Vacca, W. D., & Antonucci, R. 1997, ApJ, 490, 698

Dickman, R. L., Snell, R. L., & Schloerb, F. P. 1986, ApJ, 309, 326

Downes, D. & Solomon, P. M. 1998, ApJ, 507, 615

Downes, D., Solomon, P. M., & Radford, S. J. E. 1993, Apj, 414, L13

Draine, B. T. 1989, in Infrared Spectroscopy in Astronomy, 93

Draine, B. T. 2011, Physics of the Interstellar and Intergalactic Medium (Princeton University Press 2011. ISBN: 978-0-691-12214-4)

Drouart, G., De Breuck, C., Vernet, J., et al. 2012, A&A, 548, A45

Drouart, G., De Breuck, C., Vernet, J., et al. 2014, A&A, 566, A53

Drouart, G. & Falkendal, T. 2018, MNRAS, 477, 4981

Drouart, G., Rocca-Volmerange, B., De Breuck, C., et al. 2016, A&A, 593, A109

Dubois, Y., Volonteri, M., Silk, J., et al. 2015, MNRAS, 452, 1502

Duley, W. W. & Seahra, S. 1998, ApJ, 507, 874

Eckart, A. & Genzel, R. 1997, Monthly Notices of the Royal Astronomical, 284, 576

Elbaz, D., Daddi, E., Le Borgne, D., et al. 2007, A&A, 468, 33

Elbaz, D., Leiton, R., Nagar, N., et al. 2017, ArXiv e-prints, arXiv:1711.10047

Elmegreen, B. G. 1989, ApJ, 338, 178

Emonts, B. H. C., De Breuck, C., Lehnert, M. D., et al. 2015a, A&A, 584, A99

Emonts, B. H. C., Feain, I., Mao, M. Y., et al. 2011a, ApJ, 734, L25

Emonts, B. H. C., Lehnert, M. D., Dannerbauer, H., et al. 2018, MNRAS, 477, L60

Emonts, B. H. C., Lehnert, M. D., Villar-Martín, M., et al. 2016, Science, 354, 1128

Emonts, B. H. C., Mao, M. Y., Stroe, A., et al. 2015b, MNRAS, 451, 1025

Emonts, B. H. C., Norris, R. P., Feain, I., et al. 2014, MNRAS, 438, 2898

Emonts, B. H. C., Norris, R. P., Feain, I., et al. 2011b, MNRAS, 415, 655

Emsellem, E., Cappellari, M., Krajnović, D., et al. 2011, MNRAS, 414, 888

Erb, D. K., Steidel, C. C., & Chen, Y. 2018, ArXiv e-prints, arXiv:1807.00065

Ewen, H. I. & Purcell, E. M. 1951, Nature, 168, 356

Falkendal, T., De Breuck, C., Lehnert, M. D., et al. 2018, A&A, in press

Fanaroff, B. L. & Riley, J. M. 1974, MNRAS, 167, 31P

Fardal, M. A., Katz, N., Weinberg, D. H., & Davé, R. 2007, Monthly Notices of the Royal Astronomical, 379, 985

Feigelson, E. D. & Nelson, P. I. 1985, ApJ, 293, 192

Feng, J. & Gallo, C. 2014, Galaxies, 2, 199

Ferland, G. J., Porter, R. L., van Hoof, P. A. M., et al. 2013, Rev. Mex. Astron. Astrofis., 49, 137

Ferrarese, L. & Merritt, D. 2000, ApJ, 539, L9

Feruglio, C., Maiolino, R., Piconcelli, E., et al. 2010, Astronomy and Astrophysics, 518, L155

Finlator, K. & Davé, R. 2008, MNRAS, 385, 2181

Fioc, M. & Rocca-Volmerange, B. 1997, Astronomy and astrophysics, 326, 950

Fiorucci, M. & Munari, U. 2003, A&A, 401, 781

Flower, D. R., Nussbaumer, H., & Schild, H. 1979, A&A, 72, L1

Foltz, R., Wilson, G., Muzzin, A., et al. 2018, ArXiv e-prints

Foreman-Mackey, D., Hogg, D. W., Lang, D., & Goodman, J. 2013, PASP, 125, 306

Frayer, D. T., Ivison, R. J., Scoville, N. Z., et al. 1998, ApJ, 506, L7

Fritz, J., Franceschini, A., & Hatziminaoglou, E. 2006, MNRAS, 366, 767

Gabor, J. M. & Bournaud, F. 2013, MNRAS, 434, 606

Gaia Collaboration, Brown, A. G. A., Vallenari, A., et al. 2018, ArXiv e-prints, arXiv:1804.09365

Galametz, M., Kennicutt, R. C., Albrecht, M., et al. 2012, MNRAS, 425, 763

Gebhardt, K., Bender, R., Bower, G., et al. 2000, ApJ, 539, L13

Genzel, R., Tacconi, L. J., Gracia-Carpio, J., et al. 2010, MNRAS, 407, 2091

Ghez, A. M., Klein, B. L., Morris, M., & Becklin, E. E. 1998, The Astrophysical Journal, 509, 678

Gillessen, S., Eisenhauer, F., Trippe, S., et al. 2009, ApJ, 692, 1075

Gilli, R., Norman, C., Vignali, C., et al. 2014, A&A, 562, A67

Ginolfi, M., Maiolino, R., Nagao, T., et al. 2017, MNRAS, 468, 3468

Glover, S. C. O., Clark, P. C., Micic, M., & Molina, F. 2015, Monthly Notices of the Royal Astronomical Society, 448, 1607

Gnat, O. & Sternberg, A. 2007, The Astrophysical Journal Supplement Series, 168, 213

Goodman, J. & Weare, J. 2010, Communications in Applied Mathematics and Computational Science, Vol. 5, No. 1, p. 65-80, 2010, 5, 65

Gopal-Krishna, Subramanian, P., Wiita, P. J., & Becker, P. A. 2001, A&A, 377, 827

Greene, J. E., Murphy, J. D., Graves, G. J., et al. 2013, ApJ, 776, 64

Groves, B. A., Dopita, M. A., & Sutherland, R. S. 2004, The Astrophysical Journal Supplement Series, 153, 9

Gullberg, B., De Breuck, C., Lehnert, M. D., et al. 2016a, A&A, 586, A124

Gullberg, B., Lehnert, M. D., De Breuck, C., et al. 2016b, A&A, 591, A73

Häring, N. & Rix, H.-W. 2004, ApJ, 604, L89

Harrison, C. M., Alexander, D. M., Mullaney, J. R., et al. 2012, ApJ, 760, L15

Harrison, C. M., Alexander, D. M., Mullaney, J. R., et al. 2016, MNRAS, 456, 1195

Harrison, C. M., Costa, T., Tadhunter, C. N., et al. 2018, Nature Astronomy, 2, 198

Harwood, J. J., Hardcastle, M. J., Croston, J. H., & Goodger, J. L. 2013, MNRAS, 435, 3353

Hashimoto, T., Laporte, N., Mawatari, K., et al. 2018, Nature, 557, 392

Hatch, N. A., Wylezalek, D., Kurk, J. D., et al. 2014, MNRAS, 445, 280

Heckman, T. M., Alexandroff, R. M., Borthakur, S., Overzier, R., & Leitherer, C. 2015, ApJ, 809, 147

Heckman, T. M. & Best, P. N. 2014, Annual Review of Astronomy and Astrophysics, 52, 589

Henkel, C., Downes, D., Weiß, A., Riechers, D., & Walter, F. 2010, A&A, 516, A111

Hickox, R. C., Jones, C., Forman, W. R., et al. 2009, Apj, 696, 891

Hickox, R. C., Mullaney, J. R., Alexander, D. M., et al. 2014, ApJ, 782, 9

Hildebrand, R. H. 1983, QJRAS, 24, 267

Hill, A. R., Muzzin, A., Franx, M., et al. 2017, ApJ, 837, 147

Hilz, M., Naab, T., & Ostriker, J. P. 2013, MNRAS, 429, 2924

Hirschmann, M., Naab, T., Ostriker, J. P., et al. 2015, MNRAS, 449, 528

Hönig, S. F., Beckert, T., Ohnaka, K., & Weigelt, G. 2006, A&A, 452, 459

Hopkins, A. M. 2004, ApJ, 615, 209

Hopkins, A. M. & Beacom, J. F. 2006, The Astrophysical Journal, 651, 142

Hopkins, P. F., Hernquist, L., Martini, P., et al. 2005, ApJ, 625, L71

Huang, S., Ho, L. C., Peng, C. Y., Li, Z.-Y., & Barth, A. J. 2013, ApJ, 768, L28

Hubble, E. P. 1926, Astrophysical Journa, 64

Ilbert, O., McCracken, H. J., Le Fèvre, O., et al. 2013, A&A, 556, A55

Ishwara-Chandra, C. H. & Saikia, D. J. 1999, MNRAS, 309, 100

Ivison, R. J., Morrison, G. E., Biggs, A. D., et al. 2008, MNRAS, 390, 1117

Ivison, R. J., Smail, I., Amblard, A., et al. 2012, MNRAS, 425, 1320

Jaffe, W. J. & Perola, G. C. 1973, A&A, 26, 423

Jahnke, K. & Macciò, A. V. 2011, ApJ, 734, 92

Joblin, C., Leger, A., & Martin, P. 1992, ApJ, 393, L79

Kalberla, P. M. W., Burton, W. B., Hartmann, D., et al. 2005, Astronomy and Astrophysics, 440, 775

Kalfountzou, E., Stevens, J. A., Jarvis, M. J., et al. 2017, MNRAS, 471, 28

Kapahi, V. K., Athreya, R. M., van Breugel, W., McCarthy, P. J., & Subrahmanya, C. R. 1998, ApJS, 118, 275

Kapahi, V. K. & Saikia, D. J. 1982, Journal of Astrophysics and Astronomy, 3, 465

Kawinwanichakij, L., Papovich, C., Quadri, R. F., et al. 2017, ApJ, 847, 134

Kelly, B. C. & Shen, Y. 2013, ApJ, 764, 45

Kennicutt, Robert C., J. 1998a, ApJ, 498, 541

Kennicutt, Jr., R. C. 1998b, ARA&A, 36, 189

Klamer, I. J., Ekers, R. D., Bryant, J. J., et al. 2006, MNRAS, 371, 852

Klein, U., Mack, K. H., Gregorini, L., & Parma, P. 1995, A&A, 303, 427

Kormendy, J. & Gebhardt, K. 2001, in 20th Texas Symposium on relativistic astrophysics, Vol. 586, 363–381

Kormendy, J. & Ho, L. C. 2013, ARA&A, 51, 511

Kornei, K. A., Shapley, A. E., Martin, C. L., et al. 2012, ApJ, 758, 135

Kovac, J. M., Leitch, E. M., Pryke, C., et al. 2002, Nature, 420, 772

Krajnović, D., Emsellem, E., Cappellari, M., et al. 2011, MNRAS, 414, 2923

Krolik, J. H. & Chen, W. 1991, Astronomical Journal, 102, 1659

Kroupa, P. 2001, MNRAS, 322, 231

Kuiper, E., Hatch, N. A., Miley, G. K., et al. 2011, MNRAS, 415, 2245

L., B. A. 1920, An elementary manual of statistics, 3rd edn. (Tonawanda, NY: P. S. King & Son)

Laporte, C. F. P., White, S. D. M., Naab, T., & Gao, L. 2013, MNRAS, 435, 901

Leahy, J. P., Muxlow, T. W. B., & Stephens, P. W. 1989, MNRAS, 239, 401

Leclercq, F., Bacon, R., Wisotzki, L., et al. 2017, A&A, 608

Lee, B., Giavalisco, M., Whitaker, K., et al. 2018, ApJ, 853, 131

Lee, M. M., Tanaka, I., Kawabe, R., et al. 2017, ApJ, 842, 55

Lee, N., Sanders, D. B., Casey, C. M., et al. 2015, ApJ, 801, 80

Lehnert, M. D. & Heckman, T. M. 1996, ApJ, 472, 546

Lehnert, M. D., Heckman, T. M., Chambers, K. C., & Miley, G. K. 1992, ApJ, 393, 68

Lehnert, M. D., Tasse, C., Nesvadba, N. P. H., Best, P. N., & van Driel, W. 2011, Astronomy and Astrophysics, 532, L3

Lehnert, M. D., van Driel, W., Le Tiran, L., Di Matteo, P., & Haywood, M. 2015, A&A, 577, A112

Leitherer, C., Schaerer, D., Goldader, J. D., et al. 1999, The Astrophysical Journal Supplement Series, 123, 3

Li, A. & Draine, B. T. 2001, ApJ, 554, 778

Li, A. & Mann, I. 2012, in Nanodust in the Solar System: Discoveries and Interpretations, Vol. 385, 5

Lilly, S. J., Le Fevre, O., Hammer, F., & Crampton, D. 1996, The Astrophysical Journal, 460, L1

López Fernández, R., González Delgado, R. M., Pérez, E., et al. 2018, ArXiv e-prints, arXiv:1802.10118

Mack, K. H., Klein, U., O'Dea, C. P., Willis, A. G., & Saripalli, L. 1998, A&A, 329, 431

MacKenzie, T. P., Scott, D., & Swinbank, M. 2016, MNRAS, 463, 10

Madau, P., Ferguson, H. C., Dickinson, M. E., et al. 1996, Monthly Notices of the Royal Astronomical, 283, 1388

Magorrian, J., Tremaine, S., Richstone, D., et al. 1998, AJ, 115, 2285

Mainieri, V., Bongiorno, A., Merloni, A., et al. 2011, A&A, 535, A80

Maraston, C. 1998, MNRAS, 300, 872

Martin, C. L. 2005, ApJ, 621, 227

Martini, P. 2004, in Coevolution of Black Holes and Galaxies, 169

Martini, P. & Weinberg, D. H. 2001, ApJ, 547, 12

Matejek, M. S. & Simcoe, R. A. 2012, ApJ, 761, 112

Maxfield, L., Spinrad, H., Stern, D., Dey, A., & Dickinson, M. 2002, AJ, 123, 2321

McAlpine, S., Bower, R. G., Harrison, C. M., et al. 2017, MNRAS, 468, 3395

McCarthy, P. J., Kapahi, V. K., van Breugel, W., et al. 1996, The Astrophysical Journal Supplement Series, 107, 19

McCarthy, P. J., Spinrad, H., van Breugel, W., et al. 1990, ApJ, 365, 487

McLeod, A. F., Dale, J. E., Ginsburg, A., et al. 2015, MNRAS, 450, 1057

McMullin, J. P., Waters, B., Schiebel, D., Young, W., & Golap, K. 2007, in Astronomical Society of the Pacific Conference Series, Vol. 376, Astronomical Data Analysis Software and Systems XVI, ed. R. A. Shaw, F. Hill, & D. J. Bell, 127

McNamara, B. R. & Nulsen, P. E. J. 2012, New Journal of Physics, 14, 055023

Ménard, B., Scranton, R., Fukugita, M., & Richards, G. 2010, MNRAS, 405, 1025

Merloni, A. & Heinz, S. 2008, MNRAS, 388, 1011

Merritt, D. & Ferrarese, L. 2001, Monthly Notices of the Royal Astronomical Society, 320, L30

Merritt, D., Mikkola, S., & Szell, A. 2007, ApJ, 671, 53

Miley, G. 1980, Annual Review of Astronomy and Astrophysics, 18, 165

Miley, G. & De Breuck, C. 2008, A&ARv, 15, 67

Miley, G. K., Chambers, K. C., van Breugel, W. J. M., & Macchetto, F. 1992, ApJ, 401, L69

Miley, G. K., Overzier, R. A., Zirm, A. W., et al. 2006, ApJ, 650, L29

Morganti, R., Oosterloo, T., & Tsvetanov, Z. 1998, AJ, 115, 915

Morganti, R., Tadhunter, C. N., & Oosterloo, T. A. 2005, Astronomy and Astrophysics, 444, L9

Mullaney, J. R., Alexander, D. M., Aird, J., et al. 2015, MNRAS, 453, L83

Mullaney, J. R., Alexander, D. M., Goulding, A. D., & Hickox, R. C. 2011, MNRAS, 414, 1082

Mullaney, J. R., Daddi, E., Béthermin, M., et al. 2012, ApJ, 753, L30

Muzzin, A., Wilson, G., Yee, H. K. C., et al. 2012, ApJ, 746, 188

Nantais, J. B., Muzzin, A., van der Burg, R. F. J., et al. 2017, MNRAS, 465, L104

Nantais, J. B., van der Burg, R. F. J., Lidman, C., et al. 2016, A&A, 592, A161

Nenkova, M., Sirocky, M. M., Ivezić, Ž., & Elitzur, M. 2008, ApJ, 685, 147

Nesvadba, N. P. H., De Breuck, C., Lehnert, M. D., et al. 2011, A&A, 525, A43

Nesvadba, N. P. H., De Breuck, C., Lehnert, M. D., Best, P. N., & Collet, C. 2017, A&A, 599, A123

Nesvadba, N. P. H., Lehnert, M. D., Eisenhauer, F., et al. 2006, ApJ, 650, 693

Nesvadba, N. P. H., Neri, R., De Breuck, C., et al. 2009, MNRAS, 395, L16

Netzer, H., Lani, C., Nordon, R., et al. 2016, ApJ, 819, 123

Netzer, H., Mor, R., Trakhtenbrot, B., Shemmer, O., & Lira, P. 2014, ApJ, 791, 34

Noble, A. G., McDonald, M., Muzzin, A., et al. 2017, ApJ, 842, L21

Noeske, K. G., Weiner, B. J., Faber, S. M., et al. 2007, ApJ, 660, L43

Noirot, G., Stern, D., Mei, S., et al. 2018, ArXiv e-prints

Noirot, G., Vernet, J., De Breuck, C., et al. 2016, ApJ, 830, 90

Noll, S., Burgarella, D., Giovannoli, E., et al. 2009, Astronomy and Astrophysics, 507, 1793

Nussbaumer, H. & Schild, H. 1981, A&A, 101, 118

Oesch, P. A., Brammer, G., van Dokkum, P. G., et al. 2016, Apj, 819, 129

Ogle, P., Whysong, D., & Antonucci, R. 2006, ApJ, 647, 161

Omont, A., Petitjean, P., Guilloteau, S., et al. 1996, Nature, 382, 428

Oppenheimer, B. D. & Schaye, J. 2013, MNRAS, 434, 1043

Orr, M. J. L. & Browne, I. W. A. 1982, MNARS, 200, 1067

Osterbrock, D. E. & Ferland, G. J. 2006, Astrophysics of gaseous nebulae and active galactic nuclei (CA: University Science Books, 2006)

Papadopoulos, P. P., Bisbas, T. G., & Zhang, Z.-Y. 2018, MNRAS, 478, 1716

Papadopoulos, P. P. & Greve, T. R. 2004, ApJ, 615, L29

Papadopoulos, P. P., Thi, W. F., & Viti, S. 2004, MNRAS, 351, 147

Peek, J. E. G., Ménard, B., & Corrales, L. 2015, ApJ, 813, 7

Peng, C. Y. 2007, ApJ, 671, 1098

Peng, Y.-j., Lilly, S. J., Kovač, K., et al. 2010, ApJ, 721, 193

Pentericci, L., McCarthy, P. J., Röttgering, H. J. A., et al. 2001, The Astrophysical Journal Supplement Series, 135, 63

Pentericci, L., Van Reeven, W., Carilli, C. L., Röttgering, H. J. A., & Miley, G. K. 2000, A&AS, 145, 121

Pier, E. A. & Krolik, J. H. 1992, ApJ, 401, 99

Pilbratt, G. L., Riedinger, J. R., Passvogel, T., et al. 2010, A&A, 518, L1

Planck Collaboration, Ade, P. A. R., Aghanim, N., et al. 2016, A&A, 594, A13

Popescu, C. C., Tuffs, R. J., Dopita, M. A., et al. 2011, Astronomy and Astrophysics, 527, A109

Prescott, M. K. M., Martin, C. L., & Dey, A. 2015, ApJ, 799, 62

Prochaska, J. X., Lau, M. W., & Hennawi, J. F. 2014, Apj, 796, 140

Quider, A. M., Nestor, D. B., Turnshek, D. A., et al. 2011, The Astronomical Journal, 141, 137

Reuland, M., Röttgering, H., & van Breugel, W. 2003a, New Astron. Rev., 47, 303

Reuland, M., Röttgering, H., van Breugel, W., & De Breuck, C. 2004, MNRAS, 353, 377

Reuland, M., van Breugel, W., Röttgering, H., et al. 2003b, ApJ, 592, 755

Rocca-Volmerange, B., Le Borgne, D., De Breuck, C., Fioc, M., & Moy, E. 2004, A&A, 415, 931

Rodighiero, G., Daddi, E., Baronchelli, I., et al. 2011, ApJ, 739, L40

Roettgering, H. J. A., Lacy, M., Miley, G. K., Chambers, K. C., & Saunders, R. 1994, Astronomy and Astrophysics Supplement Series, 108, 79

Roettgering, H. J. A., Miley, G. K., Chambers, K. C., & Macchetto, F. 1995, Astronomy and Astrophysics Supplement Series, 114, 51

Rosario, D. J., Burtscher, L., Davies, R., et al. 2013, ApJ, 778, 94

Rosario, D. J., McIntosh, D. H., van der Wel, A., et al. 2015, A&A, 573, A85

Rosario, D. J., Santini, P., Lutz, D., et al. 2012, A&A, 545, A45

Rovilos, E., Comastri, A., Gilli, R., et al. 2012, A&A, 546, A58

Rubin, K. H. R., Prochaska, J. X., Koo, D. C., et al. 2014, APJ, 794, 156

Rudie, G. C., Steidel, C. C., Trainor, R. F., et al. 2012, ApJ, 750, 67

Salpeter, E. E. 1955, ApJ, 121, 161

Salpeter, E. E. 1964, Apj, 140, 796

Sandstrom, K. M., Leroy, A. K., Walter, F., et al. 2013, ApJ, 777, 5

Santini, P., Fontana, A., Castellano, M., et al. 2017, Apj, 847, 76

Santini, P., Fontana, A., Grazian, A., et al. 2009, A&A, 504, 751

Santini, P., Maiolino, R., Magnelli, B., et al. 2014, A&A, 562, A30

Sarron, F., Martinet, N., Durret, F., & Adami, C. 2017, ArXiv e-prints

Sault, R. J., Teuben, P. J., & Wright, M. C. H. 1995, in Astronomical Society of the Pacific Conference Series, Vol. 77, Astronomical Data Analysis Software and Systems IV, ed. R. A. Shaw, H. E. Payne, & J. J. E. Hayes, 433

Sawicki, M. 2012, PASP, 124, 1208

Sawicki, M. & Yee, H. K. C. 1998, The Astronomical Journal, 115, 1329

Saxena, A., Marinello, M., Overzier, R. A., et al. 2018, ArXiv e-prints

Schawinski, K., Thomas, D., Sarzi, M., et al. 2007, MNRAS, 382, 1415

Schmidt, M. 1963, Nature, 197, 1040

Schmidt, T. M., Worseck, G., Hennawi, J. F., Prochaska, J. X., & Crighton, N. H. M. 2017, ApJ, 847, 81

Schoenmakers, A. P., de Bruyn, A. G., Röttgering, H. J. A., van der Laan, H., & Kaiser, C. R. 2000, MNRAS, 315, 371

Scholtz, J., Alexander, D. M., Harrison, C. M., et al. 2018, MNRAS, 475, 1288

Schreiber, C., Pannella, M., Elbaz, D., et al. 2015, A&A, 575, A74

Scoville, N., Sheth, K., Aussel, H., et al. 2016, ApJ, 820, 83

Seyfert, C. K. 1943, Apj, 97, 28

Seymour, N., Altieri, B., De Breuck, C., et al. 2012, ApJ, 755, 146

Seymour, N., Stern, D., De Breuck, C., et al. 2007, ApJS, 171, 353

Shabala, S. S., Deller, A., Kaviraj, S., et al. 2017, MNRAS, 464, 4706

Shankar, F., Buchan, S., Rettura, A., et al. 2015, ApJ, 802, 73

Shankar, F., Weinberg, D. H., & Miralda-Escudé, J. 2009, ApJ, 690, 20

Shao, Y., Wang, R., Jones, G. C., et al. 2017, ApJ, 845, 138

Sharma, S. 2017, Annual Review of Astronomy and Astrophysics, 55, 213

Siebenmorgen, R., Heymann, F., & Efstathiou, A. 2015, A&A, 583, A120

Siebenmorgen, R., Voshchinnikov, N. V., & Bagnulo, S. 2014, Astronomy & Astrophysics, 561, A82

Silk, J. 2013, ApJ, 772, 112

Silk, J. & Mamon, G. A. 2012, Research in Astronomy and Astrophysics, 12, 917

Silk, J. & Rees, M. J. 1998, Astronomy and Astrophysics, 331, L1

Siringo, G., Kreysa, E., Kovács, A., et al. 2009, A&A, 497, 945

Smail, I., Blundell, K. M., Lehmer, B. D., & Alexander, D. M. 2012, ApJ, 760

Smith, H. E. & Spinrad, H. 1980, Publications of the Astronomical Society of the Pacific, 92, 553

Solomon, P. M., Downes, D., Radford, S. J. E., & Barrett, J. W. 1997, ApJ, 478, 144

Soto, K. T., Lilly, S. J., Bacon, R., Richard, J., & Conseil, S. 2016, MNRAS, 458, 3210

Speagle, J. S., Steinhardt, C. L., Capak, P. L., & Silverman, J. D. 2014, ApJS, 214, 15

Spilker, J. S., Marrone, D. P., Aguirre, J. E., et al. 2014, ApJ, 785, 149

Spinrad, H. & Bahcall, N. A. 1976, Publications of the Astronomical Society of the Pacific, 88, 660

Spinrad, H., Westphal, J., Kristian, J., & Sandage, A. 1977, Apj, 216, L87

Stalevski, M., Fritz, J., Baes, M., Nakos, T., & Popović, L. Č. 2012, MNRAS, 420, 2756

Stanley, F., Alexander, D. M., Harrison, C. M., et al. 2017, MNRAS, 472, 2221

Stanley, F., Harrison, C. M., Alexander, D. M., et al. 2015, MNRAS, 453, 591

Stark, D. P., Schenker, M. A., Ellis, R., et al. 2013, ApJ, 763, 129

Stevens, J. A., Ivison, R. J., Dunlop, J. S., et al. 2003, Nature, 425, 264

Strong, A. W., Moskalenko, I. V., Reimer, O., Digel, S., & Diehl, R. 2004, AA, 422, L47

Sturm, E., González-Alfonso, E., Veilleux, S., et al. 2011, Apj, 733, L16

Summerlin, E. J. & Baring, M. G. 2012, ApJ, 745, 63

Swinbank, A. M., Vernet, J. D. R., Smail, I., et al. 2015, MNRAS, 449, 1298

Tacconi, L. J., Genzel, R., Neri, R., et al. 2010, Nature, 463, 781

Tacconi, L. J., Neri, R., Genzel, R., et al. 2013, ApJ, 768, 74

Tadhunter, C., Holt, J., González Delgado, R., et al. 2011, MNRAS, 412, 960

Tasca, L. A. M., Le Fèvre, O., Hathi, N. P., et al. 2015, A&A, 581, A54

Thomas, D., Maraston, C., Bender, R., & Mendes de Oliveira, C. 2005, ApJ, 621, 673

Thomas, D., Maraston, C., Schawinski, K., Sarzi, M., & Silk, J. 2010, MNRAS, 404, 1775

Tielens, A. G. G. M., Miley, G. K., & Willis, A. G. 1979, Astronomy and Astrophysics Supplement Series, 35, 153

Tinsley, B. M. 1968, ApJ, 151, 547

Tomczak, A. R., Quadri, R. F., Tran, K.-V. H., et al. 2016, ApJ, 817, 118

Tonini, C., Bernyk, M., Croton, D., Maraston, C., & Thomas, D. 2012, ApJ, 759, 43

Trakhtenbrot, B., Urry, C. M., Civano, F., et al. 2015, Science, 349, 168

Tumlinson, J., Peeples, M. S., & Werk, J. K. 2017, Annual Review of Astronomy and Astrophysics, 55, 389

Turner, M. L., Schaye, J., Steidel, C. C., Rudie, G. C., & Strom, A. L. 2014, MNRAS, 445, 794

Urry, C. M. & Padovani, P. 1995, Publications of the Astronomical Society of the Pacific, 107, 803

van Breugel, W., De Breuck, C., Stanford, S. A., et al. 1999, Apj, 518, L61

van Breugel, W. J. M., Stanford, S. A., Spinrad, H., Stern, D., & Graham, J. R. 1998, ApJ, 502, 614 van Dokkum, P. G., Franx, M., Kriek, M., et al. 2008, ApJ, 677, L5

van Dokkum, P. G., Whitaker, K. E., Brammer, G., et al. 2010, ApJ, 709, 1018

van Ojik, R., Roettgering, H. J. A., Carilli, C. L., et al. 1996, A&A, 313, 25

van Ojik, R., Roettgering, H. J. A., Miley, G. K., & Hunstead, R. W. 1997, A&A, 317, 358

Vayner, A., Wright, S. A., Murray, N., et al. 2017, ApJ, 851, 126

Vernet, J., Lehnert, M. D., De Breuck, C., et al. 2017, A&A, 602

Villar-Martín, M., Vernet, J., di Serego Alighieri, S., et al. 2003, MNRAS, 346, 273

Volonteri, M., Capelo, P. R., Netzer, H., et al. 2015a, MNRAS, 452, L6

Volonteri, M., Capelo, P. R., Netzer, H., et al. 2015b, MNRAS, 449, 1470

Vulcani, B., Marchesini, D., De Lucia, G., et al. 2016, ApJ, 816, 86

Wagg, J., Wilner, D. J., Neri, R., Downes, D., & Wiklind, T. 2006, ApJ, 651, 46

Wang, R., Wagg, J., Carilli, C. L., et al. 2013, ApJ, 773, 44

Weiß, A., Henkel, C., Downes, D., & Walter, F. 2003, A&A, 409, L41

Wells, D. C., Greisen, E. W., & Harten, R. H. 1981, Astronomy and Astrophysics Supplement Series, 44, 363

Werk, J. K., Prochaska, J. X., Tumlinson, J., et al. 2014, ApJ, 792, 8

Werner, M. W., Roellig, T. L., Low, F. J., et al. 2004, The Astrophysical Journal Supplement Series, 154, 1

Westmoquette, M. S., Dale, J. E., Ercolano, B., & Smith, L. J. 2013, MNRAS, 435, 30

Whitaker, K. E., Franx, M., Leja, J., et al. 2014, ApJ, 795, 104

Whitaker, K. E., van Dokkum, P. G., Brammer, G., & Franx, M. 2012, ApJ, 754, L29

Willott, C. J., Bergeron, J., & Omont, A. 2015, ApJ, 801, 123

Willott, C. J., Bergeron, J., & Omont, A. 2017, ApJ, 850, 108

Wilson, W. E., Ferris, R. H., Axtens, P., et al. 2011, MNRAS, 416, 832

Wisotzki, L., Bacon, R., Blaizot, J., et al. 2016, A&A, 587

Wright, E. L., Mather, J. C., Bennett, C. L., et al. 1991, ApJ, 381, 200

Wylezalek, D., Galametz, A., Stern, D., et al. 2013, ApJ, 769, 79

Young, J. S. & Scoville, N. Z. 1991, Annual Review of Astronomy and Astrophysics, 29, 581

Younger, J. D., Omont, A., Fiolet, N., et al. 2009, MNRAS, 394, 1685

Zhang, Z.-Y., Romano, D., Ivison, R. J., Papadopoulos, P. P., & Matteucci, F. 2018, Nature, 558, 260

Zhu, G. & Ménard, B. 2013, ApJ, 770, 130

Acknowledgements

Ever since I was kid, I watched the Nobel dinner on TV. Yes, that is actually a thing in Sweden. Every year with my mum and grandmother, I remember being amazed by this celebration of Science. As my curiosity for understanding how nature work grew more and more, the idea of becoming a scientist developed and this dream has been a huge motivation for me. Now, about 15 years later, I am writing up my doctoral thesis and I would not have gotten this far without the support and encouragement from family and friends, as well as the opportunities offered to me by people who believed in me. These last three years have been more interesting and life changing than I could ever have imagined. I feel like I have grown, experienced a lot, and met many nice people who made this PhD experience great. I would like to address some of these people now.

First of all, I would like to thank my three PhD supervisors. **Matt**, thank you for believing in me and working hard to make this shared thesis between IAP and ESO become a reality. **Carlos** and **Joël**, thank you for being so supportive throughout this thesis. After having had a meeting with you, I always felt so much better. It really helped me calm down when I was stressed and it also put things in perspective. Joël, your eye for details when it comes to data analysis is impressive and inspiring. Carlos, besides very useful scientific discussions, our chats often also included some gossip, your opinions on food and laugher. Thanks for showing me that there is so much more to science and also for giving me the opportunity to do real observations.

Besides my PhD superiors, I would also like to thank my two master thesis supervisors, who led me into astronomy. **Kirsten**, you are an amazing scientist and supervisor and encouraged me to pursue a PhD. **Guillaume**, thank you for introducing me to ESO, it is because of you that I ended up working with Carlos, Joël and Matt. You are a good supervisor, and taught me about all the caveats of SED fitting. You have also been a great collaborator during my PhD and and I am glad to have you as friend.

I would like to thank ESO for giving me the opportunity to spend two years of my PhD at the headquarters in Garching, as well as providing the support to go to conferences, meetings and two observing rounds at APEX. The environment at ESO is really unique. Students, fellows and staff members create a very special environment, and I feel fortunate to have been part of it. I would also like to thank IAP for being my home institute and making this PhD possible.

Of the many other people I met in Germany and France, I would like to thank a few especially (in random order). **Marco**, you were my first office mate at ESO and I would like to thank you for being so friendly, always ready to help me if I had computer issue and also for all the nice chats about life as a scientist, happiness and personal beliefs, thanks for sharing. **Darshan**, you are one of the most sociable persons I know, which I find really cool. You contributed in making the PhD time fun, filled with trips, laughter, Friends references and nice memories. **Matthieu**, thanks for helping me with CASA problems when I started doing data reduction. It was great to have someone to ask and thanks for taking the time to help me. **Paco**, you were a fun officemate and I think your time at ESO was way too short. I am glad we got to go on a road trip together on our way to the OPC100, the rest of us in the car should actually have helped you more with the driving. **Esther**, I am so glad that you decided to sub-rent a room to me when I first arrived in Germany, you where a better flatmate than I could have hoped for. Even though we had some problems with crazy landlords, asbestos and finding a new flat, we still had a great time together. It was so nice to share a home with someone that could relate to the same things and to talk to someone outside astrophysics for once. **Thabs**, you have a great personality and I wished we would have overlapped longer at ESO, so I could have gotten to know you better. **Haakon**, my second favorite flatmate (naaah, just kidding). Sharing a flat with you was fun and it was great to have someone around to make jokes with. I know to others it may have sometimes seemed like we were a bit mean to each other, but I think then they didn't get your sense of humor. To me it felt similar to when my sisters and I tease each other. Thanks for making München feel more like home and also for being a great cook. **Oskar**, the last year of PhD is an interesting time and it was great to have someone else going through the same things to relate to. Thanks for all the times we were discussing the future, thesis writing, papers and how to handle our expectations of ourselves. **Claire, Abele** and **Corentin**, thanks for being nice officemates and helping me whenever I had French related problems and did not know how things work at IAP.

Last but not least, I would like to thank my family, who's support has always been there. My parents **Birgitta** and **Hans-Olof** encouraged me to study what I found exciting and would make me happy. You have always been there to help and support me the best you could, even though it lead me further away from home than you would probably have preferred. My dear sisters **Fathima** and **Clarinda**, you have been there whenever I needed someone to talk to or to take my mind off things and feel connected to my family. I am lucky to have a such a nice family. **Erik**, you have been there for me for so many years, helped me through gymnasium and university and also encouraged me to move abroad for my PhD. **Christian**, you helped me grow as a person and made me dare to do more things than I would have done otherwise. I cannot thank you enough for your love and support while writing this thesis.

Tack!